Advanced Space Concepts Laboratory
Department of Mechanical and Aerospace Engineering
Faculty of Engineering
University of Strathclyde

Macro-scale Space Systems for Geoengineering

Russell Bewick

Submitted in fulfilment of the requirements for
the degree of Doctor of Philosophy (PhD)
2013

This thesis is the result of the author's original research. It has been composed by the author and has not been previously submitted for examination which has led to the award of a degree.

Russell Bewick
Stevenage, United Kingdom, April 2013

Supervisors

First supervisor:

Prof. Colin R. McInnes
Advanced Space Concepts Laboratory, University of Strathclyde
Glasgow, United Kingdom

Second supervisor:

Dr. Joan-Pau Sanchez
Advanced Space Concepts Laboratory, University of Strathclyde
Glasgow, United Kingdom

Examiners

External examiner:

Prof. Chris Welch
International Space University
Illkirch-Graffenstaden, France

Internal examiner:

Dr. James Biggs
Advanced Space Concepts Laboratory, University of Strathclyde
Glasgow, United Kingdom

Acknowledgements

Writing this thesis has been a long process and there are many people and institutions that have contributed to its completion. First of all, I would like to thank Prof. Colin McInnes for giving me the opportunity to be a PhD student at the Advanced Space Concepts Laboratory. I would especially like to thank Colin for his great help and guidance throughout the duration of this PhD, the support for conference visits and journal submissions. I would also like to thank my second supervisor, Dr. Joan-Pau Sanchez, for his great support and ideas. I have really enjoyed working with you. Finally, I would like to thank all the other members of the ASCL and StrathSEDS who have been great colleagues and a wonderful source of entertainment throughout my time in Glasgow.

Next, I would like to thank the institutions that have supported me during my PhD. Firstly, I would like to thank the European Research Council (ERC) which funded my PhD through the Advanced Investigator Grant - 227571: VISIONSPACE: Orbital Dynamics at Extremes of Spacecraft Length-Scale. Secondly, I would like to thank the European Space Agency and the Royal Aeronautical Society for providing funding to attend a number of space conferences.

Finally, I would like to thank my family and friends for their support and encouragement throughout the years that have helped me to reach this milestone. My greatest gratitude goes to my wife, Charlotte, for her loving support and companionship in these years we spent in Glasgow. Thank you for all the times you have helped me when I needed encouragement and all the love you have given me. Being in Glasgow with you was the most perfect time.

Abstract

There are many pressures facing the future of human presence on the Earth. These are the effects of a changing climate and the finite resources of Earth. This thesis sets out several space-based scenarios that can be implemented to reduce these pressures, namely space-based geoengineering to offset the effect of a warming climate and the use of orbiting reflectors to reduce the challenges of human exploration of the Moon.

Several dust cloud based geoengineering methods are investigated, with the aim of improving on the previously held view that these methods are extremely costly and far-term. These include an initially static dust cloud located in the vicinity of the L_1 position, a dust cloud created by ejection from the L_1 point, a dust cloud anchored at L_1 by the mass of a large, captured, near-Earth asteroid and an Earth ring. For all of these concepts the orbital dynamics and other contributing factors were considered to determine the mass of dust required to sustain the dust cloud, which is used as the main benchmark of feasibility. As well as this, the engineering feasibility of each concept is considered with a consideration also of the effect each method has on the climate. From this analysis it is concluded that the dust cloud ejected from the vicinity of the L_1 point is the most feasible concept.

Contents

Abstract i

Table of Contents ii

List of Figures vi

List of Tables xi

Nomenclature xii

1 Introduction 1

1.1 Climate Change . . . 2

1.1.1 IPCC Emissions Scenarios . . . 3

1.2 Geoengineering methods . . . 4

1.2.1 Space-based geoengineering . . . 8

1.2.2 The geoengineered world . . . 10

1.3 Ethical and political considerations of geoengineering . . . 13

1.3.1 Should we geoengineer the climate? . . . 13

1.3.2 What constitutes geoengineering? . . . 15

1.3.3 How will geoengineering be governed? . . . 16

1.4 Thesis Contributions and Structure . . . 19

1.5 Published Work . . . 20

2 Static Cloud at L_1 22

2.1 Dust Dynamics . . . 22

2.1.1 Three-body problem . . . 22

2.1.2 Perturbation forces . . . 25

2.1.3 Effect of solar radiation pressure . . . 30

2.1.4 Transition matrix . . . 31

2.2 Solar Radiation Model . . . 34

2.2.1 Model structure . . . 34
2.2.2 Attenuation calculation . . . 36
2.2.3 Static model . . . 36
2.2.4 Dynamic model . . . 38
2.2.5 Static model testing . . . 39
2.3 Results . . . 41
2.3.1 Stability analysis . . . 41
2.3.2 Dynamic solar radiation model results . . . 42
2.3.3 Anticipated accuracy . . . 48
2.4 Discussion . . . 48
2.4.1 Comparison to previous proposals . . . 49
2.5 Conclusion . . . 51

3 Gravitationally Anchored Dust Cloud at L_1 52
3.1 Four-Body Problem . . . 52
3.2 Zero Velocity Curve . . . 54
3.3 Effect on Solar Insolation . . . 56
3.3.1 Asteroid selection . . . 56
3.3.2 Solar radiation model . . . 59
3.3.3 Results for $R_{gr} = 32\mu$m . . . 60
3.3.4 Results for $R_{gr} > 32\mu$m . . . 60
3.3.5 Insolation reduction map . . . 62
3.4 Discussion . . . 65
3.4.1 Loss mechanisms . . . 65
3.4.2 Grain lifetime . . . 66
3.4.3 Contribution of escaped grains to the insolation reduction . . . 67
3.4.4 Implementation roadmap . . . 68
3.5 Conclusion . . . 69

4 Ejected Cloud at L_1 70
4.1 Dynamics . . . 70
4.2 Solar radiation model . . . 72
4.2.1 Initial velocity distribution . . . 73
4.3 Results . . . 73
4.3.1 Optimisation of the ejection angle . . . 75
4.3.2 Sphere . . . 85
4.3.3 Cone . . . 86
4.4 Conclusion . . . 92

5 Earth Ring **93**

5.1 Orbital Dynamics . . . 93

5.1.1 Hamiltonian model of dust orbital dynamics . . . 94

5.1.2 Choice of feeder orbit . . . 96

5.2 Geoengineering scenario . . . 96

5.2.1 Dust source . . . 96

5.2.2 Dust grain size distributions . . . 98

5.3 Ring Attenuation . . . 99

5.4 Mass requirement . . . 105

5.5 Discussion . . . 107

5.5.1 Thermal radiation and solar reflection . . . 107

5.5.2 Risk to spacecraft . . . 110

5.5.3 Effect on communications . . . 112

5.6 Conclusion . . . 112

6 Climate Model **114**

6.1 Introduction to climate modelling . . . 114

6.2 One dimensional climate model . . . 115

6.2.1 Solar Flux . . . 115

6.2.2 Heat Transport . . . 118

6.2.3 Thermal Emission . . . 119

6.2.4 Climate warming . . . 119

6.2.5 Summary . . . 120

6.3 Model testing . . . 121

6.3.1 Climate sensitivity and radiative forcing . . . 121

6.4 Insolation Map . . . 124

6.5 Results . . . 128

6.6 Conclusion . . . 133

7 Engineering a Dust Dloud **135**

7.1 Asteroid Material . . . 136

7.1.1 Asteroid capture . . . 136

7.1.2 Asteroid positioning . . . 138

7.1.3 Impact Risk . . . 139

7.1.4 Asteroid Regolith . . . 140

7.1.5 Processed asteroid material . . . 145

7.2 Lunar Material . . . 145

7.2.1 Required material . . . 145

7.2.2 Material availability . . . 147
7.2.3 Transport to L_1 . . . 149
7.3 Cloud generation methods . . . 149
7.3.1 Solar collector/sublimation . . . 149
7.3.2 Mass driver . . . 151
7.3.3 Spin fragmentation . . . 152
7.3.4 Summary . . . 153
7.4 Comparison to solar reflector manufacture in-situ . . . 154
7.5 Technology Development Roadmap . . . 155
7.5.1 Phase 1 - Asteroid capture demonstration . . . 156
7.5.2 Phase 2 - Mass driver and asteroid mining . . . 158
7.5.3 Phase 3 - Capture to L_1 . . . 158
7.5.4 Phase 4 - Cloud generation . . . 159
7.5.5 Phase 5 - Insolation reduction . . . 159
7.5.6 Phase 6 - Gradual implementation . . . 160
7.5.7 Summary . . . 161
7.6 Conclusion . . . 161

8 Conclusions **164**
8.1 Summary and Conclusions . . . 164
8.1.1 L_1 dust cloud . . . 164
8.1.2 Earth ring . . . 167
8.1.3 Dust cloud engineering feasibility . . . 167
8.1.4 Main Conclusions . . . 168
8.2 Future Research . . . 169

Bibliography **172**

A Earth Ring Appendix **181**
A.1 Earth Ring Orbital Dynamics . . . 181
A.1.1 Hamiltonian model of dust orbital dynamics . . . 181
A.1.2 In-plane orbital evolution of dust . . . 184
A.1.3 Choice of feeder orbit . . . 185
A.1.4 3D orbital evolution of dust . . . 188
A.2 Ring model . . . 191
A.2.1 In-plane model . . . 191

B Beer-Lambert Law **194**

List of Figures

1.1 Radiative forcing of various environmental components. 5
1.2 Measured and predicted global mean temperature between 1900 and 2100. 5
1.3 Royal Society rating of geoengineering schemes. 6
1.4 Impression of an L_1 positioned dust cloud for space-based geoengineering [Image created by Charlotte Bewick using material from ESA and NASA]. 20

2.1 Geometry of the circular restricted three-body problem with the Sun, M_1, Earth. M_2 and dust grain m. 25
2.2 Momentum transfer coefficient of a silicate particle with respect to the solar wind. 27
2.3 Acceleration on small dust grains from solar system forces. 29
2.4 Value of β for a silicate dust grain. 32
2.5 Sunwards shift of the equilibrium position due to β in the CR3BP. 32
2.6 Motion of a dust cloud propagated using the transition matrix approach. 35
2.7 Structure of the solar radiation model. 37
2.8 Example of the distribution of nodes in the solar radiation model. 37
2.9 Solar constant on Earth calculated using the solar radiation model. 40
2.10 Solar constant calculated with a geoengineering dust cloud 40
2.11 Average lifetime of particles in a dust cloud positioned at the classical L_1 point. . . 43
2.12 Average lifetime of particles in a dust cloud positioned at the displaced equilibrium position. 43
2.13 Mass requirement of dust for clouds ejected at the L_1 point. 45
2.14 Mass requirement of dust for clouds ejected at the displaced equilibrium position. . 45
2.15 Increase in geoengineering strength to reach a steady state 46
2.16 Insolation reduction over the Earth disk for the cloud released at the classical L_1 point. 47
2.17 Insolation reduction over the Earth disk for the cloud released at the displaced equilibrium position. 47

3.1 Four-body problem with Sun m_S, Earth m_E, asteroid m_A and dust particle m. . . 53
3.2 Gravitational potential at L_1 in the CR4BP for $\beta = 0$. 57
3.3 Gravitational potential at L_1 in the CR4BP for $\beta = 0.001$. 57
3.4 Size of ZVC for a range of asteroid sizes for $\beta = 0.005$ 58
3.5 Impulse to capture the largest NEAs to L_1 58
3.6 Maximum insolation reduction using an asteroids ZVC 61
3.7 Maximum insolation reduction for grains sizes above 32μm at perihelion and aphelion for the asteroid Ganymed. 61
3.8 Mass fraction of the ZVC dust cloud for Ganymed and Eros. 63
3.9 Maximum insolation reduction for grains sizes above 32μm at perihelion and aphelion for the asteroid Eros. 63
3.10 Reduction in insolation over the Earth's surface for the ZVC method at the equilibrium position. 64
3.11 Reduction in insolation over the Earth's surface for the ZVC method at the L_1 position. 64

4.1 Diagram showing the key angles 76
4.2 Example of mean lifetimes for material ejected at various angles 76
4.3 The angular sections used to characterise the spread of particles within the useful zone 77
4.4 Time required to calculate the mean lifetime of an ejecta cloud with varying numbers of particles. 78
4.5 Standard deviation of mean lifetimes in relation to the mean of the set for varying number of ejecta particles. 78
4.6 Average lifetime of dust grains, with $\beta = 0.005$, within the useful zone when ejected from the classical L_1 point for a range of cone spread angles, θ, initial mean velocities, μ_v and velocity standard deviations, σ_v. 80
4.7 Average lifetime of dust grains, with $\beta = 0.751$, within the useful zone when ejected from the classical L_1 point for a range of cone spread angles, θ, initial mean velocities, μ_v and velocity standard deviations, σ_v. 81
4.8 Average lifetime of dust grains, with $\beta = 0.005$, within the useful zone when ejected from the displaced equilibrium position for a range of cone spread angles, θ, initial mean velocities, μ_v and velocity standard deviations, σ_v. 82
4.9 Average lifetime of dust grains, with $\beta = 0.751$, within the useful zone when ejected from the displaced equilibrium position for a range of cone spread angles, θ, initial mean velocities, μ_v and velocity standard deviations, σ_v. 83

4.10 Difference in average lifetime between the ejected dust clouds with the smallest and greatest velocity standard distributions, $\sigma_v = 0.001\mu_v$ and $\sigma = 0.1\mu_v$ respectively, for the range of cone spread angles, θ and mean velocities, μ_v. 84
4.11 Mass requirement for a spherical ejection of material at the classical L_1 point for a range of mean velocities and β values of 0.005 and 0.751. 87
4.12 Surface temperature of the Moon 87
4.13 Mass-per-year required to reduce solar insolation by 1.7% for a dust cloud ejected from the classical L_1 point under conditions to maximise the expected lifetime of the cloud. 90
4.14 Mass-per-year required to reduce solar insolation by 1.7% for a dust cloud ejected from the classical L_1 point under conditions to maximise the expected spread of the cloud. 90
4.15 Mass-per-year required to reduce solar insolation by 1.7% for a dust cloud ejected from the displaced equilibrium position under conditions to maximise the expected lifetime of the cloud. 91
4.16 Mass-per-year required to reduce solar insolation by 1.7% for a dust cloud ejected from the displaced equilibrium position under conditions to maximise the expected spread of the cloud. 91

5.1 Geometry of an in-plane orbit in the synodic reference frame. 95
5.2 Minimum eccentricity of the heliotropic orbit 95
5.3 Minimum feasible radius and geometrical efficiency of dust grains in heliotropic Earth orbit. 97
5.4 Diagram of the generator and feeder orbits for the Earth ring. 100
5.5 Probability density functions for the three distributions of grain radii considered. . 100
5.6 In-plane attenuation coefficient in polar coordinates and in relation to the maximum attenuation. 102
5.7 Sum of the in-plane number density for different solar angles θ in relation to the average. 103
5.8 Geometry of the tilt of the Earth ring with respect to the Sun 104
5.9 Variation in insolation over the course of a year for the Earth ring concept. 106
5.10 Distribution of the insolation reduction of the Earth ring. 106
5.11 Geometry of the F_{in} and F_{out} variables 109
5.12 Flux contribution to Earth of an Earth ring grain due to thermal radiation and solar reflection. 111
5.13 Impact rate of particles on a spacecraft travelling through the Earth Ring. 111

6.1 Diagram of the one dimensional climate model. 116

6.2 Solar weighting in the 1D climate model from various sources. 116
6.3 Solar constant over the period of a year as a function of latitude. 118
6.4 Response of a 1D climate model to a doubling of CO_2. 122
6.5 Reduction in solar constant for the equilibrium point cloud. 123
6.6 Reduction in solar constant for the L_1 point cloud. 123
6.7 Insolation reduction on Earth due to the Earth ring. 124
6.8 Insolation reduction averaged over an entire year for different latitude bands for the static cloud concept. 126
6.9 Insolation reduction averaged over an entire year for different latitude bands for the gravitationally anchored dust cloud. 126
6.10 Insolation reduction averaged over an entire year for different latitude bands for the case of a cloud ejected with an initial velocity distribution. 127
6.11 Insolation reduction averaged over an entire year for different latitude bands for the Earth ring. 127
6.12 Mean temperature change due to a doubling of CO_2 with different space-based geoengineering scenarios applied. 130
6.13 Temperature reduction averaged over an entire year for different latitude bands for the static cloud concept. 131
6.14 Temperature reduction averaged over an entire year for different latitude bands for the gravitationally anchored dust cloud. 131
6.15 Temperature reduction averaged over an entire year for different latitude bands for the case of a cloud ejected with an initial velocity distribution. 132
6.16 Temperature reduction averaged over an entire year for different latitude bands for the Earth ring. 132

7.1 Expected resources as a function of Δv threshold [85]. 137
7.2 Example probability density function for asteroid regolith. 143
7.3 Mass requirement for the use of an asteroid regolith size distribution when released at the classical L_1 point. 143
7.4 Probability density function for lunar dust grains, as described by [26]. 148
7.5 Mass requirement for the lunar regolith and processed asteroid regolith size distributions as well as the minimum and maximum mass requirement results described in Chapter 2. 148
7.6 Manufacturing times for the required area of thin film solar reflectors suggested in [69] for different mass deposition rates for in-situ fabrication. 155
7.7 Impression of an L_1 positioned dust cloud for space-based geoengineering [Image created by Charlotte Bewick using material from ESA and NASA]. 157
7.8 Insulation reduction for various mass ejection rates. 160

7.9 Technological development roadmap for the dust cloud method of space-based geo-engineering. 162

A.1 Geometry of an in-plane orbit in the synodic reference frame. 183
A.2 Minimum eccentricity of the heliotropic orbit 183
A.3 Orbital evolution in the $e - \phi$ phase space for grains in a circular and eliptic orbit. 186
A.4 Minimum feasible radius and geometrical efficiency of dust grains in heliotropic Earth orbit. 187
A.5 3D orbital evolution of dust grains in a heliotropic orbit. 189
A.6 Maximum and minimum inclination change for grains in a heliotropic Earth orbit. 189
A.7 Seasonal evolution of the Earth Ring after 20 years. 190
A.8 Number density relative to average number density in the phase space for different grain radius distributions. 193

B.1 Variables used in the Beer-Lambert law 195

List of Tables

1.1 The key characteristics of proposed space-based geoengineering schemes to offset global warming. 10

2.1 Solar Wind properties in the vicinity of Earth. 28
2.2 Grain radii used along with the key properties. 44

4.1 The range of velocities considered for the mean velocity, velocity standard deviation and angular spread. 73
4.2 Average, and standard deviation, of the difference in mean lifetime between the optimisations for the initial velocity standard deviations of $\sigma_v = 0.001\mu_v$ and $\sigma_v = 0.1\mu_v$. There results are shown for β values of 0.005 and 0.751 for the displaced equilibrium and classical L_1 positions. 85
4.3 Optimum mass requirement for each simulation scenario considered for the ejection of a dust cloud into a cone. 88

5.1 Mean and standard deviation values of the three dust grain distributions in a log-normal distribtuion. 99
5.2 Mass requirement for the three Earth ring dust distributions. 105

6.1 Coefficients of the 1D climate model. 119

7.1 Acceleration required to maintain the position of an object placed at the displaced equilibrium position of different grain sizes, corresponding to different values of β and distances to the classical L_1 point. 139
7.2 Approximate means and standard deviations of asteroid regolith size distribution. . 142
7.3 Mean characteristics of five sections of the lunar regolith size distribution. 146
7.4 Trade-off of different cloud generation methods based on the engineering considerations discussed in this section. 154

Nomenclature

Acronyms

CR3BP	Circular Restricted Three-body Problem
GEO	Geostationary Earth Orbit
LEO	Low Earth Orbit
MEO	Medium Earth Orbit
SBGE	Space-based geoengineering
SRP	Solar Radiation Pressure

Chapter 2 - Static Cloud at $\mathbf{L}_1$

α_{gr}	Extinction coefficient
β	Lightness parameter
μ	Mass ratio of the second body w.r.t the system mass in the CR3BP
$\Phi(t, t_0)$	Transition matrix
$\rho(\mathbf{x}; t)$	Number density of dust grains in the phase space
ρ_n	Number density of dust grains
$\rho_{1,2}$	Non-dimensional separation of the third body to the two primary bodies in the CR3BP
σ_{gr}	Grain cross-sectional area
c	Speed of light
F_{SRP}	Force due to solar radiation pressure
I	Attenuated solar flux
l	Path length
$L_\odot$	Solar luminosity
M_1, M_2	Mass of the two primary bodies in the CR3BP
Q	SRP coupling coefficient

$r_\odot$	Distance to the Sun
R_{gr}	Grain radius
U	Non-dimensional potential function in the CR3BP
$X(t)$	State vector at time t

Chapter 3 - Gravitationally Anchored Dust Cloud at L_1

γ	mass fraction of an asteroid with respect to the system mass
λ	Mean free path
μ	Mass ratio of the second body w.r.t the system mass in the CR3BP
μ_{log}	Mean of the log-normal distribution
ρ_n	Particle number density
$\rho_{1,2,3}$	non-dimensional separation of a dust grain to the Sun, Earth and Asteroid respectively
σ_{gr}	Grain cross-sectional area
σ_{log}	Standard deviation of the log-normal distribution
C	Jacobi constant
$f_{\mu_{log},\sigma_{log}}(R_{gr})$	Lognormal probability density function
l	Path length
m_A	Asteroid mass
$m_{32\mu m}$	Mass of a dust grain with a radius of $32\mu m$
R_{gr}	Grain radius
U	Potential function
V	Particle speed
V_{crit}	Ejection velocity required to reach the zero velocity curve
V_{ZVC}	Volume of the zero-velocity curve

Chapter 4 - Ejected Cloud at L_1

μ_v	Mean velocity
$\Phi(t, t_0)$	Transition matrix
$\rho_n(l)$	Number density of dust grains at a given point
σ_v	Velocity standard deviation
σ_{gr}	Cross-sectional area of a dust grain
θ	Cone spread angle
C	Jacobi constant

I_0	Flux contribution of a Sun node in the SRM
l	Path length
$X(t)$	Final state vector
$X(t_0)$	Initial state vector

Chapter 5 - Earth Ring

α_{gr}	Absorptivity of a dust grain
δi	Maximum spread in inclination of the Earth ring
Λ	Attenuation coefficient
μ_{log}	Mean of a log-normal distribution
$\rho(R_{gr})$	Number density of dust grains with radius R_{gr} at a point in the Earth ring
σ_{log}	Standard deviation of a log-normal distribution
θ	Angle between a dust grains position and the direction of solar insolation
a_g	Semi-major axis of the generator orbit
I_0	Solar constant
J_2	Earth oblateness parameter
l	Path length in the Earth ring
R	Distance to the centre of the Earth
R_{gr}	Grain radius
R_{max}	Maximum extent of the Earth ring

Chapter 6 - Climate Model

$\alpha(T_i)$	Temperature dependent albedo of the latitude band
$\bar{T}$	Mean global temperature
ΔT	Temperature change
δ	Declination at a given point in the Earth's orbit
λ	Climate sensitivity
ω	Angle to position the Earth at the vernal equinox for $\theta = 0$
θ	angle of Earth within its orbit
ε	Inclination of the Earth's axis
A	Thermal emission constant
B	Thermal emission constant
F_i	Energy transport between latitude bands
h_0	Length of day in the Sun for a given latitude

I_0	Solar constant
I_{RF}	Radiative forcing constant
K	Heat transfer coefficient
Q_{day}	Daily averaged solar flux
R_0^2	Mean distance between the Earth and Sun
R_E^2	Distance between the Earth and Sun at a point in the Earth's orbit
$R_{\uparrow,i}$	Re-radiation from a latitude band
$R_{s,i}$	Solar flux input into latitude band i
S_i	Weighting of the solar constant
T_c	Boundary temperature where the albedo changes
T_i	Temperature of the latitude band

Chapter 7 - Engineering a Dust Cloud

Δv	Change in velocity
μ_r	Mean grain size of asteroid regolith
Φ	Size parameter of lunar regolith
σ	Standard deviation of an asteroid regolith size distribution
D	Grain diameter
T_{spot}	Spot temperature of focusses sunlight
Z	Sublimated mass flux

Chapter 1

Introduction

The increase in global population and consumption of natural resources over the past century has led to an increased pressure on the global environment, chiefly in terms of global warming and the depletion of natural resources. With a western lifestyle requiring the resources of multiple worlds[1] and the aspiration of emerging economies to attain the same level of development, these pressures will increase considerably over the coming decades. To reduce this pressure, humanity must adapt to these new realities by developing new methods and technologies and alter how we interact with the environment in which we live. However, this process may not be fast enough to prevent a significant change in the Earth's climate. This thesis shall set out several methods by which the pressures exerted on the Earth can be reduced in the form of geoengineering. This will begin, in this chapter, with a review of the current state of the environment, and our situation within it, as well as an introduction to geoengineering. This will include a technical description of different geoengineering methods as well as the associated risks, and finally a discussion on the surrounding ethical and legal aspects of the implementation and governance of geoengineering. In the following chapters several methods of geoengineering based outside of the Earth's atmosphere will be described and their effects on the environment will be assessed.

[1] The Global Footprint Network [35] estimates that the global ecological footprint is 2.7 gha/per (global hectares per person) whilst the global bioproductivity is only 1.78 gha/per. In contrast the ecological footprints of consumption for Europe and North America are 4.68 gha/per and 7.9 gha/per giving values of 2.42 and 4.43 times the global mean bioproductivity.

1.1 Climate Change

One of the most pressing long-term concerns to humanity is the threat of climate change. This is driven by multiple factors, with the main contributors being the increasing concentrations of several "greenhouse gases" (GHG), mainly CO_2, CH_4 and N_2O, in the atmosphere. These gases have the effect of trapping outgoing longwave radiation, leading to a mean global temperature increase. There is now little doubt within the scientific community that the dominant factor in the changing climate of the Earth is the anthropogenic emission of these gases, as well as the emission of other contributors such as black carbon [18]. The probability of this assessment being accurate is termed "very likely" (90% probability) by the IPCC [46]. The respective contributions of the three main GHGs to date can be seen in Fig. 1.1, as well as the contributions of other factors. The contributions are presented in terms of radiative forcing [$\mathrm{W\,m^{-2}}$], which is the equivalent increase in mean solar input to the Earth's surface for the measured effect.

As seen in Fig. 1.1, the global climate has many contributing components which lead to an increase in global mean temperature. The increase in temperature and the physics of individual components can create feedback loops, which can be positive or negative. For example, the positive ice-albedo feedback, whereby increasing temperatures leads to ice loss, will cause more energy being absorbed into the climate system since less incoming solar radiation is reflected back into space. These feedback effects, many of which are not yet fully understood, make a complete understanding of the climate difficult. Apart from the anthropogenic factors affecting the global climate system there are also other natural factors that must be noted. For example, the solar cycle weakly modulates energy input into the climate system. Even small changes in input can lead to measurable differences in global temperature. During the 11-year solar cycle solar luminosity varies by 0.07%, leading to a global temperature variation of 0.2°C [101]. A long decrease in northern hemisphere temperature, known as the little ice age, is thought to be due to modulation of solar activity [51].

It is expected that global mean temperatures will rise by 1.1-6.4°C, with respect to the 1980-1999 mean temperature, by the end of the century [46]. This wide range of predictions, as seen in Fig. 1.2, is partly due to the uncertainty in the future level of CO_2 emissions, but also the uncertainties in the modelling of the climate system. The main scenarios for GHG emission can also be seen in Fig. 1.2 and are described in Sec. 1.1.1. The scenarios are not rated in terms of probability but are suggested as a guide to what could be done to reduce the effects of climate change. The A1T and B1 scenarios demonstrate the pathways that should be employed to mitigate climate change, yet they still show an increase in global mean temperature of greater than 1.1°C, but most likely higher. The climate model results also show that, if the concentration of CO_2 in the atmosphere remains constant at the level measured in the year 2000, an increase in temperature

with respect to pre-industrial levels will still be apparent, since CO_2 remains in the atmosphere for a long duration. The apparent lack of agreement on ways to reduce global GHG emissions suggests that it is likely that some temperature increase will be inevitable, with the negative impacts that this will bring, such as more extreme weather events, thawing of glaciers and ice caps and changing coast lines. This lack of action on the mitigation of climate change has led to an increase in the number of proposals for a purposeful direct alteration of the Earth's climate. This field of research is termed climate engineering or geoengineering.

1.1.1 IPCC Emissions Scenarios

Several scenarios for the future emissions of CO_2 have been constructed by the IPCC to demonstrate possible future trends in climate change [76]. The scenarios are characterised based on three categories; economic growth, population growth and technological change. The key properties of these scenarios, described in [76], are summarised below for a better understanding of the range wide in global temperature increase seen Fig. 1.2.

- **A1** - The A1 group of scenarios are generalised by a global attitude to the economy and environment i.e. problems are solved with a global solution. In this scenario there is rapid economic growth, particularly in developing countries, with a reduction in global income inequality. As a result of this there is an intermediate level of population growth which peaks in the middle of the 21^{st} century. This group is split into three sub-groups based on technology.
    - A1FI - In this subgroup the cost of fossil fuel extraction decreases, thus decreasing the rate of uptake of 'green' alternatives.
    - A1T - This subgroup is characterised by a reduction in the cost of 'green' fuels, thus leading to greater uptake of these technologies and decentralised production e.g. microturbines.
    - A1B - The subgroup displays a balance between the previous subgroups, with a general reduction in energy cost and increase in energy efficiency.
- **A2** - This group has the general characteristic of self-reliance of individual countries which leads to slow economic growth due to lower global trade. Due to this global, population growth is high and continues past the end of the century. As a result of slower economic growth there is a slower rate of technological improvement and therefore a continued reliance on fossil fuels.

- **B1** - The B groups show a high level of social consciousness, with the B1 scenario displaying this in global solutions to problems. This results in a convergence in global incomes and a reduction in social inequality. There is an intermediate level of population growth which peaks mid-century. There are large improvements in energy efficiency and a large penetration of non-fossil fuel energy sources.

- **B2** - As for B1, the B2 scenario shows high social consciousness, except that in this scenario it is applied to local attitudes on sustainability. As a result there is relatively low economic growth with a slow rate of convergence of global incomes. The population growth is intermediate and plateaus by the end of the century. There is a moderate conversion to non-fossil fuel energy sources.

The characteristics of these scenarios result in varying rates of CO_2 emissions, as seen in Fig. 1.2. For example the A1 group of scenarios show similar trends, a peak in CO_2 emissions, though the level is strongly effected by the uptake of 'green' technologies. As would be expected the fossil fuel intensive scenario shows the highest emissions and a relatively late peak. In contrast those scenarios with higher income inequality show higher levels of population growth which manifests itself in a continued increase in global emissions.

1.2 Geoengineering methods

Several proposals for possible geoengineering methods have been made and these can generally be placed into two categories; solar radiation management (SM) and carbon dioxide removal (CDR) [95]. Solar radiation management focuses on the reduction of the amount of sunlight being absorbed by the Earth's atmosphere by one of two key methods; increasing the Earth's albedo to reflect more incoming sunlight or by reducing the flux of sunlight reaching the surface, mainly by scattering incoming solar radiation before it reaches the surface. Alternatively, carbon capture techniques aim to deal with the fundamental cause of global warming, by either directly taking CO_2 out of the atmosphere, or indirectly, by inducing an increase in the ability of current carbon sinks to absorb CO_2. In general, solar radiation management techniques are expected to be fast acting, once implemented, whereas carbon sequestration will take many years to significantly reduce CO_2 levels in the atmosphere. Due to the nature of the two methods, carbon sequestration in its direct form, is inherently safer than solar radiation management methods, since the root cause is treated with the expectation of there being fewer side effects. However, this is dependent upon the storage mechanism used. Additionally, SM methods cannot mitigate all the effects of increased CO_2 concentrations, primarily the acidification of the oceans which is likely to harm the

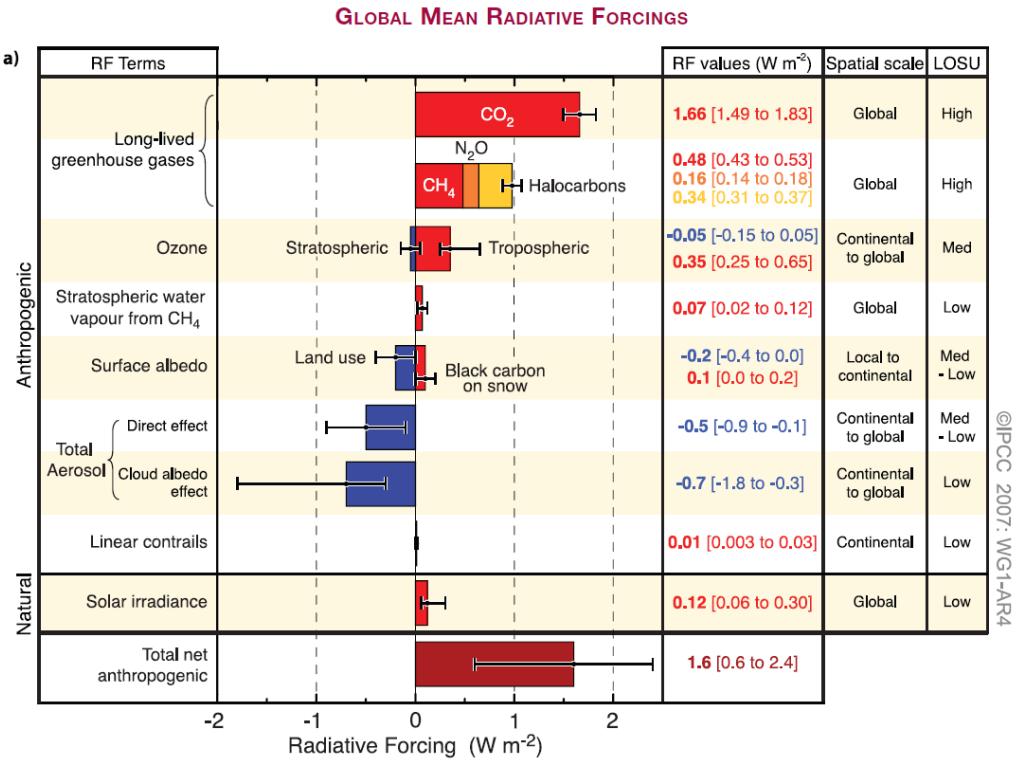

Figure 1.1: Radiative forcing of various environmental components that alter the state of the climate [46].

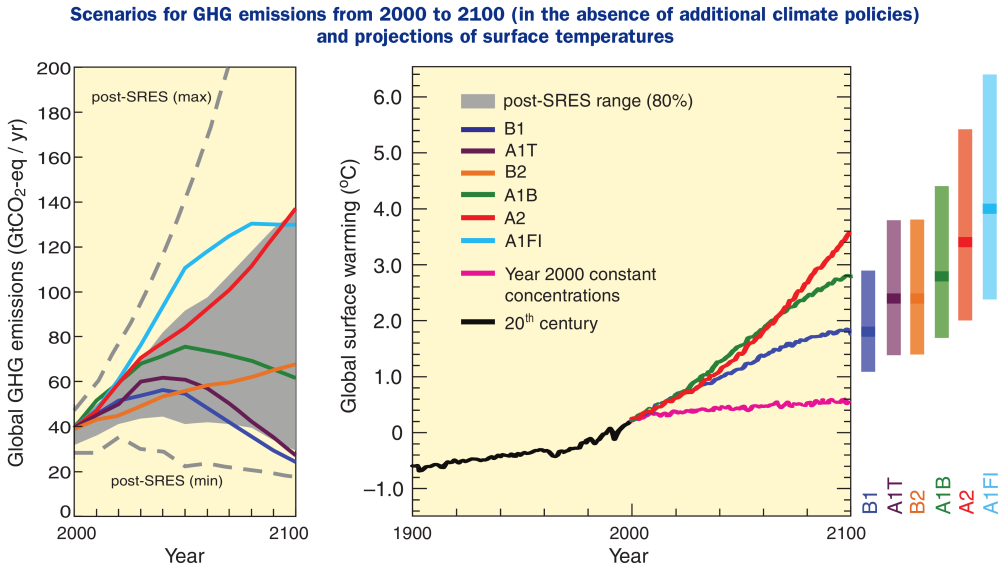

Figure 1.2: Measured and predicted global mean temperature between 1900 and 2100 [46].

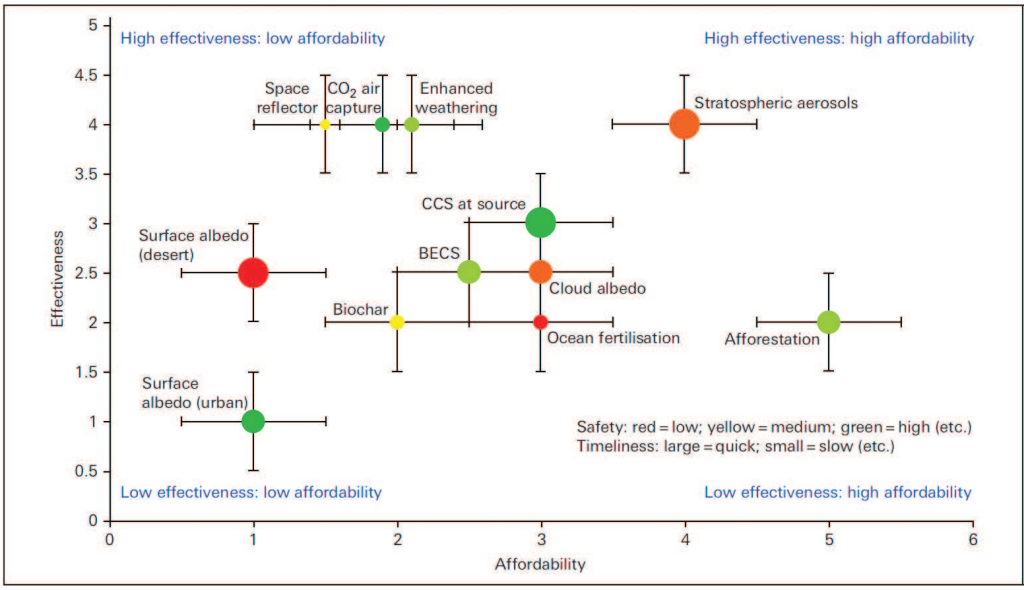

Figure 1.3: Geoengineering methods rated in terms of affordability, effectiveness, timeliness and safety by the Royal Society [95].

populations of algae and other photosynthetic organisms that provide much of the organic matter used in the ocean's food chains [80].

A report into geoengineering conducted by the Royal Society in 2009 [95] examines the feasibility of all types of geoengineering schemes based on the criteria of effectiveness, affordability, timeliness and safety, the key result of which can be seen in Fig. 1.3. In general, the report appears to show that there is no perfect solution, with the schemes that appear most effective suffering in other criteria such as affordability. Several of the different techniques shall now be discussed.

An example of an albedo enhancement technique is to increase the reflectivity of roofs and roads in an urban environment, thus reflecting more sunlight. There is also the added benefit that highly reflective roof coatings will cool the building on which it is implemented, a significant benefit in warm climates since significantly less energy is required for air conditioning. However, this method will have a reduced effectiveness in higher latitudes where darker roofs are beneficial during winter to reduce heating requirements. This method of geoengineering is rated as having a low effectiveness and affordability since the effects are small due to the low surface coverage of urban surfaces, 0.128% of the Earth's surface [48]. This method is also suggested to have a high safety index. Furthermore, more recent research suggests that altering all roofs globally will contribute a decrease of 0.02K through local cooling whilst increasing temperatures globally by 0.07K [48]. However, as noted in the study, the reduced emissions due to lower energy consumption from air conditioning is not accounted for.

Currently the most popular method of geoengineering suggested proposes that large quantities of sulphur particles be deposited into the upper atmosphere to reflect sunlight before it can be absorbed by the atmosphere, the densest area of which is below 1 km in altitude. This method is inspired by observations of volcanic eruptions which eject large numbers of dust particles into the upper atmosphere. For example, the El Chichón eruption in 1982 led to a decrease in the solar radiation reaching the Earth's surface of $35\,\mathrm{W\,m^{-2}}$ [38, 84]. Since sunlight scatters from small particles in many directions there was also an observed shift from direct solar irradiance on the Earth's surface to diffuse radiation. This had the unexpected side effect of increasing the growth of vegetation, which can increase the size of the terrestrial carbon sink [84]. There are also many negative aspects to this geoengineering method however, as noted by Robock [84], with the key drawback being that the ozone layer will be impacted. The key benefits are its relative cheapness in comparison to other geoengineering methods and that it can likely be deployed with existing technologies.

Several carbon capture methods have been suggested, the most prominent of which is carbon capture at source, as well as ocean fertilisation methods. Also worthy of discussion is afforestation. Carbon capture and storage (CCS) essentially consists of taking carbon dioxide out of the exhaust chimneys of fossil fuel power stations before being stored. This method is not a true geoengineering method as the GHG emissions are being reduced rather than atmospheric concentrations being altered directly. However, carbon capture directly from the atmosphere also exists as a geoengineering method and so CCS is included in the methods of geoengineering. Carbon capture at source has been demonstrated on a small scale, though there are few real world examples of power stations with carbon capture fitted. The key issues with CCS are the safe storage of the captured gas underground to prevent leakage back into the atmosphere and the efficiency of the capture process, since it is estimated that an extra 11-40% of fuel will be required to generate the same level of power. The extra power is required to provide energy for the carbon dioxide capture and storage process, and would increase energy prices by 21-91% whilst reducing the emitted CO_2 by 81-91% [72]. These values depend on the type of power plant in question.

Afforestation is technically a geoengineering method since the planting of trees decreases the concentration of CO_2 in the atmosphere. However, similarly to CCS it does introduce questions over the definition of what constitutes a geoengineering scheme, as will be discussed later. If it were to be used as a geoengineering scheme there will undoubtedly be a benefit to the climate, though the effectiveness will be low in the long term as ultimately once a tree has reached the end of its life it will decompose releasing the stored carbon back into the carbon cycle. The use of felled trees as a source of energy through biomass power stations is a possible remedy to this. There are many other benefits to afforestation, which is why afforestation is disputable as a geoengineering method. For example, trees are important in reducing flooding, landslides and soil erosion and

increasing urban quality of life, whilst a reduction in deforestation is essential for the preservation of many ecosystems [8, 74, 102].

Ocean fertilisation aims to increase the amount of CO_2 absorbed into the oceans by injecting iron particles into the upper layers of the oceans to encourage the growth of algae, which will then use increased amounts of CO_2 in photosynthesis. Though promising in principle, this scheme is not likely to be a successful method, as the rate of increased uptake of CO_2 is only likely to be a fraction of the total emitted annually [95], though much of the captured carbon could be sequestered for several centuries [96]. Other downsides are that side effects are likely. There is predicted to be a reduced carbon uptake in other regions of the ocean whilst some areas could become starved of oxygen. This will create 'dead zones' [95], whilst likely increasing the acidification of the ocean due to the uptake of carbon dioxide [80].

1.2.1 Space-based geoengineering

One of the most effective solutions suggested by the Royal Society is the use of space-based solar reflectors to reduce incident solar insolation. Whilst this technique is not rated by the Royal Society as being affordable or timely [95], it does have a key advantage over other schemes; neither the Earth's surface nor atmosphere needs to be physically changed directly. This is significant in comparison to stratospheric aerosol or ocean fertilisation techniques discussed previously, which are likely to have side effects. However, there will likely be some side effects related to the launch of the SBGE systems, since a large amount of launches will be needed to transport the material to the required location. These launch vehicles will inject several hundreds of tonnes of water vapor into the Earth's atmosphere each launch [97]. Therefore a large amount of launches could potentially have a significant effect on the atmosphere.

It has been estimated that in order to offset the effects of global warming caused by a doubling of the CO_2 concentration in the atmosphere (compared to pre-industrial levels and corresponding to an increase in global mean temperature of approximately 2°C) solar insolation must be reduced by 1.7% [39]. Similarly for a quadrupling of CO_2 the required insolation change is 3.6% [41].

There have been several different proposals to date regarding the reduction of solar insolation using space-based methods, the key characteristics of which can be seen in Table 1.1. The methods either utilise a cloud of dust [79, 98, 100] or solid reflectors or refractors [5, 34, 67, 69, 79] to reduce the level of solar insolation. Typically the methods that require the least mass are those that use solid reflectors/refractors, whilst the mass for dust cloud methods are orders of magnitude higher.

This is mostly due to the increased level of control that can be placed upon the solid reflectors, hence they can be stationed in optimum positions with active control to extend their lifetimes. In contrast, dust clouds cannot be controlled and can only be placed with suitable initial conditions, with subsequent replenishment necessary due to orbital decay or perturbation of the particle orbits. Conflicting with this is the consideration of the engineering complexity of the system. Whilst dust clouds are a relatively crude method, the material can be readily produced with little processing required, whereas solid reflectors must either be manufactured terrestrially and then launched into position or manufactured in-situ. Clearly taking this into account, the low rating for affordability and timeliness indicated in the Royal Society report can be understood. The main methods of space-based geoengineering (SBGE) will now be described in more detail.

The method proposed by Pearson [79] is to place a ring of dust or reflecting satellites in Earth orbit. Though the masses of these two methods are comparatively low, there are clearly possible side effects, including an increased danger to Earth orbiting satellites and to the Earth, as the dust ring method requires two shepherding satellites, each of which would be 1 km in size. As well as having a highly uneven insolation reduction pattern on Earth, discussed further in Chapter 6, the ring will have the additional side effect of increasing reflected light onto the night side of the Earth under certain conditions. For these reasons this method is not seen as the most optimal space-based geoengineering solution.

An additional factor that affects the relative mass of the different methods is the amount of time that the reflectors spend along the Sun-Earth line. For example the method proposed by Struck [98] to place clouds of dust at the L_4/L_5 Lagrange libration points of the Earth-Moon system has a clear benefit as these points are passively stable. Throughout this thesis the term 'stable' will refer to Lyapunov stability, i.e. that a 'stable' particle released near an equilibrium position will remain close to, or converge towards, the equilibrium position, whilst an unstable particle will move away from the equilibrium position. However, as these points effectively orbit around the Earth, they are only occasionally in a position to reduce solar insolation. Furthermore, the movement of the clouds will create a 'flickering' effect, albeit on a long time-scale, since the insolation reduction will alternate between having a high effect and none at all. On the occasions when insolation reduction is possible, the insolation change required will be much greater than the net 1.7% reduction.

The methods proposed by McInnes [69] and Angel [5] suggest the placement of large swarms of reflective or refractive devices at the first Lagrange point, L_1, between the Earth and the Sun. This point is unstable and thus the devices will require an active control mechanism, increasing the complexity of the system. The main challenge with these scenarios is the manufacture and placement of the reflective or refractive devices. To terrestrially manufacture and then place the

mass of material required to the L_1 point would require many thousands of launch vehicles, leading to a large amount of GHG emissions into the atmosphere. Angel describes a system of mass drivers to overcome this, though this is a hypothetical scenario, as the technology to build such a device cannot be anticipated in the near or mid-term. A more likely scenario suggested by McInnes is the in-situ manufacture of the devices from captured near-Earth objects (NEOs). Similarly, this method cannot be seen as a near-term option, though recent advancements in 3D printing technology and the interest in capturing NEOs for resource utilisation [22] suggest that this method could be seen as a mid-term possibility.

Position	Method	Insolation Change [%]	Required Mass [kg]	Estimated Energy [J]	Reference
Earth orbit	Dust ring	1.6	2.3×10^{12}	2.4×10^{19}-1.0×10^{21}	[79]
Earth orbit	Dust ring	1.7	1.0×10^{12}	1.0×10^{19}-4.3×10^{20}	Chapter 5
Earth orbit	Solar Reflector	1.6	5.0×10^{9}	2.0×10^{18}	[79]
Earth-Moon L_4/L_5	Dust cloud	1.4	2.1×10^{14}	2.2×10^{20}-4.6×10^{21}	[98]
Sun-Earth L_1	Solar reflector	1.8	2.6×10^{11}	1.8×10^{20}	[69]
Sun-Earth L_1	Solar refractor	1.8	2.0×10^{10}	1.3×10^{19}	[5]
Sun-Earth L_1	Dust cloud (10 yr duration)	1.7	1.9×10^{11}	1.5×10^{17}	Chapter 2

Table 1.1: The key characteristics of proposed space-based geoengineering schemes to offset global warming.

1.2.2 The geoengineered world

Before large-scale geoengineering schemes can be implemented, modelling of the climate response must be performed to analyse both the effectiveness and safety of the different mechanisms. Climate modelling has been performed in multiple scenarios, though still more are required before any geoengineering method can be concluded to be safe, as the current generation of climate models use many simplifying assumptions to reduce computational time to acceptable levels [7]. In addition, more experimental-scale studies are needed to verify the principles upon which geoengineering methods are based. To date the majority of modelling experiments have been conducted on solar

radiation management methods [9, 25, 33, 39, 41, 47–49, 64, 66, 74, 83, 84, 92] with some also modelling carbon capture scenarios [8, 74].

In general, these simulations show that whilst solar radiation management can be used to offset an increase in mean global temperature, this cannot be easily achieved on a regional scale. This is mainly because a global reduction in insolation will have a greater effect in the equatorial regions than in the poles, whereas the radiative forcing due to a given climate process is likely to act equally anywhere on the Earth's surface. For example, the simulation conducted by Bala et al. [9], which assumes a 1.8% reduction in the incoming solar flux to counteract a doubling of CO_2, shows a reduction in regional temperature in the equatorial regions in comparison to current levels, whereas the higher latitudes still show a warming effect. This effect is also shown in other simulations [64, 66]. As another example, in a similar simulation Irvine found a reduction of 0.5 K in the equatorial regions and a warming of 1K at the poles [47].

More detailed models of specific SM methods have also been performed. For example, the simulation run by Jones et al. [49] models the ejection of $5\,\mathrm{Tg\,yr^{-1}}$, for 20 years, of sulphur aerosol particles at an altitude between 16-23km at a single point along the equator. This simulation showed a global cooling of 0.74K and 0.69K, averaged over a period of 10-20 years after geoengineering is started, for two different models. For one of the two models the Arctic region showed a strong decrease in temperature due to the significant transport of particles away from the equator towards the northern hemisphere [49].

It has thus far been concluded that, whilst a mean temperature increase can theoretically be counteracted on a global scale, there will be cooling or warming anomalies on a local scale. Simulations performed by Caldeira and Wood [25] investigated the reduction in local and global temperature from a reduction of incoming solar insolation in the Arctic. It was found that by reducing the incoming insolation above a latitude of 61°N by 10%, a global average of 0.37%, the local temperature increase is reduced from 3.46K to 0.68K for a doubling of CO_2, with a global temperature increase of 1.83K, less than the 2.13K for the unengineered case.

As well as the changing temperature on a regional scale in a geoengineered world there are other factors that will be effected. For example, in all simulations reviewed here, there is predicted to be a global decrease in precipitation, since reduced temperatures lead to less evaporation. The amount predicted varies, with an expected range of 1.6-3.1% [9, 41, 64, 92]. This is likely to have a negative effect on global food productivity, with increased risk of droughts in Africa and Asia possible [84], and a possible disruption of the monsoon, which provides much of the moisture for the food production for several billion people [83, 92]. However, it was noted by Lunt et al. [64] that in the tropical regions a decreased temperature will lead to a reduction in evapotranspiration, resulting

in a reduced loss of soil moisture, likely negating some of the effects of reduced precipitation over this region. It has also been noted that in a world stabilised by a reduction in solar insolation, the net primary productivity (NPP) will increase due to the greater abundance of CO_2 in the atmosphere, despite the decrease in solar insolation [40, 84].

It is desirable to know in what time frame SM can be expected to become effective. Studies demonstrate that SM methods are typically fast acting with the reduction in insolation leading to a maximum decrease in temperature in about a decade [49, 66]. This also has a negative aspect. Should geoengineering be abruptly stopped, then the world could experience climate change at a rate approximately 20 times the current rate of warming ($0.2°C\ yr^{-1}$), reaching the un-engineered state in 10-20 years [49, 66]. The climate reacts quickly to changes in solar flux and, if a strong warming due to increased GHG concentrations is present, an abrupt cessation of solar radiation management will lead to this fast increase in temperature.

Other negative aspects of solar radiation management methods are that sea ice cover will be reduced with respect to the present state [7, 25, 49, 64], since a global reduction in temperature will be weighted preferentially towards the equatorial regions, the cooling of the stratosphere could lead to greater ozone depletion [7, 84] and the output from solar power stations could be reduced (by up to 40% for the stratospheric aerosol method) [84]. To counteract sea ice loss it has been determined that a 21% reduction in insolation is required above 71°N to return the surface cover to pre-industrial levels [25].

The two results modelling carbon capture techniques show the effect of afforestation in different latitude regions [8] and the effect on sea levels of afforestation, biochar (a carbon sequestration technique) and bioenergy with carbon capture at source [74]. The first result suggests that only afforestation in the tropics will lead to any significant cooling, since for higher, snowier, latitudes the increased presence of trees will reduce the local albedo leading to less reflected sunlight, offsetting any gain from the sequestration of CO_2. The second result shows that individually carbon capture techniques only modestly reduce sea level rise, but in combination can reduce the peak rise to 22-38cm [74]. It has also been shown that for a realistic space reflector or sulphur aerosol SM method sea level rise can be capped at approximately 24cm, though for larger reductions in insolation the peak can be much lower [74].

1.3 Ethical and political considerations of geoengineering

Apart from the technical considerations regarding the effectiveness and safety of the different geoengineering schemes, there are also considerations regarding ethical and political issues. These can be summarised as follows:

1.3.1 Should we geoengineer the climate?

When considering the ethical issues associated with geoengineering the primary question that must be answered is 'should we geoengineer the climate'. There are several considerations related to this question, originating from different global perspectives. The first of these arguments can be summarised by Bunzl [23]; "even if geoengineering were successful it would still have a bad effect of reinforcing human arrogance and the view that the proper relationship to nature is one of domination (Jamieson 1996) (p 332)." This point of view essentially argues that the need for large-scale geoengineering, or even the preliminary research into the topic, signifies a failure of humanity; a failure to treat the environment with respect; a failure to act without political agenda and reach an agreement based on a need to do a common good for future generations. Though by conducting research, or even implementation of geoengineering, we may fulfill this fear, it is not a significant argument against geoengineering the climate, should it become necessary.

Another widely cited argument against geoengineering, based on more pragmatic principles than the previous argument, is that of 'moral hazard', that by merely envisaging a system that can save us from catastrophic climate change, our resolve to act to mitigate climate change will be weakened [93, 108]. This is potentially a significant problem, with some nations or institutions that are likely to lose out heavily in the mitigation process possibly favouring geoengineering of some form rather than attempt serious mitigation. However, should the argument be accepted that geoengineering is necessary, as a precaution for the eventuality that a global agreement on mitigation is not forthcoming, then research must still continue and increase in scale to be ready when needed. This will further increase the risk of moral hazard, as the closer geoengineering is to being ready to implement, the greater the pressure for it to be used, as either a solution to the problem or to gain time for mitigation. In consequence this will likely increase the timescale for a mitigation agreement. Following on, if we start to geoengineer the climate, then at what point will we stop? At what point does our potential domination of nature, suggested by Jamieson, become a problem, if it has not done so already. There are many methods of geoengineering other than the large-scale global efforts described above. Some of these other schemes target specific processes, such as controlling the severity of El Niño [33] or increasing the strength of the westerly winds in

the southern ocean [112]. This opens up the question of what processes we will choose to manage. As will be discussed in Sec. 1.3.3, currently the manipulation of weather systems are prohibited, but at some point a line between the manipulation of specific weather events, such as hurricanes, will meet the global manipulation of the climate.

These two arguments lead many to disregard geoengineering as a possible tool to combat climate change before conclusive research has been performed. Undeniably, a world where geoengineering is not needed is ideal and the most useful, if not timely, way of reducing the effects of climate change is to treat the root cause by reducing GHG emissions [37, 93]. However, the complete rejection of geoengineering as a possibility also carries risks. Should we fail to reduce our emissions promptly, then geoengineering may be the only option in preventing catastrophic climate change. Should we decide not to conduct research into the feasibility of geoengineering methods, because of a fear of geoengineering, then should the need arise, we will be unprepared. In this eventuality, geoengineering could still be implemented since some methods, particularly the stratospheric aerosol method, are effective over a short period whilst not requiring a significant advance in technology, though obviously the risks will be greater. It will be a step into the unknown, where, if there is no advancement of knowledge, it could create as much change as global warming. For this reason many authors recommend an organised geoengineering programme to develop and evaluate technologies so that should they be needed they are ready, and if nothing else to show that geoengineering is not feasible. This need for an organised research programme is highlighted by the recent 'renegade' ocean acidification field test carried out by a private group [63].

Other arguments against geoengineering relate to the possible side effects discussed previously. In a scenario where geoengineering is implemented on a global scale, the effects will be uneven (see Sec. 1.2.2), just as the effects of climate change are uneven. In effect this means that there will be winners and losers, though it is not yet known precisely how this will unfold. Due to this uncertainty, the large-scale implementation of geoengineering cannot currently be justified. That there will likely be such winners and losers for large-scale deployment, especially for SM techniques, is a compelling reason for prohibiting geoengineering at present. As discussed before, risk is incurred by preventing research into geoengineering, so the side effect argument can only be used against the full implementation of geoengineering, but not against geoengineering research.

The argument against geoengineering based on unknown side effects could be countered with the argument that the geoengineered world will on average be better than the world with global warming, such that even if some regions experience a worse climate, on the whole the world will be better. This emphasises the need to mitigate climate change and not rely on geoengineering alone to solve the problem. Related to this is the possibility of local scale geoengineering that faces less risk of international disagreement, such as afforestation and urban albedo, since the global effects

are in general small. In these ways nations can probably act unilaterally. Though this is not a risk on a local scale, should a nation decide to act on a global scale, which is technologically possible [108], the risk will increase significantly. This is because it is presumed that the greatest positive effect will be tailored to the needs of that nation, likely increasing the side effects for other nations. It is imperative that the possibilities of unilateral action be minimised. As discussed by Victor, it is misleading to think that a ban on geoengineering will achieve this, since any research thus carried out will be in the hands of nations that ignore or do not participate in any such agreement [108]. In this situation other nations will have no influence on the outcomes of such research or the decision to implement. A possible method of preventing unilateral action, though the risk cannot be eliminated, is for an internationally organised research programme to determine the merits and demerits of geoengineering [108].

Returning to the first argument, is geoengineering playing God? Can we ever know enough about possible side effects to predict with any accuracy what the effects will be. To quote Schneider "to tamper with a system that determines the livelihood and life-styles of people the world over would be the height of irresponsibility if we could not adequately foresee the outcome" [93]. This can only be understood with more research, though this technological aspect may not be the greatest obstacle to the implementation of geoengineering. With such winners and losers there must be suitable methods for the governance of geoengineering with appropriate organisations that can control the multilateral implementation and allocate suitable reparations to any losers. Considering that there is little progress in the agreement of a mitigation strategy, the likelihood of there being a quick or easy agreement for an implementation strategy or regulatory mechanism for geoengineering is currently slim, with there being a strong possibility that global scale geoengineering schemes will therefore never be implemented [37].

1.3.2 What constitutes geoengineering?

The definition of geoengineering is the 'deliberate modification of the Earth's climate'. However, it has been noted previously that it is debatable whether some methods of geoengineering, such as afforestation, are truly geoengineering options. For example, afforestation has been shown to have a global effect on the climate, though clearly every planting of a tree cannot be viewed as an act of geoengineering. It does however raise interesting questions regarding our interaction with the global climate and what is and is not regulated and what should and should not be regulated. For example, Schneider states that humanity has been participating in a process of "inadvertent geoengineering" through our use of fossil fuels. Since that paper was published in 1996, knowledge of the causes and effects of climate change has increased significantly, as well as

the wider dissemination of this knowledge to the public. It could now be argued, therefore, that we no longer are accidentally modifying the climate but are in fact wilfully negligent regarding our use of fossil fuels to the extent that it is widely known that we are modifying our climate for the worse. This opens up the argument of what constitutes geoengineering? Is it the technical act or is it merely the intent to modify the climate. The planting of trees for the purposes of returning a landscape to its natural form may not be geoengineering, but planting the same trees with the intent to remove CO_2 from the atmosphere is. Similarly, manufacturing artificial trees to remove CO_2 is geoengineering, whilst the emission of CO_2 as a by product of a manufacturing process is not. It can be argued that there must be a broader recognition that everything that we do affects the climate and should come under the same legislation regarding the protection of biodiversity.

1.3.3 How will geoengineering be governed?

Considering the history of technical fixes to problems in natural systems that have spawned unpredicted and catastrophic side effects, and also considering the, at present, highly uncertain nature of geoengineering, the governance of such schemes is just as important, and just as challenging, as the technical implementation of goengineering. An example of a technical fix with unpredicted, devastating side effects, that could provide a useful analogy for geoengineering, is the introduction of invasive species. An example of this is the introduction of the cane toad into Australia to control the cane beetle, which damages sugar crops. After the introduction of the toad the population has increased dramatically and is spreading, uncontrollably, having a negative impact on native species of some flora and fauna [104].

The intentional introduction of alien species is an interesting example from which much can be learned regarding the regulation of geoengineering. For example, many of the worst examples of biological control, such as the cane toad, occurred at a time when there was very little control over the introduction of non-native species. Now there are recommendations released by the UN Convention on Biodiversity regarding the effective control of non-native species [94]. It is recommended for every country to "establish an appropriate institutional mechanism such as a 'biosecurity' agency or authority as part of legislative reforms on invasives" [94]. Geoengineering should use the example of the control of non-native species to set up suitable regulations and ensure thorough scientific research is performed, prior to implementation, to ensure the safe use of geoengineering and to avoid the possibly catastrophic consequences of not fully understanding the side effects of implementation.

It was observed by Bodansky [16] that current laws, up to 1996, only provided a "general frame of reference" for geoengineering in environmental law. In brief, nations have a responsibility

to prevent significant harm to other nations or neutral areas by their actions. It is also generally recognised that a precautionary principle should be followed whereby, when an action is proposed that carries significant risk, the burden of proof should lie on the nation carrying out the act to show no harm will occur to others. In addition, the UN Framework Convention on Climate Change (FCCC) has the requirement that a state should minimise the unfavourable outcomes of actions taken to mitigate the effects of climate change. This shall be discussed later. In these examples there is no legal framework for the enforcement of these principles or an appropriate court to seek reparation if these principles are ignored. This is partly due to the stance of the United States towards the International Court of Justice (ICJ), which is that they will agree to be subject to the court's ruling on a case-by-case basis.

The only international 'law' specifically relating to geoengineering is the declaration by the FCCC, agreed in 2010 at the Convention of the Parties (COP), that "no climate-related geoengineering activities that may affect biodiversity take place, until there is an adequate scientific basis on which to justify such activities" [103]. This is often stated as being a moratorium on geoengineering. However, this essentially extends the precautionary principle to specifically relate to geoengineering, that the burden of proof lies on the perpetrator to demonstrate the safety of their actions before it is permitted to take place. Indeed, the ruling also continues to give an exception for "small scale scientific research studies that would be conducted in a controlled setting ... and only if they are justified by the need to gather specific scientific data and are subject to a thorough prior assessment of the potential impacts on the environment". This statement, in effect, prevents full scale deployment of geoengineering until enough is known about possible side effects and, since there is no legal framework to truly prevent this from happening, it is also a voluntary regulation. The voluntary nature of this 'law' was tested in 2012 when a large-scale ocean fertilisation field study dumped 100 tonnes of iron sulphate near the Canadian coast [63]. There is some uncertainty as to whether this was indeed a geoengineering study as the project lead, who has been linked to geoengineering in the past, claims that it was an attempt to increase the population of salmon in the local area [77]. Essentially, this event proved the voluntary nature of the current moratorium on geoengineering as well as highlighting the possible ambiguity of what constitutes geoengineering.

Two other 'laws' relate to certain geoengineering activities, these being the Outer Space Treaty (OST) and the UN Convention of the Law of the Sea (UNCLOS) [16]. The OST allows free and open access to space for any nation with the requirement that nations "conduct all their activities in outer space.., with due regard to the corresponding interests". With there being no regulatory body that has the jurisdiction to decide on any breach of these laws or enforce them, this law means little. For example the anti-satellite missile test carried out by China in 2007 created many thousands of particles capable of severely damaging low Earth orbit (LEO) satellites. However, despite this being inconsistent with the peaceful uses of outer space there was no direct

legal consequence from the event. Though this is a serious event, the potential impact to the space and terrestrial environments of SBGE will be far more significant and will undoubtedly arouse more attention, though will technically still be permissible. For example, the Earth ring concept envisages many millions of tonnes of micron-sized particles in a medium Earth orbit (MEO). This will undoubtedly have an effect on LEO satellites by increasing the quantity of dust grains passing through LEO before they burn up in the atmosphere. The L_1 mirror concept will also lead to difficulties in international relations since placing a large swarm of reflectors or cloud of dust in this position will prevent access by other spacecraft and will essentially lead to the participating nation or nations staking claim over its ownership. It is suggested that in any discussions on geoengineering that such technical aspects of the law as this could well sidetrack the key discussion on the feasibility of geoengineering [108]. Bodansky states that UNCLOS is broadly similar to the OST providing that geoengineering, which in this case would be ocean fertilisation, does not take place within a non-participating nations territorial waters [16].

A summary of the laws relating to geoengineering thus far can conclude that there is no framework for the implementation or organised research of geoengineering that most authors think necessary [16, 24, 93]. This is undeniably needed before the large-scale implementation of geoengineering, though it is suggested by Victor that a binding treaty cannot be agreed upon at this time, as too little is known regarding the effects of geoengineering to make a worth while attempt at regulation [108]. Instead, research into geoengineering should be organised with the suggestion that multiple, transparent, competitive institutes be allowed to independently research geoengineering schemes under a set of internationally agreed guidelines [108]. The rules on protecting biodiversity agreed at COP10 are a likely starting point for these rules. In future, once more is known regarding the effects of geoengineering, a treaty will be required which allows the input of all nations to voice their opinions on all feasible geoengineering methods. It is strongly preferable to have a multilateral approach to geoengineering, though inevitably not all nations will agree on the same method(s) with which to proceed. Therefore, an arbiter is required that can arrange reparations to any nations that feel that they have suffered from geoengineering, whether they are pro-geoengineering or not. Who should provide the funds for the implementation of geoengineering, as well as reparations, will be a difficult question and one that will inevitably prove a significant obstacle to an agreement. Typically, the richest nations have contributed the greatest to global warming, with the poorest nations being most at risk to climate change and therefore have the most need for geoengineering. As an example, the pacific island nations can contribute very little to funding global geoengineering and so will essentially be subsidised, though they are at great risk due to rising sea levels. It may seem only fair that those that have contributed most to climate change pay the most for implementation. However, due to the short-term nature of politics it is unlikely that this will be easily agreed, especially as geoengineering schemes can potentially be extremely costly.

In summary, the laws regarding geoengineering are currently inadequate, with no single body being responsible for the regulation of geoengineering activities and with no body to enforce the current moratorium of geoengineering implementation. Therefore, a single body that can organise a concerted effort into the research of the feasibility of geoengineering, as well as the possible side effects of implementation, is required. This will likely reduce the probability of rogue geoengineers acting unilaterally and enable geoengineering to be more accurately assessed as a climate change mitigation option.

1.4 Thesis Contributions and Structure

Ultimately none of the SBGE concepts discussed in Sec. 1.2.1 are ideal for geoengineering, though should the technology become available and the necessity to act quickly on climate change become apparent they could still be implemented. The main contribution of this thesis is therefore to devise new space-based geoengineering concepts that reduce the manufacturing requirements associated with prior space-based geoengineering concepts, thus improving the affordability and timeliness of these methods. This will be achieved by investigating the use of large clouds of dust at the Sun-Earth L_1 point and re-visiting the Earth dust ring concept suggested by Pearson [79].

Previous SBGE concepts have been proposed that utilise the L_1 equilibrium position. The new contribution in this thesis is the use of dust grains, and considers the three-body dynamics of the dust grains around L_1, to generate a steady state cloud, accounting for the motion of the dust grains. This has been achieved assuming both an initially static dust cloud and dust grains ejected with a range of feasible velocities. These steady state clouds have then been used to determine the pattern of the insolation reduction experienced on Earth. The use of an initially static and dynamic dust cloud has been investigated separately in Chapters 2 and 4 respectively. An image of this method can be seen in Fig. 1.4.

An extension to the steady state cloud is the inclusion of the mass of the asteroid using four-body dynamics. This novel approach enables the calculation of the size of cloud that can be gravitationally anchored by the asteroid in the vicinity of the L_1 point. This has been performed for the largest known near-Earth objects in Chapter 3, as well as an investigation of the effect of grain size on the size of the anchored dust cloud.

The Earth ring concept has been investigated previously by Pearson [79]. However, the strong surface force effects of solar radiation pressure and atmospheric drag were not accounted for. The orbital dynamics that include these forces shall be used in this thesis to demonstrate the

feasibility of an elliptical, heliotropic, ring around the Earth. This analysis shall be detailed in Chapter 5.

A key contribution of this thesis is the use of a solar radiation model to determine a solar insolation reduction map over the Earth's disk. This is used in this thesis, in combination with a simple climate model, to assess the feasibility of each new dust cloud method of achieving the required mean global temperature decrease. The climate model used, and the temperature reduction, is discussed in Chapter 6. To assess whether there is an improvement in the suitability of these new space-based geoengineering methods, the engineering challenges involved are discussed in Chapter 7. This includes a discussion of a technology development roadmap, suggesting a likely timeframe for the implementation of the dust cloud methods of geoengineering.

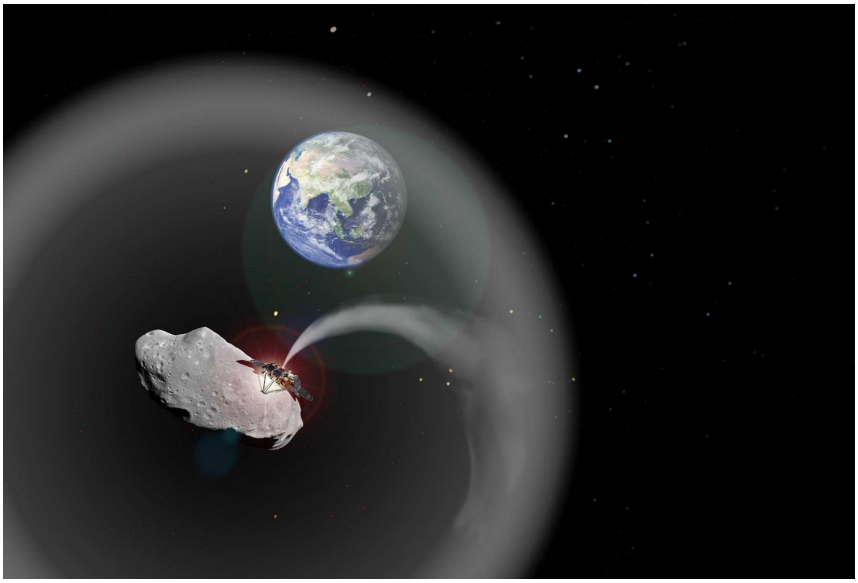

Figure 1.4: Impression of an L_1 positioned dust cloud for space-based geoengineering [Image created by Charlotte Bewick using material from ESA and NASA].

1.5 Published Work

Much of the original work presented in this thesis has been published in the journal and conference papers listed below.

Journal Papers

- Bewick, R., Lücking, C., Colombo, C., Sanchez, J.P. and McInnes, C.R., *Heliotropic Dust Rings for Earth Climate Engineering*, Advances in Space Research, *In Press*

- Bewick, R., Sanchez, J.P. and McInnes, C. R., *Gravitationally bound geoengineering dust shade at the inner Lagrange point*, Advances in Space Research, **50**(10), 1405-1410, 2012

- Bewick, R., Sanchez, J.P. and McInnes, C. R., *The feasibility of using an L_1 positioned dust cloud as a method of space-based geoengineering*, Advances in Space Research, **49**(7) 1212-1228, 2012

- McInnes, C.R., Ceriotti, M., Colombo, C., Sanchez, J.P., Bewick, R., Heiligers, J. and Lücking, C., *Micro-to-Macro: Astrodynamics at extremes of length-scale*, Acta Futura, 4, 81-97, 2011

Conference Papers

- Bewick, R., Lücking, C., Colombo, C., Sanchez, J.P. and McInnes, C.R., *Geo-engineering using dust grains in heliotropic elliptical orbits*, 62nd International Astronautical Congress, Cape Town, 2011, IAC-11.D1.1.9

- Bewick, R., Sanchez, J.P. and McInnes, C.R., *An L1 positioned dust cloud as an effective method of space-based geo-engineering*, 61st International Astronautical Congress, Prague, 2010, IAC-10.D1.1.7

Chapter 2

Static Cloud at L_1

The L_1 position offers significant benefits for Space Based Geoengineering (SBGE) with respect to the climate system, with respect to other locations such as Earth orbit or the Earth-Moon L_4/L_5 points, as there is no flickering effect and an even distribution of the insolation reduction is possible, as discussed previously. However, the effect that the instability of the L_1 position has on the feasibility of this method of SBGE must be understood. This shall be discussed in the following chapter, begining with the description of a model of a static cloud of dust at L_1 followed by the propagation of this dust cloud through the dynamics of the circular restricted three-body problem (CR3BP). A solar radiation model (SRM) to calculate the subsequent reduction in solar insolation shall be described and then used to determine the annual dust mass flow rate requirement for a variety of dust clouds.

2.1 Dust Dynamics

The following section will detail the dynamics of a dust cloud in the vicinity of the interior Lagrange point in the Sun-Earth three-body problem.

2.1.1 Three-body problem

The cloud shall be assumed to be moving in a system where only the gravitational forces due to the Sun and the Earth are significant. Hence, the circular restricted three-body problem (CR3BP) shall be used to describe the motion of the dust particles in the cloud. To use these dynamics it is

assumed that the orbits of the primary bodies are circular, the bodies are spherical and there is no interaction between the dust particles. The linearised dynamics around the L_1 point will be used to determine the motion of the dust cloud on a large-scale. The equations of motion that describe this system are given in Eq. (2.1) [88].

$$\begin{bmatrix} \ddot{x} \\ \ddot{y} \\ \ddot{z} \end{bmatrix} = \begin{bmatrix} \omega^2 x + 2\omega\dot{y} - G\left(\frac{M_1}{r_1^3}(x+x_1) + \frac{M_2}{r_2^3}(x-x_2)\right) \\ \omega^2 y - 2\omega\dot{x} - G\left(\frac{M_1}{r_1^3}y + \frac{M_2}{r_2^3}y\right) \\ -G\left(\frac{M_1}{r_1^3}z + \frac{M_2}{r_2^3}z\right) \end{bmatrix} \tag{2.1}$$

where G is the gravitational constant, M_1 and M_2 are the masses of the two primary bodies, i.e. the Sun and Earth, ω is the angular velocity of the bodies around their common centre-of-mass, and r_1 and r_2 are the separations of an infinitesimal dust particle from the primary bodies and are defined as;

$$r_1 = \sqrt{(x+x_1)^2 + y^2 + z^2} \tag{2.2}$$

$$r_2 = \sqrt{(x-x_2)^2 + y^2 + z^2} \tag{2.3}$$

where x_1 and x_2 are the positions of the two primary bodies along the x-axis. Since the bodies orbit around a common centre-of-mass they must be on opposite sides of the origin on the x-axis, hence the $+x_1$ term in Eq. (2.2). It is useful to describe the equations of motion in a dimensionless system that is in a rotating reference frame, thus the primary bodies will remain stationary and the motion of a particle with respect to them can be easily discerned. Under the assumption of circular motion the angular velocity can be defined as;

$$\omega = \sqrt{\frac{G(M_1+M_2)}{r_{12}^3}} \tag{2.4}$$

where r_{12} is the separation between the two primaries. In the dimensionless system we define this separation to be unity and thus $r_{12} = 1\text{AU}$, equal to the separation between the Earth and Sun of $1.496 \times 10^8\text{km}$. The mass of the system is also set to unity and thus the unit of mass is $M_1 + M_2$ from which the parameter $\mu = M_2/(M_1+M_2)$ is defined. Since the mass of the system is 1 the mass of the secondary body is now equal to $1-\mu$. The orbit period of the system can be set to 2π and since $T = 2\pi/\omega$ the value of ω in this dimensionless system must be 1. It follows that as the distance and mass in this system are both unity then G must also be 1. Using these definitions the dimensionless equations of motion in a rotating reference frame can be defined to be;

$$\begin{aligned} \ddot{x} - 2\dot{y} &= \frac{\partial U}{\partial x} \\ \ddot{y} + 2\dot{x} &= \frac{\partial U}{\partial y} \\ \ddot{z} &= \frac{\partial U}{\partial z} \end{aligned} \tag{2.5}$$

where the non-dimensional potential function, U, is;

$$U(x, y, z) = \frac{1}{2}\left(x^2 + y^2\right) + \frac{1-\mu}{\rho_1(x, y, z)} + \frac{\mu}{\rho_2(x, y, z)} \tag{2.6}$$

Here the parameters $\rho_{1,2}$ are the non-dimensional distances of the dust particle to each of the primary and secondary masses, defined by Eq. (2.7) and Eq. (2.8), and shown in Fig. 2.1. In dimensionless co-ordinates the Sun and Earth are positioned at $M_1(-\mu, 0, 0)$ and $M_2(1-\mu, 0, 0)$ respectively. Hence;

$$\rho_1 = \sqrt{(x+\mu)^2 + y^2 + z^2} \tag{2.7}$$

$$\rho_2 = \sqrt{(x+\mu-1)^2 + y^2 + z^2} \tag{2.8}$$

The equilibrium, or libration points, are located where the combined gravitational force of the two primary bodies on a particle is equal to the centripetal force required for it to orbit in a fixed position relative to the two primary bodies. These positions are at the stationary points of the potential function, Eq. (2.6). In particular, the equilibrium points required for this geoengineering method must lie along the Sun-Earth line and must therefore be along the x axis hence $y = z = 0$ with $\dot{x} = \dot{y} = \dot{z} = 0$. Using this requirement, and substituting Eq. (2.6) into Eq. (2.5), results in Eq. (2.9), from which the position of the L_1 point, x_{L_1}, can be found numerically;

$$x : x_{L_1} - \frac{1-\mu}{(x_{L_1}+\mu)^2} + \frac{\mu}{(x_{L_1}+\mu-1)^2} = 0 \tag{2.9}$$

For the Sun-Earth system ($\mu = 3 \times 10^{-6}$) the L_1 point is located approximately 1.5×10^6 km sunwards of the Earth.

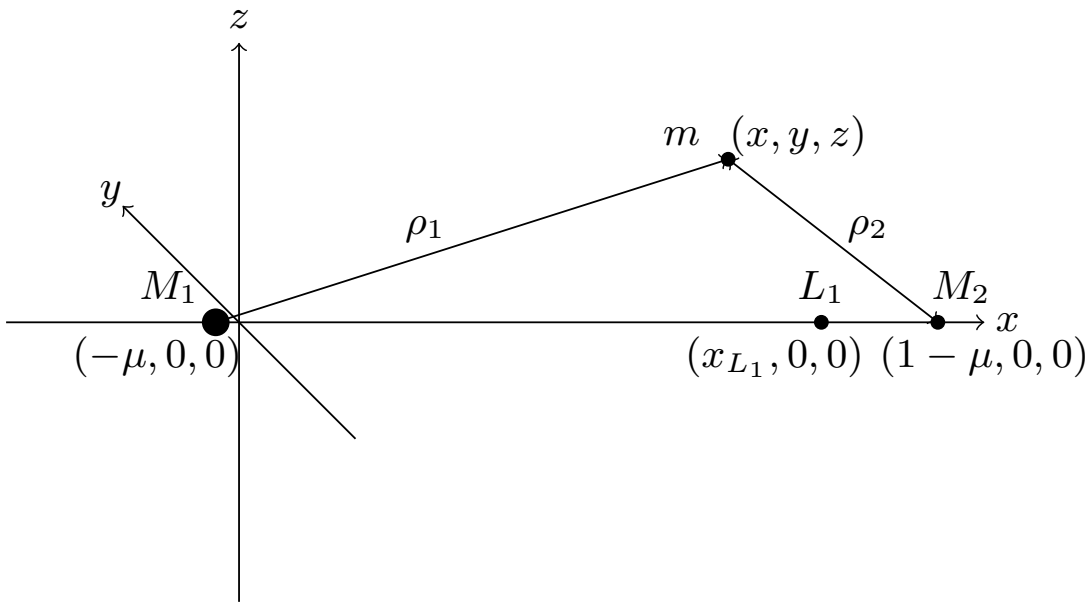

Figure 2.1: Geometry of the circular restricted three-body problem with the Sun, M_1, Earth. M_2 and dust grain m.

2.1.2 Perturbation forces

Due to the small length-scale of the dust particles considered the effects of natural perturbation forces must be analysed to determine whether they will significantly effect the motion of the dust grains. The perturbations to be analysed are due to solar radiation pressure, the Poynting-Robertson effect, interactions with the solar wind and the Lorentz force.

2.1.2.1 Solar Radiation Pressure

The effects of solar radiation pressure (SRP) will be discussed more thoroughly in Sec. 2.1.3. This effect is caused by the transfer of momentum from solar photons to the dust grain where the force can be approximated as follows [32];

$$F_{SRP} = \frac{L_{\odot}\sigma_{gr}Q}{4\pi c r_{\odot}^2} \tag{2.10}$$

where $L_{\odot}$ is the solar luminosity, σ_{gr} is the grain cross-sectional area, c is the speed of light, $r_{\odot}$ is the distance to the Sun and Q is the solar radiation pressure coefficient. The parameter Q determines the coupling effect of SRP and is dependent upon the material properties of the dust grain. For

example, a completely transparent material will have a value of $Q = 0$ whilst for a completely absorbing grain $Q = 1$ and for a completely reflecting grain $Q = 2$. The values of Q that shall be used to calculate F_{SRP} for a range of particles are interpreted from a study by Wilck and Mann [110] on the effect of SRP on interplanetary silicate grains where $\rho = 3,500\,\mathrm{kg\,m^{-3}}$. The study shows a peak for Q in the range where the grain size is approximately equal to the wavelength of visible light. Analysing Eq. (2.10) shows that as the grain size decreases the acceleration experienced by a grain increases due to the greater area-to-mass ratio since area scales as the square of the grain size while mass scales as the cube.

2.1.2.2 Poynting-Robertson Effect

This perturbation is due to the motion of a dust grain with respect to the stream of solar photons due to two effects. Firstly, the Doppler shift of sunlight due to the grain's velocity in the radial direction, and secondly the motion of the grain causes solar photons to be incident from a slightly forward direction. The resultant force, due to the Poynting-Robertson (PR) effect can, be found as follows [32];

$$F_{PR} = F_{SRP}\left(\frac{-2v_r}{c}\hat{\mathbf{r}}, \frac{-v_\theta}{c}\hat{\theta}\right) \tag{2.11}$$

where c is the speed of light, v_r is the radial velocity and v_θ is the transverse velocity in the radial, $\hat{r}$, and transverse, $\hat{\theta}$, directions respectively. Thus, there will be a drag force acting against the velocity vector of the grain.

2.1.2.3 Solar Wind

The effect that the solar wind has on a dust grain is much the same in principle to the Poynting-Robertson effect, the difference being that the momentum transfer is due to protons, electrons and Helium nuclei in the solar wind striking the dust grain. The force due to the solar wind is therefore found to be [73];

$$F_{sw} = p_{sw}\left(1 - \frac{-2v_r}{v_{sw}}\hat{\mathbf{r}}, \frac{-v_\theta}{v_{sw}}\hat{\theta}\right) \tag{2.12}$$

where v_{sw} is the speed of the solar wind and p_{sw} is the momentum transfer to the grain defined by;

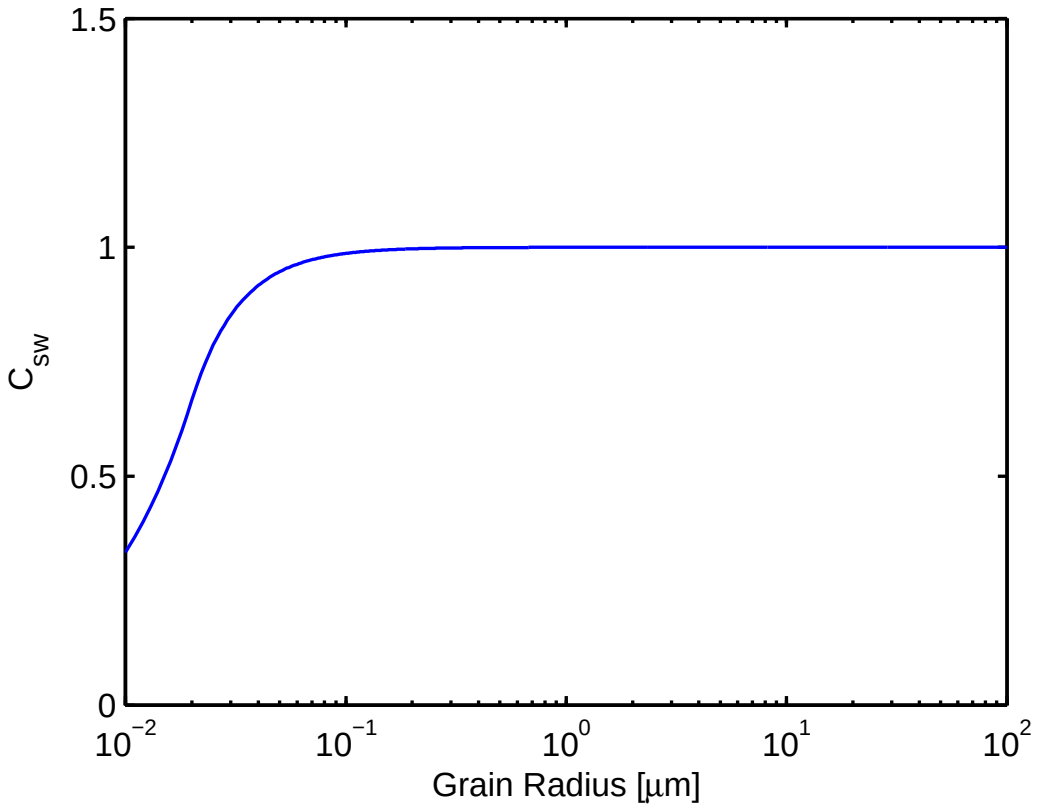

Figure 2.2: Momentum transfer coefficient of a silicate particle with respect to the solar wind [73].

$$p_{sw} = \frac{2E_{sw}\Omega_{sw}\sigma_{gr}C_{sw}}{v_{sw}} \tag{2.13}$$

Here E_{sw} is the average energy of a solar wind particle, Ω_{sw} is the flux of solar wind particles, σ_{gr} the cross-sectional area of the grain and C_{sw} is the momentum transfer coefficient. The value of C_{sw}, as can be seen in Fig. 2.2, is close to unity for grain radii $> 0.1\,\mu$m, decreasing significantly below this due to the "small particle effect" [73].

The solar wind can be considered to have three states, the fast solar wind, the quiet solar wind and the state of coronal mass ejection. The properties of the solar wind are summarised in Table 2.1. The slow and fast solar wind states do not vary significantly, with velocities at Earth in the region of a few hundred kilometers per second and proton densities close to $10^7\,\mathrm{m}^{-3}$. The number density of α-particles for the fast and quiet solar winds are typically 2-4% [52] and thus for an initial estimate they can be ignored. For the case of a Coronal Mass Ejection, where the solar wind velocity is typically 400-2,000 $\mathrm{km\,s}^{-1}$ this percentage rises to approximately 30% [52], thus in this scenario their greater mass must be taken into account.

Solar Wind	Quiet	Fast
Flux [protons m^{-3}]	5-8$\times 10^6$	0.8-1.2$\times 10^7$
Velocity [km s^{-1}]	300-500	500-900
Magnetic Field [T]	3-10$\times 10^{-9}$	8-16$\times 10^{-9}$

Table 2.1: Solar Wind properties in the vicinity of Earth [32].

2.1.2.4 Lorentz Force

The Lorentz force perturbation is due to the motion of a charged grain through the solar magnetic field. The direction of this force is defined by the cross product of the grain velocity vector, $\mathbf{v}$, and the direction of the magnetic field, $\mathbf{B}$, as seen in Eq. (2.14);

$$F_L = q\mathbf{v} \times \mathbf{B} \tag{2.14}$$

where q is the surface charge on the grain. The magnetic field of the Sun is carried by the solar wind and forms a 3D structure, the "heliospheric current sheet" [109], the shape of which is described as a Parker spiral. The magnetic field is described by de Pater in [32] as having approximately equal radial and azimuthal components at the Earth's orbit with the strength being in the region of 3-10$\times 10^{-9}$ T for a quiet solar wind and 8-16$\times 10^{-9}$ T for the fast solar wind. In addition, the magnetic field switches polarity intermittently, depending on the polarity of the region on the Sun's surface where the solar wind, found at a given position and time, originates.

An important factor that must be considered is the charge on the dust grain. This has been found to vary little with distance from the Sun [53]. For a silicate grain the surface potential is of order $U_{gr} = 3.2$V at 1AU for a grain radius of 0.281μm. Above this particle size the surface charge does not vary, with only a marginal increase below. Thus, this surface potential shall be assumed to apply for all grain sizes. The charge on the grain can be found using;

$$q = 4\pi\epsilon_0 U_{gr} R_{gr} \tag{2.15}$$

where ϵ_0 is the permittivity of free space and R_{gr} is the grain radius. Subsequently the force on a grain can be found using Eq. 2.14. It should be noted that no assumptions are made regarding

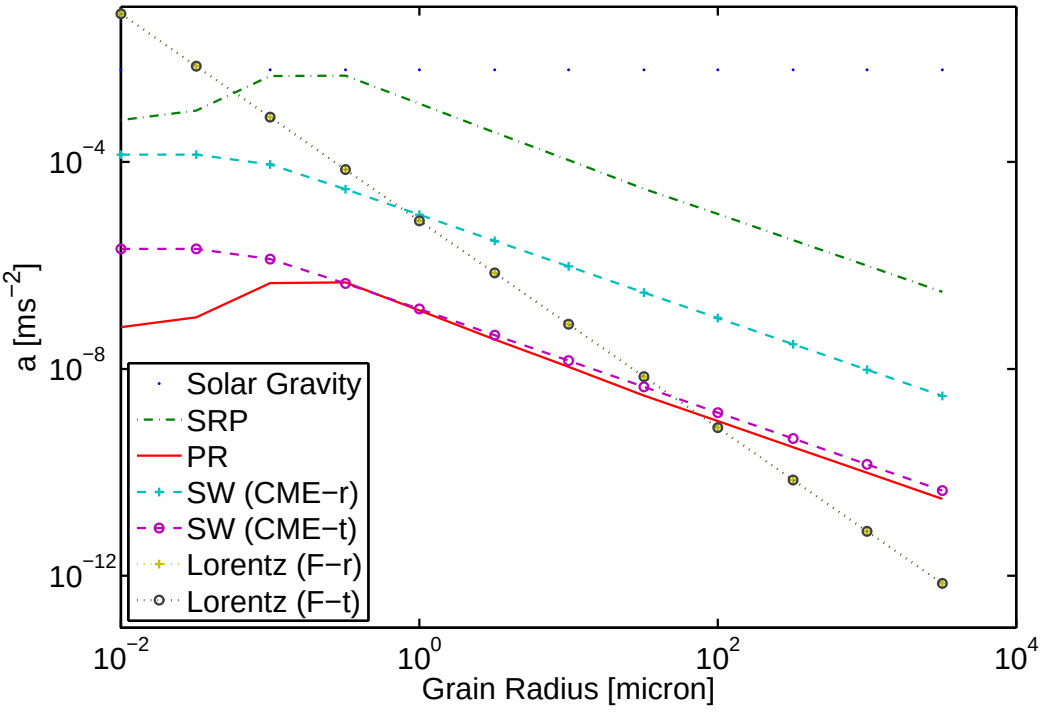

Figure 2.3: Acceleration due to solar radiation pressure (SRP), solar gravity, the Poynting-Robertson effect (PR), the solar wind (CME event) and the Lorentz force for a range of dust grain sizes for radial (-r) and transverse (-t) directions. For the solar wind and Lorentz force cases only the strongest acceleration is plotted for clarity.

the charging timescale of the dust grain as a worst case scenario is sought to determine the effect of the perturbation forces.

2.1.2.5 Perturbation Summary

To demonstrate the relative strengths of the different perturbations, the acceleration on a range of dust grain sizes shall be calculated. The grain is assumed to be initially placed at the classical L_1 position and will thus have an orbital speed of approximately $30\,\mathrm{km\,s^{-1}}$ in the transverse direction. Using the equations described above and assuming the grain is spherical with a density of $3,500\,\mathrm{kg\,m^{-3}}$ the accelerations can be calculated, as seen in Fig. 2.3.

It can clearly be seen that above a radius of $0.06\,\mu$m the dominant perturbation is SRP, with only the Lorentz force being greater below this. This force decreases rapidly with grain radius becoming an order of magnitude lower than SRP for a grain radius of $0.1\,\mu$m. Following this investigation it can be concluded that above a grain radius of $0.1\,\mu$m only SRP needs to be

taken into account. Only grain sizes above this limit will be considered and therefore only the perturbation due to SRP need be considered.

2.1.3 Effect of solar radiation pressure

Generally the effect of SRP is relatively small due to the low area-to-mass ratio of conventional satellites. However, for dust particles this is not the case. Here the surface area-to-mass ratio is large and therefore a significant momentum transfer will take place between solar photons and the dust particles. The effect of SRP can be quantified using the 'lightness' parameter, β, which is the ratio of the force due to SRP and solar gravity [32];

$$\beta = \left| \frac{F_{SRP}}{F_g} \right| \approx 570 \frac{Q}{\rho R_{gr}} \tag{2.16}$$

where ρ [kg m^{-3}] is the grain density and R_{gr} [μm] is the radius of the grain.

For relatively large radius particles, $R_{gr} > 1\mu$m, the value of Q varies little, with a value of approximately 1, but as the size decreases the interaction between the solar photons and the dust grains becomes more complex. The β-value for a range of particle radii is calculated using Mie theory for different composition models by Wilck and Mann [110]. The results for a typical asteroid dust grain can be seen in Fig. 2.4. This shows that the β-value peaks with a value of approximately 0.9 at a radius of 0.2μm before decreasing to 0.1 for a radius of 0.01μm. Also shown in Fig. 2.4 are lines defining the grain sizes that will be modelled, as described later, to their corresponding β values.

Since SRP has an inverse square relationship with heliocentric distance, its effect is to reduce the effective gravitational force of the Sun. Hence, the mass parameter, μ, for the three-body problem is now;

$$\mu = \frac{M_2}{(1-\beta)M_1 + M_2} \tag{2.17}$$

Due to the increase in the value of μ with increasing β the L_1 equilibrium point is found to shift towards the Sun. The magnitude of this effect can be seen in Fig. 2.5. For particles with $\beta > 0$ placed at the conventional L_1 point a shorter instability timescale will also be observed due to the displacement from the equilibrium position.

A beneficial effect of increased β is that the gradient of the potential function, Eq. (2.6), will be reduced around the new equilibrium point in comparison to the classical L_1 point. This will lead to improved stability if the dust cloud is positioned at this new point, though the effect that the dust cloud has on the solar insolation reduction is likely to be reduced as a smaller solid angle is subtended when viewed from the Earth.

It should be noted that it is assumed, for simplicity, that all particles within the cloud receive the same incident solar radiation. In reality this would not be the case as the attenuation of the solar photons would lead to a decreased value of F_{SRP} for particles not at the Sun facing boundary of the cloud and hence the effect of SRP would reduce. The magnitude of this effect would vary depending on the size and level of insolation change required. For example, a relatively small cloud may require a very large average attenuation of solar radiation and hence the particles at the Earth facing boundary are likely to have a smaller β-value than expected. There may also be unforseen side-effects due to other factors, for example the self gravity of the cloud or collisions between the dust grains. For the cloud lifetimes associated with this scenario these factors should be small. A large potential source for error is the mechanism by which the cloud is generated, for example the initial velocity given to the particles. These issues will be discussed later in Chapters 4 and 7.

2.1.4 Transition matrix

Critical to this study is the ability to predict the motion of dust particles relative to the L_1 point. This is because the libration point is unstable and therefore particles will naturally drift away if there is no control strategy implemented, as is the case for a passive dust cloud. The most efficient method for determining the motion of a large group of particles is to generate a transition matrix, $\Phi(t, t_0)$, which describes the motion of the cloud as a whole. This is in contrast to methods which propagate the equations of motion for each dust particle within the cloud individually. For predicting the motion of large groups of particles the transition matrix method is more computationally efficient and is sufficiently accurate for small time periods. For example, the propagation of a single particle over a period of 200 days requires a computational time of ≈0.1s. Assuming a total of 1×10^7 particles are propagated to give a sufficient spread, 11 to 12 days will be required, without computing the reduction in solar insolation. The transition matrix maps the initial state vector, $X(t_0)$, of each single dust grain into the state vector $X(t)$, as in Eq. (2.18).

$$X(t) = \begin{bmatrix} \mathbf{x}(t) \\ \mathbf{v}(t) \end{bmatrix} = \Phi(t, t_0) X(t_0) \tag{2.18}$$

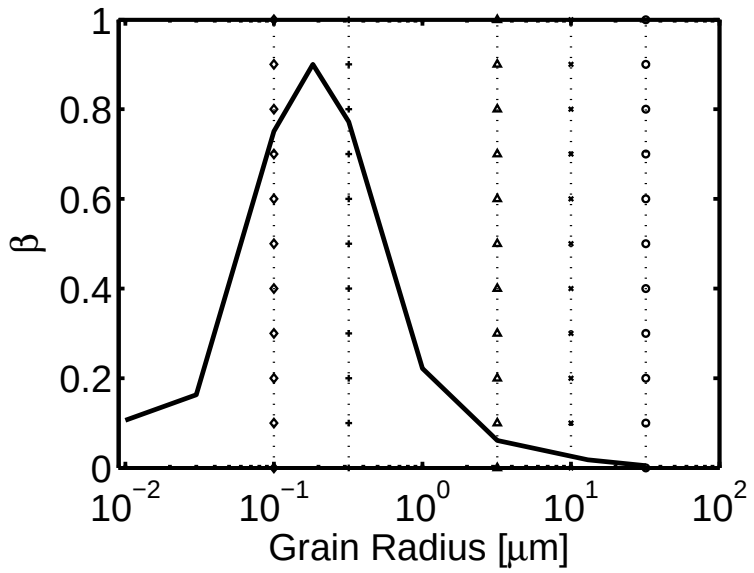

Figure 2.4: Variation in β with particle radius for an asteroid dust grain model as described by Wilck and Mann in reference [110]. The vertical lines correspond to the mass requirement results shown later in Fig. 2.13 and Fig. 2.14.

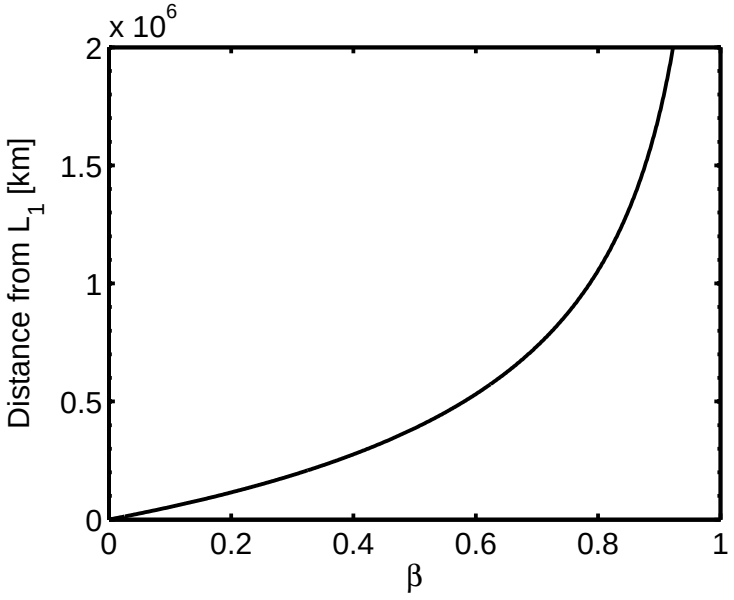

Figure 2.5: Sunward shift of the new equilibrium point, found when the effect of solar radiation pressure is included, in comparison to the conventional L_1 libration point.

where $\mathbf{x}(t)$ is position, $\mathbf{v}(t)$ is velocity and the transition matrix, $\Phi(t, t_0)$, is defined by;

$$\Phi(t, t_0) = \begin{bmatrix} \frac{\partial x(t)}{\partial x(t_0)} & \frac{\partial x(t)}{\partial v(t_0)} \\ \frac{\partial v(t)}{\partial x(t_0)} & \frac{\partial v(t)}{\partial v(t_0)} \end{bmatrix} \tag{2.19}$$

This transition matrix, $\Phi(t, t_0)$, can be generated by numerically solving the initial value problem:

$$\dot{\Phi}(t, t_0) = \mathbf{A}(t; X_0)\Phi(t, t_0) \tag{2.20}$$

with;

$$\Phi(t_0, t_0) = I_6 \tag{2.21}$$

where $\Phi(t_0, t_0)$ denotes that initially all state vectors map over themselves, thus I_6 represents a 6×6 identity matrix and $\mathbf{A}(t; X_0)$ is the Jacobian matrix of the flow field of the dynamical system evaluated over a reference trajectory [88]. The latter can be computed as:

$$\mathbf{A}(t; X_0) = \begin{pmatrix} 0 & -I_3 \\ G & 2B \end{pmatrix} \tag{2.22}$$

where;

$$G = \begin{pmatrix} U_{xx} & U_{xy} & U_{xz} \\ U_{yx} & U_{yy} & U_{yz} \\ U_{zx} & U_{zy} & U_{zz} \end{pmatrix} \tag{2.23}$$

is the Hessian matrix of the potential function, U, Eq.(2.6), and finally;

$$B = \begin{pmatrix} 0 & 1 & 0 \\ -1 & 0 & 0 \\ 0 & 0 & 0 \end{pmatrix} \tag{2.24}$$

Hence the transition matrix describing the transformation of an initial state vector to a final state vector with a large time step from t_0 to time t can be generated [55].

As this method uses the first order approximation to the equations of motion, i.e. the linearised dynamics around L_1, there will be a loss of accuracy for an increased time step. An error analysis between the method using the transition matrix and the propagation of the equations of motion was performed to determine the maximum length of time for which useable results can be generated. This concluded that for a particle with a displacement of 10,000 km from the equilibrium position, with zero initial velocity, an error in the region of 0.1%, 1% and 10% is achieved for a final time of 56, 155 and 191 days respectively.

An example showing the movement of a 3,000 km radius cloud with a grain β-value of 0.061 is shown in Fig. 2.6. It can be seen that the motion of the cloud is away from the L_1 point when the initial position is displaced from the equilibrium point. The original cloud becomes stretched with increasing distance from the equilibrium point as the relative dynamics of the particles varies throughout the cloud as described by the state transition matrix, Eq. (2.19).

2.2 Solar Radiation Model

The solar radiation model (SRM) is used to determine the reduction in insolation due to the presence of the dust cloud. The basic principle of the model is that the path length through the cloud can be found for a line connecting a point on the Sun's surface to a point on the Earth's surface. This path length is then used to calculate the fractional intensity reduction caused by the passage through the cloud.

2.2.1 Model structure

The structure of the SRM can be seen in Fig. 2.7. The surface of the Earth and Sun will be divided into segments with equal latitude and longitude spacing. At the centre of each segment there will be a node, Fig. 2.8, which has a surface area and central co-ordinates. The flux contribution to each Earth node provided by each Sun node can be calculated to determine the effect of the dust cloud.

The flux emitted by the Sun node, I_0, can be estimated using the following relation;

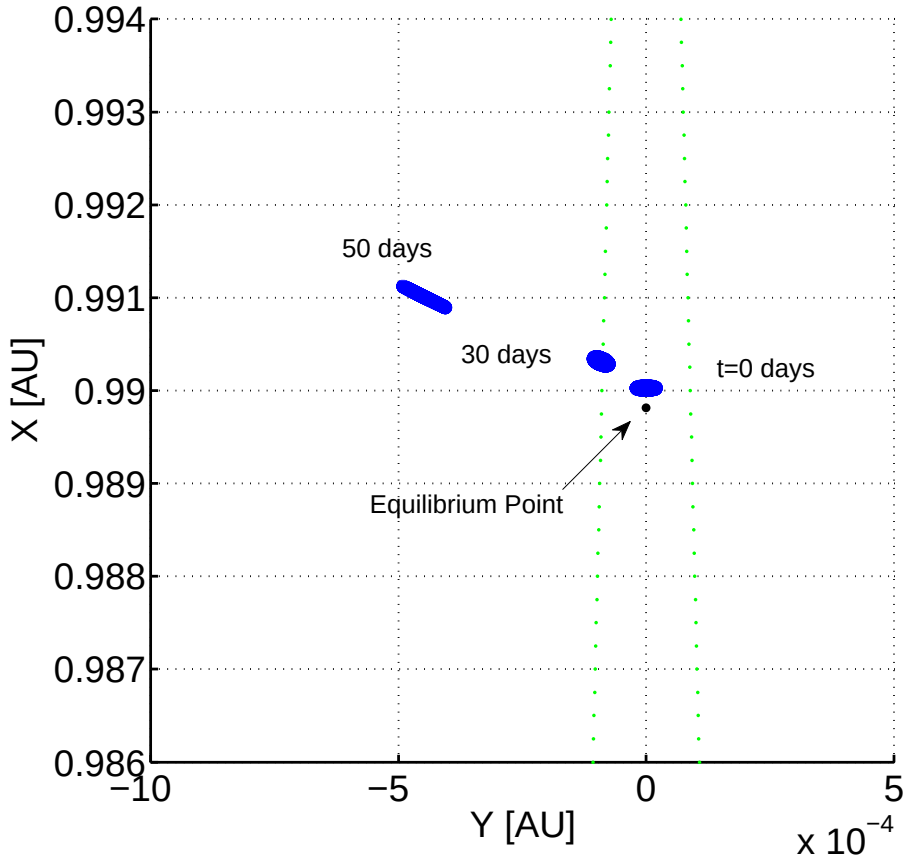

Figure 2.6: Motion of a 3,000 km radius spherical cloud of particles displaced from the equilibrium position for $\beta = 0.061$ in the x-y plane over a period of 50 days. The green dotted lines represent the extent of the useful zone along the Sun-Earth line, in which solar insolation is reduced.

$$I_0 = I_\odot \Omega_E A_E \cos\theta \tag{2.25}$$

involving the solid angle subtended by an Earth node, Ω_E, the area of the Earth node, A_E, and the angle of the line-of-sight to the Earth from the surface normal of the Sun, θ, and finally the solar radiance, $I_\odot$, of 2.01×10^7 W m^{-2} sr^{-1}.

The calculation of the solid angle subtended by the Earth node as seen from the Sun node is simplified by assuming that the Earth segment is a flat rather than curved surface but with the same area. The cross-sectional area of the sheet is then found by considering the angle of incidence of the light path in relation to this sheet, which is the angle between the light path and the surface normal, ϕ. The solid angle is then found by means of Eq. (2.26), using the distance between the nodes r;

$$\Omega_E = \frac{A_E \cos\phi}{r^2} \tag{2.26}$$

Clearly more accurate simulations, as discussed later, will use a larger numbers of nodes. This is because as the surface area of each node decreases the assumption of a flat sheet becomes more accurate and also the angle θ will better represent the whole radiating segment. For the same reason the estimation of the path length through the cloud will be more appropriate for the entire surface segment.

2.2.2 Attenuation calculation

The key to the calculation of the flux received by the Earth node is the use of the Beer-Lambert law for which the general case, Eq. (2.27), can be seen below;

$$I = I_0 e^{-\int \alpha_{gr}(l)\mathrm{dl}} \tag{2.27}$$

where I and I_0 are the intensity of the attenuated and incident light, l is the path-length through the cloud and the factor α_{gr} is the extinction coefficient due to the scattering and absorption of photons. A general approximation of this coefficient is the physical cross-section σ_{gr} of the particles multiplied by their number density ρ_n. This, in addition to the assumption of homogeneous particle size gives;

$$I = I_0 e^{-\sigma_{gr}\int \rho_n(l)dl} \tag{2.28}$$

So that only the cloud number density is now required.

2.2.3 Static model

A static model was first constructed to test the principles of the SRM. The cloud at t_0 is assumed to be spherical with a homogeneous distribution of dust particles with zero velocity. Thus, the particle density in the phase-space can be described as;

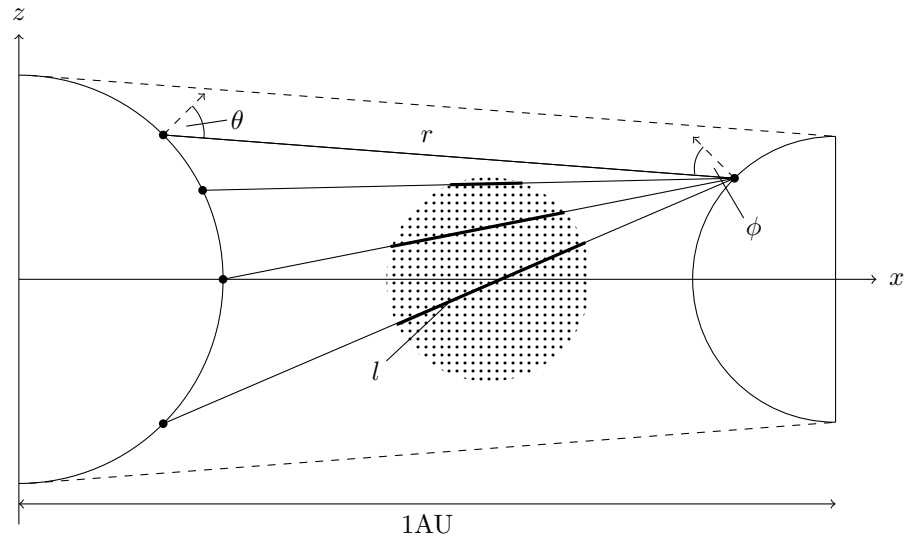

Figure 2.7: Structure of the SRM where the dashed line shows the extent of the 'useful zone' for insolation reduction.

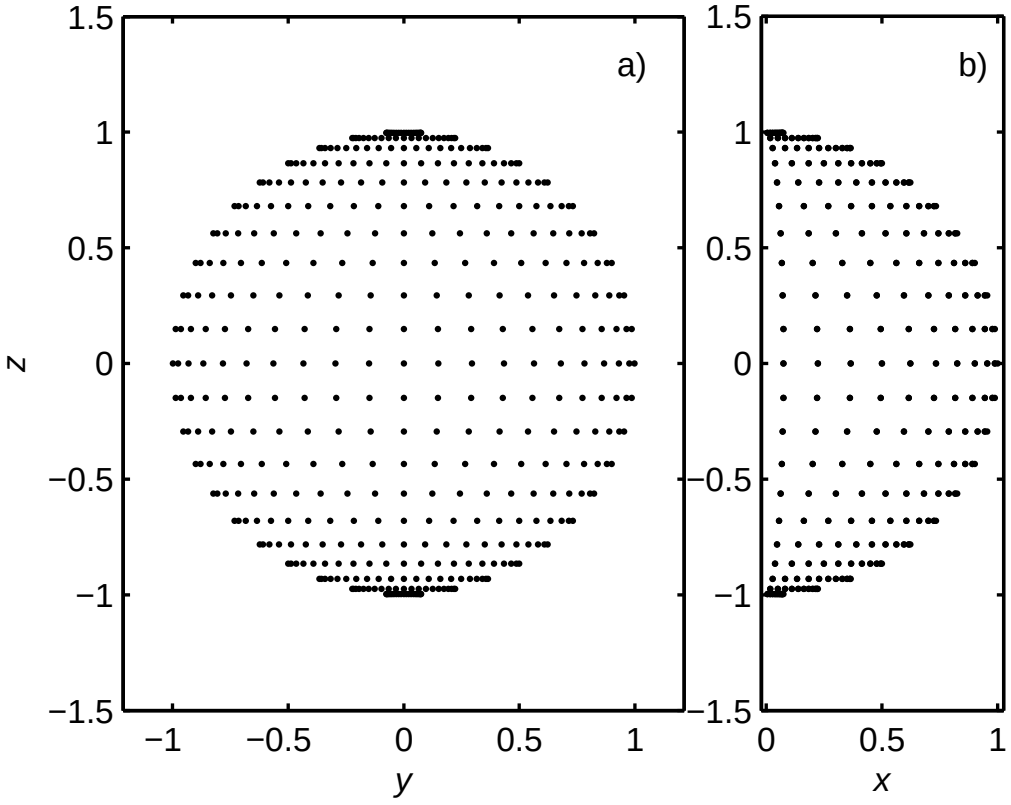

Figure 2.8: Distribution of 21×21 *nodes on a spherical surface, as used in the solar radiation model, viewed from the opposite body a) and perpendicular to the Sun-Earth axis b).*

$$\rho(\mathbf{x}, \mathbf{v}, 0) = \delta(\mathbf{v}(0)) \cdot H(r_{cloud} - ||\mathbf{x}(0) - \mathbf{x}_{centre}||) \tag{2.29}$$

where the Dirac-delta function $\delta(\mathbf{v}(0))$ describes the initial distribution of the velocity states of the dust as starting from rest, and the Heaviside function $H(r_{cloud} - ||\mathbf{x}(0) - \mathbf{x}_{centre}||)$ defines the volume of the spherical cloud of radius r_{cloud} centred at $\mathbf{x}_{centre}$. Here, and for the dynamic model, the path length integral through the cloud, Eq. (2.28), is calculated by the use of a numerical quadrature method. For the case of the static cloud the density variable is that described by Eq. (2.29). Thus the solar flux transmitted from each Sun node to each Earth node can be calculated, and hence the flux received by each segment of the Earth's surface can be determined and an intensity map can be constructed.

2.2.4 Dynamic model

For the case of a cloud that has been propagated using the transition matrix, the method involved in calculating the path length is slightly different and can be described as follows:

Assuming that the dynamics of the dust cloud satisfies Liouville's Theorem[1], which is equivalent to neglecting dissipation of energy by processes such as inelastic collisions, fragmentation or coalescence, one can define the density on the phase space at time t as:

$$\rho_\Gamma(\mathbf{x}, \mathbf{v}; t) = \rho_\Gamma(\phi^{-t}(\mathbf{x}, \mathbf{v}); 0) \tag{2.30}$$

where $\phi^{-t}(\mathbf{x}, \mathbf{v})$ denotes the flux of the system, or evolution of the state $X(t) = [\mathbf{x}(t)\ \mathbf{v}(t)]^T$ over a time-span $-t$ so that $\phi^{-t}(\mathbf{x}, \mathbf{v})$ is equal to $[\mathbf{x}(-t)\ \mathbf{v}(-t)]^T$. This *flux* of the system can be computed as described by Eq. (2.18), which requires the transition matrix, as seen in Eq.(2.19), to be computed. Now, since the density of dust particles for a given time t is required, the phase space density, $\rho(\mathbf{x}, \mathbf{v}; t)$, must to be integrated over the velocity components at time t:

$$\begin{aligned} \rho(\mathbf{x}; t) &= \int_\Gamma \rho_\Gamma(\mathbf{x}, \mathbf{v}; t) d\upsilon(t) \\ &= \int_\Gamma \rho_\Gamma(\phi^{-t}(\mathbf{x}, \mathbf{v}); 0) d\upsilon(t) \end{aligned} \tag{2.31}$$

[1]Liouville's theorem states that the density of particles is constant along a trajectory in any given phase-space i.e. the relative density is constant with time.

where $d\upsilon(t)$ is the product of the one-dimensional differential components of the velocity, $dv_x \cdot dv_y \cdot dv_z$. Now, Eq.(2.31) can be rewritten using Eq.(2.29) as:

$$\rho(\mathbf{x};t) = \int_{\Gamma} \delta(\phi^{-t}(\mathbf{x},\mathbf{v})_{\mathbf{v}}) \cdot H(r_{cloud} - ||\phi^{-t}(\mathbf{x},\mathbf{v})_{\mathbf{r}}||) d\upsilon(t) \tag{2.32}$$

where $\phi^{-t}(\mathbf{x},\mathbf{v})_{\mathbf{r}}$ and $\phi^{-t}(\mathbf{x},\mathbf{v})_{\mathbf{v}}$ are, respectively, the components of the position and velocity of the *flux*, $\phi^{-t}(\mathbf{x},\mathbf{v})$. The integral in Eq. (2.32) can be solved using the Dirac delta definition by substituting the infinitesimal volume of the phase space $d\upsilon(t)$ by:

$$d\upsilon(t) = \left\| \frac{\partial \mathbf{v}(t)}{\partial \mathbf{v}(0)} \right\| d\upsilon(0) \tag{2.33}$$

Thus resulting in;

$$\rho(\mathbf{x};t) = \left\| \frac{\partial \mathbf{v}(t)}{\partial \mathbf{v}(0)} \right\| H(r_{cloud} - ||\phi^{-t}(\mathbf{x},\mathbf{v}_*)_r||) \tag{2.34}$$

where $\mathbf{v}_*$ is the solution of the equation $\phi^{-t}(\mathbf{x},\mathbf{v}_*)_{\mathbf{v}} = 0$, such that $\delta(\phi^{-t}(\mathbf{x},\mathbf{v})_{\mathbf{v}}) = 1$.

This definition of the density can then be substituted into Eq. (2.28) to enable the solar insolation reduction to be found for any time.

2.2.5 Static model testing

To test the accuracy of the SRM, the average solar insolation over the Earth's surface can be found for different numbers of longitude and latitude nodes on the Sun's surface whilst the number of nodes on the Earth's surface remains constant at 21×21. The results can be seen in Fig. 2.9. This shows that as the number of nodes increases the solar constant levels off quickly to a value of 1381.9 W m^{-2}. This value compares favourably against those found in the literature, e.g. 1367 W m^{-2} [41] or 1371 W m^{-2} [32] as there is an approximately 1% difference at the highest number of nodes used.

A similar test was carried out to determine the number of longitude and latitude nodes required on both surfaces to provide a reliable result of the insolation change. This test essentially aims to determine the node number where a further increase would lead to a negligible change in the result. This was performed by placing a spherical cloud of radius 4,000 km with a grain size

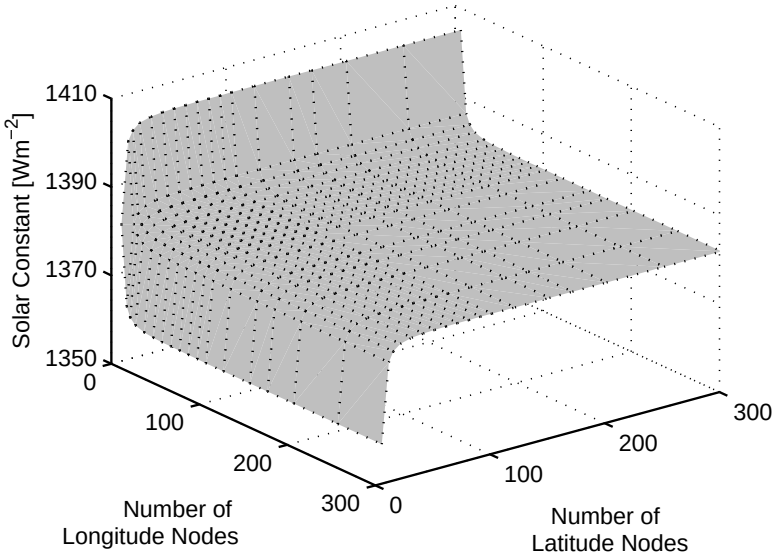

Figure 2.9: Average solar constant over the Earth's surface obtained using the SRM for varying numbers of longitude and latitude nodes on the surface of the Sun with 21×21 *nodes on the Earth's surface.*

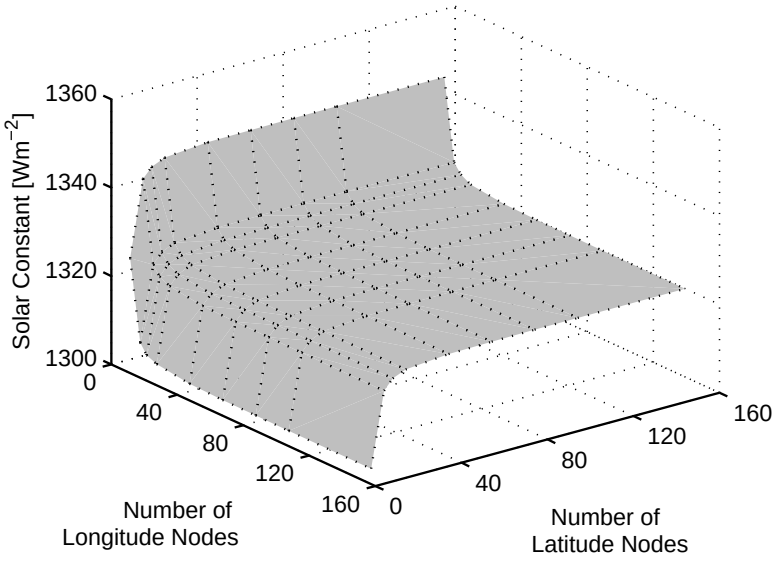

Figure 2.10: Average solar constant on the Earth's surface calculated for varying node numbers in a test of the SRM using a 4,000 km cloud placed at the L_1 *point.*

of 10 μm and number density of 110 m^{-3} at the L_1 position. The average solar constant on the Earth's surface was then calculated for varying numbers of nodes on the surfaces of both bodies with the number of longitude and latitude nodes being equal. The *quadgk* function in MATLAB, using adaptive Gauss-Kronrod quadrature, is used for this process. The result of this test can be seen in Fig. 2.10. This shows a similar shape to that seen in Fig. 2.9 and it can be concluded that node numbers of 61×61 is the number required to produce a consistent result. The variation in the result between this number of nodes and the highest used, 151×151 nodes, is of the order 10^{-5}. However, it is possible to use 21×21 nodes on the surfaces of both bodies with a variation from the highest node result of the order of 10^{-4}. The motivation for finding the minimum number of nodes is to minimise the computation costs. For example, a simulation involving 41×41 nodes on each sphere requires 15 times more path length calculations in comparison to a 21×21 simulation. Thus using 21×21 nodes rather than 61×61 nodes will considerably decrease the computational requirement whilst maintaining an acceptable level of accuracy. As an example, to calculate a data point shown in Fig. 2.13 or Fig. 2.14 for 21×21 nodes requires 2.1 hr to calculate whilst the same point for 61×61 nodes requires 143.5 hr for a 3GHz processor.

2.3 Results

2.3.1 Stability analysis

This section will discuss the numerical quantification of the stability of the L_1 point i.e. the length of time a particle takes to drift away. This is necessary as the L_1 point does not have Lyapunov stability. The stability analysis begins by considering the simplest case, a spherical cloud of dust of uniform density with a grain β-value of zero placed at the classical L_1 point. For all cases considered the initial velocity is assumed to be zero. For various radii of cloud the movement of a sample of evenly spaced test particles can be observed using the transition matrix, Eq. (2.18). The lifetime of a particle is then determined to be the length of time that it is in a position to block solar photons near the Sun-Earth line. The boundary of this 'useful zone' can be seen in Fig. 2.6 and Fig. 2.7. For cloud radii from 500-14,000 km the average lifetime of these test particles can be seen in Fig. 2.11. The maximum size of 14,000 km was chosen as this is the approximate extent of the useful zone at the classical L_1 point. It can clearly be seen that the average lifetime of the particles decreases significantly with cloud radius. This result sets a limit for later stability analyses as the effect of SRP is not added. It is expected, therefore, that for the scale of dust grains investigated, the average lifetime of the dust particles will fall below this level when the cloud remains at the L_1 point. In contrast, it is expected that the average lifetime of a cloud placed at the displaced

equilibrium position should increase slightly with β due to the reduced gradient of the potential function at this position.

The average lifetime of a cloud positioned at the L_1 point for varying radii and β-values can also be seen in Fig. 2.11. This shows that when SRP is taken into account the average lifetime of particles within the cloud decreases significantly when placed at the classical L_1 point, as expected. This is irrespective of cloud radius, though the smaller clouds do show a slightly increased average lifetime. As noted previously, this is due to the increased displacement from the classical equilibrium point. In contrast, when a cloud is centred at the new displaced equilibrium point the average lifetime increases with β, shown in Fig. 2.12. Again the smaller cloud radii have longer lifetimes. This increased lifetime is due to the shallower gradient of the potential function caused by the decrease in the effect of solar gravity as β increases. Comparing these results indicates that a cloud placed at the displaced equilibrium point is likely to be a more mass efficient option. However, it cannot yet be concluded that this equilibrium point is the most suitable position without taking into account the engineering challenges involved. These aspects will be discussed later in Chapter 7.

2.3.2 Dynamic solar radiation model results

The key quantifiable parameter for this method of geoengineering is the cloud mass necessary to create the required level of solar insolation reduction. This shall be presented in terms of the mass-per-year of asteroid material required. This is calculated using the SRM as described in Sec. 2.2.4 which allows the path length through the cloud to be calculated for any given time. Hence, the evolution of the reduction in solar insolation due to the cloud dynamics can be found for different initial cloud and grain radii.

The results shall be found for dust clouds placed at the classical Lagrange point and the new displaced equilibrium points created for different β-values of asteroid material. The initial clouds are assumed spherical with sizes ranging from 1,000-12,000 km for five different grain sizes. These grain dimensions are based on the investigation performed in [110] and can be found in Table 2.2, along with their corresponding values of β shown in Fig. 2.4. In terms of terrestrial aerosol particles the three larger grain sizes correspond to relatively coarse particles, e.g. terrestrial silt particles blown up by the wind. In contrast the smaller particles correspond to the size of condensed gas particles. The distance by which the equilibrium point for the different particles is displaced sunwards of the conventional L_1 point can also be seen in Table 2.2.

Each result was calculated using 20 time steps with the length of each step being dependent

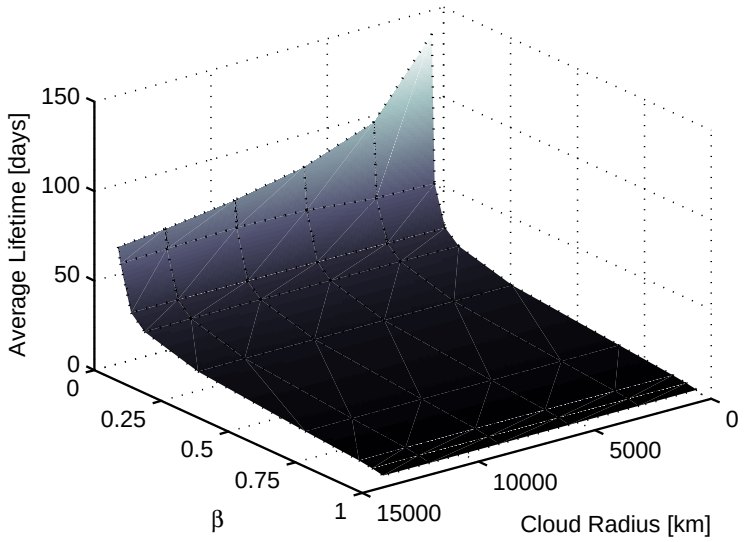

Figure 2.11: Average lifetime of particles in a dust cloud positioned at the classical L_1 point for varying radii and values of β.

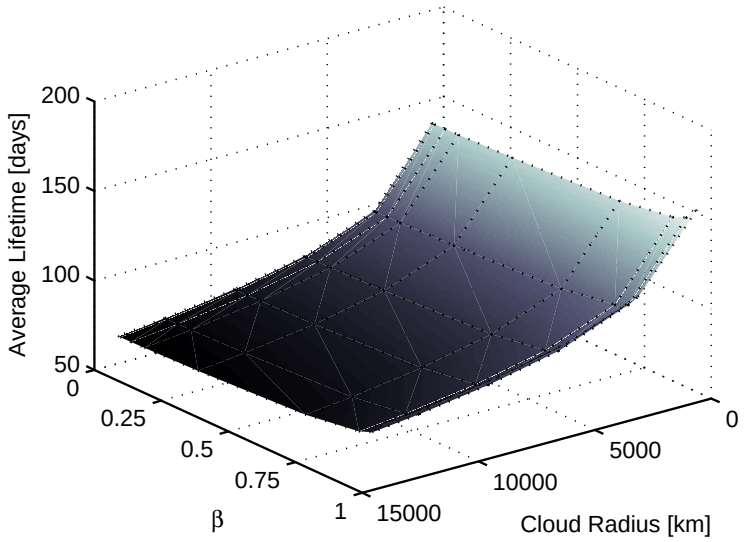

Figure 2.12: Average lifetime of particles in a dust cloud positioned at the displaced equilibrium point for varying radii and values of β.

Grain Radius [μm]	β	Displacement [km]
32	0.005	2,500
10	0.018	9,000
3.2	0.061	32,000
0.32	0.772	950,000
0.1	0.751	875,000

Table 2.2: Grain radii simulated and the corresponding values of β and displacement of the equilibrium position with respect to the classical L_1 point.

upon the lifetime of the cloud. A steady state solution is then calculated using the combined effect of the cloud at each time step by summing the relative phase-space densities, as in Eq. (2.34), for the times used for each individual path.

$$I = I_0 e^{-\sigma_{gr} \int_{t_{20}}^{t} \int \rho(l,t) dl dt} \tag{2.35}$$

$$= I_0 e^{-\sigma_{gr} \sum_{t_0}^{20} \int \rho(l,t_n) dl} \tag{2.36}$$

Following this, the initial density of the cloud was optimised to achieve the required 1.7% insolation reduction when the attenuation is calculated. Subsequently, knowing the time step and grain properties, the mass that is required to be ejected per year can be determined. The results for all five grain sizes for clouds ejected at the L_1 point can be seen in Fig. 2.13 and for the displaced equilibrium position in Fig. 2.14.

In general, the result expected was that the larger particles, which have smaller values of β, would require less mass per year due to their greater average lifetime. This is not the case however and the decrease in grain size provides a greater mass saving than the longer lifetime of the larger particles with the optimum solution occurring for the smallest grain radius of 0.1 μm.

For the optimum cloud radius of 4,000 km, which is similar to the stationary SRM result, the mass requirement is $7.60 \times 10^{10}\,\mathrm{kg\,yr^{-1}}$. In comparison to the method proposed by Struck [98] this is a mass saving of several orders of magnitude. For this scenario the average mass ejection rate must be of the order of $850\,\mathrm{kg\,s^{-1}}$. The feasibility of this estimate will be discussed later. The results for the steady state solution for a cloud ejected at the equilibrium point show a similar shape to the results shown in Fig. 2.13 with the optimum mass requirement being $1.87 \times 10^{10}\,\mathrm{kg\,yr^{-1}}$.

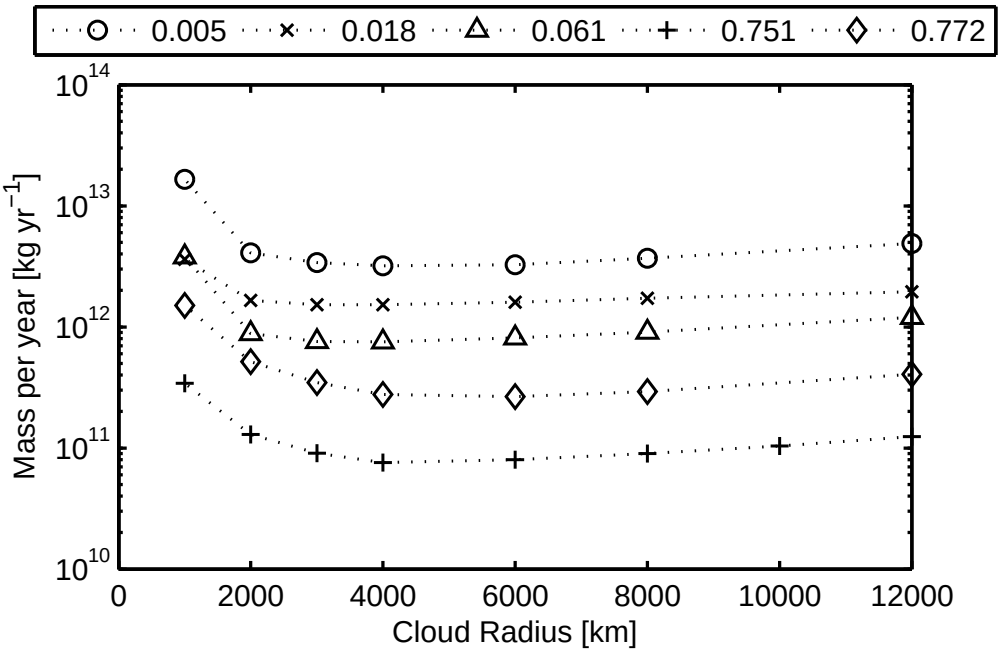

Figure 2.13: Mass requirement of dust for the steady state solution of clouds ejected at the L_1 point for varying initial cloud radii for the five grain β-values used.

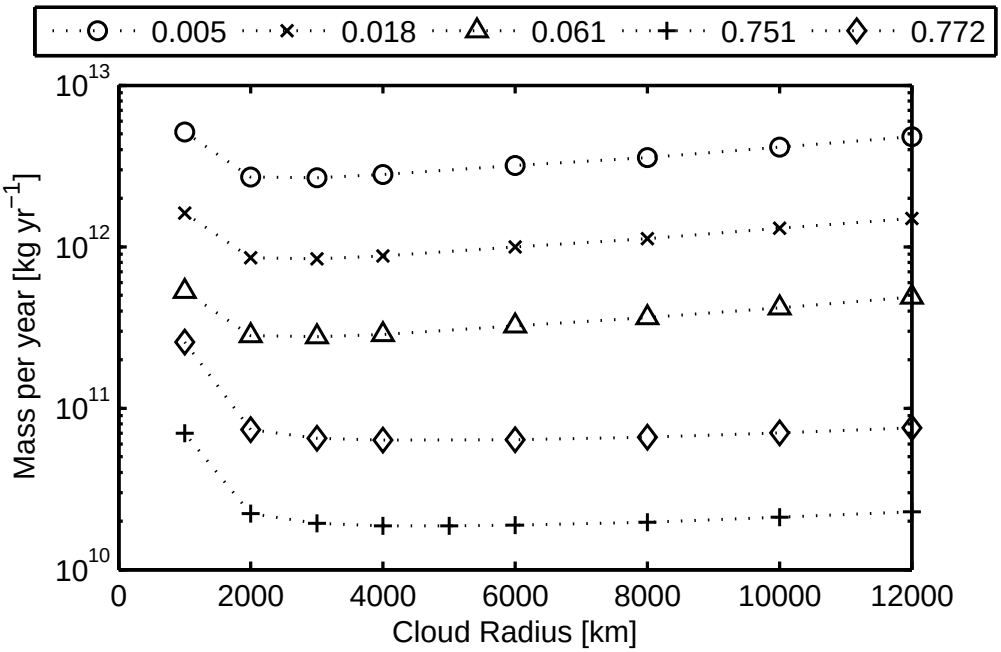

Figure 2.14: Mass requirement of dust for the steady state solution of clouds ejected at the new displaced equilibrium points of the four grain β-values used for varying initial cloud sizes.

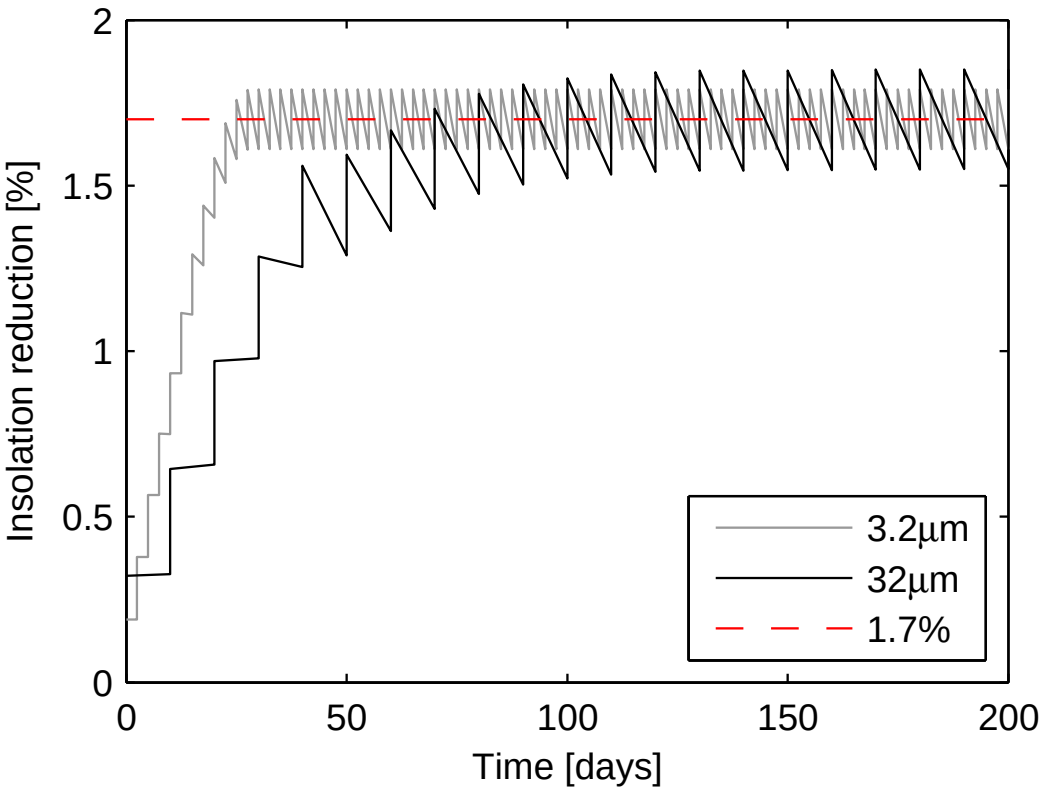

Figure 2.15: Variation in insolation reduction expected during the activation phase of the geoengineering method for the case of a cloud of 32 μm and 3.2 μm sized grains placed at the L_1 point for a final insolation change of 1.7%.

The result for the case of a 0.1 μm grain is clearly more optimal than for larger grains in more than just the mass requirement. Since the effective lifetime of smaller particles is shorter the steady state will be achieved sooner and is thus a more immediate solution. Figure 2.15 shows the time to achieve a steady-state for grain radii of 3.2 μm, this value is shown rather than for 0.1 μm for clarity, and 32 μm where at each time step a new cloud is released. As can be seen, the 3.2 μm case reaches the desired insolation change in approximately 20-30 days whilst the 32 μm case takes of the order of 100 days. For a grain size of 0.1 μm this falls to approximately 10 days.

The same principle applies to the deactivation period for the cloud. When geoengineering is no longer required, or if the cloud proves to have unforeseen side-effects on the Earth's climate and must be discontinued, then the lower grain size cloud will be beneficial since the cloud will disperse in a much shorter time. This will not apply to a scheme where the cloud is released at the classical equilibrium point however, as the smaller particles are likely to have a longer lifetime.

The change in insolation seen in Fig. 2.15 is highly uneven. This is due to the periodic

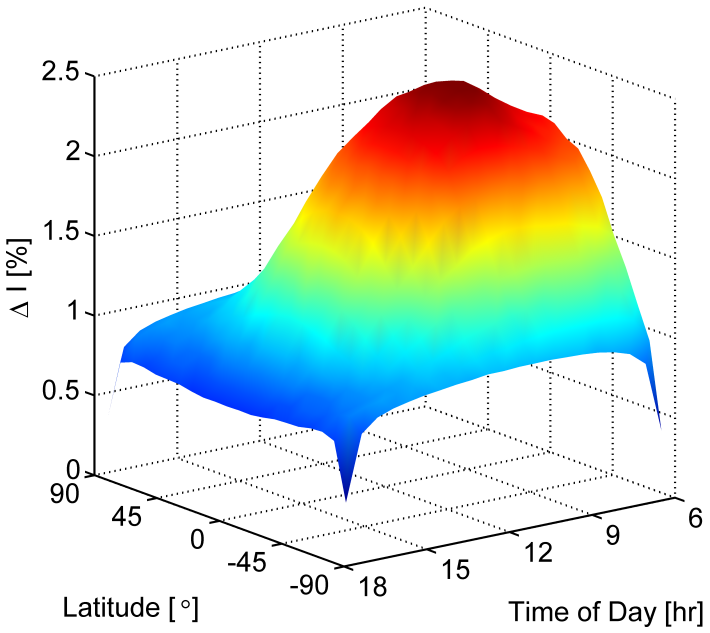

Figure 2.16: Percentage insolation reduction over the surface of the Earth for the steady state solution of an initial cloud of radius 4,000 km and grain size of 0.1 μm released at the classical L_1 point.

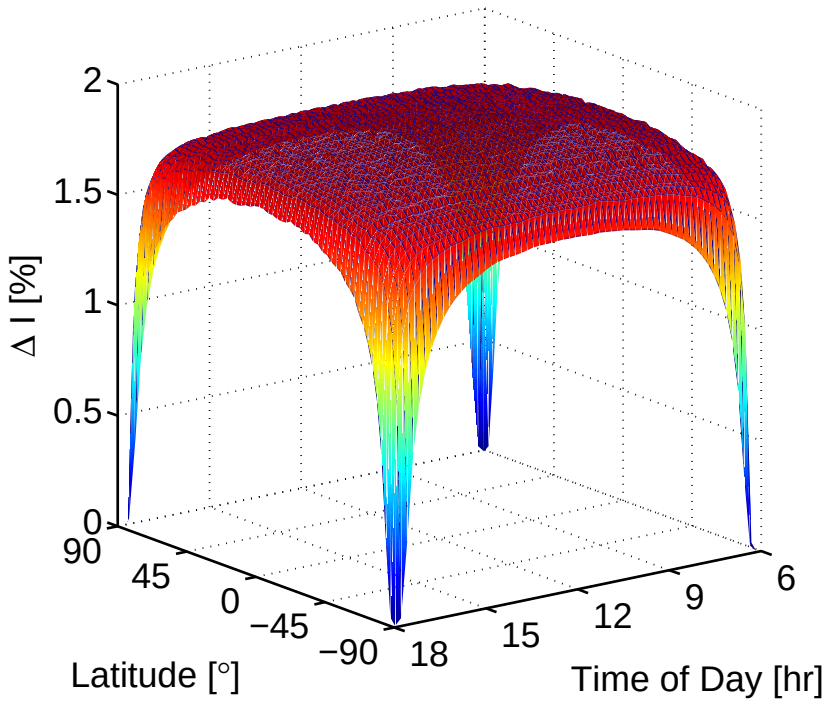

Figure 2.17: Percentage insolation reduction over the surface of the Earth for the steady state solution of an initial cloud of radius 4,000 km and grain size of 0.01 μm released at the displaced equilibrium point.

mass ejections used to generate the steady state condition. A steady state condition based on a continuous ejection of mass would eliminate this 'flickering' effect.

A map showing the insolation change over the Earth's surface for a cloud of radius 4,000 km and grain size 0.1 μm released at the L_1 point and the new displaced equilibrium point for 61×61 nodes on the surface of each body can be seen in Fig. 2.16 and Fig. 2.17. It should be noted that the tilt of the Earth's axis is not taken into account and the axes labelled 'Latitude" refer to a reference sphere with its equator parallel to the ecliptic plane. The correspondence to the Earth's latitude and time of day will change over the course of a year due to the tilt and orientation of the axis of rotation of the Earth. The results in terms of this motion will be discussed in Sec. 6.4. As can be seen, the schemes where the cloud is released at the new displaced equilibrium point show a more symmetrical pattern. The insolation appears evenly spread as the cloud is initially positioned directly along the Sun-Earth line. This is additionally caused by the largest dispersion of the cloud occurring within the ecliptic plane whilst dispersion does not occur along the z-axis. The insolation change map for the case of a cloud released at the classical L_1 point shows a different pattern. Here the insolation change is shifted towards one side of the Earth due to the movement of the cloud away from the initial position being in one direction. This will lead to greater shading in the 'morning' region of the Earth. The possible effects of uneven shading will be discussed further in Sec. 6.

2.3.3 Anticipated accuracy

A final issue concerning the accuracy of the methodology proposed here can be tackled by comparing the particle evolution by using both the transition matrix and direct propagation of the equations of motion, Eq. (2.5). The results show that high β-value clouds are significantly effected by propagation error, accumulating averages of 10% error after only a few tens of days. Fortunately, on the steady state solution the dust that has been drifting for these periods only contributes less than 5% of the solar insolation reduction, thus the overall accuracy of the method is not compromised.

2.4 Discussion

From Sec. 2.3 the mass of asteroid material required to create an insolation reduction of 1.7% for dust clouds placed at the classical Lagrange point and new displaced equilibrium point has been calculated to be $7.60 \times 10^{10}\,\mathrm{kg\,yr^{-1}}$ and $1.87 \times 10^{10}\,\mathrm{kg\,yr^{-1}}$ respectively. This is considerably

lower than the dust cloud methods suggested by Struck [98] and Pearson [79]. It is also in line with the solid reflector/refractor proposals by Angel [5] and McInnes [69] whilst reducing the need for manufacturing considerably. As well as mass, the first order feasibility of these different methods can be compared using the energy required to be placed in the required position. This shall be discussed in the following section. A discussion of the engineering requirements of the different cloud generation mechanisms will be discussed to determine the feasibility of this, and other SBGE, methods in Chapter 7.

2.4.1 Comparison to previous proposals

The estimates of the energy required for launch, or material transport, energy required for each of the proposals discussed in this section can be seen Table 1.1. The energy required to launch a 2,100 kg spacecraft, with 1,000 kg payload, to the L_1 point using a mass driver is estimated by Angel to be 6.35×10^{11} J [5]. Given the total system mass of 2.0×10^{10} kg for the refractor method proposed by Angel results in a total energy requirement to launch of 1.27×10^{19} J. It can be assumed that the solid reflectors proposed by McInnes can be launched in a similar fashion, thus giving an energy requirement of 1.78×10^{20} J, from a total system mass of 2.6×10^{11} kg. To supply the material for the dust cloud method described in this Chapter would require $1.19 \times 10^{19}\,\mathrm{kg\,yr^{-1}}$ and $4.83 \times 10^{19}\,\mathrm{kg\,yr^{-1}}$ for the displaced equilibrium position and classical L_1 position clouds respectively. The annual global energy consumption in 2009 was 8.353 Mtoe[2][45], which equates to 3.5×10^{20} J. Thus, at current levels of energy consumption, the dust cloud method would require in excess of 3.4% of the global energy budget if launched with mass drivers from Earth. This figure, for the dust cloud method as well as the other methods mentioned in this section, does not include the energy required for the manufacture, maintenance and operation of the SBGE method.

Struck comments on the capture of comets or use of lunar material as possible sources for the dust cloud. A lower bound on the energy required to re-position a comet can be made for the proposal by Struck by computing the change in Jacobi constant associated with the transfer of material. The Jacobi constant is expressed as;

$$C = V^2 - 2U \tag{2.37}$$

where V is the speed of the object and U is the gravitational potential described in Eq. (2.6). For this calculation it is assumed that the object is stationary at both the initial and final positions.

[2]A common unit of energy is tonnes of oil equivalent (toe) and is the approximate amount of energy released upon the consumption of one tonne of crude oil. This value is equivalent to 41.87 GJ [45].

The transfer of material from the Sun-Earth L_4/L_5 points to the Earth-Moon system is assumed to occur in two phases. First a transfer from the Sun-Earth L_4/L_5 points to the Sun-Earth L_1 point, after which the object is assumed to be in the Earth-Moon system. Then, the change in Jacobi constant between the Earth-Moon L_2 point and L_4/L_5 points is considered as a worst case scenario. The energy required for the first phase is $0.79\,\mathrm{MJ\,kg^{-1}}$ with an additional $0.19\,\mathrm{MJ\,kg^{-1}}$ being required within the Earth-Moon system. For the total system mass of $2.1 \times 10^{14}\,\mathrm{kg}$ the energy required for the transfer is $2.06 \times 10^{20}\,\mathrm{J}$. Alternatively, the energy required to overcome the gravitational potential associated with moving an object from the surface of the Moon to the Earth-Moon L_4/L_5 points can be determined. Using the lunar escape velocity of $2.37\,\mathrm{km\,s^{-1}}$ gives an energy of $5.90 \times 10^{20}\,\mathrm{J}$ though in reality a greater mass will be needed to account for the spacecraft that are required to deliver the lunar dust. By following the methods used by Angel [5] for a mass driver but neglecting losses due to atmospheric drag and the associated shielding gives an energy of $4.6 \times 10^{21}\,\mathrm{J}$.

The energy requirement for the two proposals made by Pearson [79] for a dust ring and satellite ring can similarly be estimated using the methods described by Angel [5]. These energies are $2.0 \times 10^{18}\,\mathrm{J}$ and $1.0 \times 10^{21}\,\mathrm{J}$ for the satellite ring and dust ring respectively. These energies are optimistic in the respect that the atmospheric drag is likely to be greater than calculated. This is because to achieve the orbital radius required of 1.2-1.6 times the radius of the Earth the elevation of the mass driver tube will be much lower than for a transfer to L_1. In comparison, for the dust ring, the energy required to capture the material in the form of a near Earth object is $8.9 \times 10^{19}\,\mathrm{J}$. This was calculated in a similar way as the estimate for the Earth-Moon system dust cloud. First a transfer to the Sun-Earth L_1 point was calculated followed by a transfer to an Earth orbit in the Sun-Earth CR3BP. The Jacobi constant was averaged over an entire orbit for an orbital radius of 10,250 km. An additional factor must be added to the energy of the particle ring. This is the energy required to capture two shepherding asteroids, the upper mass of which is $1.4 \times 10^{11}\,\mathrm{kg}$. This will add an extra $5.4 \times 10^{18}\,\mathrm{J}$ to the dust ring energy.

A similar estimate can be used to determine the energy required to manoeuvre the necessary mass of asteroid material to the L_1 position for the method proposed in this paper. Assuming that geoengineering is required for a minimum duration of 10 years the energy required to capture the required material is approximately $1.5 \times 10^{17}\,\mathrm{J}$. This figure will be increased when the energy required to launch the spacecraft used to capture the NEA is taken into account but this can be assumed to be negligible in comparison to the mass of the asteroids. The method of geoengineering proposed in this chapter can be seen to have a lower energy requirement than other proposals. As a comparison, the energy required for this proposal is equivalent to the maximum generation capacity of the Three-Gorges Dam running continually for approximately 3 months. Using the same comparison, the mass of concrete used to construct the Three-Gorges Dam is in the region of $10^{10}\,\mathrm{kg}$

[60]. Hence the geoengineering schemes discussed here will be large-scale ventures, highlighting why the engineering demands of space-based geoengineering must be reduced.

2.5 Conclusion

In this Chapter a method of geoengineering has been investigated that involves the use of large clouds of dust placed in the vicinity of the L_1 point as an alternative to the use of thin film reflectors. It has been concluded that the mass requirement for a cloud placed at the classical L_1 point, to create an average solar insolation reduction of 1.7%, is $7.60 \times 10^{10}\,\mathrm{kg\,yr^{-1}}$ whilst a cloud placed at a displaced equilibrium point created by the effect of solar radiation pressure is $1.87 \times 10^{10}\,\mathrm{kg\,yr^{-1}}$. These mass ejection rates are considerably less than the mass required in the methods proposed in [98] and [79] and are comparable to the thin film reflector methods proposed in [5], [69] and others. It has also been shown that the energy required to position the method proposed here at the L_1 position is less than other methods.

The method described here assumes an initially static dust cloud. In Chapter 7 this will be shown to be difficult to accomplish, though as will also be discussed in Chapter 3 it may be possible for small dust clouds. Therefore, the effect that the initial velocity has on the evolution of the dust cloud must be investigated. This shall be discussed in the following chapters.

Chapter 3

Gravitationally Anchored Dust Cloud at L_1

The concept of an L_1 positioned dust cloud for geoengineering has been described in the previous chapter. These methods use the dynamics of the CR3BP and do not take into account the mass of the asteroid from which the dust cloud is generated. This is a logical assumption for small asteroids. However, there are many asteroids in the population of near Earth objects that have a considerable mass. This mass can be accounted for using four-body dynamics and the resultant effect on the gravitational potential in the vicinity of the L_1 point can be observed. These dynamics can be seen to generate a zero velocity curve which bounds the asteroid and within which dust grains ejected from the asteroid will remain trapped if ejected below the escape velocity. This will gravitationally anchor a dust cloud in the vicinity of the L_1 point which can be then used for geoengineering. The methods required to generate such an anchored dust cloud will be discussed in this chapter as well as a combined method of geoengineering that uses the dynamics described in Chapter 2 to utilise any escaping particles.

3.1 Four-Body Problem

The dimensionless equations of motion of a dust grain in the circular restricted Sun-Earth three-body problem (CR3BP) were defined in Sec. 2.1. These equations can be modified to define a circular restricted four-body problem (CR4BP) which includes a small asteroid captured at L_1. Assuming that the effect of the asteroid on the Earth's orbit is negligible and the asteroids gravity

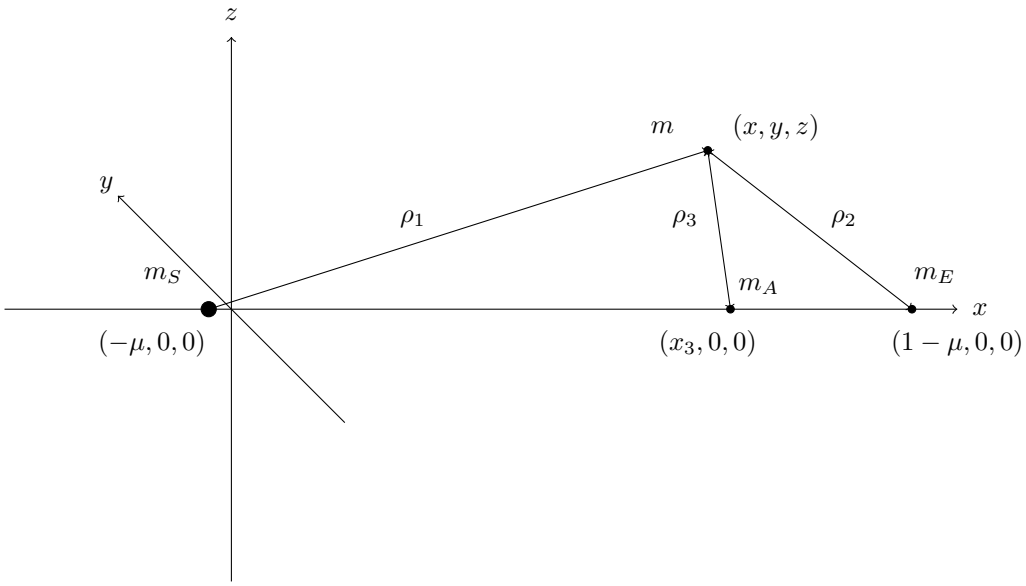

Figure 3.1: Four-body problem with Sun m_S, Earth m_E, asteroid m_A and dust particle m.

field is homogeneous the new effective potential is defined by;

$$U = \frac{1}{2}\left(x^2 + y^2\right) + \frac{1-\mu}{\rho_1} + \frac{\mu}{\rho_2} + \frac{\gamma}{\rho_3} \tag{3.1}$$

The parameter γ is the mass fraction of the asteroid in relation to the mass of the three-body system, $\gamma = m_A/(m_s + m_E)$, and μ is the mass ratio of the Earth to the mass of the Earth and Sun, $\mu = m_E/(m_s + m_E)$. The scalar distances ρ_1, ρ_2 and ρ_3 are the separations between the primary and secondary bodies, the asteroid and dust particle respectively, as shown in Fig. 3.1, and can be defined as;

$$\rho_1 = \sqrt{(x+\mu)^2 + y^2 + z^2} \tag{3.2}$$

$$\rho_2 = \sqrt{(x+\mu-1)^2 + y^2 + z^2} \tag{3.3}$$

$$\rho_3 = \sqrt{(x-x_3)^2 + y^2 + z^2} \tag{3.4}$$

When the gravitational potential of a body placed at the classical L_1 point is considered, two new collinear equilibrium positions appear. These can be found by substituting the potential function of the CR4BP, seen in Eq. (3.1), into the equations of motion defined in Eq. (2.5). The

location of the equilibrium positions along the x-axis can be then found by setting $y = z = 0$ and $\ddot{x} = \dot{y} = 0$, thus resulting in the following equation:

$$x : x - \frac{1-\mu}{(x+\mu)^2} + \frac{\mu}{(x+\mu-1)^2} \pm \frac{\gamma}{(x-x_3)^2} = 0 \tag{3.5}$$

The new collinear equilibrium positions are located on either side of the classical L_1 position, as shown in Fig. 3.2 and Fig. 3.3. These new equilibria, like the conventional L_1 position, are unstable, but will bound the asteroid, thus approximating the size of the dust cloud. Similar to the previous work, small dust grain sizes will be used and therefore the effects of SRP must be included by the addition of the factor β to the equations of motion to reduce the effective mass of the Sun by $(1 - \beta)$.

3.2 Zero Velocity Curve

Assuming that the asteroid is rotating in the same plane as, and in phase with, the CR3BP the speed of a particle in the restricted 4-body system can be described by the Jacobi integral as;

$$V^2 = 2U(x, y, z) - C \tag{3.6}$$

where V is the particle speed and C is the Jacobi constant. Since kinetic energy can only be strictly positive, it follows from Eq. 3.6 that the particle can only move within a region delimited by a zero velocity curve (i.e., when the right hand side of Eq. 3.6 vanishes). This constraint can then be used to investigate the size of the region around the third body, the asteroid at L_1, where a particle can become trapped if the energy, or Jacobi constant, of the particle is not large enough for escape. It is assumed that within this region particles are collisionless, as will be confirmed later. Clearly, the maximum enclosed volume will be found for a zero velocity surface with a Jacobi constant equal to that of one of the new equilibrium points in the CR4BP. Combining Eq. (3.1) and Eq. (3.6), the Jacobi constant can be expressed as;

$$C = x^2 + y^2 + 2\left(\frac{1-\mu}{\rho_1} + \frac{\mu}{\rho_2} + \frac{\gamma}{\rho_3}\right) \tag{3.7}$$

where x_3 is the position of the asteroid, again shown in Fig. 3.1. Noting that the equilibrium points lie on the x-axis, i.e. $y = 0$, the Jacobi constant for these positions can be found using Eq. (3.7).

By numerically solving Eq. 3.7 to find the positions of the new equilibrium points for a body of a given mass, these two values of C can be then found. The surfaces that arise from this analysis can then be plotted in the CR4BP, two examples of which can be seen in Fig. 3.2 and Fig. 3.3 for an asteroid with a mass of 1×10^{15}kg placed at the classical L_1 position for $\beta = 0$ and for $\beta = 0.001$ respectively. It can be seen that for even small values of β the shape of the zero-velocity curve becomes distorted and shrinks in size. It is also observed that only one of the two equilibrium positions will have a Jacobi constant that creates a surface that fully bounds the asteroid position, which is of particular importance for the case of the asteroid placed at the L_1 point. The fully bounding surface corresponds to the equilibrium point with the higher Jacobi constant which will be termed the critical Jacobi constant, C_{crit}.

The volume and approximate width of the zero velocity surfaces for a selection of near Earth asteroids, discussed later, can be seen in Fig. 3.4. An asteroid at the classical L_1 position and the displaced equilibrium position is considered. The displaced position accounts for the radiation pressure perturbation on the dust grains and ensures that a large zero velocity curve still exists. The volume enclosed within the zero velocity surface, V_{ZVC}, can be determined by noting that within the bounded volume the Jacobi constant will be higher than the value of C_{crit}. The Heaviside function can then be used in a numerical integration as follows;

$$V_{ZVC} = 4(x_{S,2} - x_{S,1}) y_S z_S \int_{x_{S,1}}^{x_{S,2}} \int_{-y_S}^{y_S} \int_{-z_S}^{z_S} H(C(x, y, z) - C_{crit}) \, \mathrm{d}z \, \mathrm{d}y \, \mathrm{d}x \tag{3.8}$$

where $x_{S,1}$ is the distance between the asteroid position and the bounding equilibrium position and $x_{S,2}$ is the distance to the point on the zero velocity surface on the opposite side to the equilibrium position where the Jacobi constant is equal to C_{crit} for $y = z = 0$. The factors y_S and z_S are the maximum width of the zero velocity curve in the y and z axes over the range of x values and are determined by finding where Eq. (3.7) equals C_{crit} first for $z = 0$ to find y_S and subsequently for $y = 0$ to find z_S. Since the zero velocity surface is symmetrical about the x-axis only the volume integral is multiplied by $(x_{S,2} - x_{S,1}) 2 y_S 2 z_S$ to find the final volume.

The absence of results for the classical L_1 case for small asteroid masses in Fig. 3.4 arises because the contour with the Jacobi constant of the equilibrium positions no longer bounds the asteroid surface. As expected both the width and volume enclosed is higher for an asteroid placed at the new displaced equilibrium position. Hence it can be concluded that, to maximise the inso-

lation reduction possible, an asteroid should be positioned at the slightly displaced equilibria. The feasibility of achieving this will be discussed in Sec. 3.3.1.

3.3 Effect on Solar Insolation

3.3.1 Asteroid selection

The effect that the dust cloud, confined by the zero velocity surface, has on the solar insolation has been determined for a set of real asteroids. Firstly, in order to assess the best set of candidates for the geoengineering scheme proposed, a complete list of near Earth objects was retrieved from the NASA NEO program database[1]. Even if only the absolute magnitude of each object is known, the approximate mass of each near Earth asteroid can be estimated by means of the Bowell et al. relation [20] and assuming an average density and albedo (i.e. 2,600 kg m^3 and 0.154 [29]). Then, the minimum Δv of the Lambert-arc connecting the asteroid and the Earth is optimised for the 250 largest objects, which includes all objects larger than 1×10^{13}kg. A global optimisation procedure is used to select the optimal Lambert arc conditions to transfer the asteroid to an Earth-like orbit. The design parameters of the optimisation are the true anomalies at both departure and arrival. A global optimisation method is used that blends a stochastic search with an automatic solution space decomposition technique [105, 106]. Next, a Pareto front with the largest objects and lowest transfer impulse (i.e. $I = m_A \Delta v$ as a measure of incremental engineering effort) can be constructed leaving a set of 28 candidates as gravitational anchors. The Pareto front is shown in Fig. 3.5 and provides the list of the, a priori, most efficient asteroids to capture with masses ranging from 1×10^{13}kg to the largest known near Earth asteroid mass of approximately 1.3×10^{17}kg for the asteroid 1036 Ganymed. The impulse obtained from the Lambert arc method is used here as a sorting parameter only, since we envisage continuous low thrust used for capture.

The masses of these near Earth asteroids range from $1 \times 10^{13} - 1.3 \times 10^{17}$kg. It was previously stated that the optimum position is likely to be the displaced equilibrium position to compensate for the radiation pressure on the dust grains. However, it must be determined whether it is feasible for asteroids of such large mass to be so displaced. The acceleration required to maintain the position at the displaced equilibrium position for a value of β of 0.005, corresponding to a physical displacement of 2,500km, can be determined using Eq. (2.5) by assuming $\dot{y} = \dot{x} = 0$. This gives a result of $9 \times 10^{-7}\,\mathrm{m s^{-2}}$, which is small, as would be expected. However, when the force required to maintain the position is calculated the displaced equilibrium point appears challenging. The force required for the largest asteroid Ganymed is 1.17×10^{11} N whilst the force required for the

[1] Data available online at http://neo.jpl.nasa.gov/ [retrieved 11/2010].

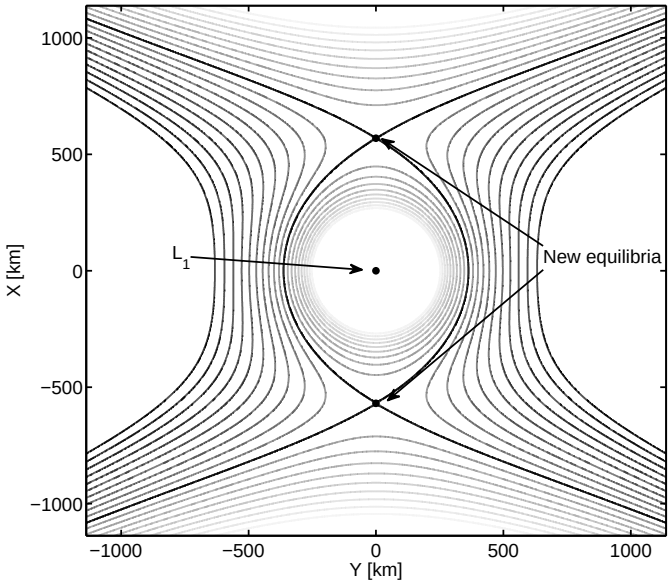

Figure 3.2: Contour plot showing the variation in the effective potential of the four-body problem for a body of mass $1 \times 10^{15} kg$ placed at the conventional L_1 point for $\beta = 0$, with bold lines showing the contours with the Jacobi constant of the equilibrium points.

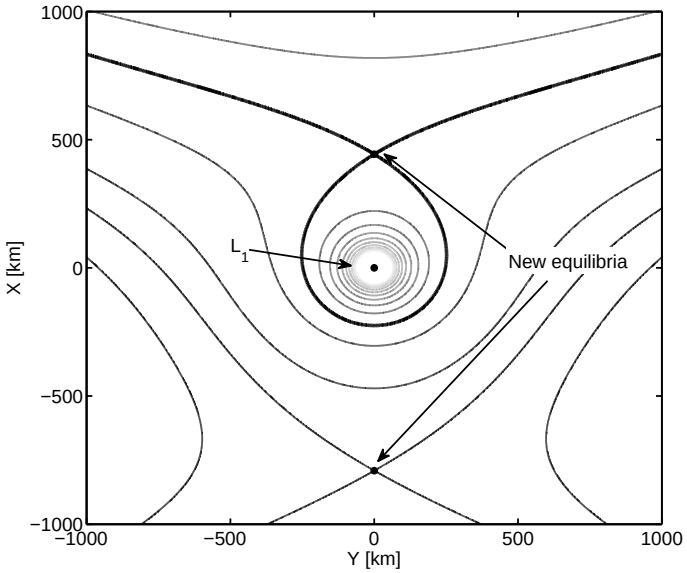

Figure 3.3: Contour plot showing the variation in the effective potential of the four-body problem for a body of mass $1 \times 10^{15} kg$ placed at the conventional L_1 point for $\beta = 0.001$, with the bold line showing the contour with the Jacobi constant of the equilibrium point that encloses the asteroid.

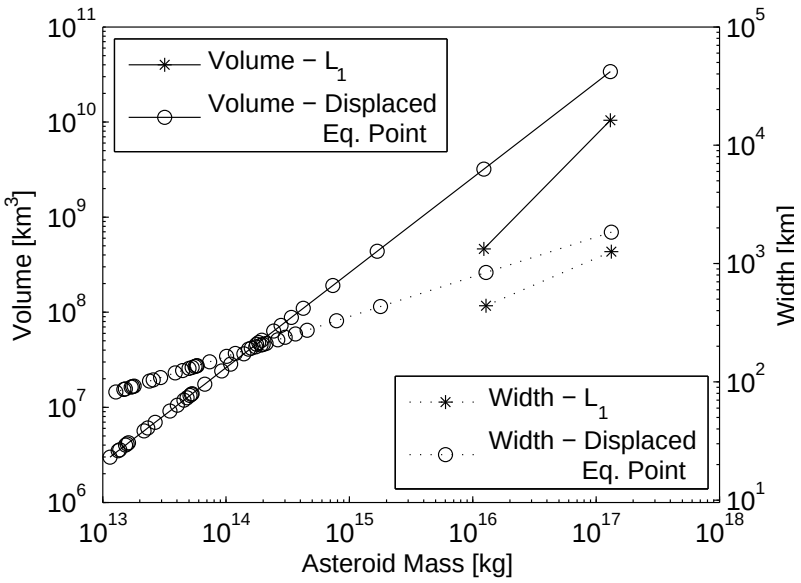

Figure 3.4: The width of the zero velocity curve and the volume it encloses for a selection of asteroid masses placed at the conventional L_1 point and new displaced equilibrium positions assuming grains with a value for β of 0.005. Each data point represents an asteroid from the NASA NEO program database.

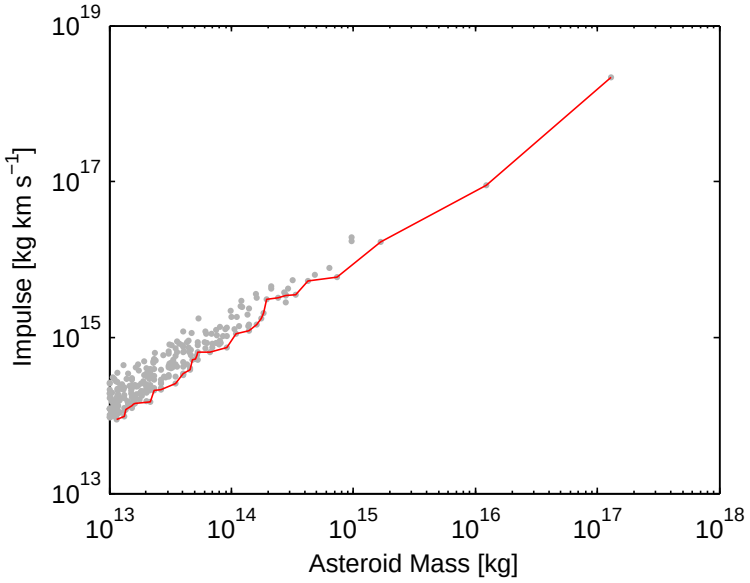

Figure 3.5: Impulse required for capture to the L_1 point for the population of near Earth asteroids with masses above $1 \times 10^{13} kg$ with a Pareto front showing the optimum bodies for capture.

smallest asteroid is 9 MN, a figure similar to capabilities of current launch technology, though it still cannot be seen as feasible. The insolation change for both positions shall be calculated as a comparison.

The maximum possible change in solar insolation was calculated for the masses on the Pareto front for both positions for a dust grain size of 32μm, equivalent to a β value of 0.005 [110]. This grain size was initially chosen as representative of real material and, as the largest of the grain sizes investigated by Wilck and Mann [110], will lead to the least distortion on the zero velocity curve at L_1 and thus will give the largest enclosed volume of the grain sizes. Larger grain sizes will be discussed later in Sec. 3.3.4.

3.3.2 Solar radiation model

The insolation reduction was computed using the solar radiation model (SRM), described previously in Sec. 2.2, which uses the Beer-Lambert law to calculate the attenuation experienced by a beam of photons travelling through the dust cloud. In contrast to the previously discussed SRM, this version uses the value of the Jacobi constant, of the bounding equilibrium position C_{crit}, to determine whether a point along the integration path is within the cloud in order to determine the attenuated path length. This can be expressed mathematically as:

$$l = \int_{X(x_{S,1})}^{X(x_{S,2})} H(C(x,y,z) - C_{crit})\,\mathrm{d}l \tag{3.9}$$

where $X(x_{S,1})$ and $X(x_{S,2})$ are the start and end points of the integration path (corresponding with the maximum extent of in x of the ZVC), with x, y and z components, between the respective Sun and Earth nodes, discussed in Sec. 2.2.1, and correspond to the values of x that set the limits of the zero velocity curve, $x_{S,1}$ and $x_{S,2}$. A matrix can be generated containing the path lengths through the cloud when passing between each Sun node to each Earth node and, since the distribution of dust grains within the zero velocity curve is assumed to be homogeneous, the Beer-Lambert law describing the attenuation will reduce to its basic form for each path:

$$I = I_0 e^{-\sigma_{gr}\rho_n l} \tag{3.10}$$

with σ_{gr} being the cross sectional area of a single grain and ρ_n being the number density of particles within the zero velocity curve. Using the matrix of path lengths the total insolation reduction can be estimated for a given value of ρ_n by applying Eq. (3.10) to all paths.

3.3.3 Results for $R_{gr} = 32\mu$m

Initially, where the maximum achievable insolation reduction is desired, it is assumed that all light passing through the zero velocity curve is blocked, implemented by setting $\rho_n = 1 \times 10^{99}\,\mathrm{m}^{-3}$. These results, Fig. 3.6, show a linear trend on a log-log plot with the maximum insolation reduction of 6.58% being achieved for the asteroid Ganymed at the displaced equilibrium position, as was expected, with a maximum insolation reduction of 3.3% for the L_1 position for the same asteroid. This result meets the required 1.7% reduction in solar insolation required to offset expected climate change [39]. The maximum change in solar insolation reduces significantly for the next largest asteroid, to 1.42% and 0.42% for the displaced equilibrium and L_1 positions respectively. These values do not meet the required 1.7% insolation reduction noted previously to offset anticipated global warming. However, these results, and some of the insolation reductions achieved by the next few asteroids, could still be significant enough to be considered as part of a portfolio of geoengineering schemes. The smallest asteroids considered, with a mass in the region of 10^{13}-10^{14} kg are capable of offsetting the 1-2 $\mathrm{W\,m^{-2}}$ variation in solar insolation experienced over a solar cycle [101, 111] though are not capable of contributing significantly to a space based geoengineering scheme.

3.3.4 Results for $R_{gr} > 32\mu$m

As discussed previously, positioning a sizeable captured asteroid at the displaced equilibrium position is likely to be challenging due to the large station-keeping force required. Therefore, the potential for insolation reduction at the conventional L_1 position must be maximised. Since the zero velocity curve at the L_1 point quickly disappears as β increases, the use of dust grains much larger than the 32μm previously investigated will now be discussed. Figure 3.7 shows the variation in maximum insolation reduction for the asteroid Ganymed for increased grain radii. As well as for the mean Sun-Earth distance, the maximum insolation reduction was also calculated for the separation of the Earth and Sun at aphelion and perihelion. This was achieved using the same model as described in this chapter by simply altering the mean distance to the perihelion and aphelion distances of 0.983 AU and 1.017 AU respectively. The results shown in Fig. 3.7 show that as the grain size increases, and β decreases, the maximum insolation reduction can be seen to

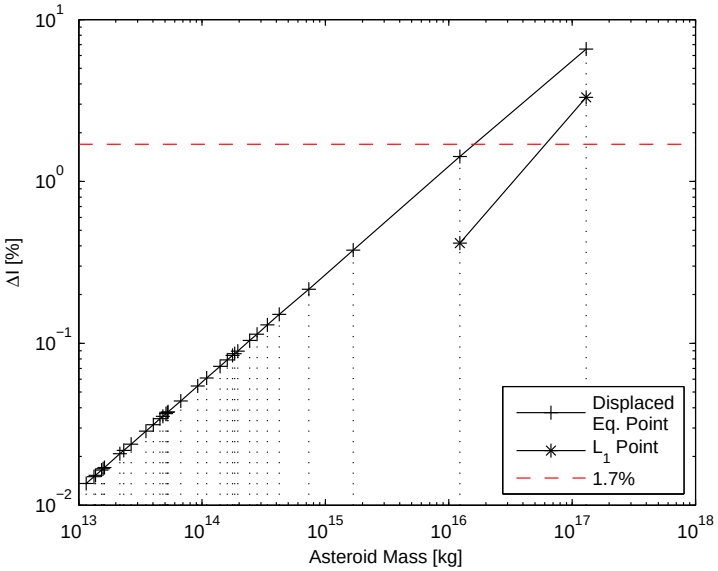

Figure 3.6: Maximum insolation change available for the masses of the asteroids on the Pareto front situated at the displaced equilibrium position and the classical L_1 point.

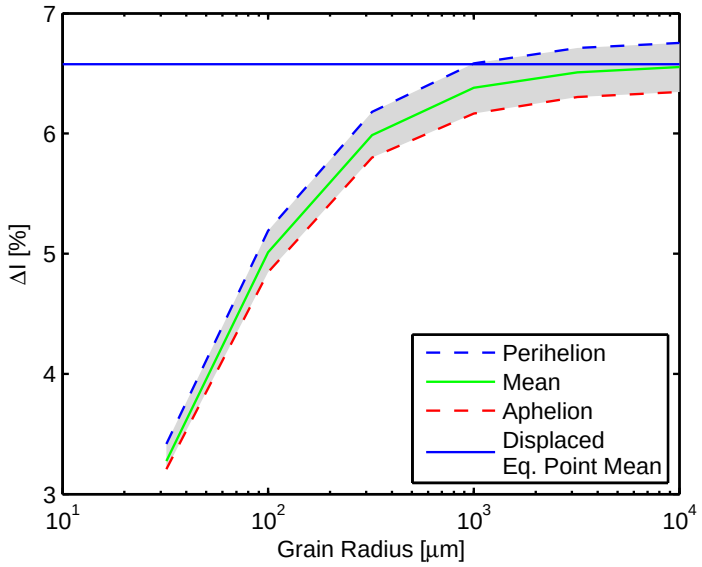

Figure 3.7: Maximum insolation reduction for the asteroid Ganymed at the L_1 position for the Sun-Earth distance at perihelion and aphelion and the mean distance for grains sizes of 32µm and above. Also shown is the maximum insolation reduction for the same asteroid placed at the dispaced equilibrium position for a grain size of 32µm.

increase significantly before levelling off for the largest grain radii assessed, at a level similar to the equilibrium case. This is because as β decreases the zero velocity curve shape will resemble the equilibrium position shape and volume as seen in Fig. 3.2.

A similar analysis can be carried out for the next largest asteroid Eros to determine the maximum potential insolation reduction of the L_1 position. It can be seen that the insolation reduction at the L_1 point can be improved by the use of larger grain sizes, though as the maximum reduction at the displaced equilibrium position is less than 1.7%, the maximum for the L_1 position will similarly be less than the desired amount. Nevertheless it can be shown that the geoengineering potential is close to the amount necessary and can therefore be considered as an option to provide a large portion of any insolation reduction required.

The negative aspect of the increase in grain size is the reduction in efficiency associated with a decrease in area-to-mass ratio. Therefore, a greater mass of dust grains is required to block the same level of sunlight. The fraction of the asteroids Ganymed and Eros that must be used, assuming no loss of particles (an assumption that will be discussed in Sec. 3.4), can be seen in Fig. 3.8. To achieve the maximum insolation reduction for the largest grains would require a mass greater than that of each asteroid, whilst to achieve an insolation reduction of 1.7% for Ganymed, the mass fraction does increase though remains many orders of magnitude less than the mass of Ganymed itself.

3.3.5 Insolation reduction map

Finally, the reduction in insolation over the Earth's surface, calculated using the SRM described previously, can also be shown. In contrast to the SRM used in Chapter 2, this version requires a higher fidelity due to the potentially small size of the zero velocity surfaces, as shown in Fig. 3.4. In this instance a minimum of 101×101 nodes were used on each body with this resolution increasing for the lower mass asteroids. The insolation reduction for the asteroid Ganymed at the equilibrium position and the classical L_1 point is shown in Fig. 3.10 and Fig. 3.11 respectively. It can be seen that the insolation reduction is relatively flat when close to the centre of the Earth for both cases, whilst towards the limbs the insolation reduction decreases significantly. This is because the zero velocity curve is centred along the Sun-Earth line and so many photons emitted towards the limbs of the Sun will pass without being attenuated. This is in contrast to the method described in the previous chapter where the dust grains will cover a larger region away from the Sun-Earth line due to the motion in the CR3BP, thus creating a greater spread of the insolation reduction over the surface.

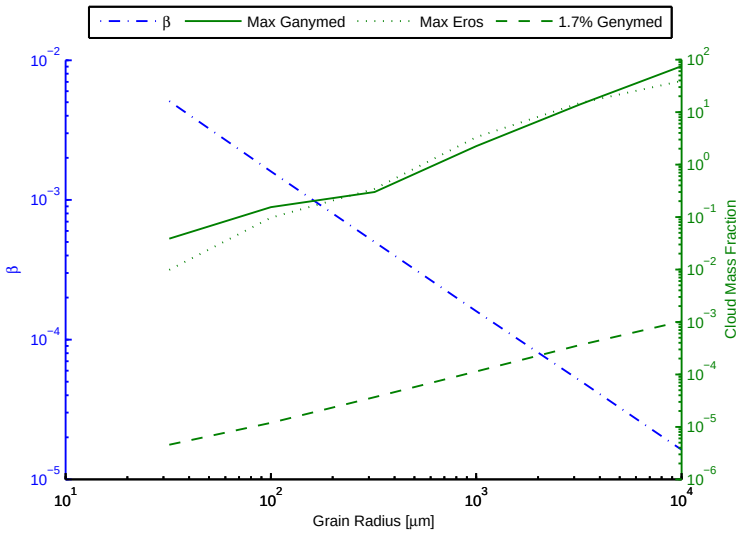

Figure 3.8: Mass fraction of the dust cloud necessary to achieve the maximum insolation reduction possible for the asteroid Ganymed and Eros and a 1.7% reduction for the asteroid Ganymed for grain sizes larger than 32μm. Also shown is the corresponding values for β.

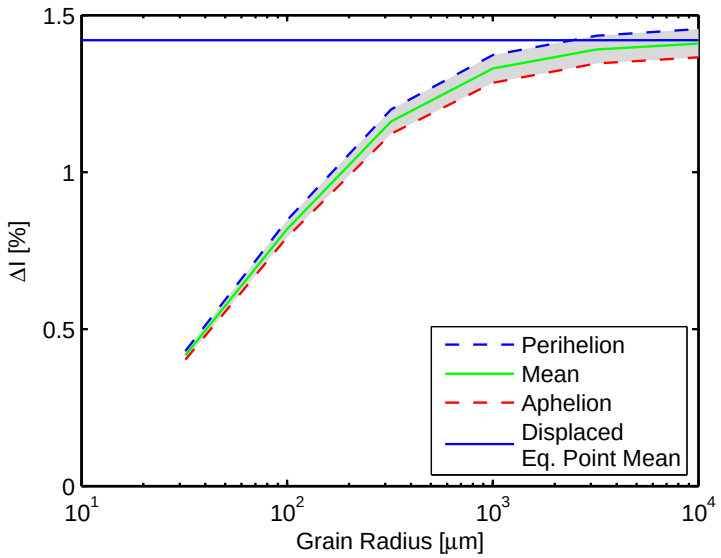

Figure 3.9: Maximum insolation reduction for the asteroid Eros at the L_1 position for the Sun-Earth distance at perihelion and aphelion and the mean distance for grain sizes of 32μm and above. Also shown is the maximum insolation reduction at the displaced equilibrium position for a grain size of 32μm.

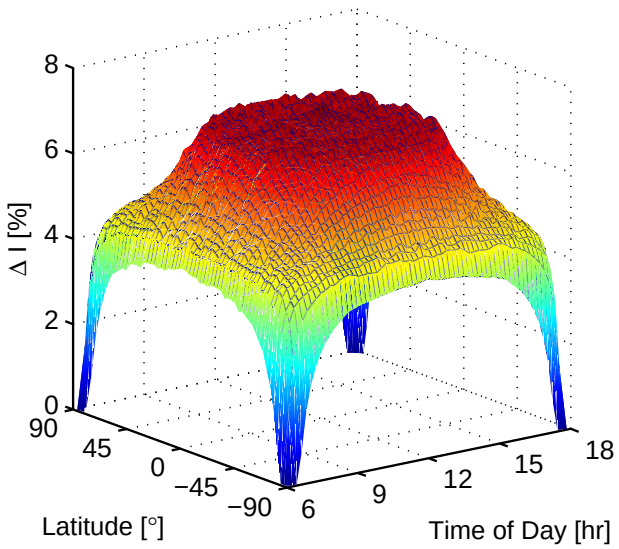

Figure 3.10: Maximum reduction in insolation over the Earth's surface for the zero velocity curve generated by the asteroid Ganymed at the displaced equilibrium position for a β value of 0.005.

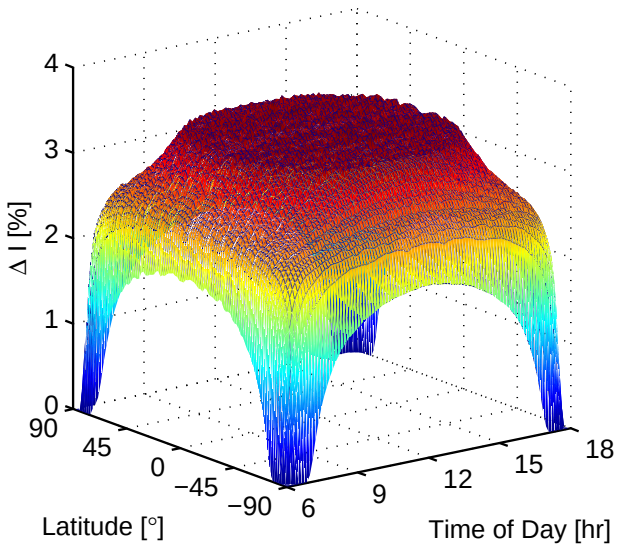

Figure 3.11: Maximum reduction in insolation over the Earth's surface for the zero velocity curve generated by the asteroid Ganymed at the classical L_1 point with a β value of 0.005.

3.4 Discussion

3.4.1 Loss mechanisms

Of importance to this method of geoengineering is knowledge of the lifetime of the dust grains within the zero velocity curve. There are several possibilities for natural loss of material from the dust cloud. These include re-contact with the surface of the asteroid, variations in solar intensity, particle collisions leading to a spread of velocities, with an energetic tail reaching escape, and finally the escape of material smaller than the designed grain radius when assuming a certain size distribution.

It has previously been assumed that the particles within the zero velocity curve are collisionless, thus implicitly assuming that no particle ejected with a velocity less than the escape velocity will escape. A short calculation will follow to prove this assumption. To achieve an insolation change of 1.7% it is found that a homogeneous number density within the zero velocity curve, at the displaced equilibrium position, of $29\,\mathrm{m}^{-3}$ is required. This was determined by using the *fminsearch* function in MATLAB to optimise the value of ρ_n for a target insolation reduction of 1.7% using the method described in Sec. 3.3.2. If it is assumed that the particles move as a gas a mean free path of approximately 2,500 km can be calculated using Eq. (3.11);

$$\lambda = \frac{1}{4\pi R_{gr}^2 \rho_n} \tag{3.11}$$

where R_{gr} is the grain radius. The escape velocity from the surface of Ganymed, assuming a radius of 31.7 km, can be calculated using Eq. (3.6) to be $23.3\,\mathrm{m\,s}^{-1}$. Using this value the collision time scale can be determined as follows:

$$\tau = \frac{\lambda}{V_{crit}} \tag{3.12}$$

where V_{crit} is the ejection velocity required to reach the zero velocity curve. This results in a collision timescale of 1.3 days. It is therefore assumed that the relaxation time of the particles will be greater than their lifetime limited by other process, as will be discussed later, thus validating the assumption of collisionless particles.

It has been stated previously that the effect of solar radiation pressure is the dominant perturbation on the dust grains. In addition, as the variation in solar insolation over the course of the solar cycle is only $1 - 2\,\mathrm{W\,m^{-2}}$ [101, 111], it is assumed that the effect that this has on the possible loss of material is negligible. The eccentricity of the Earth's orbit around the Sun will have a noticeable effect on the size of the zero velocity curve around the asteroid. When placed at the conventional L_1 position the volume, as calculated using Eq. (3.8) at perigee and apogee, varies by $\pm 5\%$ with respect to the mean volume with a corresponding variation in the maximum insolation reduction of $\pm 0.1\%$, calculated using the solar radiation model. This fluctuation in volume will not lead to any loss of material as the Jacobi constant of the bounding zero velocity curve will not change and hence the dust grains will remain bound.

Loss of material due to the size distribution of the dust grains is likely. The grain sizes below those desired will have a greater value for β and thus the size of the zero velocity curve will decrease, thus decreasing the effectiveness of these smaller particles. In addition, as the grains will be ejected with a similar velocity, the smaller dust grains will have an energy above that of the bounding Jacobi constant and thus are likely to escape. For example, assuming a log-normal distribution, Eq. (3.13), with a mean of $\mu_{log} = -10.34$ and standard deviation of $\sigma_{log} = 0.25$, 21% of the mass ejected has a radius below $32\mu m$ and hence is likely to escape. Conversely for a greater standard deviation of $\sigma_{log} = 0.5$, only 6.5% will escape due to the mass being dominated by the larger particle sizes. The distribution can be modelled as;

$$f_{\mu_{log},\sigma_{log}}(R_{gr}) = \frac{1}{R_{gr}\sigma_{log}\sqrt{2\pi}} e^{-\frac{(\ln R_{gr} - \mu_{log})^2}{2\sigma_{log}^2}} \tag{3.13}$$

where $f_{\mu_{log},\sigma_{log}}(R_{gr})$ represents the probability density function.

3.4.2 Grain lifetime

The motion of dust grains around an asteroid is a non-trivial problem as discussed by Scheeres [89], where it is noted that the majority of particles randomly ejected, in a simulation of a meteorite impact, will fall into one of two short-lived classes of orbit; immediate re-contact or immediate escape. As the escape velocity is known then this second category can be avoided and therefore avoiding immediate re-impact is the most important issue. The large range of random velocities that fall into the immediate re-impact category is due to the origin of the orbit being on the surface of the asteroid. Other classes of orbit exist and are expected to be more long-lived, up to the region of hundreds of days, and are achieved through the specific selection of the initial conditions [91]. It

is assumed here that the grains can be given the correct ejecta velocity to achieve long-lived orbits whilst it is conservatively assumed that the grains with a β value greater than 0.005 will escape very quickly.

Previously, it has been shown that the collision timescale is long and thus it can be assumed that the velocities of the grains will not follow a Maxwell-Boltzmann distribution, meaning there will be little spread in their speed. Therefore, it is assumed that this will have a negligible effect on particle escape. For the grains that escape due to higher values of β the useful lifetime will be greater than their lifetime within the zero velocity curve as they will be in a position to block solar radiation for approximately 50 days after escape [12].

An approximate calculation can now be made of the rate that material must be ejected from the surface to achieve the required 1.7% reduction in insolation. The number density of particles of radius 32 μm required at the L_1 point is 120 m^{-3} giving, for a total volume of $1 \times 10^{19}\,\mathrm{m}^3$, a cloud mass of 6×10^{11} kg. Scheeres shows that for the asteroid Toutatis orbits exist with a lifetime of several hundred days and possibly up to several years, with a specific example given of an orbit with a lifetime of 257 days [91]. Here, it will be assumed that dust grains will have a lifetime of 180 days before re-impact or escape, giving an ejection rate of $1.4 \times 10^8\,\mathrm{kg\,hr}^{-1}$. As a comparison to the thrust required to maintain the asteroid at the displaced equilibrium position, this ejection rate gives a force of 0.9 MN, assuming ejection in one direction only. This is much less than the required thrust to maintain a position at the displaced equilibrium point for the asteroid Ganymed. However, it would contribute 10% of the required thrust to maintain a displaced position for the smallest asteroid mass considered. The reduced efficiency of the system due to the dust size distribution can be approximated. For a log-normal mean of $\mu_{log} = -10.34$ (32 μm) and standard deviations of $\sigma_{log} = 0.25$ and $\sigma_{log} = 0.5$ the mean masses are $1.4m_{32\mu\mathrm{m}}$ and $3.2m_{32\mu\mathrm{m}}$ respectively, where $m_{32\mu\mathrm{m}}$ is the mass of a grain with a radius of 32 μm, whilst the ratio of the mean cross-sectional area of the distribution and that of a 32 μm radius particle are 0.81 and 1.42. This gives final ejection rates that are 1.7 and 2.2 times larger than the nominal case. These mass ejection rates are large, however, should the technology become available to capture such an asteroid become available these mass ejection rates may not be unfeasible.

3.4.3 Contribution of escaped grains to the insolation reduction

The contribution that this loss of mass from the zero velocity curve has on the reduction of insolation can be estimated using the model described in Chapter 2. The reduction in insolation for a cloud with an initial size equal to that of the zero velocity curve can be calculated and weighted proportionally to the escape lifetime of dust. This can then be combined with the calculation for

the insolation reduction of the zero velocity curve and the number density of grains surrounding the asteroid can be re-calculated. This process suggests that for the asteroid Ganymed positioned at the L_1 point the number density of particles reduces to $93\,\mathrm{m}^{-3}$ whilst for the equilibrium position the number density required is $27\,\mathrm{m}^{-3}$, a reduction from $30\,\mathrm{m}^{-3}$. The reduction in insolation that the propagated cloud has can also be determined. For the equilibrium position, the escaped particles will contribute 0.65% of the 1.7% requirement whilst for the L_1 point this reduces to just 0.13%. This is due to the smaller lifetime of the particles with respect to the escape lifetime. For example, if the escape lifetime were assumed to be 90 days rather than 180 days, then the contribution of the escaped dust would increase to 0.20% though naturally the mass required would double. The mass of escaped dust in the first case is $9.35 \times 10^{11}\,\mathrm{kg\,yr}^{-1}$, which is a third of the mass required for the static dust cloud placed at the L_1 point, for a value of β of 0.005, described in Chapter 2.

3.4.4 Implementation roadmap

The loss timescale suggested here is short in comparison to the probable lifetime necessary for geoengineering, which is likely to be for several decades or even potentially centuries. This will reduce the risks associated with this method and enables some control by simply decreasing the ejection rate of material. Should the insolation reduction need to be immediately stopped due to major unforeseen side effects, then the asteroid can be displaced away from the L_1 point and allowed to drift. It will still be prudent to test the safety and efficiency of the method suggested here by first capturing a small asteroid 5-10 m in size to the L_1 point. Then the station-keeping and dust ejection mechanisms as well as the ability of the dust to block sunlight on a small scale can be tested as well as verifying that solar radiation pressure is the dominant perturbation on the dust grains. Subsequently, a larger asteroid 100-200 m in size, can be captured to test the principles of the zero velocity curve using larger dust grains to maximise the size of the zero velocity curve. The zero velocity curve is likely only to be marginally bigger than the asteroid but the dynamics can be observed and tested against current predictions [90]. In addition a small insolation reduction at Earth can be generated by ejecting dust grains from the asteroid using the principles described in Chapter 4 to verify space-based geoengineering in general. This test can be used to help determine whether there are any unintended side effects with large-scale solar radiation management. The effect that the dust enclosed within the zero velocity curve generated by an asteroid of this size will be negligible in comparison to the reduction provided by the ejected dust. Subsequently, the necessity for such large-scale geoengineering schemes can be assessed before continuing as well as the cost efficiency of this method of space based geoengineering.

3.5 Conclusion

In this section a novel method of space-based geoengineering has been presented which uses the mass of a captured near Earth asteroid to gravitationally anchor a cloud of unprocessed dust in the vicinity of the L_1 position to reduce the level of solar insolation at Earth. The captured asteroid also provides the source of dust in-situ. It has subsequently been shown that a cloud contained within the zero-velocity curve of the largest near Earth asteroid, Ganymed, can lead to an insolation reduction of 6.58% when placed at the displaced equilibrium position and 3.3% when placed at the classical L_1 point. Both of these values are significantly larger than the 1.7% required to offset the worst effects of a global warming of 2°C. The masses of the next largest near Earth asteroids are not quite large enough to achieve the required level of insolation reduction, however, they are significant enough to be used as part of a portfolio of geoengineering schemes.

It has also been shown that there are significant challenges associated with placing an object the size of Ganymed at the displaced equilibrium position and therfore the L_1 point is a much more reasonable position. It is possible to use larger dust grain sizes to increase the size of the zero velocity curve when placed at the L_1 point to increase the viability of these options. The mechanisms by which dust grains can escape from the bound region caused by the asteroid mass have been discussed and used to estimate the lifetime of the dust grains within the zero velocity curve. The contribution of the escaped dust to the reduction in insolation has been determined and used to show that the mass required to maintain the cloud is reduced. The mass escaping from the zero velocity curve for the asteroid Ganymed at the classical L_1 position for a scenario where there is a reduction in solar insolation by 1.7% is $6.77 \times 10^{11}\,\mathrm{kg\,yr^{-1}}$. This result is an order of magnitude reduction in comparison to the lowest mass requirement for the static loud released at the L_1 point for a grain size of $32\mu m$, as calculated in Chapter 2.

Chapter 4

Ejected Cloud at L_1

The method of space based geoengineering described in Chapter 2, of an initially static, spherical dust cloud propagated over time, is a first approximation of the dynamics of a cloud of dust in the vicinity of the first Lagrange point. This simplified model fits to the cloud generation scenario, of a cloud generated by the escape of dust from a zero velocity curve, found when the mass of a significantly large asteroid is included into the circular restricted three body problem (CR3BP), as discussed in Chapter 3. This is due to the approximately spherical shape of the zero velocity curve and, since a particle can be given a velocity which is just above the escape velocity, it can be approximated as being stationary at the boundary of the zero velocity curve. However, the feasibility of capturing such a large asteroid cannot be viewed as a near-term option. Therefore, the effects of the ejection mechanism, namely the initial velocity, to generate a dust cloud from a small asteroid must be determined. This will be achieved by investigating the dynamics of dust ejected from a single point with an initial velocity distribution. This will simulate the ejection of material from the surface of a captured near Earth object using a machine, such as a mass driver, or the sublimation of material from the surface using concentrated solar radiation or a laser. These ejected particles will then drift and spread from the ejection point to create a steady-state cloud which can be used for the purposes of geoengineering.

4.1 Dynamics

The linearised dynamics of a cloud of dust in the vicinity of the L_1 point have been discussed in Chapter 2 using the CR3BP. It was stated that, due to the relatively short lifetimes of dust grains around the classical L_1 and new displaced equilibrium positions, found when the effects of solar

radiation pressure (SRP) on the dust grains are accounted for, that these linearised dynamics are suitable to describe the motion of the dust grains, without the need to propagate each particle with the full equations of motion. This will greatly reduce the computational cost of propagating the dust cloud over time. It is assumed here that the asteroid mass will be small and therefore the asteroid will not effect the motion of the ejected dust grains. Using the three-body dynamics discussed in Chapter 2 a transition matrix can be generated. This uses the linearised dynamics around L_1 to propagate large numbers of particles, whereas the full equations of motion would require particles to be propagated individually. The process by which this matrix can be generated is shown in Sec. 2.1.4. The transition matrix, $\Phi(t, t_0)$, finds the final state vector, $X(t)$, using the initial state vector, $X(t_0)$ as follows;

$$X(t) = \begin{bmatrix} \mathbf{x}(t) \\ \mathbf{v}(t) \end{bmatrix} = \Phi(t, t_0) X(t_0) \tag{4.1}$$

where the transition matrix is defined by;

$$\Phi(t, t_0) = \begin{bmatrix} \frac{\partial x(t)}{\partial x(t_0)} & \frac{\partial x(t)}{\partial v(t_0)} \\ \frac{\partial v(t)}{\partial x(t_0)} & \frac{\partial v(t)}{\partial v(t_0)} \end{bmatrix} \tag{4.2}$$

Since the number density of particles, at a specific location and time, is required to calculate the reduction in insolation, only the final position vector component must be calculated using the transition matrix. Therefore the state vector equation can be simplified to;

$$x(t) = x(t_0) \frac{\partial x(t)}{\partial x(t_0)} + v(t_0) \frac{\partial x(t)}{\partial v(t_0)} \tag{4.3}$$

As for the static dust cloud discussed previously in Chapter 2, the size of grains assumed here requires the inclusion of the effects of solar radiation pressure, described by the lightness parameter β, defined as the ratio of the force due to solar radiation pressure and solar gravity. Small dust grains have a high area-to-mass ratio, meaning that surface forces act strongly upon such objects. Solar radiation pressure is the strongest surface force for grains greater than 0.1μm in radius, as described in Sec. 2.1.2. As discussed in Sec. 2.1.3, for values of β greater than zero, the equilibrium position for the dust grains, accounting for the gravitational forces of the Sun and Earth on the dust grain, as well as the acceleration due to the circular motion of it's orbit around the Sun, will shift towards the Sun with respect to the classical L_1 point. This will lead to any particles initially positioned at the classical L_1 point no longer being in equilibrium, meaning they will drift away

from their initial position. This arises from the increased gradient of the gravitational potential function, U, which includes the three forces acting on a dust grain.

4.2 Solar radiation model

The solar radiation model that will be used to determine the reduction in insolation in this scenario is principally the same as that described in Sec. 2.2, whereby the surfaces of the Earth and Sun are divided into sections, each with a central node which is considered to have the properties of that section, such as surface area. Every node on the surface of each body is connected to each individual node on the surface of the opposite body by a path. The solar radiation model will integrate along this path to determine the attenuation of the flux emitted by the Sun node, described by Eq. (2.25), which would normally be incident upon the Earth node. As for the previous versions of the solar radiation model described in this thesis, the solar radiation model will use the Beer-Lambert law to calculate the attenuation. In this scenario only a single dust grain size is assumed, thus the Beer-Lambert law can be expressed as;

$$I = I_0 e^{\sigma_{gr} \int_0^l \rho_n(l)\,\mathrm{d}l} \tag{4.4}$$

where I_0 is the flux emitted by the Sun node defined by Eq. (2.25), σ_{gr} is the cross sectional area of the dust grain and $\rho_n(l)$ is the number density of grains at position l along the integration path.

The key difference between the model used in this scenario and previous models is that this model first calculates the motion of an ejecta cloud with the given characteristics of mean velocity, μ_v, velocity standard deviation, σ_v, and the initial angular width of the ejecta cloud, θ, over a given time frame. This motion is then used to construct a "density matrix" which divides the area around L_1 into regions, each containing the number of propagated particles that fall within it after the propagation of the cloud over a given period of time. The number density of particles within each region can then be estimated by dividing by the total volume of the region. This data can then be used by the integration of the Beer-Lambert law shown in Eq. (4.4) to determine $\rho_n(l)$.

Mean Velocity μ_v [$\mathrm{m\,s^{-1}}$]	0.01, 0.1, 1 3.2, 10, 32, 100 320, 1,000, 3,200, 10,000
Velocity Standard Deviation, σ_v [$\mathrm{m\,s^{-1}}$]	$0.001\mu_v$, $0.01\mu_v$, $0.1\mu_v$
Angular spread, θ [°]	1, 10, 32, 90

Table 4.1: The range of velocities considered for the mean velocity, velocity standard deviation and angular spread.

4.2.1 Initial velocity distribution

It is necessary to describe the initial velocity of the ejecta particles with a distribution of velocities. This is because the ejection mechanisms used to generate the ejecta cloud will not be able to eject at a single velocity alone, or similarly in a single direction. Therefore a mean velocity will be assumed for a normal distribution of velocities with a given standard deviation. The values for mean velocity and velocity standard deviation that are considered in this chapter can be seen in Table 4.1. The velocity standard deviation will be expressed as a fraction of the mean velocity for consistency. As well as the velocity distribution, the spread of the material must be considered. For simplicity a homogeneous distribution was assumed for all angles within a set angle away from the centre of the ejected cloud. An example of this can be seen in Fig. 4.1.

4.3 Results

Before the density matrix can be generated for use in the solar radiation model it is advantageous to understand the practical implications of the dynamics of material ejected in the vicinity of the L_1 point. It would be expected that for particles ejected from the classical L_1 point, for a value of $\beta > 0$, that there will be an optimum angle and velocity that maximises the lifetime of ejecta. Therefore, two methods will be used to analyse the feasibility of this method of geoengineering. These are, firstly, the homogeneous ejection of material into all directions and, secondly, the ejection of material into a cone with an angular spread of θ. Both of these scenarios will use varying values of mean velocity and standard deviation of the velocity.

It is expected that for dust grains ejected at the displaced equilibrium position, created by the inclusion of the β lightness parameter into the equations of motion, that the highest average lifetime will be found for the smallest velocities. This hypothesis is drawn from the fact that the equilibrium position is the most stable point in the region and hence any initial velocity will push a dust grain towards a steeper gradient of the potential function, which will accelerate the dust grain away from the equilibrium position. In contrast, for dust grains ejected at the classical L_1 point it is anticipated that there will be an optimum velocity and ejection angle where the average lifetime of the dust grains will be at its maximum. This is, again, due to the gradient of the potential function. If the correct velocity and angle of ejection is given to the ejecta, such that the dust grains approach the equilibrium position, then the value of the potential function, U, will increase. The values of U and the speed, V, are related by the following relationship;

$$C = 2U - V^2 \tag{4.5}$$

where C is the Jacobi constant. The value of C_J will remain constant after ejection unless an additional thrust were given to the dust grains by some means. Hence, for an increase in the value of U, the velocity will reduce, causing the dust grains to linger at the equilibrium position temporarily. This will increase their overall lifetime.

For dust grains ejected at both the classical L_1 and displaced equilibrium positions it is expected that a narrow angular spread of the ejecta cone will increase the average time a dust grain spends in between the Sun and Earth, as this will increase the efficiency of placing the ejected material into the optimum direction. The same applies for the variation in the standard deviation of the velocity, with a smaller standard deviation expected to lead to an increase in the average lifetime of the ejected dust grains.

An example showing the mean lifetime of a set of ejecta particles for evenly spaced initial ejection angles, within the rotational plane of the CR3BP, can be seen in Fig. 4.2. In this scenario the grains were assumed to have a mean velocity of $100\,\mathrm{m\,s^{-1}}$, a standard deviation of $20\,\mathrm{m\,s^{-1}}$ and cone spread of $10°$, with a β value of 0.751. For both the ejection at the classical L_1 and displaced equilibrium positions it can clearly be seen that there is an optimum angle at which the lifetime is greatest. Of particular interest is the L_1 case where the lifetime of the ejected material oriented towards the displaced equilibrium point, at an angle of $180°$, is greater than the maxima in the opposite direction. These results also highlight the likelihood that a smaller range of ejection angles will lead to a greater mean lifetime of the ejecta particles. For example, the maximum mean lifetime seen in Fig. 4.2 is 17 days whilst the values within an angle of $15°$ reduces to 10.8 or 10.3

days, a reduction of over a third.

4.3.1 Optimisation of the ejection angle

The optimum ejecta angle within the plane, ϕ, will be determined for a range of initial parameters, as noted previously, by propagating the cloud, ejected in a cone, over a period of 200 days, using the transition matrix with a time step of 0.5 days. The mean lifetime of a particle is the length of time spent within the 'useful zone', defined as the region where a grain can block sunlight impinging on the Earth. This is the primary variable that will be optimised. It is useful to also determine what effect the spread of the particles throughout the useful zone will have on the effectiveness of the insolation reduction. Therefore a second optimisation will also take place. This will optimise the mean lifetime multiplied by a variable describing the spread of the dust grains over the phase space. This function is quantified by;

$$f_{opt} = \delta t \sum_{t_1}^{t_f} \frac{N_{t-1} + N_t}{2} \varepsilon \tag{4.6}$$

where δt is the time step, N_t and N_{t-1} are the fraction of particles within the useful zone at the current and previous time steps and ε is the variable characterising the spread of the dust grains. For this, the cross-section of the useful zone, perpendicular to the Sun-Earth line, is divided into sections using two parameters; the angle away from the Sun-Earth line and the anti-clockwise rotation around the Sun-Earth line starting at the positive y-axis. This can be seen in Fig. 4.3. The value of ε, for a given time step, is then the fraction of the sections that contain a propagated dust grain. This method is used to describe the spread, rather than an equal division of the physical space in cartesian co-ordinates, as the extent of the useful zone changes along the Sun-Earth line and the spread in a cross-section perspective is likely to be more beneficial than along the x-axis. This is because the ejecta cloud will subtend a greater solid angle upon the sky, as seen from the Earth, therefore likely intercepting more incoming photons, whilst a spread in x will likely lead to a greater attenuation along a certain path, though the efficiency of this will be decreased. A disadvantage of this description of the spread is the difference in weighting due to the smaller sizes of the regions close to the Sun-Earth line.

Before the optimisation can take place, the number of particles must be determined that give a sufficiently accurate result whilst reducing the computational cost, since the optimisation will require many iterations of the function.

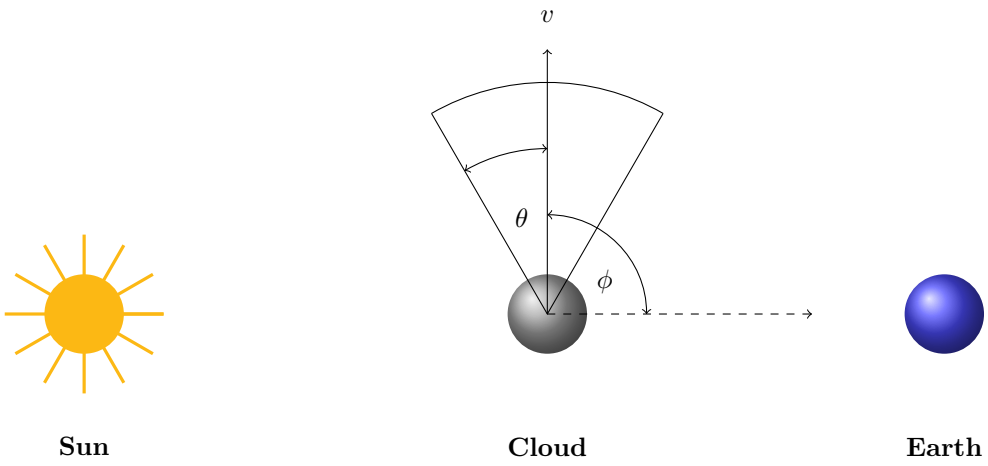

Figure 4.1: Diagram showing the key angles

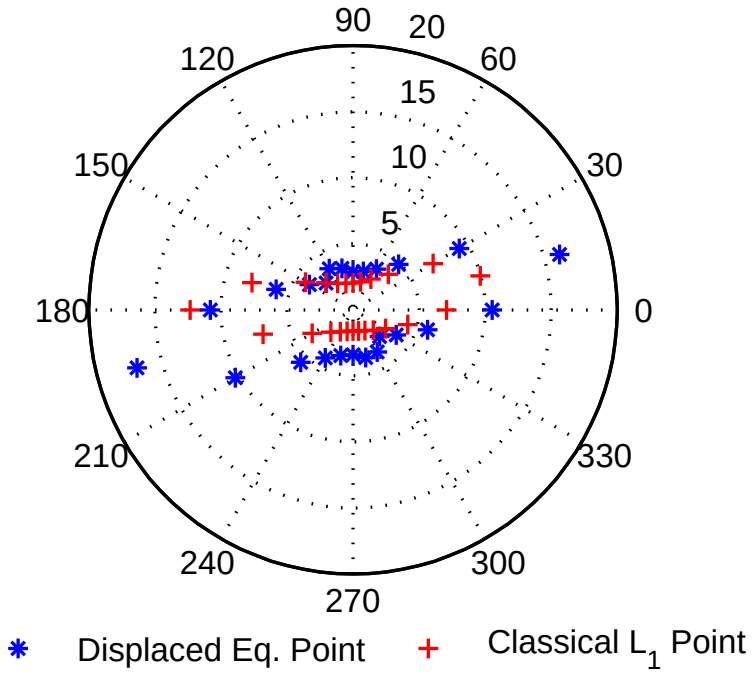

Figure 4.2: Mean lifetime, in days, of dust grains ejected with a mean velocity of $100\,\mathrm{m\,s^{-1}}$*, standard deviation of* $20\,\mathrm{m\,s^{-1}}$ *and cone spread of* $\theta = 10°$ *ejected at a range of angles,* ϕ *at the classical* L_1 *and displaced equilibrium positions for a value of* β *of 0.751.*

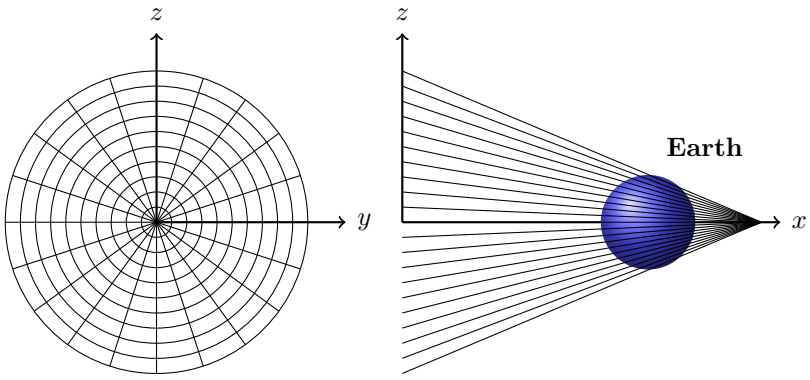

Figure 4.3: The angular sections used to characterise the spread of particles within the useful zone

4.3.1.1 Required number of ejecta particles

Two parameters determine the total number of particles; the number of initial velocities propagated, N_v, and the number of directions within the cone spread angle, N_θ, giving a total number of particles ejected of $N_T = N_v N_\theta$.

A function was used that randomly distributes points on the surface of a sphere such that if any point lies within an angle of θ with respect to the ejection direction then it is stored until the required number is reached. Naturally, to achieve a more consistent result a greater number of points will be required, though this will come at greater computational cost. To select the velocities, the normal distribution was divided into N_v sections with equal probabilities. For each section the median velocity was selected to represent the whole section. The time taken to calculate the mean particle lifetime, averaged over 20 samples, for the example scenario discussed previously for the equilibrium position can be seen in Fig. 4.4. The ratio of the standard deviation of the average dust grain lifetimes to the mean of the average lifetimes, for each pair of values for N_v and N_θ, can be seen in Fig. 4.5. No results were calculated for the combination of N_v=10,000 and N_θ=1×10^7 as the time taken to calculate a single result was too long to be practical. As the values of N_v and N_θ increase the mean of the average lifetimes over the 20 iterations stabilises with the ratio of the standard deviation to the mean particle lifetime decreasing. Ultimately values of 10 and 1000 for N_v and N_θ respectively were selected as giving an acceptable accuracy for the optimisation whilst minimising computational time. For the calculation of the density matrix, which will be used in the solar radiation model, these numbers will be increased to increase the accuracy of the solar radiation model.

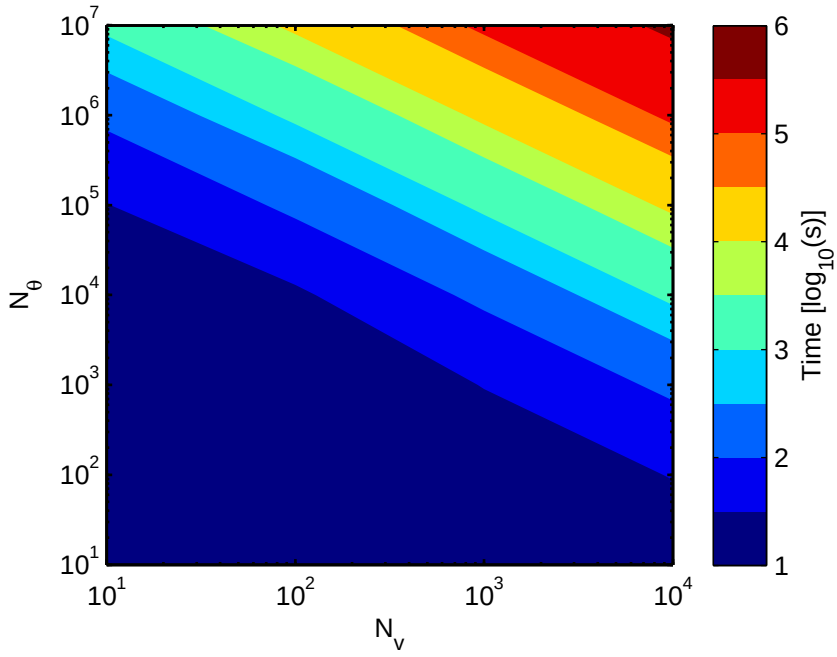

Figure 4.4: Time required to calculate the mean lifetime of an ejecta cloud with varying numbers of particles.

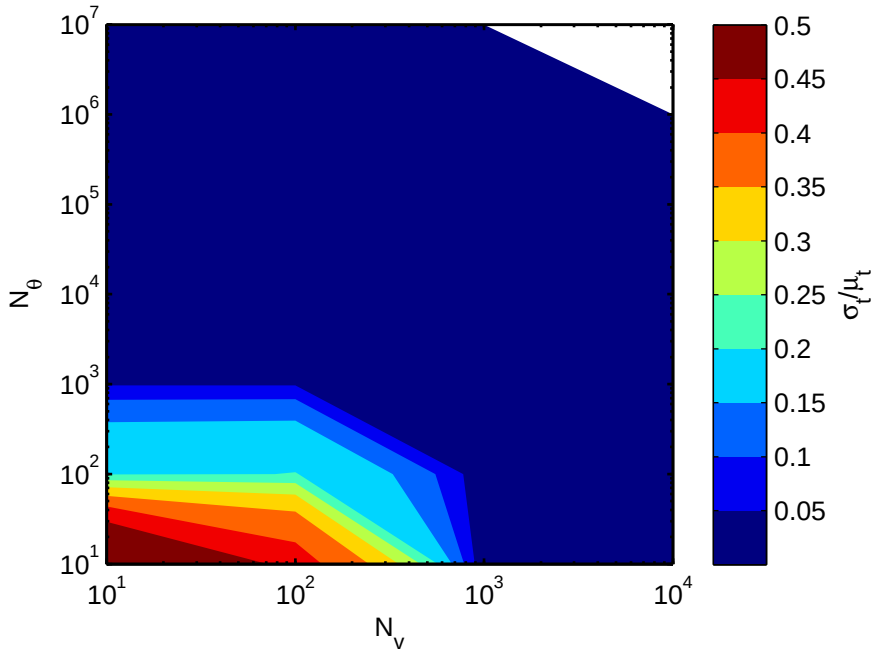

Figure 4.5: Standard deviation of mean lifetimes in relation to the mean of the set for varying number of ejecta particles.

4.3.1.2 Optimum mean lifetime

Using the values for N_v and N_θ discussed previously, the ejection angle was optimised to achieve the maximum mean lifetime using the *fminsearch* function in MATLAB for two values of β, 0.005 and 0.751, corresponding to grain radii of 32 μm and 0.1 μm respectively, and a range of initial values of μ_v, σ_v and θ, which can be seen in Table 4.1. The mean lifetime for the cases of material ejected at L_1 for $\beta = 0.005$ and $\beta = 0.751$ can be seen in Fig. 4.6 and Fig. 4.7 respectively, whilst for the displaced equilibrium position the results for the same values of β can be seen in Fig. 4.8 and Fig. 4.9. Only these two values of β are shown as a comparison between the expected worst and best mass requirement, based on the results from Chapter 2. As discussed previously, it is expected that a peak in velocity would be apparent for the ejecta at L_1 and this is indeed the case, where the greatest mean lifetimes for the $\beta = 0.005$ and $\beta = 0.751$ cases are 168 days and 27.5 days respectively. For the displaced equilibrium position the maximum lifetime increases to 187 days and 190 days, for the β values of 0.005 and 0.751, found for the minimum velocity considered of $1\,\mathrm{m\,s^{-1}}$. This is in keeping with the average lifetime results shown in Chapter 2, where it is observed that the average lifetime increases slightly with increasing values of β.

The maximum average lifetime occurs in all cases for the displaced equilibrium position for the minimum angular spread used of 1° and the minimum standard deviation of $\sigma_v = 0.001\mu_v$. The greatest mean lifetimes observed here are greater than those observed for the static cloud case, for both the displaced equilibrium position and classical L_1 position, presumably due to the optimisation on the initial angle. For example the greatest mean lifetime observed in Fig. 4.2 is 16.9 days whilst the mean over all angles sampled is only 6 days. However, the benefit of the ejection of material at the equilibrium position is not apparent over the whole parameter space, as the mean lifetime quickly reduces as the mean velocity increases, with the maximum mean lifetimes for an initial mean velocity of $10\,\mathrm{m\,s^{-1}}$ being 62 days, which is similar to the minimum value found for the static cloud. The highest velocities of $10\,\mathrm{km\,s^{-1}}$ show a mean lifetime of, at best, 2.2 days for the smallest cone spread whilst a value of 0.25 days is observed for the largest. This velocity is likely to be unrealistic, however, the velocities in the region of $1\,\mathrm{km\,s^{-1}}$ are likely to be generated by some cloud generation techniques, as will be discussed in Chapter 7.

Of interest also is a comparison of the results for different standard deviations of the mean velocity. An example of this can be seen in Fig. 4.10 for the L_1 position with a value of β of 0.751. It is seen that for the majority of data points the difference in mean lifetime between the results for a standard deviation of $0.001\mu_v$ and $0.1\mu_v$ is less than 5% with only a handful of points being greater. The highest value of 14.4% corresponds to the data point with the highest mean lifetime, with the higher standard deviation having the shorter lifetime. Several other points are observed

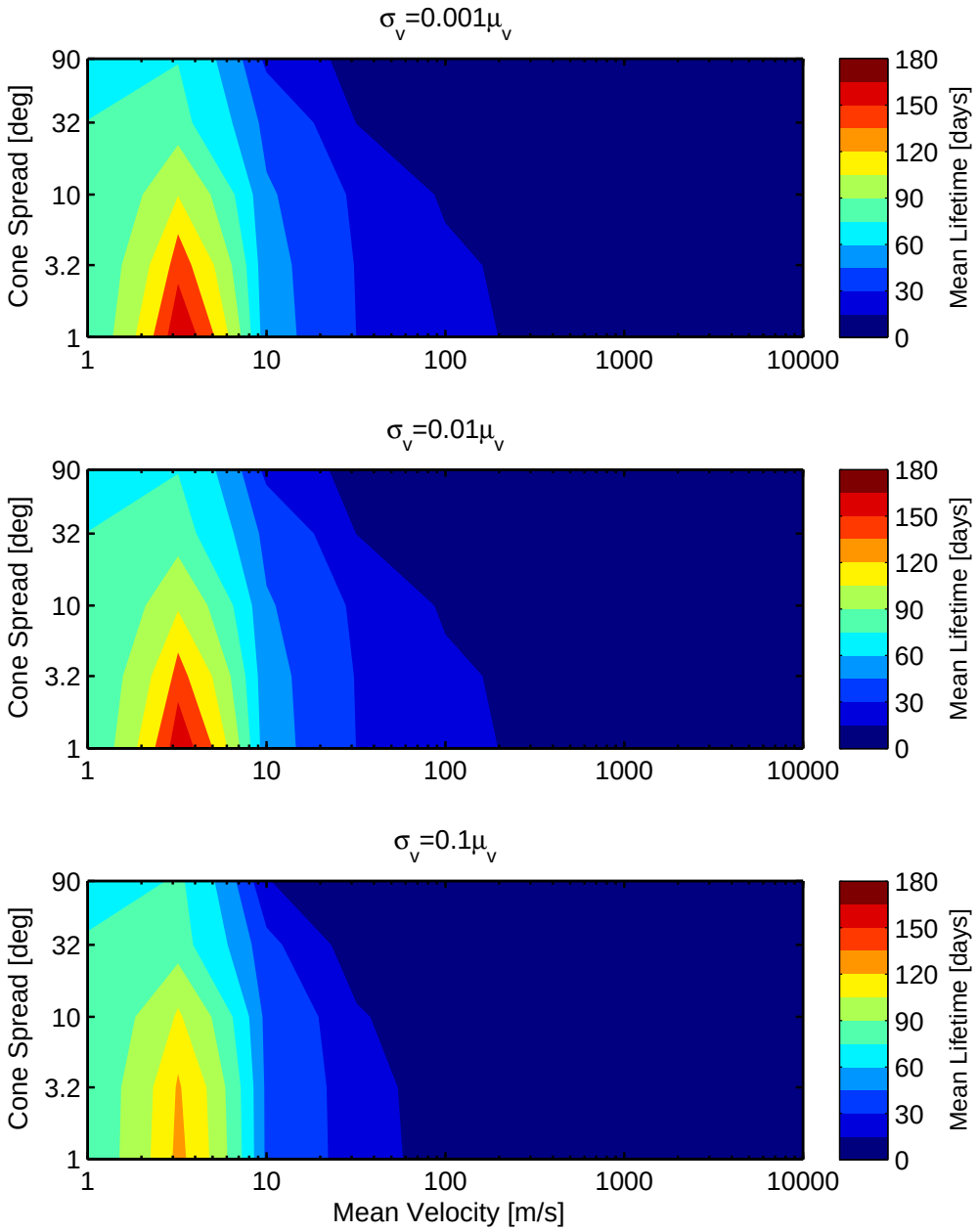

Figure 4.6: Average lifetime of dust grains, with $\beta = 0.005$, within the useful zone when ejected from the classical L_1 point for a range of cone spread angles, θ, initial mean velocities, μ_v and velocity standard deviations, σ_v.

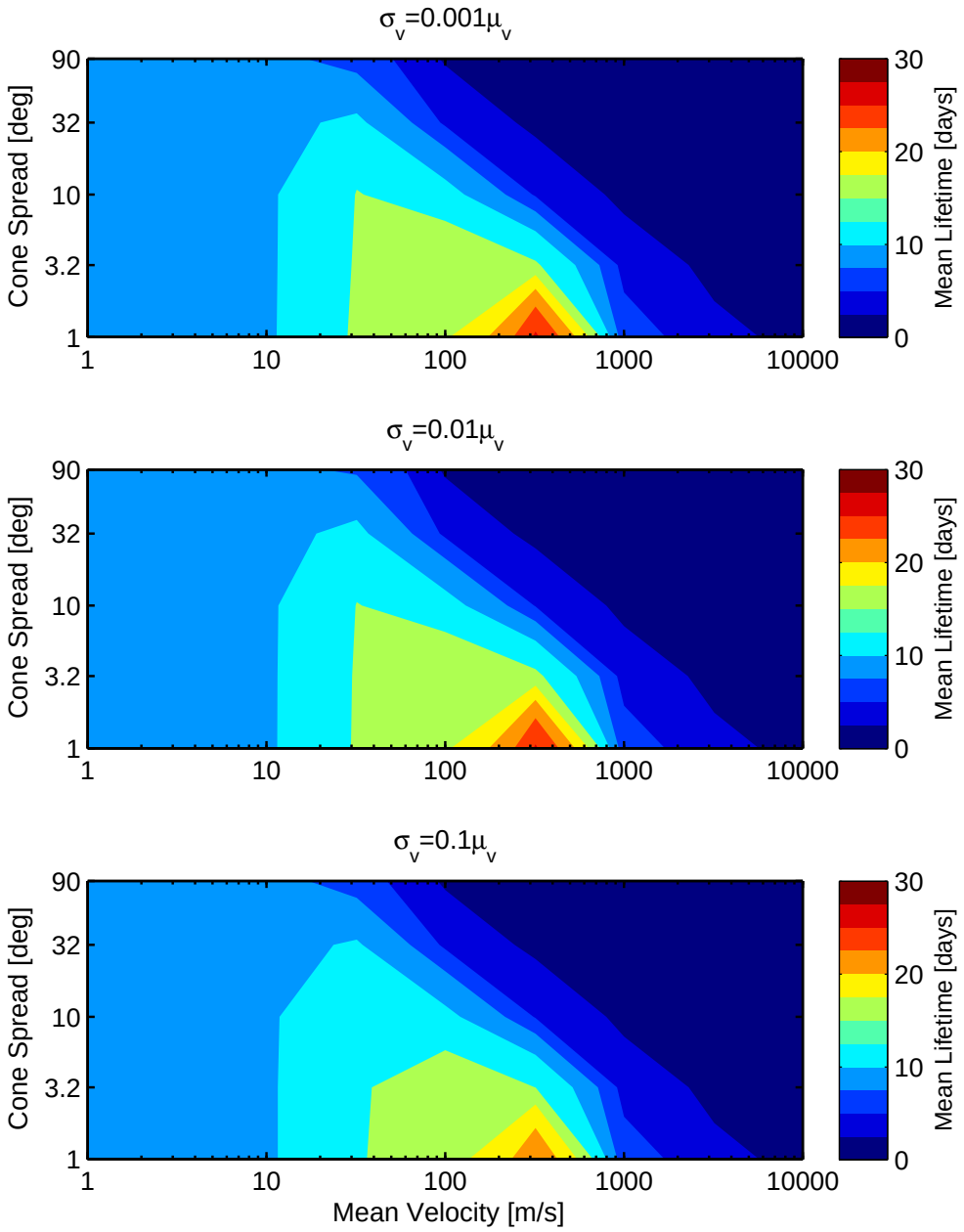

Figure 4.7: Average lifetime of dust grains, with $\beta = 0.751$, within the useful zone when ejected from the classical L_1 point for a range of cone spread angles, θ, initial mean velocities, μ_v and velocity standard deviations, σ_v.

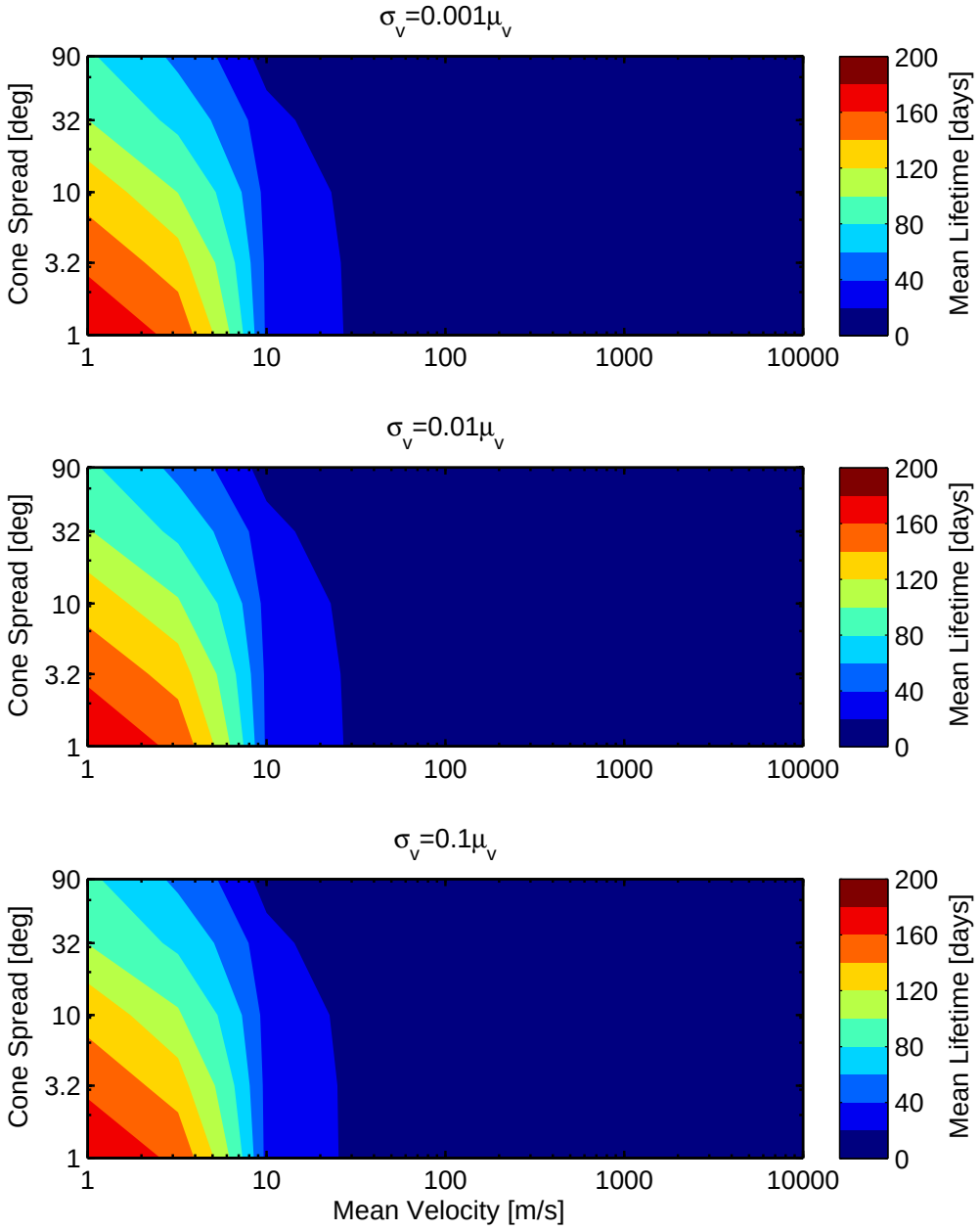

Figure 4.8: Average lifetime of dust grains, with $\beta = 0.005$, within the useful zone when ejected from the displaced equilibrium position for a range of cone spread angles, θ, initial mean velocities, μ_v and velocity standard deviations, σ_v.

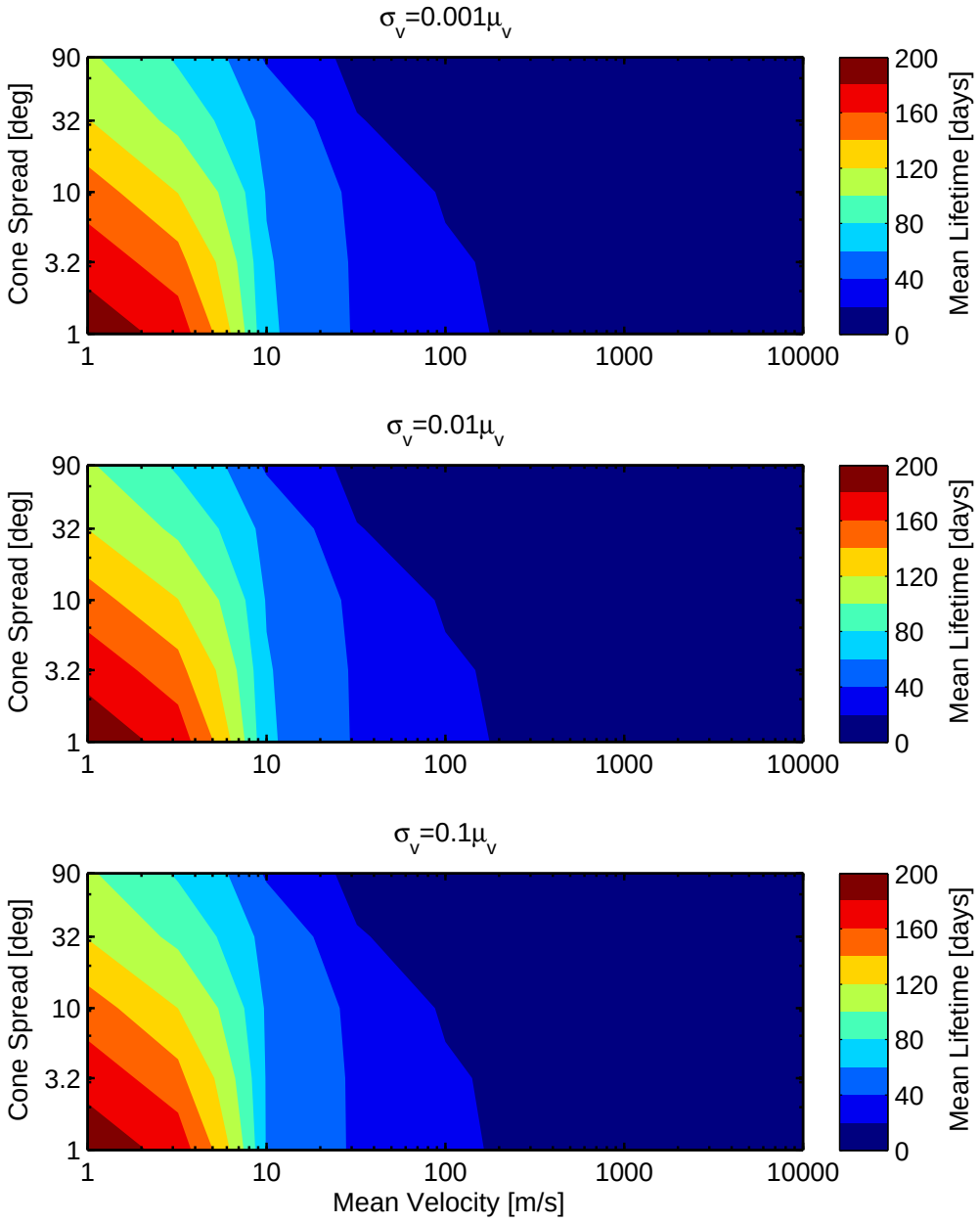

Figure 4.9: Average lifetime of dust grains, with $\beta = 0.751$, within the useful zone when ejected from the displaced equilibrium position for a range of cone spread angles, θ, initial mean velocities, μ_v and velocity standard deviations, σ_v.

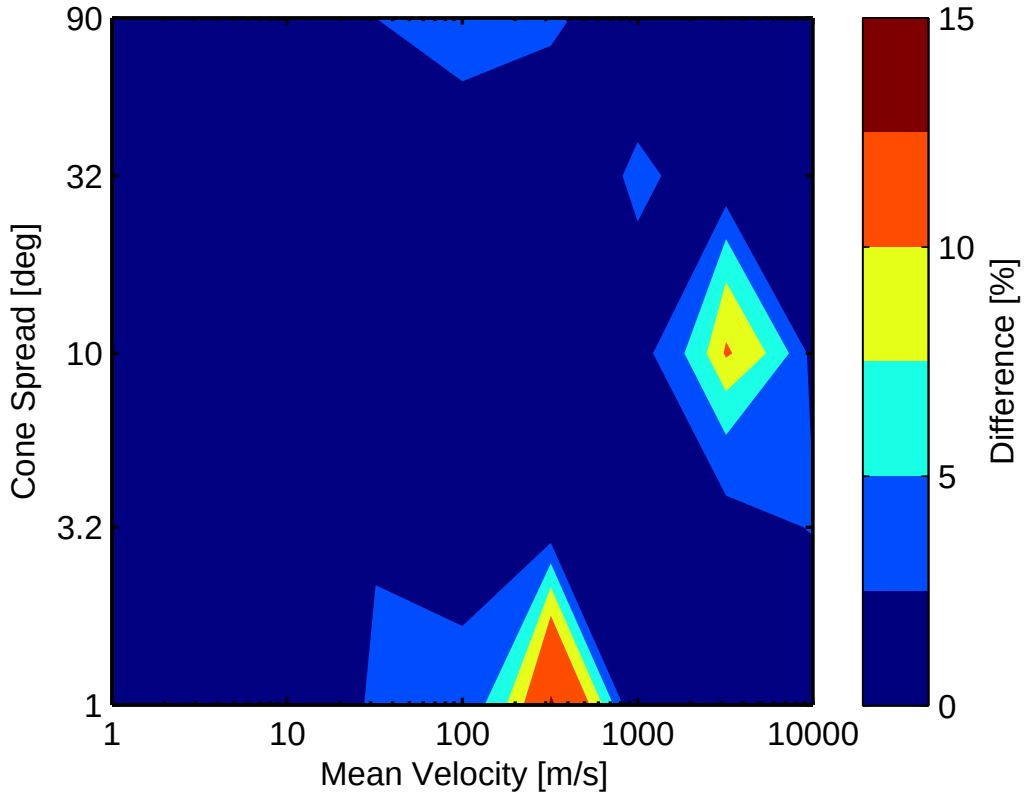

Figure 4.10: Difference in average lifetime between the ejected dust clouds with the smallest and greatest velocity standard distributions, $\sigma_v = 0.001\mu_v$ and $\sigma = 0.1\mu_v$ respectively, for the range of cone spread angles, θ and mean velocities, μ_v.

with noticeable differences, however, these are due to the numerical manner of the optimisation. This confirms that, like the angular spread, greater standard deviations decrease the efficiency of the ejection, in terms of lifetime. It is still to be determined whether this is a detrimental effect on the ability of the ejecta cloud in reducing solar insolation. For example, a greater spread of material will lead to a greater region in space where sunlight can be blocked.

As noted for the example shown in Fig. 4.10, the majority of data points show little difference between the two standard deviations, with the mean difference being 2.8%. The mean differences for all four figures between Fig. 4.6 and Fig. 4.9 can be seen in Table 4.2 as well as the standard deviation of the difference values. All four plots show relatively small mean differences, however, the standard deviations are all comparable to the mean values, indicating a high degree of variability around the mean values.

Position	β	$\Delta\bar{T}$ [%]	σ_{Δ_T} [%]
L_1	0.005	2.8198	3.9772
	0.751	2.4399	2.7238
Equilibrium	0.005	1.7620	1.7582
Position	0.751	2.2463	2.5049

Table 4.2: Average, and standard deviation, of the difference in mean lifetime between the optimisations for the initial velocity standard deviations of $\sigma_v = 0.001\mu_v$ and $\sigma_v = 0.1\mu_v$. There results are shown for β values of 0.005 and 0.751 for the displaced equilibrium and classical L_1 positions.

4.3.2 Sphere

The spherical ejection of material can be imagined as being deployed by various methods. For example, an asteroid which is disintegrated by an explosion will presumably eject material in all directions, though the size and velocity of these ejecta particles will likely be unpredictable. An alternative mechanism is the multiple deployment of small mass driver equipped landers, which, if evenly spaced on the surface of an asteroid, will approximate a spherical ejecta cloud. As this method of ejection is not optimised to maximise the lifetime of the dust cloud, it is anticipated that this method will have a reduced mass efficiency in comparison to the conical ejection methods. There may be some advantages in this method of ejection, however, as there will be a greater spread of material and thus a more even reduction in insolation over the Earth.

The mass required for the continual ejection of material using this spherical ejection method can be seen in Fig. 4.11 and 4.12 for the classical L_1 point and displaced equilibrium positions respectively, for β values of 0.05 and 0.751. For both positions it can be seen that lower velocities require the least mass-per-year and, as for the initially static cloud discussed in Chapter 2, the high β case requires orders of magnitude less mass than the β value of 0.005.

Specifically, for ejection at the classical L_1 point, it can be seen that the minimum mass requirement for grains with a β value of 0.005 is $3.3 \times 10^{12}\,\mathrm{kg\,yr^{-1}}$, whilst for a β value of 0.751 this result reduces to $8.3 \times 10^{10}\,\mathrm{kg\,yr^{-1}}$. These values occur for mean velocities of $1\,\mathrm{m\,s^{-1}}$ and $10\,\mathrm{m\,s^{-1}}$ respectively. Both optimal results have a standard deviation of $0.1\mu_v$, though the difference between the results for the three standard deviations of $0.1\mu_v$, $0.01\mu_v$ and $0.001\mu_v$ is small, approximately 0.2% between the smallest and largest result for a β value of 0.005 and mean velocity of $1\,\mathrm{m\,s^{-1}}$. The optimum velocities for the two β values are broadly in the vicinity of the optimum velocities seen in Fig. 4.6 and Fig. 4.7, for an angular spread of 90°, which equates to ejection into a complete hemisphere. Additional results were calculated for mean velocities of $0.01\,\mathrm{m\,s^{-1}}$ and $0.1\,\mathrm{m\,s^{-1}}$,

however, the insolation reduction requirement of 1.7% was not reached. This is likely primarily due to the low spread, of the grains because of the low velocities, before the cloud exits the useful zone.

For the ejection of material at the displaced equilibrium position the minimum mass requirement is found for a velocity of $1\,\mathrm{m\,s^{-1}}$ for both β values. Specifically, the mass requirements are $2.2 \times 10^{12}\,\mathrm{kg\,yr^{-1}}$ and $1.4 \times 10^{10}\,\mathrm{kg\,yr^{-1}}$ for the β values of 0.005 and 0.751 respectively. As for the ejection of material at the classical L_1 point, the standard deviation of the velocity distribution has little effect on the mass requirement. The ejection of dust grains with velocities below $1\,\mathrm{m\,s^{-1}}$ can achieve an insolation reduction of 1.7%, the mass requirements of which are greater than the results for the velocity of $1\,\mathrm{m\,s^{-1}}$. From these results for the spherical ejection of material it can be concluded, similarly to the release of a static cloud from the vicinity of the L_1 point, that the equilibrium positions is preferable for the release of the cloud.

4.3.3 Cone

A more realistic scenario for the ejection of material from an asteroid, at least when considering the use of only a few ejection devices, is the ejection of material into a certain direction. In this scenario it can be imagined that a small number of devices land on the surface of an asteroid and eject material. The mass required per year to reduce solar insolation by 1.7% using this method was determined for the four main scenarios, the ejection of material at the classical L_1 and displaced equilibrium positions under the assumption that either the lifetime of the dust grains, or the spread of material, is optimised. The values for these scenarios were determined for grain β values of 0.005 and 0.751, cone widths of $\theta = 1°$, $\theta = 10°$ and $\theta = 32°$ and for a velocity distribution with a standard deviation of $0.1\mu_v$. As a cone spread angle of 100° encompasses a range of angle greater than a hemisphere, a smaller angle of 32° was chosen as the larger spread. This value was chosen as it is equidistant between 10 and 100 on a log-scale. The standard deviation value of $0.1\mu_v$ was chosen as it is assumed to be a worst case scenario. The results for the optimisation of the mean lifetime and the optimisation of the spread of the cloud for ejection at the classical L_1 point can be seen in Figures 4.13 and 4.14 respectively, whilst for the same optimisations the results for ejection at the displaced equilibrium position can be seen in Figures 4.15 and 4.16.

For the cloud released at the classical L_1 point, for the optimised lifetime, the minimum mass requirements are $4.9 \times 10^{12}\,\mathrm{kg\,yr^{-1}}$ and $5.8 \times 10^{10}\,\mathrm{kg\,yr^{-1}}$ for the β values of 0.005 and 0.751 respectively. This is in keeping with the results from Chapter 2, where the greater mass efficiency of the smaller dust grains provides the least mass, despite a reduced average lifetime. For the lower β value case the minimum value occurs for a cone spread angle of 32° whilst for the higher β

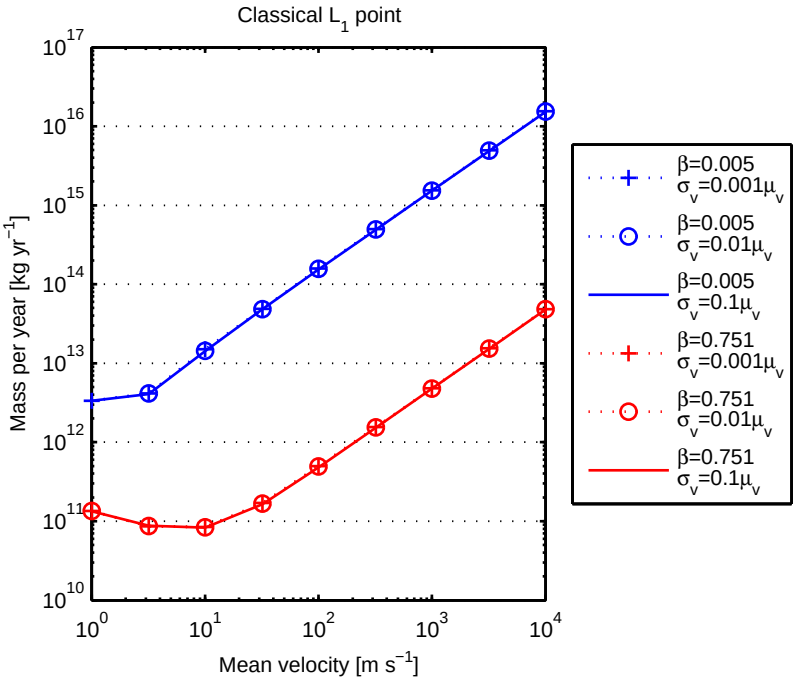

Figure 4.11: Mass requirement for a spherical ejection of material at the classical L_1 point for a range of mean velocities and β values of 0.005 and 0.751.

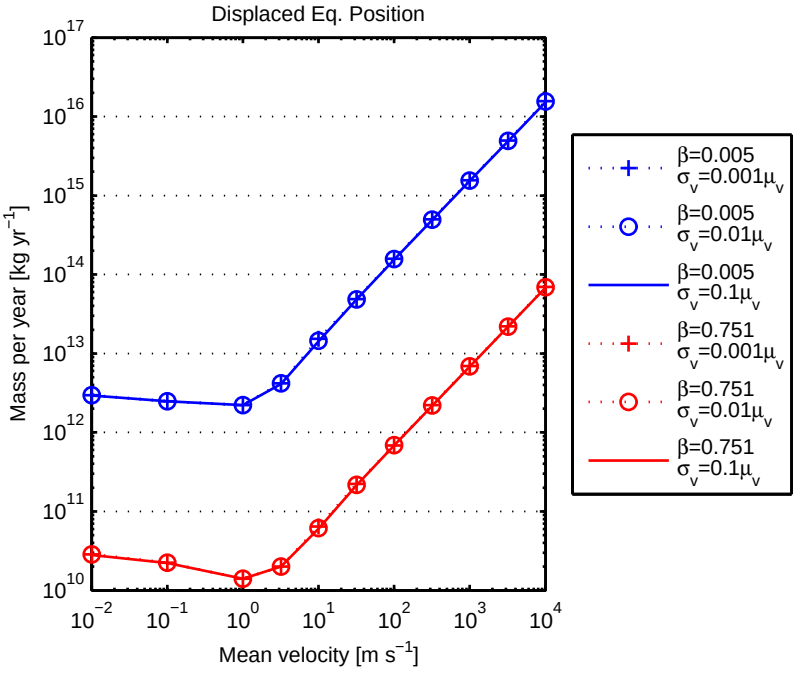

Figure 4.12: Mass requirement for a spherical ejection of material at the displaced equilibrium position for a range of mean velocities and β values of 0.005 and 0.751.

Position	Optimisation	β	Mass requirement [$\mathrm{kg\,yr^{-1}}$]
Classical L_1 point	Lifetime	0.005	4.9×10^{12}
		0.751	5.8×10^{10}
	Spread	0.005	4.8×10^{12}
		0.751	6.3×10^{10}
Displaced equilibrium position	Lifetime	0.005	2.1×10^{12}
		0.751	1.3×10^{10}
	Spread	0.005	2.2×10^{12}
		0.751	2.5×10^{10}

Table 4.3: Optimum mass requirement for each simulation scenario considered for the ejection of a dust cloud into a cone.

value the smallest cone spread provides the best result, though all three angular spreads provide very similar minimum results for $\beta = 0.751$. The minimum value occurs for the lower β value at a velocity of $1\,\mathrm{m\,s^{-1}}$, though the values for μ_v =$1\,\mathrm{m\,s^{-1}}$ are less than a factor of 2 different. The optimum velocity, out of the lifetime results calculated, which can be seen in Fig. 4.6, for $\beta = 0.005$ is $3.2\,\mathrm{m\,s^{-1}}$. This occurs for the lowest cone spread angle of 1°. This is in general agreement with the mass requirement results which suggests the most favouable ejection velocity to be in the region of 1-10$\mathrm{m\,s^{-1}}$. Unfortunately, the mass requirements for the intermediate values were not calculated due to processing time constraints. To ascertain whether a mean velocity of $1\,\mathrm{m\,s^{-1}}$ has the minimum mass requirement results were calculated for mean ejection velocities of $0.1\,\mathrm{m\,s^{-1}}$ and $0.01\,\mathrm{m\,s^{-1}}$. For these velocities the insolation reduction target of 1.7% was not met. This is due to the low spread of the ejecta cloud before leaving the useful zone due to the very low velocities.

For the higher β value, the most favourable mean ejection velocity is seen at $10\,\mathrm{m\,s^{-1}}$, though the value is similar to the mass requirement for a mean ejection velocity of $100\,\mathrm{m\,s^{-1}}$. The minimum results occur for the lowest angular spread, though, again, the results for the three angular spreads are similar in this velocity region. It would be expected that, for the lowest angular spread, the minimum mass values would be for a higher velocity, since the optimum lifetime occurs for a mean ejection velocity of $320\,\mathrm{m\,s^{-1}}$. For the two larger angular spreads this velocity region would be where the minimum mass requirement would be expected when the optimum lifetimes from Fig. 4.7 are studied.

The mass requirement for the scenario of material ejected at the classical L_1 point with the intention of optimising the spread of the material can be seen in Fig. 4.14. The general shape of the

results are seen to be similar to the optimised lifetime scenario, with the minimum for $\beta = 0.0.05$ and $\beta = 0.751$ being $4.8 \times 10^{12}\,\mathrm{kg\,yr^{-1}}$ and $6.3 \times 10^{10}\,\mathrm{kg\,yr^{-1}}$ respectively. As with the lifetime optimisation scenario, this value occurs for the lowest angular spread. In Fig. 4.14 it can be seen that some results do not exist for an insolation reduction of 1.7% whilst they do for the lifetime optimisation scenario. Both of these missing results occur for the lowest angular spread for low velocities. This suggests that the solar radiation model used to calculate these results is particularly sensitive to changes in the input parameters when a low spread of the ejecta cloud is expected.

The results for material ejected from the displaced equilibrium position for the scenario of the optimised lifetime of the dust grains can be seen in Fig. 4.15. As for the case of the material ejected at the classical L_1 point there is a clear decrease in mass requirement for decreasing mean velocity for all cone widths modelled. There is an optimum mean ejection velocity, $1\,\mathrm{m\,s^{-1}}$, where the mass requirement is $2.1 \times 10^{12}\,\mathrm{kg\,yr^{-1}}$ for a β value of 0.005 and $1.3 \times 10^{10}\,\mathrm{kg\,yr^{-1}}$ for a β value of 0.751. These values both occur for a cone spread of 32°, though for the low velocities the results for all three cone widths are similar. The mass requirement can be seen to increase slightly for the very low ejection velocities below $1\,\mathrm{m\,s^{-1}}$. As noted previously, this is likely due to the lower spread of the ejected material over the course of the lifetime of the dust. Again, similar to the results discussed in Chapter 2, the mass requirement for the release of a dust cloud at the displaced equilibrium position is lower than that found when the cloud originates from the classical L_1 point.

The results for the optimisation of the spread of the ejected material when released from the displaced equilibrium position can be seen in Fig. 4.16. These results show the same shape and general results for the optimisation of the lifetime discussed previously. A comparison of the results for the varying angular spreads shows that, in general, for higher velocities the narrower angular spread provides a lower mass requirement for ejecta clouds at both the classical L_1 and displaced equilibrium positions. As the velocity decreases the difference in the results for the three angular spreads decreases and, for the lowest velocities considered, the highest angular spread then provides the lowest mass requirement. This is observed for both ejection positions, though the effect is more pronounced for the classical L_1 case. Here the higher mass requirement is several times that of the lower value, though for the displaced equilibrium position it is only marginally greater.

The results for the homogeneous spherical ejection of material and the collimated ejection of material are broadly similar in terms of mass requirement and shape of the results, whereby the higher velocities display a result that is several orders of magnitude greater than for velocities in the region of 1-10 $\mathrm{m\,s^{-1}}$. The result that the mass requirement is similar to the results for the collimated ejection is, in some ways, unexpected. This is most notably because there is no

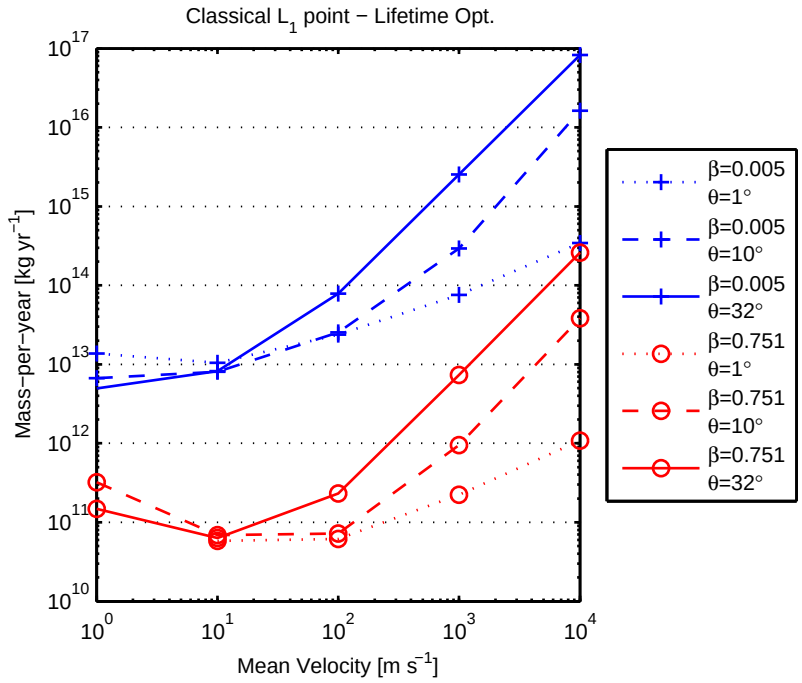

Figure 4.13: Mass-per-year required to reduce solar insolation by 1.7% for a dust cloud ejected from the classical L_1 point under conditions to maximise the expected lifetime of the cloud.

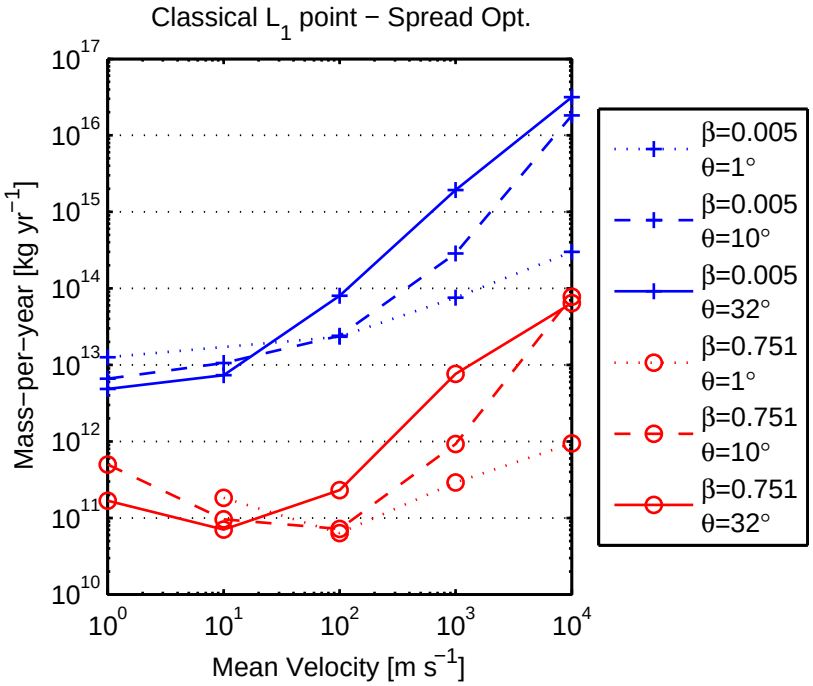

Figure 4.14: Mass-per-year required to reduce solar insolation by 1.7% for a dust cloud ejected from the classical L_1 point under conditions to maximise the expected spread of the cloud.

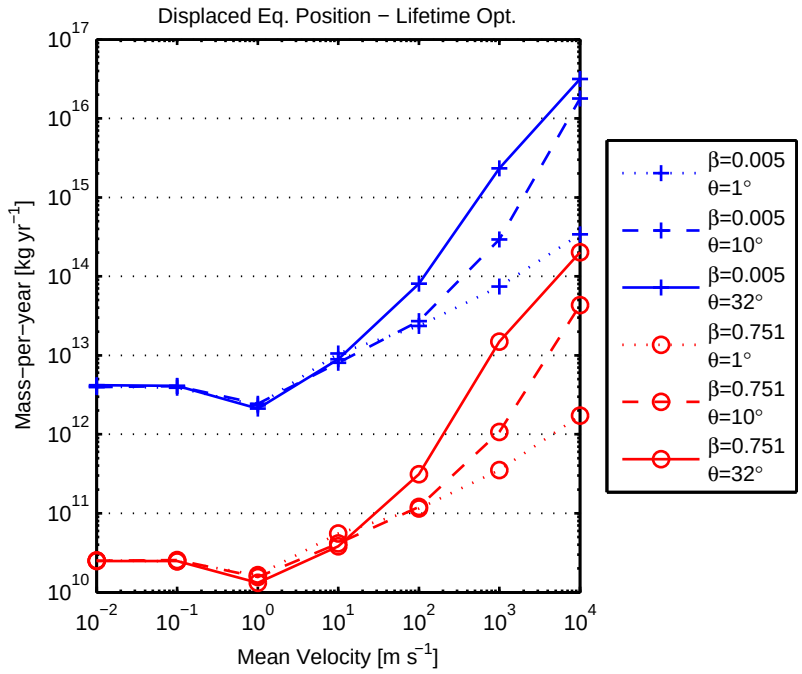

Figure 4.15: Mass-per-year required to reduce solar insolation by 1.7% for a dust cloud ejected from the displaced equilibrium position under conditions to maximise the expected lifetime of the cloud.

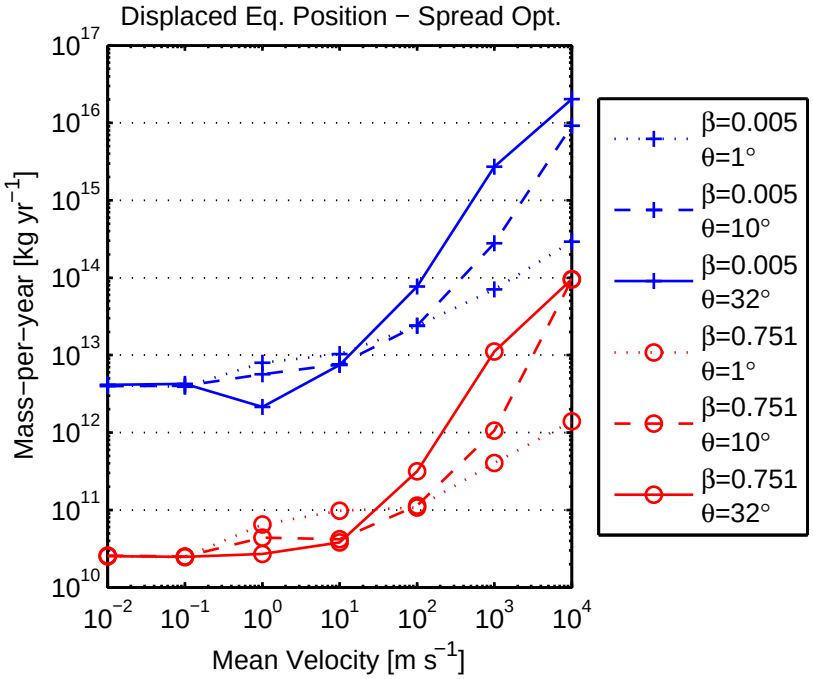

Figure 4.16: Mass-per-year required to reduce solar insolation by 1.7% for a dust cloud ejected from the displaced equilibrium position under conditions to maximise the expected spread of the cloud.

optimisation of the initial ejection angle involved and hence it is expected that the efficiency of the method will be reduced. However, it can be observed that the least collimated results, $\theta = 32°$, show a strong resemblance to the spherical ejection results. This suggests that above the smallest collimation, the variability in the results for different angular spreads decreases.

4.4 Conclusion

In this chapter the effect that the initial velocity conditions have on the efficiency of the dust cloud method has been investigated. The mass required per year to achieve an insolation reduction of 1.7% has been calculated for the ejection of material from a point source, under the assumption of both homogeneous ejection over all angles and the collimation of material into jets orientated within the orbit plane of the circular restricted three-body problem. The results for the collimated ejection of material is calculated for an initial angle of ejection based, separately, on the optimisation of the lifetime and spread of the ejected material. For the spherical, homogeneous ejection of material over all angles the mass requirement is found to be $8.3 \times 10^{10}\,\mathrm{kg\,yr^{-1}}$ and $1.4 \times 10^{10}\,\mathrm{kg\,yr^{-1}}$ for the initial positions of the classical L_1 point and the displaced equilibrium positions respectively. For the optimisation of the lifetime of the ejected dust grains the mass requirements are $5.8 \times 10^{10}\,\mathrm{kg\,yr^{-1}}$ and $1.3 \times 10^{10}\,\mathrm{kg\,yr^{-1}}$ for the classical L_1 and displaced equilibrium positions, whilst for the optimisation of the spread of the dust grains the results increase to $6.3 \times 10^{10}\,\mathrm{kg\,yr^{-1}}$ and $2.5 \times 10^{10}\,\mathrm{kg\,yr^{-1}}$. These results compare favourably to the case of the static cloud discussed in Chapter 2, where the mass is of order $10^{10}\,\mathrm{kg\,yr^{-1}}$, and it can be concluded that the velocity of the ejected dust grains will not greatly alter the mass efficiency of this method of space-based geoengineering.

Chapter 5

Earth Ring

In comparison to the Earth ring concept, the main disadvantage of positioning a cloud of dust at the L_1 point for geoengineering, as described in Chapters 2, 3 and 4, is that constant replenishment is necessary. As discussed previously, the concept of an Earth ring for geoengineering has been suggested by Pearson [79]. In this concept a stable, circular ring in the equatorial plane is suggested that is designed to require no replenishment of material, at least in the short-term. However, the previous work on this concept does not assume any influence from solar radiation pressure (SRP) or the J_2 Earth oblateness effect. The dynamics of high area-to-mass ratio dust grains and spacecraft around Earth, researched by Charlotte Lücking and Camilla Colombo and summarised in Sec. 5.1, are used as a basis for the Earth ring concept described in this chapter (found in Sec. 5.2 to Sec. 5.6). In this concept it is proposed that dust grains can be extracted from an asteroid and ground before being ejected to form the dust ring.

5.1 Orbital Dynamics

In this section the orbital dynamics of high area-to-mass ratio dust grains around Earth will be discussed, with the inclusion of the perturbations of solar radiation pressure and the J_2 effect. This section is a summary of work conducted by Charlotte Lücking and Camilla Colombo and can be found in full in Appendix A.

5.1.1 Hamiltonian model of dust orbital dynamics

To analyse the effect that solar radiation pressure and the J_2 perturbations have on the orbit of dust grains around the Earth a planar model is used that ignores the tilt of the Earth's axis with respect to the ecliptic, i.e. the orbit lies in the ecliptic, and ignores the effect that eclipses have on the orbit. To describe the motion of a dust grain in this planar orbit four key parameters are used; orbital eccentricity, e, semi-major axis, a, the angle between the direction of solar radiation and the direction of the orbit perigee with respect to Earth, ϕ, and the position of the dust grain in the orbit, θ. The angle θ is defined as the angle ϕ plus the true anomaly, f, of the grain in the orbit. This geometry can be seen in Fig. 5.1.

Under the assumptions that there are no eclipses and that the orbital plane lies in the ecliptic a Hamiltonian has been found [42, 56] that describes the orbital evolution of the dust grains. This Hamiltonian is defined as:

$$H(e,\phi) = -\sqrt{1-e^2} + \alpha e \cos\phi - \frac{\kappa}{3\sqrt{1-e^2}^3} \tag{5.1}$$

In this equation α is a parameter describing the effect of solar radiation pressure, which is dependent upon the area-to-mass ratio, on the evolution of dust grain orbits and κ describes the effect of the J_2 perturbation. Equations A.3 and A.4 can be used to calculate α and κ respectively. Under the assumptions used in the Hamiltonian, the orbital evolution can be seen only to vary the eccentricity of the orbit and the perigee angle ϕ, with the semi-major axis remaining constant. A full discussion of the equations describing this evolution can be found in Appendix A.

It has been shown by Colombo et al. [31] that the Hamiltonian has a stable equilibrium point located at $\phi = 0$, for an initial eccentricity of e_0, with respect to the progression of the angle between the position of the Earth on its orbit around the Sun and the vernal equinox. This equilibrium position represents frozen orbits that precess such that their apogee is constantly Sun-pointing. These orbits are termed heliotropic orbits. It is shown that the minimum value of e_0 is found when the effect of solar radiation pressure is zero and increases with an increased SRP force. This can be seen in Fig. 5.2. When the perigee altitude is considered it can be seen that the minimum value for e_0 causes the perigee altitude to fall below 0 km, i.e. it will impact the surface of the Earth, when $a > 16,000$ km. Marked in Fig. 5.2 is a shaded region showing when the value of e_0 when the perigee altitude falls below a value of 2,000 km. Here the effects of atmospheric drag are experienced and a dust grain is considered to de-orbit. Therefore, it can be seen in Fig. 5.2 that these heliotropic orbits only exist for certain combinations of e, a and dust grain size, and so area-to-mass ratio. However, if a dust cloud is constructed using a range of dust grain sizes

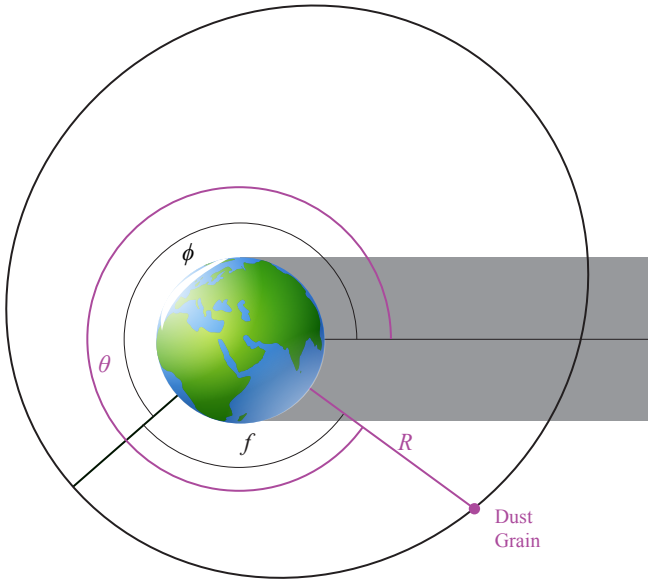

Figure 5.1: Geometry of an in-plane orbit in the synodic reference frame [62].

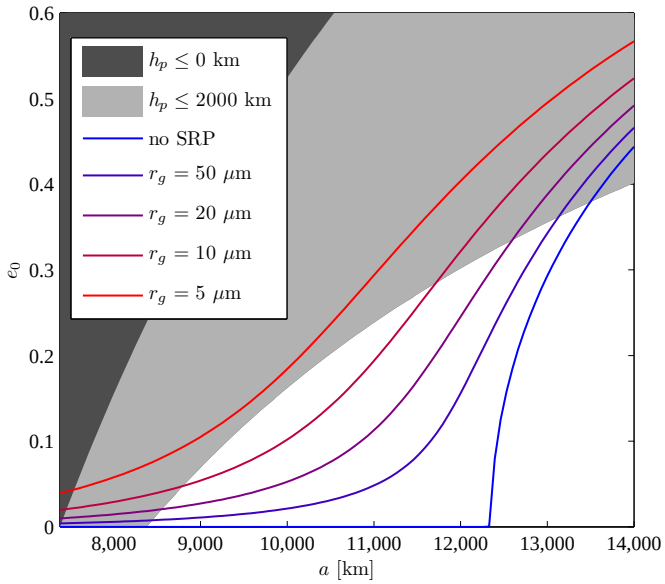

Figure 5.2: Minimum eccentricity ($\alpha = 0$) of the heliotropic equilibrium orbit $min(e_0)$ as a function of semi-major axis [62].

the value for e_0 will not be constant. It has been observed that if a dust grain is released with an eccentricity between the minimum allowed value of e_0 and the value where the perigee altitude is $2,00\,\text{km}$ then the dust grains will librate around the equilibrium position [14, 62] and will not de-orbit.

5.1.2 Choice of feeder orbit

From previous chapters it has been observed that a decrease in the grain size used in space-based geoengineering strongly affects the mass of dust required. Therefore, it is advantageous to find the minimum grain size with which a heliotropic orbit can be found. However, a trade-off must be performed with the fraction of an orbit that a grain of a certain size will spend in between the Sun and Earth. An equation describing the minimum grain size possible has been derived in Appendix A and has been shown in Fig. 5.3. The fraction of an orbit that a grain blocks sunlight is dependent on the orbital geometry and will be termed the geometrical efficiency. The range of values for the geometrical efficiency associated with a range of dust grains sizes being ejected (discussed in Sec. 5.2.2) is also shown in Fig. 5.3. From these results the initial orbit from which the dust will be ejected, termed the feeder orbit, is chosen to have a radius of 10,250km ($a = 9318\,\text{km}$) and an eccentricity of $e_f = 0.1$.

5.2 Geoengineering scenario

5.2.1 Dust source

Some consideration must be given to the source of dust that is to be dispersed from the feeder orbit as it is expected that a significant quantity is required. Previous space-based geoengineering (SBGE) concepts have suggested the use of dust sourced from the Earth, Moon, asteroids and comets [12, 13, 79, 98]. It has been shown that the amount of asteroid material that can be captured into a weakly bound Earth orbit with a threshold velocity lower than that of the lunar escape velocity of $2.37\,\text{km}\,\text{s}^{-1}$ is $6 \times 10^{13}\,\text{kg}$ [86]. For the material required in this SBGE scenario an extra velocity increment of $2.37\,\text{km}\,\text{s}^{-1}$ would be required to lower the orbit to the position of the feeder orbit, therefore doubling the velocity requirement.

Despite the additional costs of transporting asteroid material to a medium Earth orbit, the use of captured asteroid resources would still be more efficient than lifting material from the surface of the Earth. This also applies for schemes that require solid reflectors to block solar

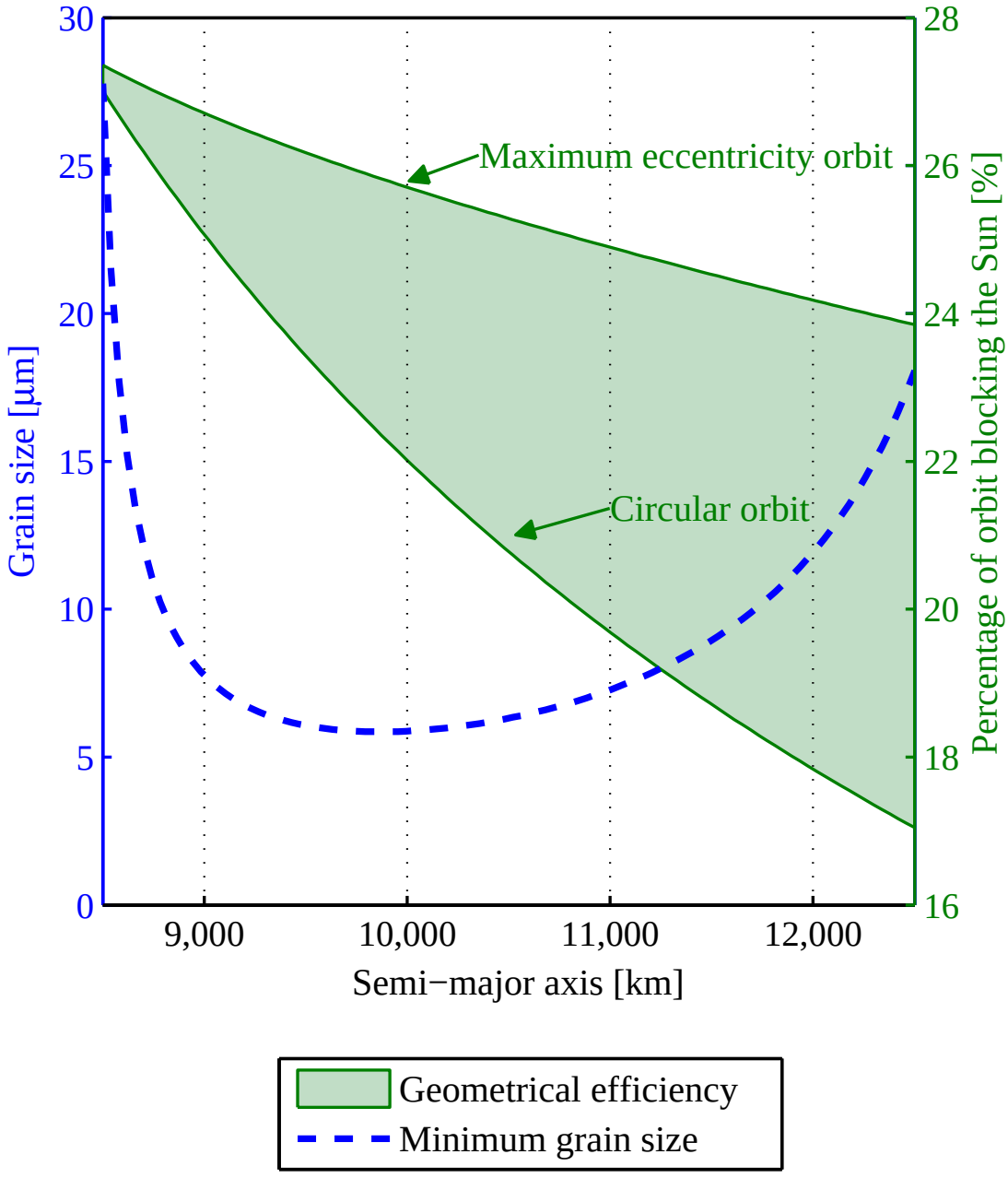

Figure 5.3: Geoengineering efficiency indicators (grain size and orbit geometry) with semi-major axis. The minimum grain size which can be deployed at the given semi-major axis without rapid decay is given on the left axis. The geometrical efficiency is given on the right axis as a range from a circular orbit to an orbit with critical eccentricity and Sun-pointing apogee [14].

radiation where large devices must be manufactured and then launched into the correct position. Lifting such large masses (of the order of 10^{10} kg) is beyond current launch capabilities. Using asteroid material rather than lunar dust has the added benefit that the material can be sourced and ground to finer grain sizes, if required, whilst in the feeder orbit before being released, thus removing the requirement to transport material from the Moon.

An additional source of material could possibly be spent rocket stages and other debris that can be ground to dust. The NORAD database of tracked space objects reveals that there are over 1,000 spent rocket stages and over 10,000 pieces of other debris in LEO and MEO orbits. Assuming a minimum mass of 1 metric tonne per rocket stage gives a lower bound of 1×10^6 kg in this region. This is a relatively small amount of material in comparison to the scale of typical geoengineering schemes but would potentially be useful.

The asteroid is envisaged to be captured into a circular, equatorial generator orbit with an orbital radius of $a_g = 10,250$km (see Figure 5.4). It follows that 10,250 km is also the radius of the apogee for the feeder orbit, with a semi-major axis of 9,316 km, selected in the previous section. Since the area-to-mass ratio of an asteroid is clearly small, the effect of solar radiation pressure is negligible. The orbit is thus assumed to be unperturbed.

The dust grains will be continuously extracted from the asteroid, milled to achieve a certain radii distribution and collected during one orbit. Whenever the generator passes directly between the Earth and Sun it ejects the collected dust with the correct Δv to inject it into the feeder orbit using a mass driver. From this feeder orbit the grains will then evolve and spread due to their different area-to-mass ratios and thus form the dust ring. Because the period of the generator orbit and the feeder orbit are different, grains will be distributed at all positions in the orbit. After a maximum of one year all positions on the libration curves in the phase space will be filled and after 4 years the orbits will be spread over all inclinations smaller than 0.2° with respect to the equator. Figure 5.4 shows a scale illustration of the concept.

5.2.2 Dust grain size distributions

The milled dust is assumed to be distributed log-normally in grain radius R_{gr}:

$$f_{\mu_{log},\sigma_{log}}(R_{gr}) = \frac{1}{R_{gr}\sigma_{log}\sqrt{2\pi}} e^{-\frac{(\ln R_{gr} - \mu_{log})^2}{2\sigma_{log}^2}} \tag{5.2}$$

Distribution	Mean, μ_{log}	Standard deviation, σ_{log}
D1	-11.5	0.1
D2	-11.35	0.15
D3	-11.2	0.25

Table 5.1: Mean and standard deviation values of the three dust grain distributions in a lognormal distribtuion.

where $f_{\mu_{log},\sigma_{log}}(R_{gr})$ is the probability density function where μ_{log} and σ_{log} represent the mean and standard deviations of the distribution respectively. Three possible distributions have been chosen. D1 is an optimistic estimate with small mean and low standard deviation. D2 is a realistic distribution and achievable with existing terrestrial milling machinery[1,2]. D3 is a pessimistic estimate with high mean and large standard deviation. Table 5.1 shows the chosen values for mean and standard deviation and Figure 5.5 shows the three distributions as probability density functions.

5.3 Ring Attenuation

To calculate the reduction in insolation provided by the ring a modified version of the Beer-Lambert law, shown in Eq. (2.28), is used in a simplified solar radiation model. The SRM no longer connects nodes on the surfaces of the Sun and Earth but instead assumes that the incident solar radiation is plane parallel. The maximum angle away from the Sun-Earth line that an incoming photon can have, due to the Sun being an extended body rather than a point source, is 0.005 radians. Assuming an initial position at the L_1 point, the difference in position between such an angle and the Sun-Earth line will be in the region of 7,500 km, greater than the radius of the Earth. For an initial position at the outer edge of the ring, 10,250 km away from the centre of the Earth, corresponding to an altitude of 3,872 km, this gives a difference of only 19.4 km. This distance is sufficiently small in comparison to the accuracy of the model to justify the assumption of the incoming solar radiation being parallel. The modification of the Beer-Lambert law is based on the different grain sizes used in the ring model. As described in detail in Appendix A, and particularly demonstrated in Fig. A.8, different grain sizes, assuming a constant density, will inhabit different orbits. The attenuation coefficient, Λ, experienced at any point can be described as;

[1] http://www.zenithcrusher.com/ Last accessed 05 Sep 2011
[2] http://www.crushermills.com/ Last accessed 05 Sep 2011

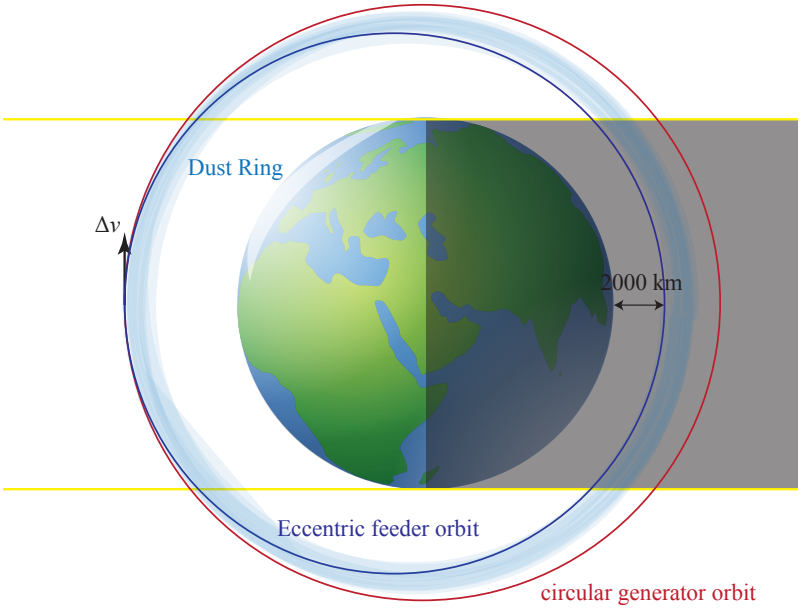

Figure 5.4: Diagram of the generator and feeder orbits for the Earth ring [62].

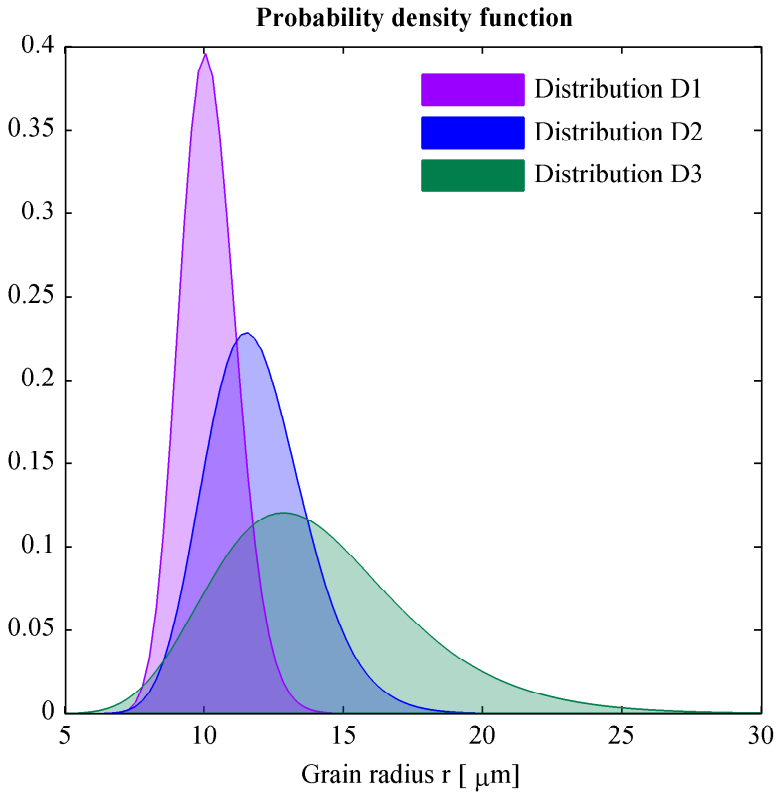

Figure 5.5: Probability density functions for the three distributions of grain radii considered.

$$\Lambda = \int_{R_{gr,1}}^{R_{gr,2}} \pi R_{gr}^2 \rho(R_{gr})\, \mathrm{d}R_{gr} \tag{5.3}$$

where R_{gr} is the grain radius and $\rho(R_{gr})$ is the number density for the same grain radius. Since the attenuation coefficient will change throughout the ring, the attenuation coefficient must be integrated along the path length of an incoming beam of photons, such that;

$$I = I_0 e^{-\int_0^l \Lambda(l) dl} \tag{5.4}$$

A map can be constructed showing the attenuation coefficient through the ring in a polar coordinate system in a rotational reference frame with fixed orientation towards the Sun. Any position in the orbital plane is determined by R, the distance to the centre of the Earth, and θ, the angle with respect to the direction of solar radiation as shown in Figure A.1. This map is constructed by determining the fraction of the total number of particles that will fall within $R-\theta$ boxes. This will be a multiplication of the fraction of particles that will be on an orbit in the $e-\phi$ phase space that falls within the target area and the fraction of this orbit which lies within the area. The determination of the first factor is described in detail in Sec. A.2.1 whilst the latter is a simple orbital dynamics calculation. The maps for the three grain distributions, initially in a 2D planar model, can be seen in Fig. 5.6. Using this map the reduction in insolation is calculated by numerically integrating along the path through the ring for given values of y and z.

All three distributions show similar features, with the attenuation coefficients peaking strongly along the feeder orbit with much smaller values in the majority of the ring. The maximum attenuation occurs directly in between the Sun and Earth, at $\theta = 180°$, which is the intersection of the feeder orbit with the generator orbit in which the captured asteroid is to be positioned. In addition, the grain distribution that has the smallest mean size has the largest portion of the attenuation coefficient at $\theta = 180°$, as can be seen in Fig. 5.7. This is due to the dynamics of the system as smaller particles are more greatly perturbed by SRP and will have higher mean eccentricities.

To fully determine the mass of dust required to offset the 1.7% insolation change a 3D model of the ring must be constructed. The first stage in this process is to transform the in-plane attenuation coefficient into a three-dimensional attenuation coefficient. This is estimated by dividing the in-plane coefficient by the out-of-plane width at radius R, which essentially equates to transforming the 2D number density of the planar model to a 3D number density;

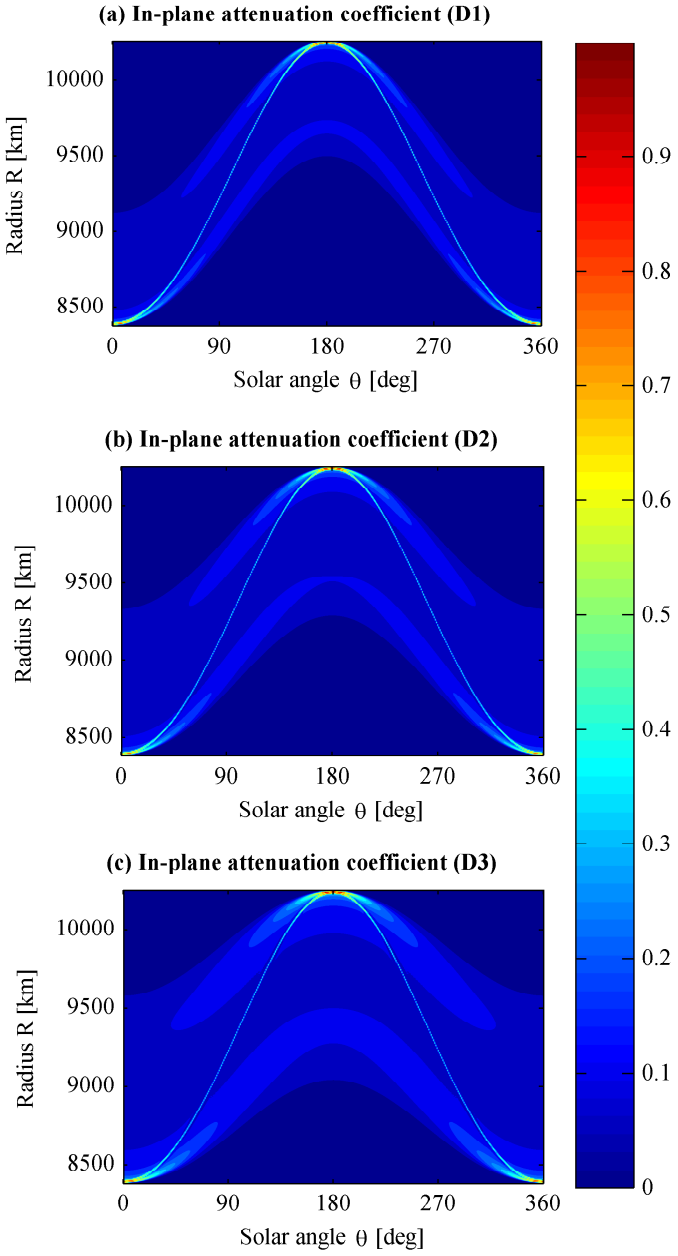

Figure 5.6: In-plane attenuation coefficient, Λ_0, in polar coordinates in relation to the maximum attenuation.

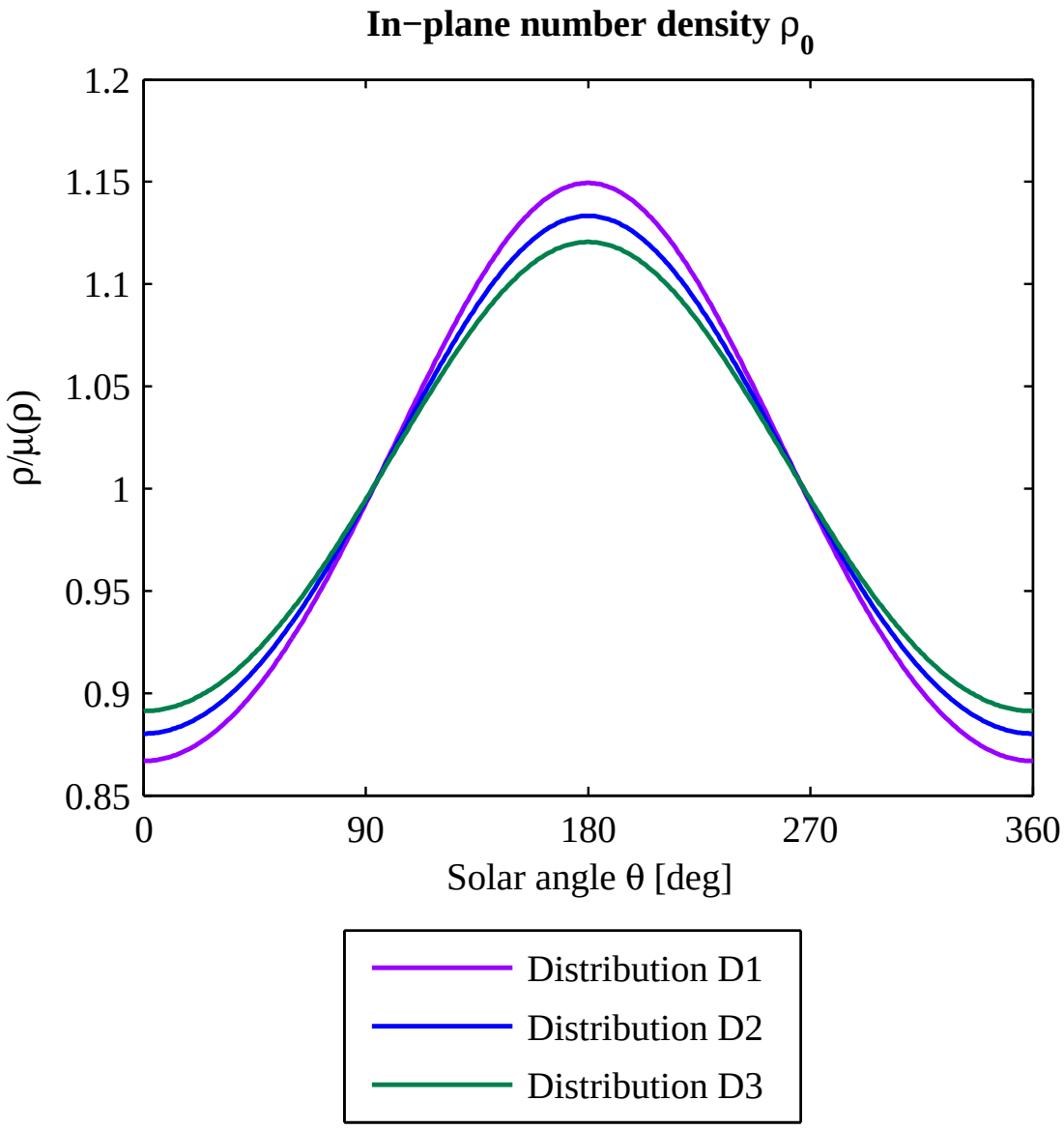

Figure 5.7: Sum of the in-plane number density for different solar angles θ in relation to the average.

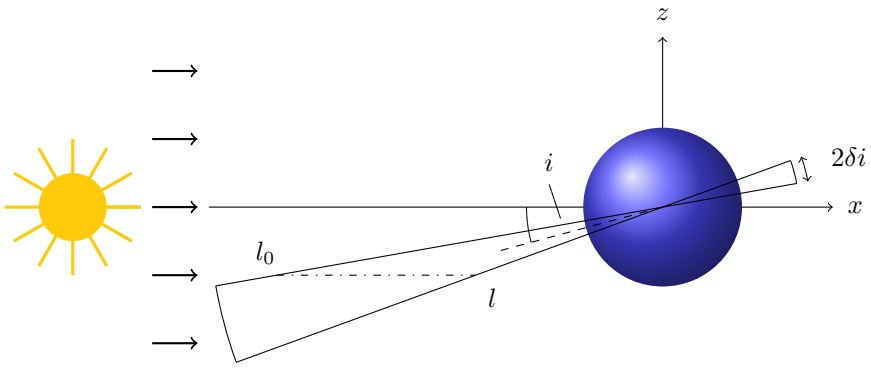

Figure 5.8: Diagram showing the geometry of the Earth ring concept when tilted away from the ecliptic plane.

$$\Lambda(R,\theta) = \frac{\Lambda_0(R,\theta)}{2R\delta i} \tag{5.5}$$

where δi is the inclination spread of the ring. This value was taken as 0.2° as discussed in Sec. A.1.4. Now the 3D ring model can be tilted to account for the tilt of the Earth's axis with respect to the Sun and the integration of the Beer-Lambert equation will take place along the x-axis for given values of y and z. The geometry of the problem can be seen in Fig. 5.8. For a given inclination of the ring to the Sun-line the entry, l_0, and exit, l, points of the integration can be calculated and the Beer-Lambert law can be applied between these two positions. For each point along the integration line the position must be transformed from Cartesian coordinates to the (R,θ) system that describes the attenuation coefficient. This value can then be multiplied by the path length step to give the fractional intensity before being integrated. As for the versions of the SRM discussed in previous chapters, a matrix of the attenuation for each point on the Earth's surface can be constructed which can then be used to optimise the total number of particles required to achieve an insolation reduction of 1.7%.

To find an accurate determination of the mass required, this process must be averaged over time. This is necessary as the angle between the equatorial and ecliptic planes, from the viewpoint of the Sun, will change over the course of a year. It can be found that the inclination angle between the Sun-line and the equatorial plane for a circular orbit around the Sun is described by a sinusoidal oscillation, assuming the starting point is at the northern hemispheres spring. The view of the Earth, as seen from the Sun, is shown in Fig. A.7 for different times of the year. Next the mass required for the three different dust distributions can be found.

Scenario	Mass [kg]
D1	5.94×10^{11}
D2	5.67×10^{11}
D3	8.97×10^{11}

Table 5.2: Mass requirement for the three Earth ring dust distributions.

5.4 Mass requirement

The mass required is determined by first optimising the number of particles required, of a given distribution, to achieve an insolation reduction of 1.7%, using the attenuation matrices noted previously, averaged over the course of an entire year. This value is then multiplied by the mean mass for the given distribution to find the final required mass. The mass requirements for each of the dust distributions described previously can be seen in Table.5.2. It can be seen, as would at first be expected, that the distribution with the greatest fraction of its number density along the Sun-line requires the lowest mass of 5.94×10^{11} kg. This is additionally due to the smaller grain sizes leading to greater efficiency. It is noteworthy that the difference between the D1 and D2 distributions is considerably smaller than the difference with the D3 distribution. A large fraction of this difference will be due to the increase in grain size, however it was expected that the increased spread seen in Fig. 5.6 would partially offset this decreased efficiency, as is the case between D1 and D2. This increased spread is particularly useful at increased inclinations as it spreads the insolation change away from being a very narrow band to a slightly wider band.

The mean insolation change as a function of time can be seen in Fig. 5.9. It shows that the insolation change is variable, with a wide, flat peak greater than the 1.7% required but minima as low as 0.5%. These minima occur during spring and autumn where the inclination of the equatorial to ecliptic plane is low. During these phases the visible cross-sectional area of the ring as seen from the Sun, as seen in Fig. A.7, is reduced to $2\delta i R_{max}$ at its maximum, where R_{max} is the maximum distance to the centre of Earth of the ring. The slight depression in the middle of the peak is situated at the winter time for each hemisphere. This phenomena is due to the changing tilt of the Earth's axis to the ecliptic. As the tilt increases the ring will present a larger cross-sectional area to the Sun, proportionally to $\sin i$, thus casting a greater shadow. However, as the inclination angle, i, increases this shadowed region will shift polewards on Earth, where the curvature of the Earth reduces the area of the Earth that can be shaded, thus decreasing the effect of the greater aspect angle of the ring.

Also of interest is an understanding of where the insolation change over the Earth's surface

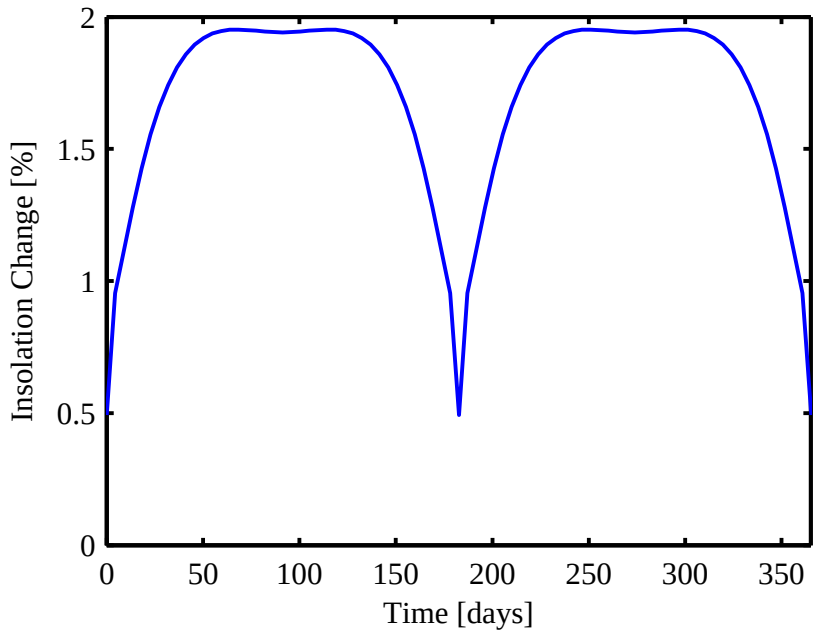

Figure 5.9: Variation in insolation over the course of a year, giving an average of 1.7%.

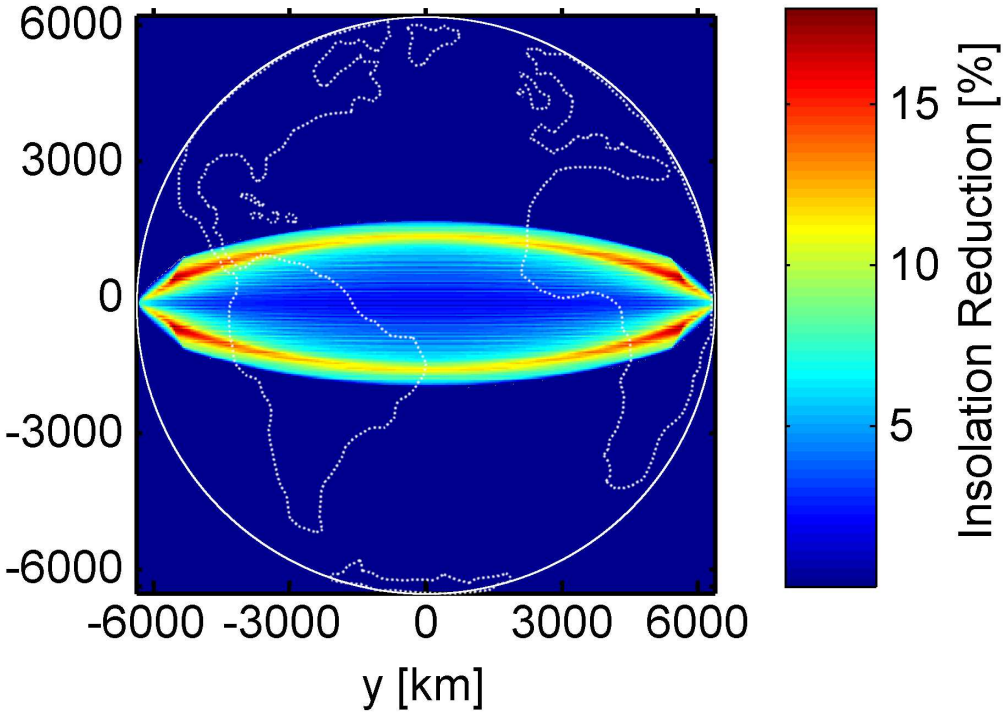

Figure 5.10: Insolation reduction over the Earth's surface summed over an entire year displayed over a map of Earth.

will be greatest. An analysis of this can be seen in Fig. 5.10 where the tilt of the Earth's axis is subtracted and summed over a year to reveal the latitudes most greatly effected by the ring. Clearly the greatest effect will be felt in the equatorial and low tropical regions. In addition, it can be seen in Fig. A.7 that each hemisphere experiences the greatest effects during its winter season. The precise effect that this will have on the local climate requires high-fidelity climate simulation which will not be investigated in this thesis. However it is assumed that strong local effects are likely [95].

5.5 Discussion

5.5.1 Thermal radiation and solar reflection

An additional factor must now be taken into account to correct for black body radiation and reflection of sunlight received at Earth from the dust ring, as described by Pearson [79]. These factors will lead to a reduced efficiency of the ring over the day side of the Earth, primarily due to thermal radiation from the dust particles, and an increased temperature over the night side of the Earth due to reflection of sunlight and the black body radiation from the ring. The influence that these effects have on the insolation reduction as a function of position on the Earth's surface are not directly accounted for, instead a weighting factor is applied to the final mass to calculate the grain mass needed to account for the greater insolation reduction to achieve the final 1.7% value once these effects are approximated.

Individually the dust particles have a small effect, however, due to the large number of particles used these two effects combined can reduce the effectiveness of the scheme. The temperature of a single dust grain will, assuming radiation as a black body and that the grain is in thermal equilibrium, be independent of grain radius so that;

$$\alpha_{gr} I_0 \pi R_{gr}^2 = \varepsilon \sigma 4 \pi R_{gr}^2 T_{gr}^4 \tag{5.6}$$

$$T_{gr}^4 = \frac{\alpha_{gr} I_0}{\varepsilon \sigma 4} \tag{5.7}$$

where α_{gr} is the absorptivity of the dust grain, assumed to be 0.55, ε is the thermal emissivity of the silicate grain of 0.9, σ is the Boltzmann constant, R_{gr} is the grain radius and T_{gr} is the temperature of the grain. This gives an equilibrium temperature in the region of 247K. During

eclipse periods the temperature of a dust grain will quickly fall below 100K and to a level where the thermal emission will be several orders of magnitude less than the sunlit case. In these periods a temperature of 50K is assumed, the minimum temperature reached. Once the temperature is known the key factor to determine the influence of black body radiation is the view factor of the Earth as seen from the grain. This can be calculated as [79];

$$F_{gr,E} = \frac{1}{2}\left(1 - \sqrt{1 - \left(\frac{R_E}{r_o}\right)^2}\right) \tag{5.8}$$

where R_E is the radius of the Earth and r_o is the distance between the grain and the centre of the Earth at a given point on the grains orbit, defined by the true anomaly θ_o, and can be found using;

$$r_o = \frac{a(1-e^2)}{1 + e\cos\theta_o} \tag{5.9}$$

Therefore, the flux received by the Earth due to thermal emission from a single particle on a given point of its orbit will be;

$$F_{IR} = Q_{bb} F_{gr,E} \alpha_{IR,E} \tag{5.10}$$

where $\alpha_{IR,E} = 0.9$ is the absorptivity of the Earth in the infra-red spectrum.

Naturally the solar insolation reflected by a grain is also dependent upon the view factor of Earth but also the fraction of the surface incident by sunlight that is also in view of the Earth. This is approximated using the following relation, where the key angles are shown in Fig. 5.11;

$$F_t = F_{in} F_{out} \tag{5.11}$$

$$= \left(1 - \frac{\phi}{\pi}\right)\left(1 - \frac{\gamma}{\pi}\right) \tag{5.12}$$

where the angles ϕ and γ can be found using simple geometry. Then, it follows that the flux received by the Earth in the visible spectrum for a single particle is;

$$F_{vis} = (1 - \alpha_{gr})\pi R_{gr}^2 I_0 F_t F_{gr,E} \alpha_{vis,E} \tag{5.13}$$

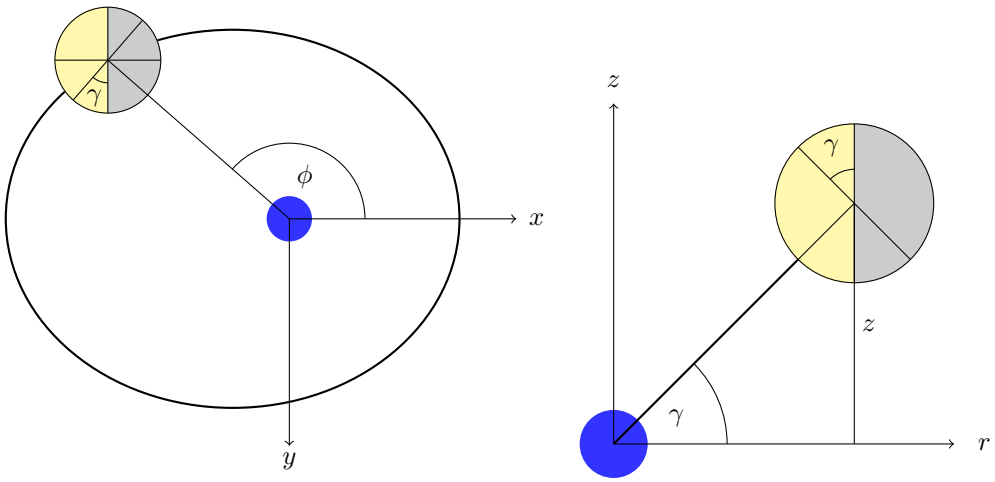

Figure 5.11: Geometry of the factor describing the fraction of the grains surface that is illuminated and with a view to Earth, for the in-plane factor (l) and the out of plane factor (r).

where $\alpha_{vis,E} = 0.6$ is the absorptivity of the Earth in the visible spectrum. For the case of solar reflection, eclipses are accounted for, such that when in eclipse a particle will not reflect any sunlight. Using the relationships described in Eq. (5.10) and (5.13) the influence that a grain will have over its entire orbit can be found, an example of which can be seen in Fig. 5.12. By using the relative densities of the particles in the different orbits as shown in Fig. A.8 the total negative effect of the thermal and visible radiation can be determined. It is thus found that an extra 40% of mass is required. This gives an estimate of the final mass of the ring of 1×10^{12} kg for the lowest mass case. This mass is still smaller than the value of 2.3×10^{12} kg found by Pearson in [79].

The amount of sunlight reflected onto the night side of the Earth can be estimated as well as the infra-red radiation received from the ring. Assuming no attenuation of thermal and visible radiation through the ring, an average power of 5×10^{14} W and 3×10^{14} W will be received by the night side of the Earth in the infra-red and visible spectrums respectively. Averaging over the cross-sectional area of the Earth gives an incident solar flux of $2.3\,\mathrm{W\,m^{-2}}$, a value that is several orders of magnitude greater than the $0.0017\,\mathrm{W\,m^{-2}}$ of sunlight reflected onto Earth by the Moon. The averaged flux in the infra-red regime is $4\,\mathrm{W\,m^{-2}}$. Naturally this will have a significant effect on astronomy on Earth.

The fact that the particles used by Pearson have a mean radius of $2.35\,\mu$m would suggest that the method used in this chapter should have a larger mass. This is not the case however, as the mass of a grain size distribution is dominated by larger dust grain sizes, which range up to $24.5\,\mu$m in Pearson, whereas in this paper the most pessimistic distribution, D3, only just reaches this upper limit. The orbital dynamics described in Appendix A show, as can be seen in Fig. A.3, that the smallest particle sizes used in [79] would quickly deorbit due to atmospheric drag. The

inclusion of the effects of solar radiation pressure and the J_2 effect and their use to find a heliotropic ring that will be long-lived will therefore lead to a reduction in the overall mass in comparison to Pearson if these effects were accounted for. In addition, this is essential for the success of the scheme described here as the length of time that such a scheme must be in place cannot be known and would depend on many factors related to tackling global warming.

5.5.2 Risk to spacecraft

There are other effects that this form of geoengineering scheme will have on the Earth environment, most notably there will be a danger to spacecraft. The ring will generally operate in an orbital region above LEO and below the high MEO orbits of satellite navigation constellations. However, spacecraft in equatorial geostationary transfer orbits (GTO) will pass through the ring and may require protective shielding for this passage. It can be estimated that a spacecraft 2m in radius, a size in between the upper stages of the Arianne and Soyuz launchers, will collide with a maximum of 4×10^{14} particles. This figure is dominated by a small portion of the ring which has a very high density relative to the surrounding regions, as seen in Fig. 5.6. As a comparison, it is expected that a spacecraft in LEO will receive a total flux of particles above $1\,\mu$m of $4 \times 10^6\,\mathrm{m}^{-2}\,\mathrm{yr}^{-1}$ [1]. To calculate the number of particles striking the spacecraft the number density of particles in an R-θ plot similar to Fig. 5.6 was calculated. Then a simple Hohmann transfer orbit from LEO (300km altitude) to GEO was assumed to determine the position of the spacecraft in the R-θ plot and the volume swept out in each section used to calculate the number of particles struck assuming a homogeneous density within the section. An example showing the number of particles struck per second by the spacecraft can be seen in Fig. 5.13. As would be expected there is a sharp peak at the high density region of the ring with other, much smaller maxima, corresponding to other regions where the total cross sectional area of the grains, as characterised by the attenuation coefficient, is higher than nominal, as can be observed in Fig. 5.6. The number of particles swept out can be compared to the total number of particles in the ring to give a mass of particles 7,800kg. This is a high mass that will impart a significant Δv on the spacecraft and make the transfer orbit unusable.

Since the ring has a small range of inclinations it will be simple for higher inclination GTOs to be used to avoid the high density regions to greatly reduce the shielding requirement. Also a dog-leg manoeuvre can be used to avoid the ring entirely for a small increase in the velocity required. Also a small fraction, <1%, of very fine grained material will de-orbit shortly after injection. These grains have radii of less than 6 microns. They will pass through the busiest region of LEO (<500 km) quickly because of their very high area-to-mass ratio and thus pose little danger to satellites

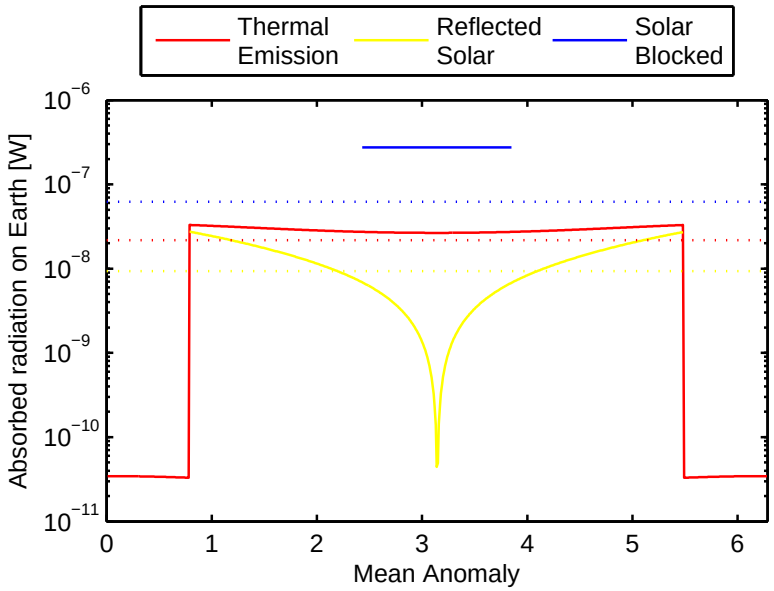

Figure 5.12: The flux contribution to Earth of a single particle due to black body radiation of the particle and reflection of sunlight. Also shown is the fraction of sunlight blocked during geoengineering and the mean $(\cdots)$ of all three factors. The orbit of the particle is $e = 0.055$, $\phi = 0$ and $i = 0°$.

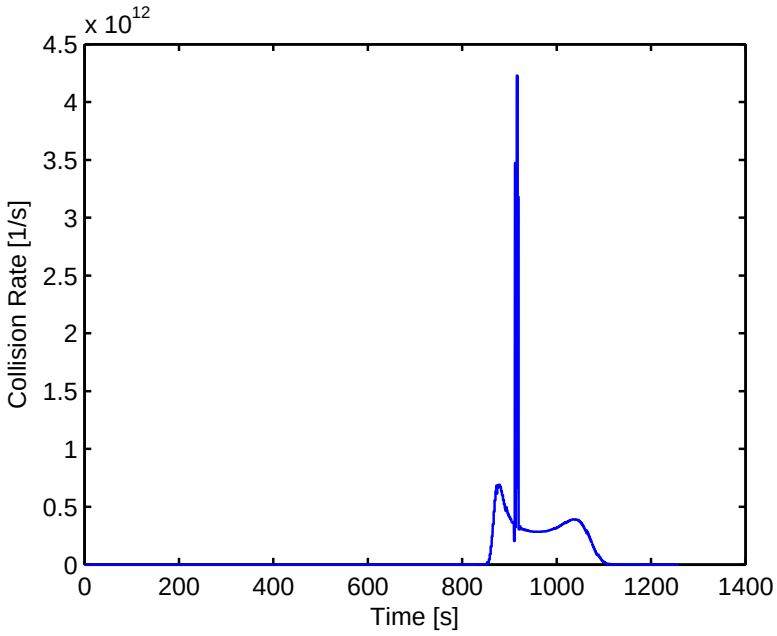

Figure 5.13: The impact rate of particles on a spacecraft or radius 2m travelling through the ring on a Hohmann orbit from LEO to GEO.

there. The long lived nature of the greatest part of the rings particles leads to the disadvantage that it cannot easily be removed. To reduce these risks the ring should be populated over many years to enable close monitoring of the effect on the climate.

5.5.3 Effect on communications

Another side effect that must be discussed is the attenuation of communication signals from geostationary satellites. It is important to consider this since the majority of telecommunication services utilise satellites in the geostationary ring. By taking the maximum extent of the Earth ring out of the equatorial plane, approximately 2,000 km, the maximum latitude where a telecommunication signal will be attenuated is determined to be 0.45°. This is a small range of latitudes that does not encompass any of the worlds major cities.

The approximate attenuation can be determined using the assumption that the interaction between the asteroid dust grains and the microwave telecommunications signal is the same as for sand grains, a phenomenon which has been studied by Hong *et al.* [44]. These results show that, at a frequency of 36.5GHz, the minimum extinction efficiency, Q_{ext}, unit is 0.1 for a size parameter of approximately 0.5. This size parameter equates to a grain radius of 650 μm, which is much greater than the grains required by the dust ring. Since the results from Hong *et al.* [44] show that below this size parameter the extinction efficiency reduces, an upper estimate of the attenuation can be made using $Q_{ext} = 0.1$. Since $Q_{ext} = \sigma_{ext}/\pi R_{gr}^2$, the extinction cross section, σ_{ext}, is estimated to be $1.3 \times 10^{-10}\,\mathrm{m}^2$. For the attenuation calculation the Beer-Lambert law is used with the assumption of a homogeneous grain distribution with the maximum path length through the ring used, to provide the upper estimate of the attenuation. This gives a maximum attenuation of 0.5, though the majority of paths through the ring will give an attenuation much less than this. For the regions covered by the ring this reduction in communications signal strength will be a concern, though it can be imagined that ground based communications links can be established from an unaffected region should this attenuation become problematic.

5.6 Conclusion

The concept of an Earth ring comprised of dust grains to offset global warming, first investigated by Pearson [79], has been investigated by considering novel families of heliotropic orbits. By the inclusion of the perturbations of solar radiation pressure and the J_2 effect the orbital dynamics of these high area-to-mass ratio dust grains has been analysed in the e-ϕ phase space using a

Hamiltonian approach. From this analysis stable, Sun-pointing orbits have been found that enable a ring to remain in equilibrium for long periods. Using these orbits as a location for geoengineering enables an estimate of the mass of dust required to offset a 2°C increase in temperature increase by a 1.7% reduction in solar insolation. The result of this estimate is a dust mass of 1×10^{12} kg, including a reduced efficiency due to particle emission and reflection, which is less than the dust cloud methods found in [79] and [98] but larger than the solid reflector method suggested in [69] and the refractor method seen in [5]. The use of dust rather than large reflective or refractive devices has the great advantage of reducing the complexity of the system since the dust cloud does not need to be launched from Earth or actively controlled, and also, if the dust is sourced from an asteroid, reduces greatly the launch costs of the system.

Chapter 6

Climate Model

The space based geoengineering schemes discussed in the previous chapters have the target of reducing the incoming solar insolation by 1.7%, a value defined by Govindasamy and Caldeira [39] to negate the majority of the adverse effects associated with a 2°C increase in global mean temperature. This value of 1.7% is defined by assuming a homogeneous reduction in insolation in the climate models used, however, the insolation reduction provided by the space based geoengineering methods described in this thesis do not have a uniform insolation reduction. Therefore it is necessary to appraise the reduction in temperature that these variations in insolation reduction over the Earth's surface provide. This shall be achieved by the use of a simple 1D climate model. The model generated by McGuffie and Henderson-Sellers [68] is summarised in Sec. 6.2 with Sec. 6.2.4 describing a modification used for the work described in this thesis.

6.1 Introduction to climate modelling

The climate system is complex, with many interactions and feedback loops, many of which are not yet fully understood. Therefore, the precise effects of the alteration of the incoming solar insolation cannot be conclusively determined. Furthermore, the complexities of implementing a full Global Circulation Model (GCM) prevent their use in this thesis. However, as discussed by McGuffie and Henderson-Sellers [68], the use of a simplified 1-dimensional climate model can reveal valuable insights into the climate that may not be evident in more complex models. The simple climate model described by McGuffie and Henderson-Sellers [68], that will be used later, will therefore suffice in giving a general validation of the methods of space based geoengineering described previously, with the ability to test the temperature reduction for different latitude regions as well as the global

mean reduction. This climate model was also used by Pearson et al. [79] to assess the temperature reduction provided by the Earth ring concept. In summary, the 1D model will be used in this thesis to test the temperature reduction over the Earth on a broad scale, using simplifications that do not require detailed knowledge of the climate system, but can none-the-less reveal the likely changes in the climate system.

6.2 One dimensional climate model

The climate model described by McGuffie and Henderson-Sellers [68] is summarised in Fig. 6.1. The model is a simple one dimensional energy balance model, with the Earth split into nine evenly spaced latitude bands, with only a single hemisphere considered due to symmetry. The following energy flow processes are included; the influx of solar energy, the energy transport between latitude zones and the output of energy from the Earth via black body radiation. The climate model assumes an equilibrium state, i.e. that any initial change in the in-going or out-going energy has led to a change in mean global temperature. Now, from conservation of energy, the solar flux input into a latitude band, $R_{s,i}$, must equal the sum of the radiated flux, $R_{\uparrow,i}$, and the heat transport towards the pole, F_i.

$$R_{s,i} = R_{\uparrow,i} + F_i \tag{6.1}$$

This model, as described by McGuffie and Henderson-Sellers [68], makes no assumptions on the future changes in carbon dioxide concentration in the atmosphere, changes in land use or, in general, any human activity. To account for global warming, this climate model will be modified, as described in Sec. 6.2.4. Before that is discussed the contributing factors to the climate model will first be introduced in more detail.

6.2.1 Solar Flux

The incoming flux is described by;

$$R_{s,i} = S_i \frac{I_0}{4}(1 - \alpha(T_i)) \tag{6.2}$$

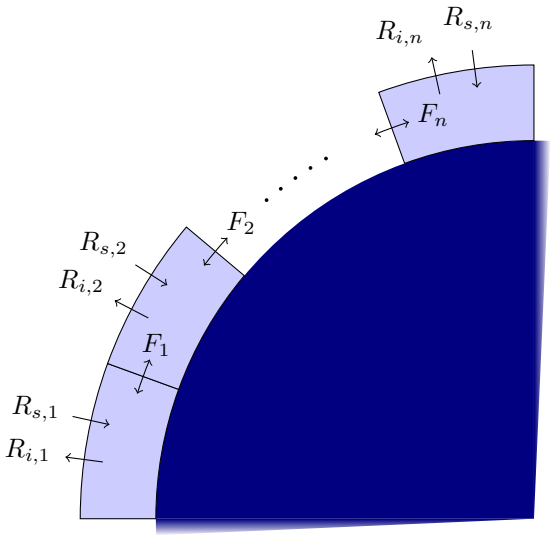

Figure 6.1: Diagram showing the interactions of the 1D climate model used to determine the temperature reduction of the different space based geoengineering schemes.

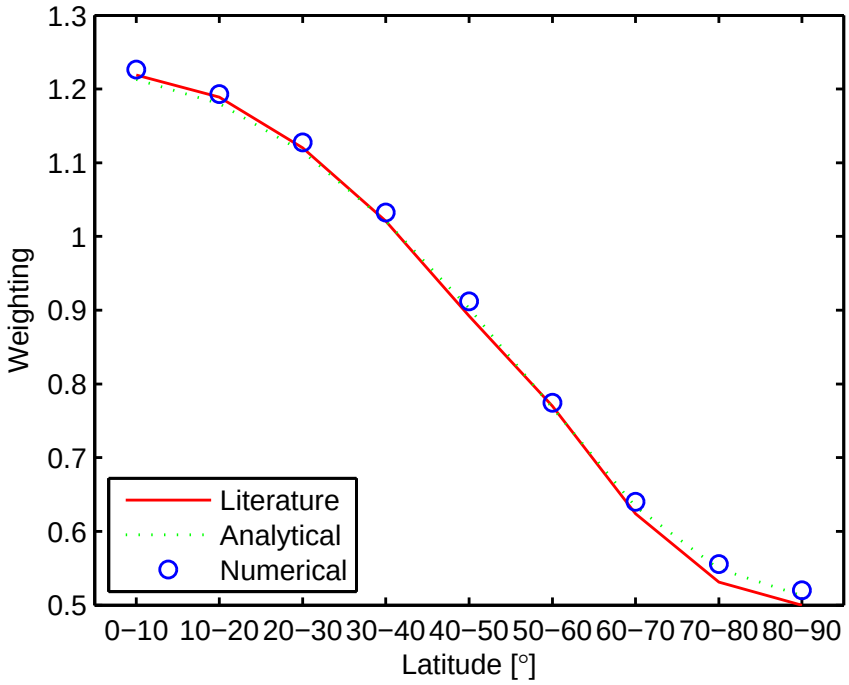

Figure 6.2: Weighting of the solar constant as a function of latitude averaged over a the period of a year. Three sets of values are plotted; a literature value from [68]; the weighting calculated analytically using Eq. (6.4)*; a numerical calculation where the solar constant calculated using the SRM is used.*

where S_i is the relative weight of the incoming flux for band i, I_0 is the solar constant and $\alpha(T_i)$ is the albedo. The albedo is a function of temperature, T_i, following the subsequent rule;

$$\alpha_i \equiv \alpha(T_i) \begin{cases} = 0.6 & T_i \leq T_c \\ = 0.3 & T_i > T_c \end{cases} \tag{6.3}$$

This describes the tipping point when a latitude band is assumed to be covered by a layer of ice, which has the greater albedo of 0.6, and the ice free regions. The critical temperature, T_c is assumed to be -10° [68].

The value for S_i is assumed to be averaged over an entire year. The values suggested in [68] can be seen in Fig. 6.2 as well as a numerical and analytical calculation of the weighting of the solar constant. The numerical values are derived from the solar radiation model, used to calculate the insolation reduction of the L_1 point clouds, without a cloud present. Rotation matrices are applied to determine the position on the Earth of the insolation pattern for evenly spaced values of time of year and day. The apparently high values for the weighting of the highest latitudes is due to the weighting being the annual average over the Earth. Therefore the highest latitudes will experience continual sunshine during some months, thus increasing their weighting.

The analytical, daily averaged, solar flux experienced as a function of latitude over the course of a year can be seen in Fig. 6.3. The daily averaged flux, Q_{day}, for a given latitude, ϕ, can be found analytically and is as follows [3];

$$Q_{day} = \frac{I_0}{\pi} \frac{R_0^2}{R_E^2} \left[h_0 \sin(\phi) \sin(\delta) + \cos(\phi) \cos(\delta) \sin(h_0) \right] \tag{6.4}$$

where I_0 is the mean flux, R_E is the distance between the Earth and Sun at a given date, R_0 is the mean distance between the Earth and Sun, δ is the declination at a given point in the Earth's orbit and h_0 is the length of day for a given latitude in units of radians. The declination can be found using the following relationship [3];

$$\sin(\delta) = \sin(\varepsilon) \sin(\theta - \omega) \tag{6.5}$$

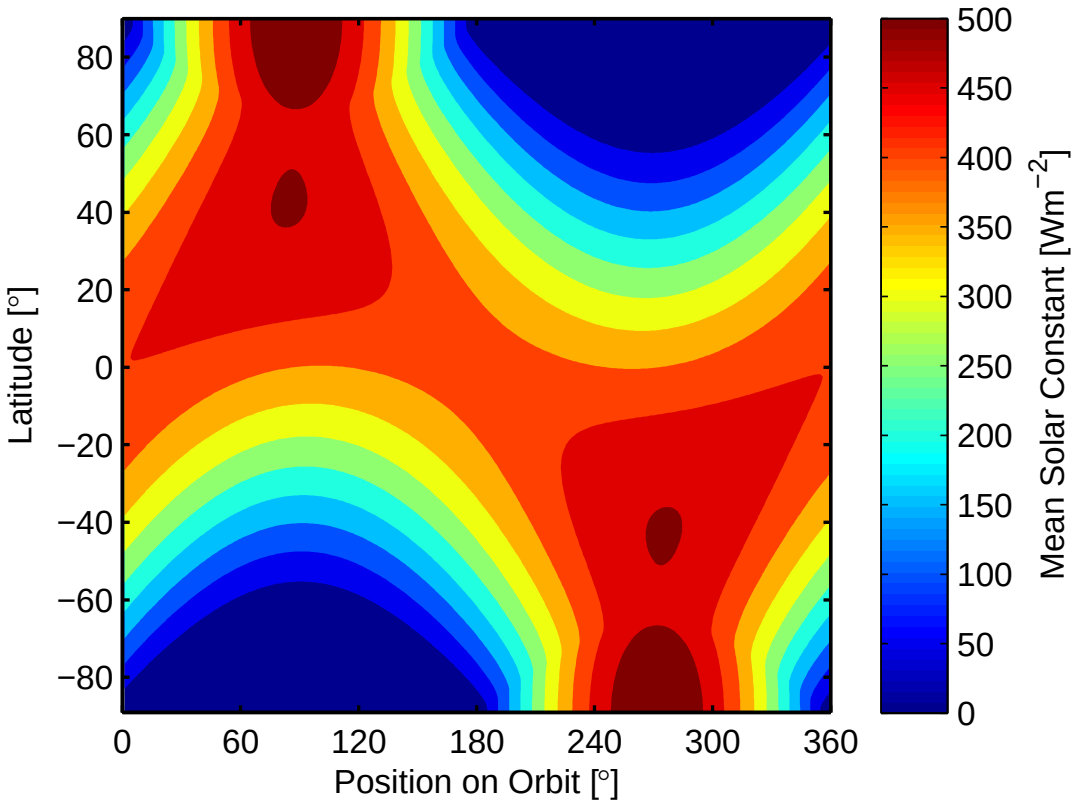

Figure 6.3: Solar constant averaged for each latitude band over the period of a year calculated analytically using Eq. (6.4).

where ε is the inclination of the Earth's rotation axis, θ is the position angle of the Earth within its orbit and ω is a correctional factor to set $\theta = 0$ to the vernal equinox. The value of h_0 is found using the following relation;

$$h_0 = \begin{cases} 0 & \tan(\phi)\tan(\delta) < -1 \\ \pi & \tan(\phi)\tan(\delta) > 1 \\ \arccos(-\tan(\phi)\tan(\delta)) & else \end{cases} \tag{6.6}$$

to capture all geometries.

6.2.2 Heat Transport

The heat transport is considered to occur between two regions with unequal temperatures, with a flow from the warmer regions to the cooler regions, so in general a polewards flow of energy is

Coefficient	Value
A	$204\,\mathrm{W\,m^{-2}}$
B	$2.17\,\mathrm{W\,m^{-2}\,K}$
K	$3.8\,\mathrm{W\,m^{-2}\,K}$

Table 6.1: Coefficients required in the one dimensional climate model as described in [68].

observed in the model. The flow is dependent upon the temperature difference between the latitude band and the mean global temperature, $\bar{T}$, as follows;

$$F_i = K(T_i - \bar{T}) \tag{6.7}$$

where K is the heat transfer coefficient and T_i is the temperature of the latitude band.

6.2.3 Thermal Emission

The thermal emission out of a latitude band is described by the following relation;

$$R_{\uparrow,i} = A + BT_i \tag{6.8}$$

where A and B are empirical coefficients describing the weighting of the thermal emission, as defined in Table 6.1. They account for the average absorption, reflection and re-emission contributions of CO_2, water vapor and cloud cover.

6.2.4 Climate warming

The climate model must be altered to account for warming of the Earth due to climate change. This is most easily done by the inclusion of a radiative forcing term, I_{RF}, in the climate model. Radiative forcing, with units of $\mathrm{W\,m^{-2}}$, is a net change in the global energy balance between ingoing and outgoing radiation, i.e. a positive value for I_{RF} represents a higher level of incoming radiation than outgoing. A positive radiative forcing will lead to a warming of the Earth, until a new equilibrium state is reached, in which case the radiative forcing will then be zero. Of course

this assumes that an equilibrium state is reached and the Earth does not enter a state of runaway warming.

Radiative forcing is a generally accepted measure of the contributions that different components, not directly related to the radiation balance, have on climate change, since the link between a net change in the solar energy balance and a change in temperature is simple to understand. The estimated radiative forcing of different climate factors can be seen in Fig. 1.1, Sec. 1.1, where it is observed that not all factors have a positive radiative forcing and also that there is large variability in the predicted forcing of each factor. For that reason a range of radiative forcing values will be applied in this climate model to achieve a range of temperature changes for the different space-based geoengineering scenarios. The radiative forcing values, for a doubling of the concentration of CO_2 in the atmosphere, that will be used are $3.3\,\mathrm{W\,m^{-2}}$, $3.7\,\mathrm{W\,m^{-2}}$ [46] and $4.17\,\mathrm{W\,m^{-2}}$ [39].

Due to the nature of the radiative forcing term it can be implemented in the climate model in one of two ways; firstly by adding the radiative forcing term to the incoming radiation, as in Eq. (6.9), and secondly by reducing the outgoing thermal radiation by the radiative forcing factor, as in Eq. (6.10).

$$R_{s,i} = S_i \left(\frac{I_0}{4} + I_{RF} \right) (1 - \alpha(T_i)) \tag{6.9}$$

$$R_{\uparrow,i} = A + BT_i + I_{RF} \tag{6.10}$$

It is expected that the reduction of the thermal emission factor will prove to be the most accurate method for describing the temperature change. This is because an increase in the concentration of CO_2 in the atmosphere will increase the opacity in the infrared regime, thus decreasing the outgoing radiation. Therefore, applying the radiative forcing parameter in this way is closer in principle to the physical reality. The effects that applying the radiative forcing in the two ways mentioned will be discussed in Sec. 6.3.1.

6.2.5 Summary

Combining the terms for the solar input, thermal re-radiation and heat transport allows the equilibrium temperature of a latitude band to be calculated. This can be seen in the following relationship;

$$T_i = \frac{S_i(I_0/4)(1 - \alpha(T_i)) + K\bar{T} - A}{K + B} \tag{6.11}$$

Since the model requires the mean temperature of the Earth, which is dependent upon the temperatures of the different latitude bands, the model must be solved iteratively. The method described by [68] uses 50 iterations to reach a stable result. An initial temperature is assumed for each latitude band, from which the albedo can be determined and the mean temperature calculated. The latitude dependent temperature is then calculated using Eq. 6.11 using the previously determined values for global mean temperature and latitude dependent albedo. These steps are then repeated.

6.3 Model testing

6.3.1 Climate sensitivity and radiative forcing

One of the key values quoted in climate modelling is that of climate sensitivity, λ, and is defined as the temperature increase likely due to a doubling of CO_2;

$$\Delta T = \lambda I_{RF} \tag{6.12}$$

The temperature increase suggested by the IPCC to be caused by a doubling of CO_2 is in the range of 2-4.5°C [46], with a best guess of 3°C. It is also suggested that a temperature increase of less than 1.5°C is "very unlikely", which in quantitative terms means that a temperature of less than 1.5°C has a 10% probability of occurring [46]. The statements of probability used in the IPCC report are a combination of statistical results and expert judgement. Using Eq. 6.12 and a radiative forcing of $3.7\,\mathrm{W\,m^{-2}}$ a bound can be placed on the expected climate sensitivity using the temperature values cited above. The climate sensitivity is therefore $\lambda = 0.8^{+0.42}_{-0.26}\mathrm{K\,m^2\,W^{-1}}$.

The temperature change from a doubling of CO_2 found with the one-dimensional climate model used here can be seen in Fig. 6.4. In this test no reduction in insolation due to the space-based geoengineering method was assumed and the mean increase in global temperature was calculated using the three values of radiative forcing described in Sec. 6.2.4. The mean value corresponds to a radiative forcing of $3.7\,\mathrm{W\,m^{-2}}$ whilst the uncertainty corresponds to the range found when using the highest and lowest values. The results show a mean global temperature increase of $\Delta T_s = 1.18^{+0.15}_{-0.13}$ and $\Delta T_\uparrow = 1.71^{+0.22}_{-0.18}$ for the application of the radiative forcing to the incoming and outgoing radiation respectively. Both of these values fall short of the range predicted by the IPCC. However, two caveats must be stated. Firstly the temperature increase predicted by Govindasamy [39], which is the basis of the insolation reduction target in this thesis, for a doubling of CO_2 is 1.75K (for a

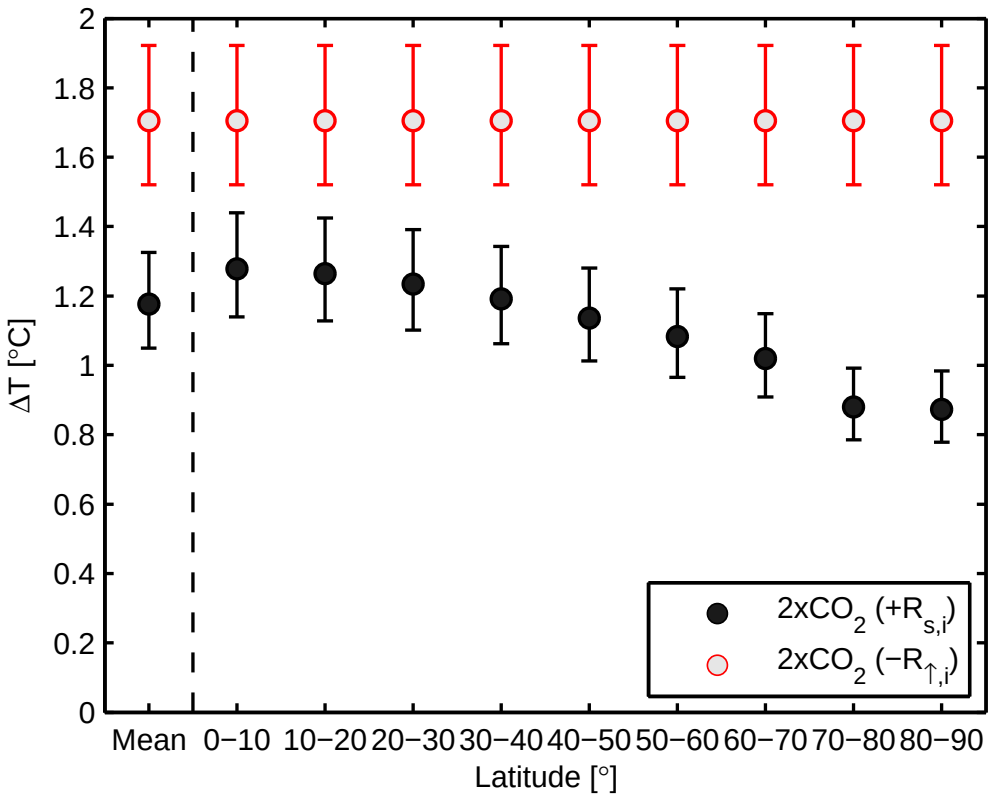

Figure 6.4: The response of the one-dimensional climate model to a doubling of CO_2 for three values of radiative forcing and two methods of application, an increase in the incoming radiation ($R_{s,i}$) and a decrease in the outgoing thermal radiation ($R_{\uparrow,i}$).

radiative forcing of $4.17\,\mathrm{W\,m^{-2}}$), which fits to the range of the latter result for the application of the radiative forcing to the outgoing radiation. Secondly, it is suggested that a doubling of CO_2 will directly only lead to an increase of 1°C. The remaining temperature increase is due to numerous feedback factors such as water vapor, ice-albedo and clouds. Given that only the ice-albedo feedback is directly included in any detail in this model, the other two feedbacks are considered in the factors A and B, then this result may also be viable.

The final remarks on the two radiative forcing methods is regarding the temperature change patterns over the range of latitude bands. This result can also be seen in Fig. 6.4. The temperature increase is flat over the latitude bands for when the outgoing thermal radiation is reduced whereas for the second method the temperature increase tails off significantly for high latitudes. This is opposite to what is calculated using high fidelity GCMs where the high latitude regions are expected to show a much higher sensitivity to global warming. The results calculated by Govindasamy and Caldeira [39] shows a temperature increase of 4°C at the poles in comparison to only 1-2°C in the equatorial regions.

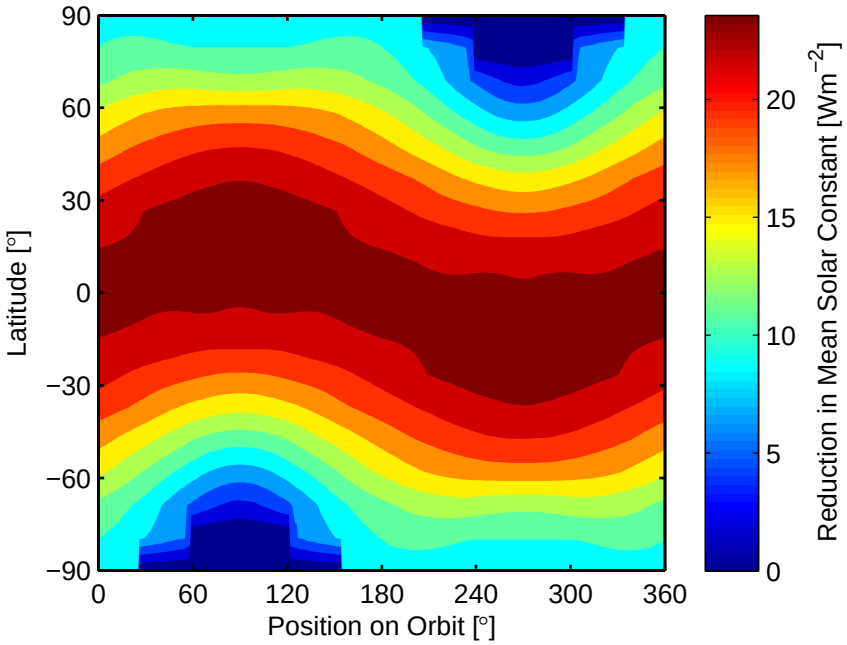

Figure 6.5: Reduction in daily averaged solar constant averaged over the course of a year for the displaced equilibrium point cloud.

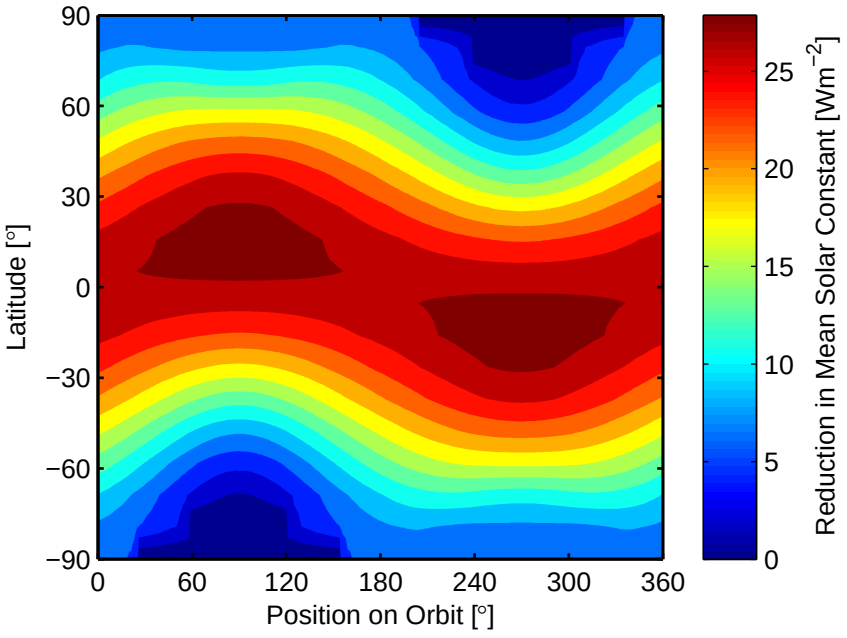

Figure 6.6: Reduction in daily averaged solar constant averaged over the course of a year for the L_1 point cloud.

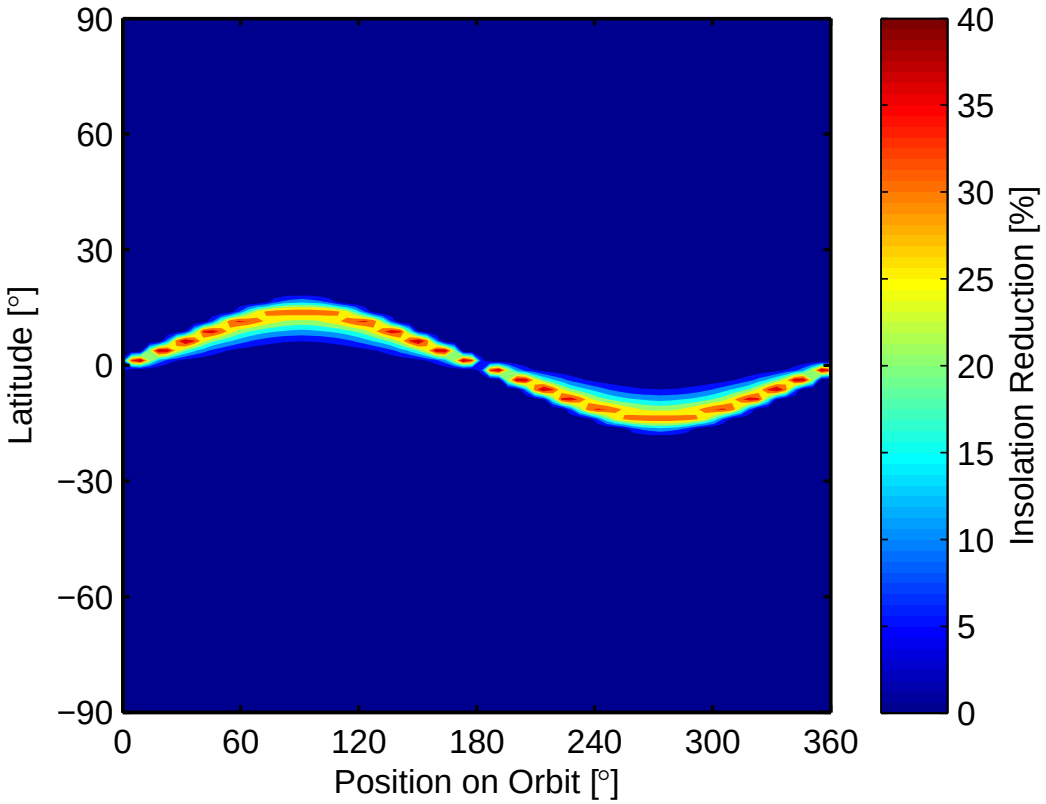

Figure 6.7: Insolation reduction as a function of latitude and time of year for the Earth ring concept.

6.4 Insolation Map

To calculate the temperature change due to the reduction in insolation associated with the space-based geoengineering scenario, the yearly averaged reduction for the nine latitude bands must be found. The daily averaged insolation over all latitudes for the period of a year can be seen in Fig. 6.5 and Fig. 6.6 for the case of the static cloud, released at the displaced equilibrium position and the classical L_1 points respectively. From this data the yearly average can be found and will be discussed later. The insolation reduction plots for the gravitationally anchored dust cloud at L_1 and the ejected dust clouds are similar to those for the static dust cloud and will not be shown. An example of the insolation reduction for the case of the Earth ring, discussed in Sec. 5.4, is shown in Fig. 6.7. Whilst the insolation reduction for the static cloud case is spread over the majority of latitudes, the insolation reduction for the Earth ring is concentrated in specific latitude regions. This would be expected when considering the specifics of the Earth ring concept, as discussed in Chapter 5. The static cloud case, in general, shows a much greater spread over the Earth due to the greater distance between the Earth and the dust cloud. Over this larger distance, the relatively

small difference in the direction of photons from different regions on the Sun's surface, up to 0.005°, will lead to large differences in final position. In contrast, the Earth ring can only expect a difference of a few kilometres between photons when reaching the surface of the Earth. This, in combination with the often narrow aspect angle of the ring as seen from the Sun, leads to the high level of insolation reduction seen for the latitude bands in Fig. 6.7.

The yearly averaged weighting of the solar insolation as a function of latitude can be seen for the case of the static cloud in Fig. 6.8. The cloud released from the displaced equilibrium position shows a relatively flat weighting, close to the required 1.7%. It appears that the average is below 1.7%, since the insolation reduction at the higher latitudes is slightly less than 1.7%. This is not the case, however, as the lower latitude bands, which contribute a much larger value for the incoming solar flux due to the larger surface area and hence have a stronger weighting, are slightly above 1.7%. The cloud released at the classical L_1 position shows a larger insolation reduction in the equatorial regions whilst it can be seen to decrease to less than 1% for the polar regions. From this it can be considered that the displaced equilibrium position is more likely to be beneficial to the reduction of climate change, since the polar regions are more sensitive to increased greenhouse gas (GHG) concentrations, and hence a larger insolation reduction in these regions will be beneficial.

The results for the gravitationally anchored dust cloud, discussed in Sec. 3.3.5, can be seen in Fig. 6.9. All the plots show a relatively flat insolation reduction over the latitude bands, with the maximum insolation reductions that can be achieved with the anchored cloud method for the asteroid Ganymed being much greater than the 1.7% required. The maximum insolation reductions for the asteroid Eros, the second largest NEO, fall below the 1.7% requirement. These plots also show a relatively flat distribution over the latitude bands. As for the static cloud released at the displaced equilibrium position, the flat distribution will be beneficial for the purposes of geoengineering.

The insolation reduction distribution for the case of the cloud ejected from the vicinity of the L_1 point with an initial velocity can be seen in Fig. 6.10. The four distributions correspond to the mass-optimum clouds ejected from the displaced equilibrium position and the classical L_1 point, where the angle of ejection is optimised to; a) maximise the average lifetime of the ejected material, and, b) to maximise the spread of the material before leaving the region where an insolation reduction can be affected. Some results have been smoothed by applying a polynomial fit to the data, due to the uneven insolation reduction calculated when using a low number of Earth and Sun nodes in the solar radiation model described in the previous chapters. The distribution of the insolation reduction for the displaced equilibrium position, for the ejection angle optimised to maximise the lifetime of the particles, shows a relatively homogeneous insolation reduction. This is similar to the results for the static cloud and the gravitationally anchored cloud released from the

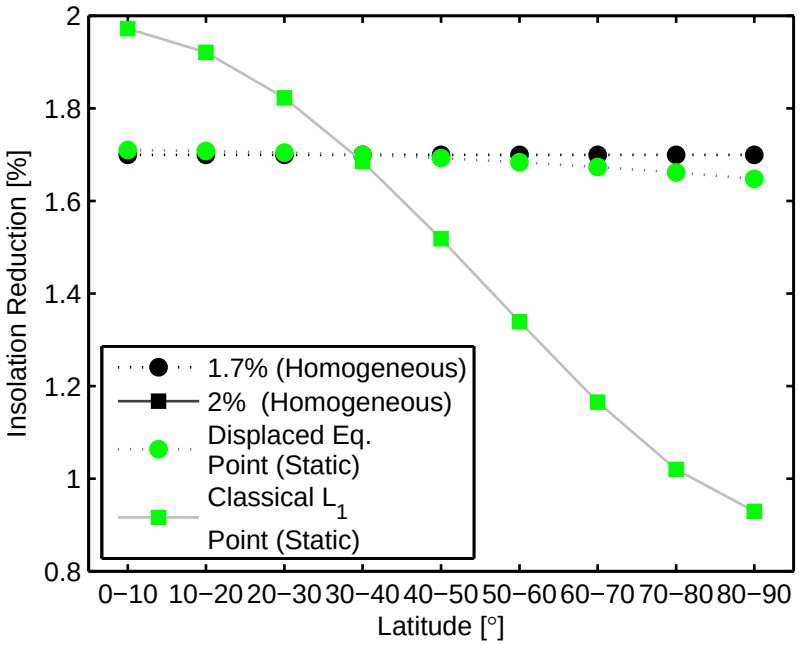

Figure 6.8: Insolation reduction averaged over an entire year for different latitude bands for the static cloud concept.

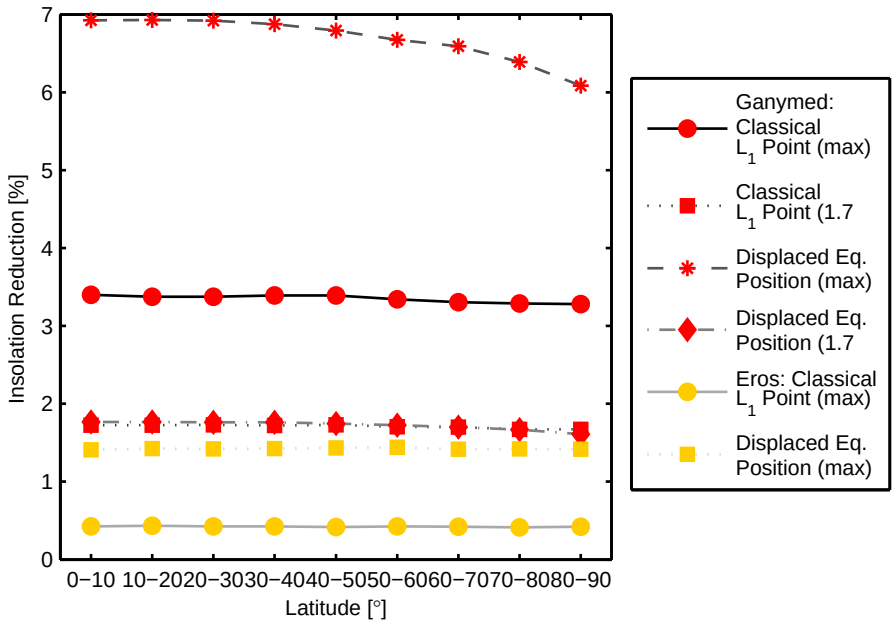

Figure 6.9: Insolation reduction averaged over an entire year for different latitude bands for the gravitationally anchored dust cloud.

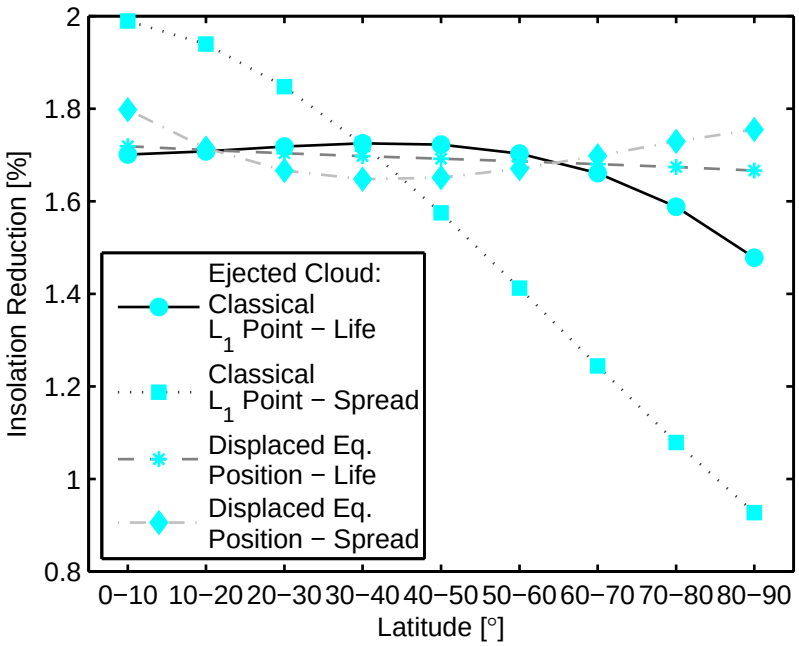

Figure 6.10: Insolation reduction averaged over an entire year for different latitude bands for the case of a cloud ejected with an initial velocity distribution.

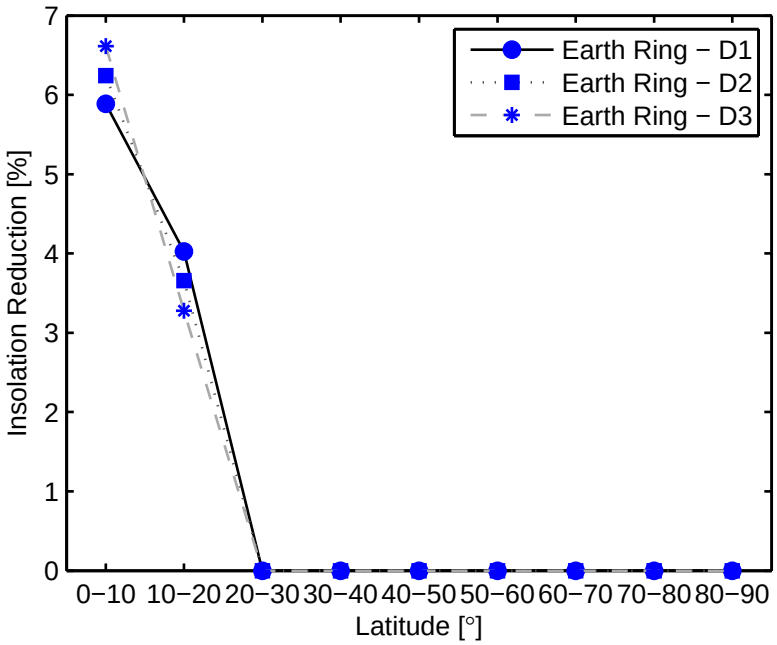

Figure 6.11: Insolation reduction averaged over an entire year for different latitude bands for the Earth ring.

same position. For the optimisation to maximise the spread of the particles the reduction is less homogeneous, with an apparent minima of 1.65% in the region of 20-40° latitude, with high values in the equatorial and polar regions. The cloud ejected at the classical L_1 point is less homogeneously distributed still, with the optimised lifetime case showing a distinct reduction towards the polar regions and the spread optimisation decreasing from 2% at the equator to 0.9% at the poles.

The three distributions that show the insolation reduction for the Earth ring can be seen in Fig. 6.11. Each of the data sets correspond to a different dust grain distribution within the size range of 1-50 μm, the precise details of which are described in Sec. 5.2.2. All three distributions show a strong peak insolation reduction in the equatorial latitude bands before quickly reducing to zero for higher latitudes. The D3 distribution, which has the smallest peak insolation reduction, therefore has a greater insolation reduction in the lower latitude regions. This small difference is unlikely to have a strong effect on the calculation of the mean global temperature change.

6.5 Results

Using the solar weightings shown in the previous section, the change in temperature over the range of latitude bands can be calculated using the 1-dimensional climate model discussed in this chapter. A summary of the mean temperature reduction, accounting for the doubling of CO_2, for all the cases considered can be seen in Fig. 6.12. The radiative forcing applied leads to a mean reduction in temperature of 1.7°C. All cases lead to a net reduction in the global mean temperature, in comparison to the radiative forcing applied, with the exception of the gravitationally bound dust cloud method for the asteroid Eros. This, combined with the engineering challenges involved with capturing such an asteroid, makes the use of this asteroid for the purposes of geoengineering impractical.

As would be expected, the reduction in mean temperature is greatest for the dust cloud gravitationally anchored by the asteroid Ganymed. It can be seen that the global mean temperature has a net reduction of 5.7°C and 2.0°C when the asteroid is positioned at the displaced equilibrium position and the classical L_1 point respectively. These results are expected as the insolation reduction is greater than the 1.7% target, which is particularly the case for the displaced equilibrium position. The absolute temperature reduction for the case of the asteroid Ganymed positioned at the classical L_1 point is in the region of 3.7°C. Given that the asteroid will most likely be positined at the classical L_1 point, due to the large engineering challenge of maintaining the asteroid at the displaced position (discussed in Sec. 3.3.1), this method gives little margin should attempts to control climate change be unsuccessful and the temperature reduction target

increase. In this scenario, large dust grains can be used to increase the size of the cloud that can be gravitationally anchored, as discussed in Sec. 3.3.4, giving an insolation reduction, and consequently the temperature decrease also, close to that of the equilibrium position. This method, however, has the disadvantage of increasing the required mass of the dust cloud to several times the mass of the asteroid.

The results for all other cases fall below a net zero temperature reduction. The Earth ring method appears to show a greater net temperature reduction of -0.5°C, in comparison to the other methods, which are in the region of -0.15°C to -0.4°C. This is a surprising result, since the mean insolation reduction is 1.7%.

The temperature reduction, for each latitude band considered, can be seen in Fig. 6.13, for the static cloud and a homogeneous insolation reduction. The error bars show the range in temperature found when using the three different values of radiative forcing for a doubling of CO_2 described previously. The results show a decrease in temperature of approximately -0.4°C for the 0-10° latitude band, which increases with latitude, reaching zero in the 40-50° region. The values for the polar latitudes increase to approximately 0.4°C. Due to the greater weighting of the insolation reduction towards the equatorial region for the static cloud released at the classical L_1 point, the temperature reduction is greatest here, with a reduction smaller than the equilibrium position cloud in the polar regions. The results for the equilibrium position cloud are broadly in keeping with the homogeneous insolationn reduction of 1.7%. This would be expected when considering the similar distribution of the insolation reduction as seen in Fig. 6.8 and the flat appearance of the result of the SRM for this case, Fig. 2.17.

The results for the gravitationally anchored dust cloud, seen in Fig. 6.14, show the wide range of temperature reductions for the different cases. The general shape of the results are similar to the static and homogenous cases, with the greatest net change being in the equatorial region, before reducing towards the poles. This is the same for all cases, though the effect is scaled with respect to the overall temperature reduction. The results calculated by [39] show that the net temperature change for a homogeneous reduction, to compensate for a doubling of CO_2, is relatively flat, with a slightly smaller temperature reduction towards the poles. This is, in general, in keeping with the results presented here thus far, though the precise difference in temperature between the regions is not evident in [39].

The results for the ejected cloud shows a similar distribution of the temperature reduction to that of the static cloud, as would be expected considering the similarities in the insolation reduction distribution. The most significant deviation is the case of the cloud ejected from the L_1 point with the spread of the ejected cloud optimised. This case shows a greater reduction in

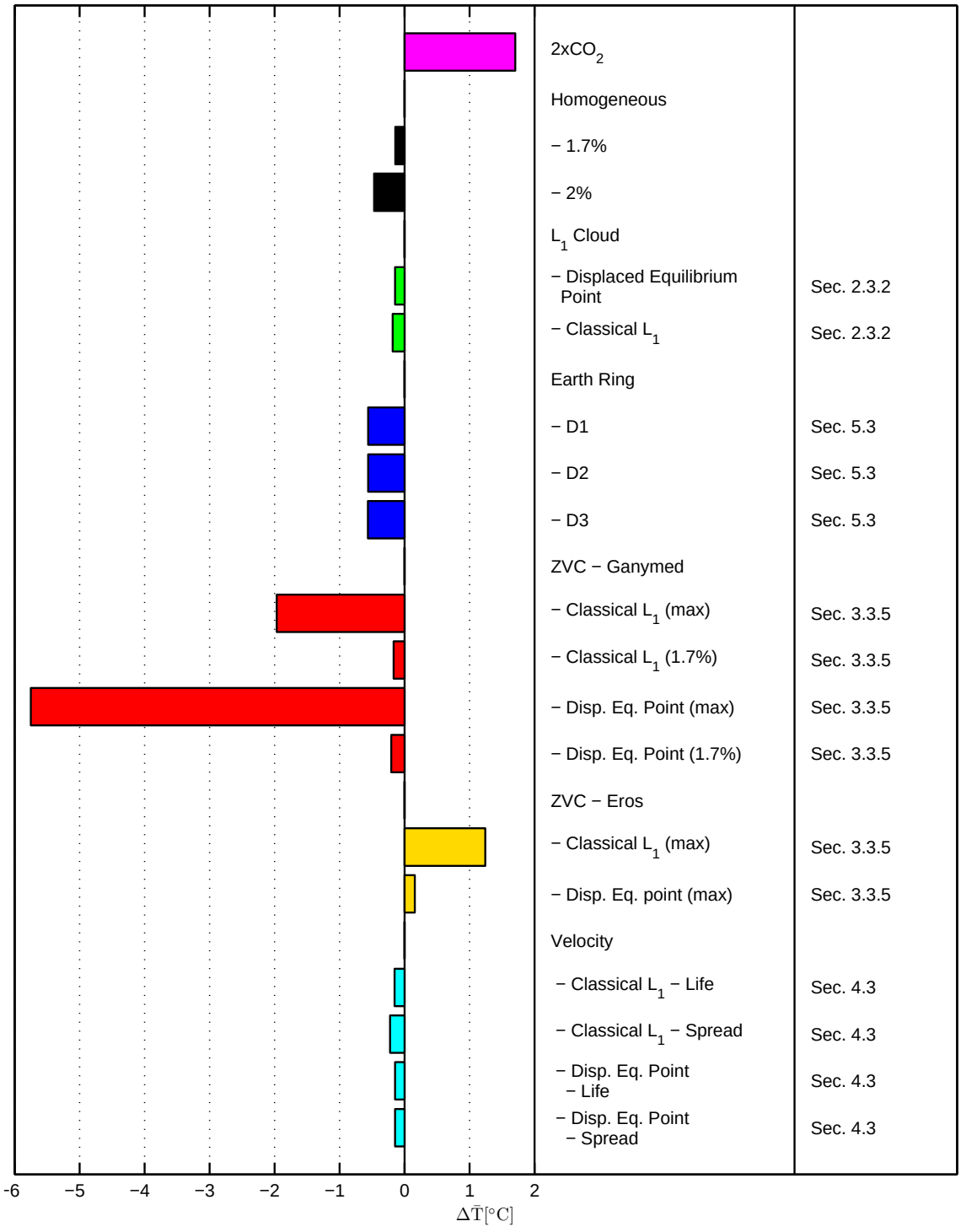

Figure 6.12: Mean temperature change due to a doubling of CO_2 with different space-based geoengineering scenarios applied.

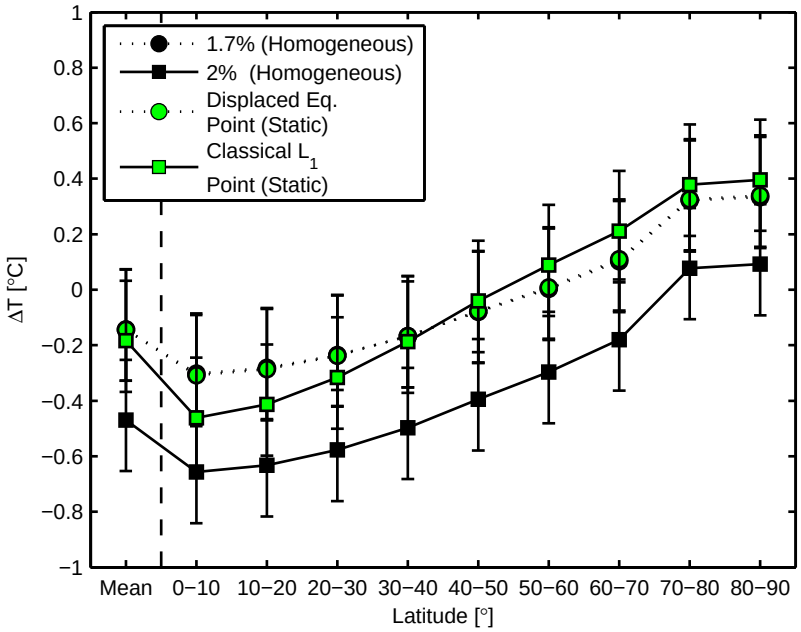

Figure 6.13: Temperature reduction averaged over an entire year for different latitude bands for the static cloud concept.

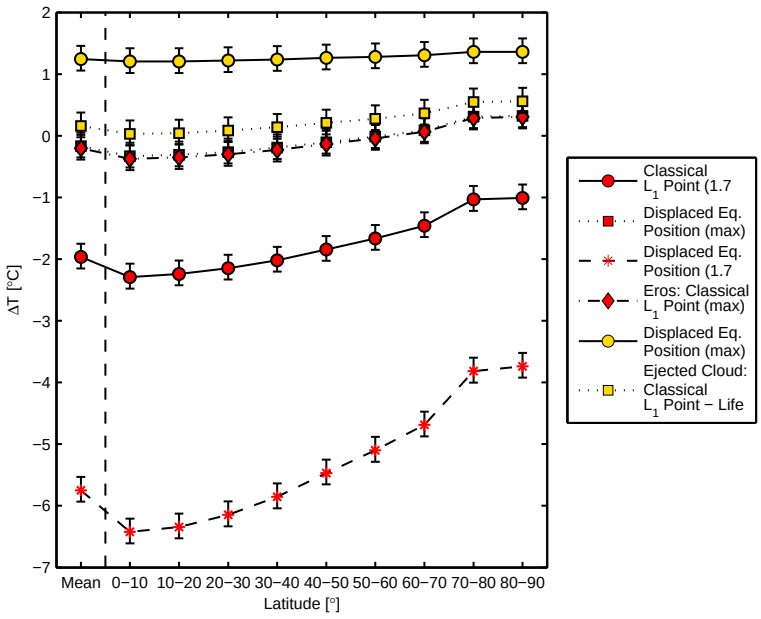

Figure 6.14: Temperature reduction averaged over an entire year for different latitude bands for the gravitationally anchored dust cloud.

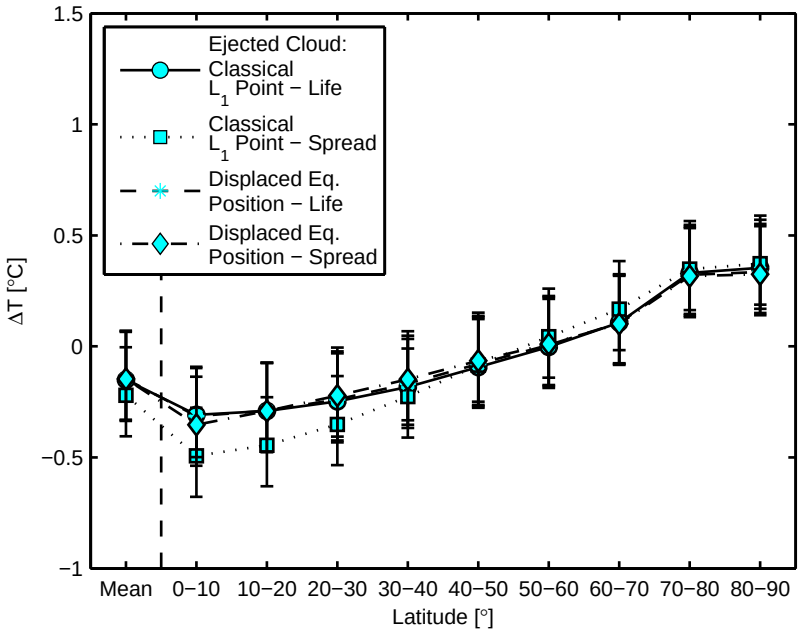

Figure 6.15: Temperature reduction averaged over an entire year for different latitude bands for the case of a cloud ejected with an initial velocity distribution.

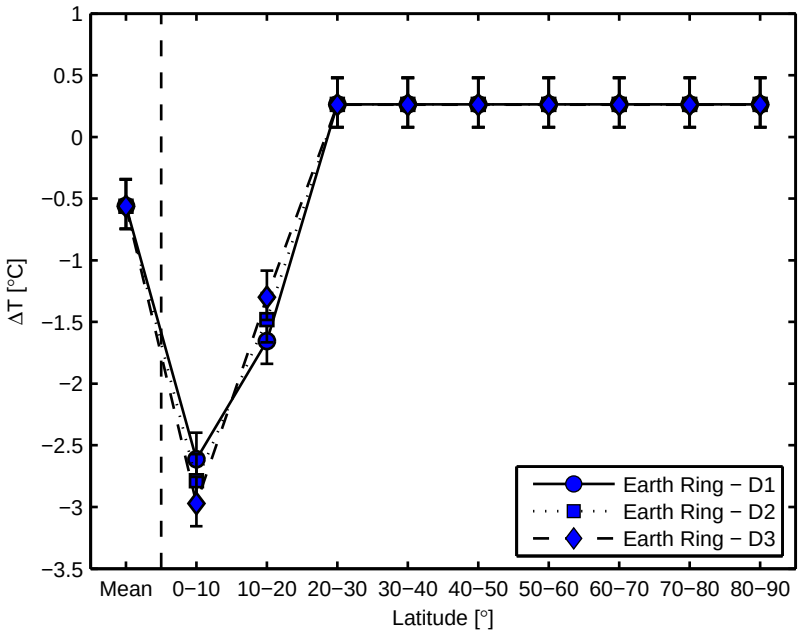

Figure 6.16: Temperature reduction averaged over an entire year for different latitude bands for the Earth ring.

temperature near the equator, with a lower reduction in temperature near the poles. The mean temperature reduction is greater than the other three cases, though not by a greatly significant margin.

The temperature reduction for the Earth ring in the mid and high latitude regions, seen in Fig. 6.16, shows a reduction in temperature, in comparison to the doubled CO_2 case. This is despite the lack of a reduction in the incoming solar insolation in these bands. This reduction in temperature is due to the decreased heat transfer towards the poles, due to the large temperature reduction in the equatorial region. The temperature reduction is similar for the three dust grain distributions, with a maximum difference of less than 0.5°C. The absolute temperature reduction in the equatorial regions is nearly 5°C. This is a large reduction that will, it is assumed, have a strong impact on the local climate that will be difficult to predict. Considering the large reduction in insolation apparent in the equatorial region, Fig. 6.7, the further potential for a temperature reduction using the Earth ring method is limited, for multiple reasons. From purely engineering considerations, the efficiency of the Earth ring will decrease quickly with the insolation reduction required, due to the exponential component of the Beer-Lambert law used to calculate the insolation reduction. This will lead to a far greater mass being used for the ring, which will subsequently increase the number of asteroids required, increasing the complexity further. Going beyond simple engineering considerations, the ethical and political aspects of significant reductions in insolation over certain portions of Earth will meet strong opposition and could have strong physical negative feedback effects, reducing the efficiency of the method further. For example, the potential for solar power will be greatly reduced in the equatorial and tropical regions, likely leading to a slower decrease in the anthropogenic GHG emissions. Also, in the regions where there will be a strong insolation reduction, there are significant emissions of black carbon, which has a large effect on the climate, second only to CO_2, due to wood, biomass and coal burning [54]. If a strong insolation reduction is experienced in these regions then it would be expected that, at least in the short term, there will be an increase in the emissions of black carbon, leading to a negative feedback effect and reducing the overall efficiency of the Earth ring.

6.6 Conclusion

In this chapter a simple one-dimensional climate model has been introduced that calculates the yearly averaged, steady-state temperature reduction as a function of latitude. Using this, the initially static dust cloud, gravitationally anchored dust cloud, the ejected dust cloud and Earth ring methods of space-based geoengineering, described in the previous chapters, have been analysed to determine the mean temperature reduction over the Earth. It is found that all cases, except

for the dust cloud gravitationally anchored by the asteroid Eros, provide a net reduction in mean global temperature when accounting for the radiative forcing due to a doubling of CO_2. The largest temperature reduction is found for the dust cloud gravitationally anchored by the asteroid Ganymed, the largest near Earth object, when positioned at the displaced equilibrium position. The net temperature reduction for this case is 5.75°, which could potentially lead to an ice age if no global warming is included. The maximum potential of the remainder of the gravitationally anchored dust clouds analysed is less than this value, to the extent that, should an insolation reduction greater than the 1.7% be required to offset a greater increase in global temperature, the gravitationally anchored dust cloud may not be a practicable solution. Of the dust cloud methods that use a 1.7% reduction in insolation as their target, the Earth ring concept leads to the greatest reduction in temperature, with a net temperature change of -0.5°. The remainder of the dust clouds methods show a net change in temperature of -0.15° to -0.4° when the 1.7° increase due to the doubling of CO_2 is accounted for.

Chapter 7

Engineering a Dust Dloud

This chapter shall discuss the engineering feasibility of the space-based geoengineering concepts discussed in this thesis, concluding on the most likely method of implementation. A technological roadmap for the development of the key technologies required for the most near-term space-based geoengineering scheme will be discussed.

To assess this, the feasibility of capturing a sufficient quantity of dust material shall first be analysed, to test the assumption that the material can be found in the population of near-Earth asteroids. The possibility of using lunar material for the dust cloud shall also be included. The analysis of the feasibility of asteroid capture (Sec. 7.1.1) was undertaken by Dr. Joan-Pau Sanchez [85, 86]. Subsequently, several considerations regarding the use of asteroid material shall be discussed, such as the impact risk and regolith grain size, to aid the discussion on the most feasible method. The use of lunar material for the dust cloud will also be discussed with a discussion on the amount of material required to generate the dust cloud and the feasibility of transport to L_1.

The final engineering dicsussion will focus on the possible methods through which the cloud can be generated. This will include a summary of work undertaken on solar sublimationb by Kahle et al. [50] and is found in Sec. 7.3.1. The cloud generation techniques will be compared to the assumptions on the initial conditions of the dust clouds used in the previous chapters and a comparison to the use of solar reflectors will also be made before a technological development roadmap will be presented.

7.1 Asteroid Material

So far in this thesis the only consideration of the quantity of asteroid material available for use in the dust cloud methods for space-based geoengineering is found in Sec. 3.3.1, where the impulse required to capture the most massive near-Earth objects is calculated. The masses considered are above a value of 1×10^{13} kg, orders of magnitude greater than the amount of mass required to sustain an unstable cloud in the vicinity of the first Lagrange point. Therefore, more consideration must be given to the capture of asteroids with lower mass. This shall be discussed in the following section, as well as a general discussion on the use of asteroid material.

7.1.1 Asteroid capture

The mass of asteroid material required for the space-based geoengineering methods ranges from $10^{10}\,\mathrm{kg\,yr^{-1}}$ for the static and ejected L_1 clouds to 2×10^{12} kg for the Earth ring concept, with the gravitationally anchored dust cloud requiring in the region of $9 \times 10^{11}\,\mathrm{kg\,yr^{-1}}$ of dust material, not including the mass of the anchoring asteroid. All of these methods require significant amounts of material to achieve a 1.7% reduction in insolation. Nevertheless, these results represent orders of magnitude improvements with respect to previous concepts envisaging the passive use of dust as a geoengineering method [79, 98]. A paramount issue for any geoengineering proposal requiring dust or raw material is the source of this material and its accessibility.

By assuming here that the accessibility of asteroid/comet material from the Sun-Earth L_1 point is, as a first approximation, similar to the asteroid accessibility from weakly-bound Earth orbits, the approximate amount of material accessible at an energy lower than that required to exploit the Moon can be shown to be of order 6×10^{13} kg [86]. This estimation results from summing up the mass of all objects, described by a near-Earth object population distribution, that can reach a weakly-bound Earth orbit (i.e., Earth parabolic orbit) with a total Δv budget lower than $2.37\,\mathrm{km\,s^{-1}}$ (i.e., Moon's escape speed) [85, 86]. In particular, for the value presented here, a three impulse transfer model was used to assess the Δv cost of the transfer [86]. A simplified version of Fig. 10 in [85] is presented here as Fig. 7.1. This figure shows the average available resources by using the first, tenth, hundredth and thousandth largest accessible asteroid or cometary object in near Earth space. The figure also represents the 90% confidence region, which accounts for the statistical uncertainty of the near Earth object population distribution. This particular figure has been updated with the accessibility provided by the three impulse transfer model as described in [86].

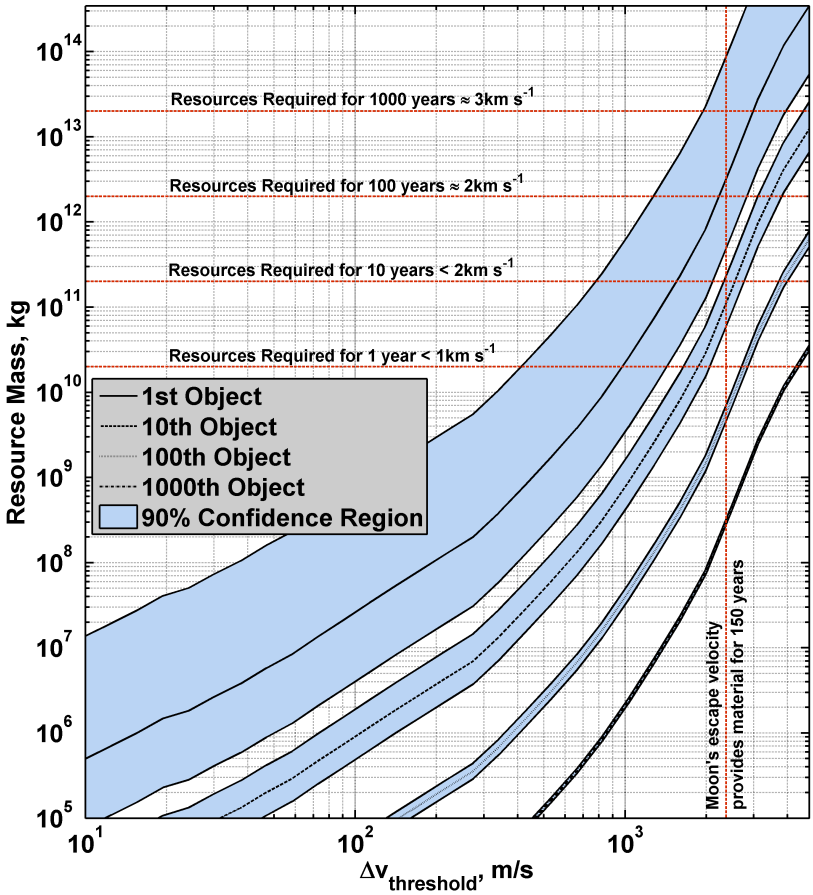

Figure 7.1: Expected resources as a function of Δv threshold [85].

Figure 7.1 suggests that it is possible to find objects able to sustain the initially static dust cloud concept, when released from the displaced equilibrium position, for at least 150 years with a Δv lower than that required to exploit the resources of the Moon. Similarly, the static cloud released from the classical L_1 point can be sustained for approximately 26 years. The minimum size object to sustain the cloud for 1 year, when released from the displaced equilibrium position, is found to be accessible with a Δv of order $1\,\mathrm{km\,s^{-1}}$, while $3\,\mathrm{km\,s^{-1}}$ would be needed to provide 1 large object able to sustain the concept for 1,000 years. By capturing all the material accessible with a velocity below the velocity required to exploit the Moon, the static cloud method could be sustained for 3,000 years. The same applies to the ejected cloud method, which requires a similar quantity of mass to the static cloud case. On the other hand, Struck's Earth-Moon L_4/L_5 dust cloud could not be generated, even by depleting the same asteroid material resource.

The amount of material that can be captured to L_1 below the velocity required to exploit lunar resources is great enough to also supply the Earth ring concept. However, an additional velocity of $3.3\,\mathrm{km\,s^{-1}}$ is required to transport the material to medium Earth orbit, where the ring will be positioned, from the L_1 point.

7.1.2 Asteroid positioning

For the space-based geoengineering methods that require the capture of an asteroid in the L_1 region, the static, gravitationally anchored and ejected dust cloud methods, it is desired that the asteroid is positioned at the centre of the cloud, either at the L_1 or neighbouring equilibrium positions, to enable continual ejection of material. Therefore, a key technological requirement is the ability to stabilise an asteroid at or near L_1. Since an asteroid has a low area-to-mass ratio surface forces such as solar radiation pressure will not strongly perturb the asteroid and therefore it is likely to be possible to stabilise such an asteroid in the vicinity of the classical L_1 position using the mass ejection methods that will be discussed in Sec. 7.3, e.g. a solar collector or mass driver which will generate a thrust due to the ejection of material. To control the asteroid when it is approaching the L_1 point its velocity must be low, since a large instantaneous impulse is not likely to be feasible from the ejection mechanisms considered. This may place constraints on the number of suitable asteroids, unless a chemical propulsion system is used to brake the asteroid before reaching the L_1 point. This may be possible for small asteroids, however, the overuse of such devices will begin to negate the benefit of the dust cloud concepts over solid reflector devices.

As has already been discussed in Sec. 3.3.1, a constant acceleration will be required to maintain the position of an asteroid at the displaced equilibrium position found when the effects of solar radiation pressure are included, or an intermittent acceleration large enough to provide the required acceleration on average. The acceleration required to maintain the position of the asteroid at the displaced equilibrium position for the five dust grain sizes investigated in Chapter 2 can be seen in Table 7.1. It is desirable to minimise the number of objects that must be captured to sustain the dust cloud, i.e. to capture one reasonably large object rather than many smaller asteroids. Assuming that an object is captured with a mass in the region of 1.9×10^{10} kg, capable of sustaining the optimum static L_1 cloud for an entire year, the thrust required to maintain the asteroid at the displaced equilibrium position is 3,927 kN, since the optimum mass is for the smallest grain size. The same object maintained at the displaced equilibrium position for the largest grain size of 32μm requires a thrust of 16.8 kN, approximately 25-50% of the thrust provided by the second stage of an Ariane 5 launcher. However, the capture of an asteroid with this mass will sustain the cloud generated from a grain size of 32μm for only a handful of days. These facts make the use of an asteroid positioned at the displaced equilibrium position unfeasible with current technology. However, using the thrust generated by the mass driver can be envisaged, though, again this is not a near-term option.

In addition, the practicality of the displaced equilibrium position is reduced when considering that it is not possible to use a single size of dust grain, since, to achieve a grain radius of 0.1μm,

Grain Radius [μm]	β	Displacement [km]	Acceleration [$\mathrm{m\,s^{-2}}$]
32	0.005	2,500	9.0×10^{-7}
10	0.018	9,000	3.2×10^{-6}
3.2	0.061	32,000	1.1×10^{-5}
0.32	0.772	950,000	2.3×10^{-4}
0.1	0.751	875,000	2.1×10^{-4}

Table 7.1: Acceleration required to maintain the position of an object placed at the displaced equilibrium position of different grain sizes, corresponding to different values of β and distances to the classical L_1 point.

processing of the asteroid will be required, resulting in a range of dust grain sizes being ejected, as first discussed in Sec. 5.2.2. Therefore the dust grains will also have a range of values of β, each with an associated equilibrium position. Very few of the dust grains will therefore be released at the optimum position. This makes the use of a single displaced equilibrium position less advantageous, considering the station-keeping requirements. A more likely scenario than maintaining a stationary asteroid at the displaced equilibrium position is to place the captured asteroid in a periodic orbit around L_1. An example of such an orbit is a Lyapunov orbit, where the maximum displacement along the Sun-line can be tailored to pass through the equilibrium position. Material would then be ejected within a region close to this position. To reduce the requirements on the mass ejection system, several asteroids would be required, regularly spaced along the same orbit.

7.1.3 Impact Risk

A factor that must be considered is the risk presented to Earth due to the presence of the asteroids used to generate the dust clouds. To make an estimate of the danger of capturing an asteroid at L_1 the kinetic energy associated with a collision can be estimated. This calculation shall assume that upon striking Earth the asteroid will have a velocity equal to the Earth's escape velocity, since it is assumed to be initially at rest at the L_1 point. Using the example of an asteroid with a mass of 1.87×10^{10} kg will give a resultant kinetic energy of 1.2×10^{18} J. In the Torino scale of asteroid impacts risk the kinetic energy is represented in units of megatons of TNT (MT), where 1 MT is equal to 4.3×10^{15} J [15], giving a resultant kinetic energy of 280 MT for this example.

In comparison, the energy of the Tunguska event, which destroyed a large area of Siberian forest in 1908, is thought to be in the region of 10-15 MT [19, 21], approximately a factor of 20 lower. From these brief estimates of the potential impact energy of an asteroid captured at L_1,

it can be concluded that to reduce the risk to the Earth from a single impact, the size of the asteroids used should be reduced wherever possible. This suggests that the risk of implementing the gravitationally anchored dust cloud method examined in Chapter 3, which entails capturing the largest known near-Earth object, Ganymed 1036, with an estimated mass of 1.73×10^{17} kg is potentially high. The impact energy will be in the region of 2.5×10^{9} MT, which is an order of magnitude greater than the estimated 1.2×10^{8} MT of the Chixalub impact [75]. Clearly, detailed orbit design would require that the envelope of potential trajectories departing from the vicinity of the L_1 point do not intersect the Earth.

The mass of a single asteroid deemed not to pose a significant threat, below an impact energy of 1 MT corresponding to a threat of 0 on the Torino scale [15], is in the region of 6.9×10^{7} kg. This rating does not strictly mean that the asteroid poses no risk to Earth, more that the consequences of an impact will not be significant on a global, or regional, scale. To supply the optimum L_1 cloud would therefore require approximately 275 small asteroids every year.

7.1.4 Asteroid Regolith

The comparison of masses used in this chapter have so far assumed that all the material on an asteroid is milled to fine dust and expelled with no losses to form the dust cloud. It is useful to determine how much material can be easily found on the surface of an asteroid that does not require significant processing, thus reducing the need for complex extraction systems. An estimate of the quantity of regolith, as well as the expected size distribution is a useful starting point. Regolith is the loose material found on the uppermost layer of a body and is generated over significant periods by processes such as meteorite impacts, which create ejecta which then either escapes or falls back to the surface. Asteroids are thought to be one of three types; monolithic objects that are likely large, single fragments of a larger object, rubble piles, which are loose collections of smaller rocks held together by gravity, and extinct cometary nuclei [65]. Upon this structure the layer of regolith is expected to be found, ranging from small grains to boulders and pebbles.

7.1.4.1 Size Distribution

Unlike for lunar regolith, there are very few direct measurements of asteroid regolith. The only in-situ measurement of the size of asteroid regolith is the Hayabusa mission, which visited the asteroid 25143 Itokawa, although this cannot be concluded to be representative of a size distribution of asteroid regolith due to the partial failure of the sampling mechanism [113]. The grains collected were kicked up by the impact of the spacecraft on the surface, and trapped in a capture mechanism,

therefore any distribution based on these results will be biased towards smaller particles. The size distribution of asteroid regolith can then only be inferred from remote observation.

It has been observed, due to differences in scattering characteristics, that asteroid regolith is likely coarser than lunar regolith [32], suggesting a mean grain size greater than the value of 72 μm found for lunar regolith [26]. For example, it is observed on the asteroid Eros 433 that the regolith has grain sizes in the region of 50-100 μm [59], with another observation suggesting that the regolith is predominantly below a grain size of 1150 μm [82]. Another estimate of the regolith size comes from Riner et al. [81]. It is suggested that the phenomena of electrostatic levitation plays a significant role in the transport of material on Eros. In this process ultra-violet photons positively charge the surface grains, creating charge differentials that cause the grains to levitate above the surface. Other factors, including solar radiation pressure, may then cause the grains to migrate over the surface. If the charge on the grain is large enough the particle may escape from the asteroid. It is estimated that particles in the range of 10μm-1mm are likely to migrate over the surface of Eros without escaping, whilst particles of radius $< 10\mu$m are likely to have sufficient energy to escape, thus placing a lower bound on the grain size. A lower bound can also be placed on the regolith for the asteroid Itokawa. Riner et al. [81] also calculate that for Itokawa, with its lower mass, particles of radius $< 200\mu$m are able to escape. It is further suggested that the mean grain size in the regolith of an asteroid is likely to be inversely proportional to the mass of the asteroid.

Due to the paucity of precise information regarding the size distribution of asteroid regolith, and the variability with asteroid size, a range of values of mean and standard deviation will be suggested to generate a size distribution. All possible combinations of these values can then be used to evaluate the feasibility of using unprocessed asteroid regolith to generate the dust cloud. Three values were chosen for the mean, μ_r, and standard deviation, σ_r, for distributions based on the Eros and Itokawa data, considered in a log-normal distribution. These values can be seen in Table 7.2. From the information described previously, several reasonable approximations for the mean grain size can be made to illustrate the range of grain sizes found on various asteroids. However, there is less information for the standard deviation of the regolith distributions, therefore four values are used to test the feasibility of the use of asteroid regolith, ranging from a narrow distribution to a broad distribution.

7.1.4.2 Mass Requirement

To calculate the approximate amount of regolith material required to create a 1.7% reduction in insolation the static solar radiation model was used, as described in Chapter 2. This model

	Case	1	2	3	4
μ_r	[mm]	0.01	0.1	1	
	[log(m)]	-11.51	-9.21	-6.91	
σ_r	[log(m)]	0.5	0.75	1	1.25

Table 7.2: Approximate means and standard deviations of asteroid regolith size distribution.

was extended beyond the original version, which uses only a single grain size, by dividing the size distribution into five sections, each having the same total probability of a grain being found within the size boundaries. An example of a probability density function (PDF) for the broadest size distribution using the largest mean grain value can be seen in Fig. 7.2, with the five equal probability regions shown. Within each section the mean grain radius, grain mass and mean cross-sectional area were then found. The dynamic solar radiation model was then applied to each of these five "grains", with the additional intermediate step of storing the integral of the Beer-Lambert law for each section. It is demonstrated in Appendix B that the Beer-Lambert integrals, along the same integration path, can be summed to determine the combined attenuation due to all five grain sections. This can be used to combine the Beer-Lambert integral results for the five sections of the size distribution before optimising the initial number density to find the mass requirement.

This process was implemented for the classical L_1 point only, since the different "grains" all have different values for β, due to their different sizes, which means that the displaced equilibrium position, that occurs due to the inclusion of the effect of solar radiation pressure, will be at different locations for the different grain sizes. It would be impractical to release the material at a specific displaced equilibrium position. This is especially the case considering that the largest grain size, which contributes 98% of the total cross-sectional area of the distribution, has a small β value that leads to a negligible displacement of the new equilibrium position from the classical L_1 point. In this use of the solar radiation model a time step of 5 days was assumed, up to a period of 200 days This is due to the different mean lifetimes of the dust grains in the cloud for the different values for β, which will lead to the five sections of the size distribution having different lifetimes. Hence, to ensure that the spread of the cloud is adequately described, more time steps are needed than is used for the solar radiation model first described in Chapter 2.

The mass required to achieve the necessary 1.7% reduction in solar insolation, using the asteroid regolith size distributions detailed in Sec. 7.1.4.1, can be seen in Fig. 7.3. The mass requirements are all above a value of $1 \times 10^{12}\,\mathrm{kg\,yr^{-1}}$, with the optimum value being $1.167 \times 10^{12}\,\mathrm{kg\,yr^{-1}}$ for the smallest mean grain size and standard deviation for an initial cloud radius of 3,000 km. This result is of the same order as the result presented in Chapter 2 for a single grain radius of 10μm. The optimum mass for the greatest mean grain size and standard deviation is $7.43 \times 10^{14}\,\mathrm{kg\,yr^{-1}}$.

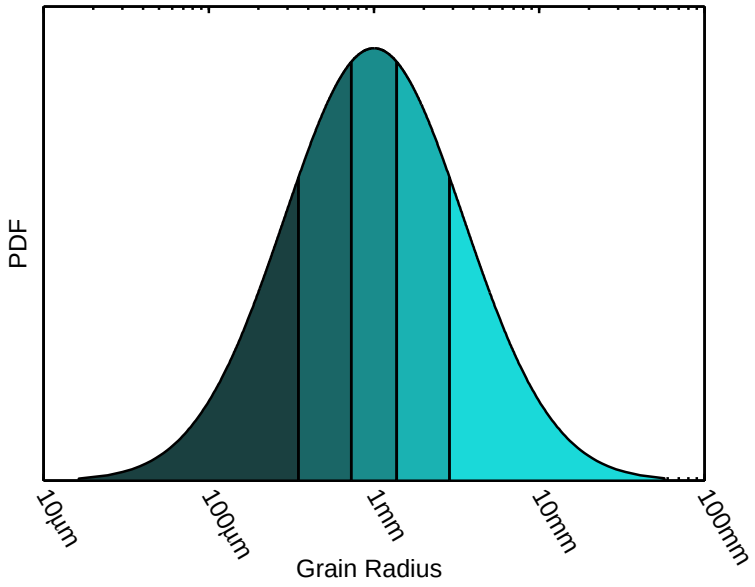

Figure 7.2: Example probability density function for asteroid regolith.

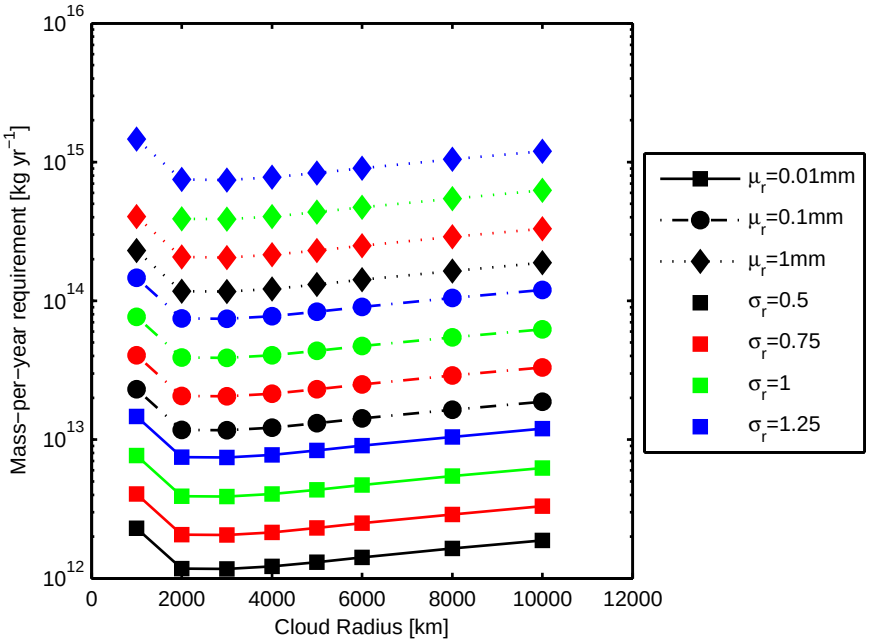

Figure 7.3: Mass requirement for the use of an asteroid regolith size distribution when released at the classical L_1 point.

7.1.4.3 Quantity of regolith

It is thought that the thickness of the regolith layer found on the asteroid surface is proportional to the mass or size of the asteroid, with objects greater than 100 km diameter having a layer many metres deep, whilst objects of less than 10km are likely to only have a covering in the range of a few centimetres [32]. This is due to the mass of the object, as larger bodies will have a greater gravitational attraction that can better trap material ejected after a meteorite impact. For example, the regolith depth on the asteroid Itokawa, an asteroid with a mass of 3.58×10^{10} kg [2], is thought to be in the region of 0.42m [10], whilst the regolith depth on the asteroid Ida has been estimated to be in the range 50-100m [28], with one estimate suggesting a depth of up to 150m [99]. Ida has a mass of approximately 4.2×10^{16} kg [11]. Using these estimates for the regolith depth suggests a total regolith mass on Itokawa of 2.8×10^{8} kg and 4×10^{14}-1×10^{15} kg on Ida. These values correspond to 0.8% of the total mass of the asteroid for Itokawa and range from 0.95% to 2.84% of the total mass of the asteroid Ida. These are both significant quantities of material. However, the capture of an asteroid such as Itokawa would not be sufficient to generate a suitably effective cloud without the processing of material. If the unprocessed regolith were used from Itokawa, the mass requirement calculated for the mean grain size of 1mm is most applicable, considering that grain sizes less than 200μm are capable of escape due to the electrostatic levitation of charged grains above the surface [81]. This suggests a mass requirement of at least $10^{14}\,\mathrm{kg\,yr^{-1}}$, which is six orders of magnitude greater than the quantity of regolith found on Itokawa.

If, on the other hand, the asteroid Ida were captured, the results for the size distribution with the lowest mean value becomes applicable. The quantity of unprocessed regolith can then be seen to be capable of sustaining the dust cloud for 10-10,000 years, depending upon the precise depth of the regolith layer and width of the size distribution of regolith. The quantity of regolith material found on this large asteroid is also of interest for the gravitationally anchored method of space-based geoengineering described in Chapter 3. It is calculated in Sec. 3.4.3 that, assuming the lifetime of ejected dust grains before escape from the zero-velocity curve or collision with the surface is 90 days, the mass escaping is $9.32 \times 10^{11}\,\mathrm{kg\,yr^{-1}}$, for a grain size of 32$\mu$m. Now, the lower estimate for the quantity of regolith of 1% of the total mass of the largest near-Earth object used in the gravitationally anchored dust cloud method, Ganymed, suggests a regolith mass of order 10^{15} kg. Since the size distribution is dominated by larger grains, a large proportion of this mass will be above the grain size of 32μm, thus suggesting that the dust cloud can be sustained for up to several thousand years without the need to process material from the surface. However, the capture of such a large asteroid is clearly technologically challenging, also posing a potential risk to Earth, and hence the use of smaller asteroids will be preferable. Therefore, some form of processing will be required to extract material from the surface and generate a size distribution of

the appropriate size.

7.1.5 Processed asteroid material

It has been shown previously that the mass of unprocessed regolith material required to achieve a 1.7% insolation reduction can theoretically be found on some asteroids. However, this would involve capturing an asteroid of such a scale as to prove technologically challenging, even when considering very far-term technologies, as well as posing a potential risk to Earth. Therefore, the feasibility of using processed asteroid material will now be considered.

An approximate size distribution for processed asteroid regolith has been described in Chapter 5 and can be seen in Fig. 5.5. This distribution can be used in the solar radiation model in a similar manner to the loose regolith distributions discussed previously. The resulting mass requirement for varying sizes of dust cloud can be seen in Fig. 7.5. As before there is an optimal cloud radius in the region of 3,000-4,000 km with a value similar to that of the lowest standard deviation considered for the loose asteroid regolith. This is due to similarity between the mean grain sizes for the two distributions, whilst the difference in the standard deviations is also small. In conclusion the realistic mass requirement for the dust cloud method of space-based geoengineering, assuming the use of asteroid material, is in the region of $1 \times 10^{12}\,\mathrm{kg\,yr^{-1}}$.

7.2 Lunar Material

So far only the use of asteroid material has been mentioned. However, another possible source of material is the Moon. This is of particular interest for larger mass scenarios, such as that proposed by Struck, where the population of near-Earth objects cannot provide sufficient material which can be transported with an energy less than material from the surface of the Moon.

7.2.1 Required material

The energy required to transfer material from the lunar surface is much less than transferring the same amount of material from the Earth, although the capture of an asteroid passing close to Earth will still be more efficient, as described in Sec. 7.1.1. The use of lunar material is an interesting possibility, since the capture of asteroid material poses many challenges that must be overcome. For example, a significant challenge is providing sufficient control on the asteroid to enabled it to

Mean	1	2	3	4	5
Radius [μm]	551	92	36	14	3.9
Cross Section [m^2]	1.9×10^{-6}	2.9×10^{-8}	4.3×10^{-9}	7.0×10^{-10}	6.2×10^{-11}
Mass [kg]	1.2×10^{-5}	1.3×10^{-8}	7.0×10^{-10}	4.7×10^{-11}	1.5×10^{-12}
β	6.0×10^{-4}	2.2×10^{-3}	5.6×10^{-3}	0.015	0.107

Table 7.3: Mean characteristics of five sections of the lunar regolith size distribution.

be placed at the desired location, be it the classical L_1 or displaced equilibrium point, and then maintaining that position. Another potential problem with the capture of asteroid material is the likely negative public response to the capturing of near Earth asteroids that could potentially pose a threat to Earth, no matter how small. Additionally, the Moon presents a practically limitless supply of material and it can be imagined that should the Moon be used in the future for resource utilisation, that the dumping of waste material into the vicinity of the L_1 point may be possible.

The size distribution of lunar regolith, the uppermost layer of small grains that originates from weathering of lunar rock, has been described by Carrier [26]. It can be characterised by a log-normal distribution, described previously in Chapter 5 as a normal distribution with a log scale on the horizontal axis, with the probability density function being calculated using Eq. (5.2). Carrier [26] found the mean grain radius to be $\mu = 3.84\Phi$ with a standard deviation of $\sigma = 2.52\Phi$, where the function Φ is related to grain diameter, D, by;

$$\Phi = -3.322 \log_{10} D \tag{7.1}$$

The subsequent grain size distribution can be seen in Fig. 7.4. The feasibility of using lunar material as a source of dust for geoengineering purposes was determined using the static solar radiation model described in Chapter 2, using the same sampling principles discussed in Sec. 7.1.4.1. The values for the average grain size, cross-sectional area and value of β for each of the five sections of the size distribution of lunar regolith can be seen in Table 7.3. The value for β was calculated by using the estimate for asteroid dust grains calculated by Wilck and Mann [110] using the assumption that the grain sizes remain above the region where the size is equivalent to the wavelength of light, where Mie theory is used to calculated the value of β. However, the lower mass density of lunar regolith, of 3,000 kg m^{-3}, must be corrected for. This can only be used as an approximation, since lunar regolith has been noted to be highly irregular in shape, which will likely have an effect on the coupling between solar radiation pressure and the resultant momentum transfer.

The mass-per-year requirement for lunar regolith material released from a static cloud at the classical L_1 point can be seen in Fig. 7.5. As well as the result for lunar regolith, the mass requirement for asteroid grain radii of 32μm and 0.1μm, corresponding to β values of 0.005 and 0.751 respectively, are also shown as well as the mass requirement for processed asteroid regolith. It can be seen that the mass requirement for lunar material is significantly larger than that of the results of the static cloud calculated in Chapter 2, with the minimum result being $1 \times 10^{14}\,\mathrm{kg\,yr^{-1}}$ for a cloud radius of 3,000 km. This is due to the size distribution. Though the mean grain size is similar to 32μm, one of the values used in Chapter 2, the number of larger grain sizes results in a mean grain mass greater than that of a 32μm grain. Since the efficiency of a particle in blocking solar insolation is essentially a function of the area-to-mass ratio, it can be seen from Table 7.3 that the largest grain size of 551μm is only 2.6% as efficient as the middle grain size, or 0.3% as efficient as the smallest grains. In comparison to the smallest grain size of asteroid material of 0.1μm, the area-to-mass ratio of the largest lunar regolith size is only 0.007% as large, thus explaining the relatively high mass of the lunar regolith distribution. Considering this, some form of processing will be required on the lunar surface, as for the asteroid regolith, to reduce the average grain size of the material that would be transported to the L_1 point. This is most easily achieved by sorting the material so that only grains below a certain size are transported. Alternatively, the material can be ground to the correct size distribution, whether on the lunar surface or in the vicinity of the classical L_1 or displaced equilibrium positions.

7.2.2 Material availability

An estimate of the amount of regolith that can be easily collected can be made by using the approximate depth of the lunar regolith and it's bulk density. The lunar regolith varies in depth depending on the region of the moon, ranging from depths of 4-5m in the Mare to 10-15m in the highland regions [70]. This depth of regolith is relatively shallow in comparison to the depth estimated for the larger near-Earth asteroids, presumably due to the much larger gravity found on the Moon, leading to a more compact sub-surface in comparison to asteroids. Using the radius of the moon of 1,738 km [32] and the lower bound to the lunar regolith depth of 4 m gives an estimate of the total volume of lunar regolith of $1.5 \times 10^{14}\,\mathrm{m^3}$. The bulk density of the lunar regolith is in the region of 870-1,890 $\mathrm{kg\,m^{-3}}$ [27]. This gives an estimate of the total mass of lunar regolith of 1.3×10^{17}-2.9×10^{17} kg. This value is more than sufficient to supply material to the dust cloud method for several thousand years, as well as the method proposed by Struck [98] at the Earth-Moon L_4/L_5 points which requires in the region of 10^{14} kg of material. However, the method by which this material can be re-positioned from the lunar surface is not a trivial matter as indicated in the study of space-based geoengineering undertaken by the ISU [4].

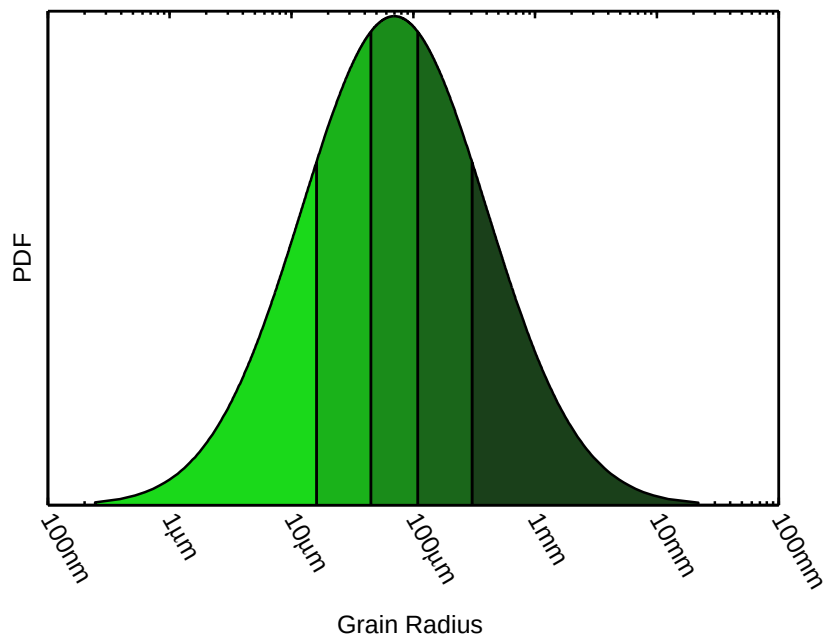

Figure 7.4: Probability density function for lunar dust grains, as described by [26].

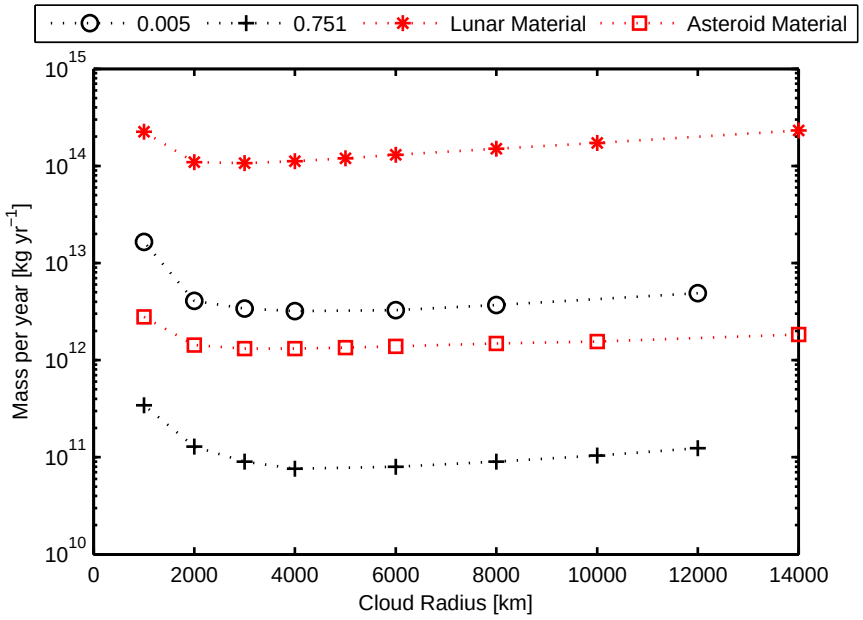

Figure 7.5: Mass requirement for the lunar regolith and processed asteroid regolith size distributions as well as the minimum and maximum mass requirement results described in Chapter 2.

7.2.3 Transport to L_1

Should lunar material be used, a suitable delivery strategy will be required. There are two possibilities for the launch of material from the Moon to the vicinity of the L_1 point; conventional chemical propulsion and a mass driver system. Chemical propulsion systems have the benefit of being very mature and relatively cheap, though the main disadvantage is that the amount of propellant required will be large due to the number of launchers required. The second launch option is the use of a mass driver, similar in principle to that proposed by Angel for the launch of refractor devices from the Earth to the L_1 point. This option is currently technologically unfeasible at the scale required, although it has the advantage of not requiring propellant and being able to use power generated from solar plants situated on the Moon. Both of these launch options have the advantage that the difficulty of launching from the Moon is much less than launching from the Earth, due to the much lower escape velocity and the absence of an atmosphere that creates drag on a launched object. However, the scale of the infrastructure required to construct and maintain the respective systems will be large. An estimate of the number of launch vehicles required to place the infrastructure for a solid reflector goeengineering scheme at L_1 has been made [4]. It was found that in the region of 6,600 heavy launch vehicles, on a similar scale to the Saturn V launchers, would be required. This would be followed by 100,000 mass driver launches to transport the reflectors to the L_1 point from the Moon. These mass driver launches will have a payload in the region of 500,000kg, meaning that were lunar regolith to be used, a total of 200 million mass driver launches would be required. Therefore, the use of lunar material can be seen to be unfeasible at present.

7.3 Cloud generation methods

The feasibility and challenges associated with manufacturing the dust cloud using solar concentrators, mass driver equipped landers and by spin fragmentation will now be discussed. This discussion shall focus on their ability to manufacture the desired grain sizes and the probable deployment scenario with some brief comments on other engineering issues.

7.3.1 Solar collector/sublimation

The sublimation method involves heating the surface of an asteroid to high temperatures, such that material sublimates directly from a solid to a gas. This technique has been investigated for asteroid hazard mitigation and is a novel approach that can either be performed with a laser or a

large solar collector. The latter method was first proposed in [71] and will be the method discussed here. The results for the two methods will in principle be similar, due to the adiabatic expansion involved with both the solar collector and laser ablation methods [6, 50].

An analysis of the physical principles and practical implications of this method was examined by Kahle et al. [50]. It was concluded that the plume of material created is analogous to the expansion of a gas exiting a nozzle into a vacuum. The mass flux, Z [$\mathrm{kg\,s^{-1}}$], leaving the asteroid and the average speed, v, of the particles can be estimated using the relationships in Eq. (7.2) and Eq. (7.3) respectively;

$$Z = \frac{p_{spot}}{\sqrt{2\pi R_s T_{spot}}} \tag{7.2}$$

$$v = \sqrt{\kappa R_s T_{spot}} M_n \left(1 + \frac{\kappa - 1}{2} M_n^2\right)^{-1/2} \tag{7.3}$$

For an S-class asteroid, comprised mostly of silicate based minerals, it is acceptable to assume that it is comprised solely of forsterite. It follows that the specific gas constant, R_s, for diatomic forsterite has a value of $206.7\,\mathrm{J\,kg^{-1}\,K^{-1}}$ and that the gas pressure at the beam spot, p_{spot}, can be calculated as follows;

$$p_{spot} = C_1 e^{C_2/T_{spot}} \tag{7.4}$$

Here the constants C_1 and C_2 have the values 7.62×10^{13} Pa and -65,301 K respectively. The spot temperature, T_{spot}, was shown by Kahle to increase with the illumination time of the spot before reaching a value in the region of 2,280 K [50].

Kahle concluded that for a solar collector with a diameter of 630 m, creating a spot of diameter 16 m, the mass flux is $16\,\mathrm{g\,m^{-2}\,s^{-1}}$. The result is a mass flow rate of $3.2\,\mathrm{kg\,s^{-1}}$. It follows that for the mass ejection rate requirements of the static clouds released at the classical L_1 and new displaced equilibrium points to be met 4,400 and 21,400 solar collectors respectively would be required. This is a significant requirement with a total area of 6,700 $\mathrm{km^2}$ for the asteroid being positioned at the classical L_1 point. However, this remains considerably lower than the quantity of solar reflectors required to create the total insolation change in conventional approaches to geoengineering with the total area required for the reflector method being $6.57 \times 10^6\,\mathrm{km^2}$ [69].

The velocity of the ejected plume can be estimated to be $741\,\mathrm{m\,s^{-1}}$ at the throat when the

heat capacity ratio, κ, is 1.4 and the Mach number, M_n, at the throat is 1. After this the gas will expand, increasing in speed until the transition boundary between continuum and free-molecular flow is reached. After this point the velocity is constant. By following the principles described in Kahle, the velocity at this point is found to be $1.79\,\mathrm{km\,s^{-1}}$. This velocity is too high for the assumptions of the static cloud and therefore this method can only be applied to the ejected cloud method described in Chapter 4. For a cone of material with an angular width of 32°, an ejection velocity of $1.79\,\mathrm{km\,s^{-1}}$ and a grain size of 0.1μm the mass requirement, from Fig. 4.13 and Fig. 4.15, will be in the region of 2-3 $\times\, 10^{13}\,\mathrm{kg\,yr^{-1}}$. This would suggest a total collector area of 1.47-2.22 $\times\, 10^{6}\,\mathrm{km^2}$, which is only a third of the total for the solid reflector system.

The ejected gas particles (mostly Mg, SiO_2 and O_2) will be less than 1 nm in size, though if the particles condense this will increase. However, the likely grain diameter will still be considerably smaller than the scale used in this thesis. However, the gas particles will likely re-condense to form larger particles, once ejected, and furthermore, it can be assumed that larger particles will also be emitted from the spot as some grains will be ejected by the flow of gas before being completely sublimated. Such larger particles will likely have lower velocities than the gas plume due to the equipartition of energy. The scale of these effects cannot yet be determined though they may increase the feasibility of this method due to the greater mass efficiency.

The final consideration for this method is the complexity and reliability of the systems involved. Firstly, it will be complex to provide an autonomous orbit control system for the thousands of collectors required. Secondly, the lifetime of the collectors may be short, a matter of hours, due to the impingement of the ejected dust on the surface of the collectors [50]. However, it is noted that the lifetime can be increased greatly by the use of smaller secondary mirrors to re-focus the collected sunlight to reduce contamination. Several of these secondary mirrors can be used and rotated once contaminated to increase the lifetime.

7.3.2 Mass driver

A mass driver concept would involve a spacecraft landing on the surface of a suitably large asteroid and then extracting material from the surface. This material would then be ejected using the mass driver. The extraction technique would be required to generate the correct scale of dust and therefore some processing will be required.

Mass drivers are generally envisaged as high velocity devices, most suitable for launching objects into orbit cheaply and efficiently. However, they could also be used for low ejection velocity applications. An advantage of this method is that the ejection velocity can be more controlled than

for the solar collector method.

The use of mass drivers for asteroid hazard mitigation has previously been investigated for a spacecraft design that incorporates a nuclear powered mass driver [78]. A swarm of these 500-1000 kg spacecraft are envisaged landing on an asteroid and ejecting material from the surface with a velocity of $187\,\mathrm{m\,s^{-1}}$ at the rate of approximately $120\,\mathrm{kg\,hr^{-1}}$. As with the case of the solar collector spacecraft, many of these units would be required to meet the ejection rate demands, in the region of several thousand. However these vehicles have been designed to maximise the impulse generated on the host asteroid and hence may not be best suited for the scenario envisaged here. In addition, as with the case of the solar collector, the velocity of the ejecta may not be optimum for this scenario and therefore it can be imagined that, assuming the same spacecraft power consumption, a greater mass of material could be launched at lower velocities.

The complexity of this scenario is not as great as for the solar collector concept as there is no complex motion of the spacecraft. Some control is required to ensure that the required thrust is in the correct direction to maintain stability of the asteroid at L_1 or its orbit around L_1, however this will be modest. The key issue in this case is the lifetime of the mining equipment since regular maintenance will be unlikely due to both the scale of the systems and the risk to spacecraft of passing through the dust cloud.

7.3.3 Spin fragmentation

An additional method of cloud generation is the possibility of imparting angular momentum to an asteroid such that the rotation rate increases. It is considered that a large number of small asteroids are 'rubble piles' [43] loosely held together by self-gravity, and as such material could easily be ejected from the surface under the correct conditions.

The angular velocity required, ω_{crit}, to cause the liberation of material can be estimated by equating the centripetal and gravitational forces. This relationship, can be found to depend only on the mass, M_a, and radius, R_a, of the asteroid and is;

$$\omega_{crit} = \sqrt{\frac{GM_a}{R_a^3}} \tag{7.5}$$

This would be sufficient to eject the regolith from the surface of the asteroid, however a larger angular velocity would be required to tear the asteroid apart. It has been suggested that a sub-kilometre sized asteroid can be spun-up to the point of fragmentation by the use of tethered

satellites transferring torque in the same manner as a reaction wheel [17]. The scale of material ejected in this scenario is likely to vary greatly as it will depend on the grain size of the surface of the asteroid as well as the internal structure. As stated previously the smaller asteroids that are more feasible to capture to L_1 will have a larger grain size than the largest asteroids, thus decreasing the efficiency of the space-based geoengineering method unless processing were possible. It is unlikely that the material could be ejected at the displaced equilibrium point and hence this method of cloud generation is best suited for creating clouds at the L_1 point. An additional factor that must be considered is that the cloud shape obtained from spinning an asteroid is likely to be a disk rather than a sphere. Finally, the engineering challenge of this method is considerable as the tether length required to spin-up a reasonably sized asteroid is in the region of several kilometers, but also the method to transfer the torque to the asteroid will be complex.

7.3.4 Summary

In this section several possible methods with which the dust cloud can be generated have been described. None of them are sufficiently close to the static cloud model first used to characterise the L_1 cloud to accept it as an accurate model of the system, though it is still useful as a guage of the mass required for the different position and grain size variations. To judge the relative benefits of the different ejection mechanisms with relation to the solar radiation model, the ejection cloud described in Chapter 4 must be used. From this comparison it can be seen that, as has already been discussed, the solar collector method is not suitable for the ejection of material for the creation of the cloud due to the high mass requirement. In addition, the solar collector method is complex whilst enabling little control over the size and velocity of the ejected particles. Furthermore, the lifetime of the solar collectors is potentially short requiring large numbers to be manufactured for this purpose, in part negating the benefits of the dust cloud method. The spin fragmentation method is also not suitable as there is little control over the sizes of the ejected grains though the overall complexity is lower as far fewer spacecraft will be required. However, significant challenges remain in transferring the torque to the asteroid. The mass driver is the most suitable of these methods as there is the greatest level of control over the system. The ejection velocity can be tailored to give the most mass efficient impulse. The methods are rated in terms of complexity, reliability, cloud characteristics and efficiency in Table 7.4 based on the factors discussed previously.

Method	Complexity	Reliability	Efficiency	Sum
Solar Collector	High (1)	Low (1)	Medium (2)	4
Mass Driver	Medium (2)	Medium (2)	High (3)	7
Spin Fragmentation	Medium (2)	Medium (2)	Low (1)	5

Table 7.4: Trade-off of different cloud generation methods based on the engineering considerations discussed in this section.

7.4 Comparison to solar reflector manufacture in-situ

An interesting comparison for the proposed geoengineering scheme is with manufacturing solar reflectors in-situ using captured asteroid material. At a qualitative level this may be a viable scheme, given the appropriate technology becomes available, and it may have some significant advantages over terrestrial manufacture and launch. It also has the key advantage that the reflectors will not need to be launched to L_1 and the conditions for manufacturing may be superior in space. As suggested by Lippmann [61], the main limitations on the thinness of manufacturing films are gravity, electrostatics and contamination. An additional factor is the oxidisation of the film which will change the reflective properties of the surface and hence the perturbation by solar radiation pressure. As such solar reflectors manufactured in the vacuum of space are likely to be of higher quality than terrestrial manufacture. The disadvantage in this method however is that the manufacture process will need to be automated, which will increase the level of complexity greatly. Lippman used the example of a heliogyro film to analyse the feasibility of such manufacturing techniques in laboratory experiments. A material deposition rate of $0.2\,\mathrm{kg\,hr^{-1}}$, corresponding to an area of $27.8\,\mathrm{m^2\,hr^{-1}}$, was found to be achievable, though no comment was made on higher deposition rates.

There is some further precedent to automated manufacture, for example recently commercialised 3D printers. Given future technological development it may be possible to 'print' solar reflectors in-situ given the correct bulk material is available. This again leads to the possibility of capturing asteroids from which material can be extracted and used in manufacture. For example, an M-class asteroid is mostly comprised of iron and nickel elements which could be used in the fabrication of reflectors. Additionally, S-class asteroids are mostly comprised of silicate based minerals such as forsterite, which also contain large amounts of magnesium, which would also be a suitable material for reflector manufacture.

A model can be constructed to estimate the time scale required to manufacture the required area of solar reflectors, as suggested by McInnes to be of order $6.57 \times 10^6\,\mathrm{km^2}$ [69], given several

different scenarios. The first scenario will estimate the time taken to eject the required mass of material from an asteroid, using the plume model suggested in [50], given an initial solar collector diameter of 630 m, while assuming there is no time lag required to manufacture subsequent reflectors. The second scenario will estimate the time required for manufacture by selecting the longest time from either the time to gather the material or the time to deposit based on different deposition rates. The results can be seen in Fig. 7.6.

This clearly shows that the manufacturing rate is the major limiting factor with the highest value of $1 \times 10^6\,\mathrm{kg\,hr^{-1}}$ requiring in the region of 30 years to produce the necessary area of solar reflector. Should the technology become feasible, there are advantages to this approach, as the time required for manufacture enables observations of changes in the Earth's climate to be made before fully committing to the scheme.

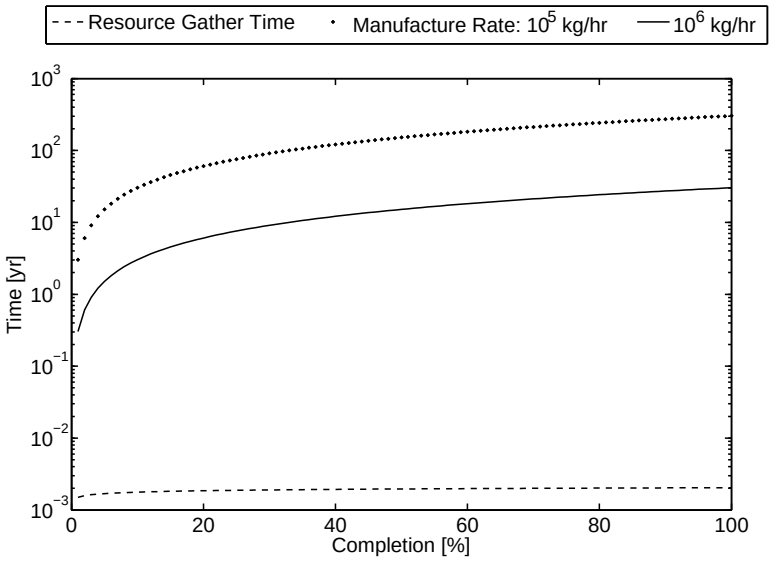

Figure 7.6: Manufacturing times for the required area of thin film solar reflectors suggested in [69] for different mass deposition rates for in-situ fabrication.

7.5 Technology Development Roadmap

Considering the engineering aspects discussed in this, and previous, chapters the proposal to use large clouds of dust to mitigate the effects of climate change appears challenging. This is both in terms of the scale of the infrastructure that must be put in place to capture the required asteroid material, or transport the material from the Moon, but also in terms of the technologies that must be developed to the stage where the autonomous operation of many spacecraft can be achieved with minimal human input.

Though the scale of the space-based geoengineering schemes are formidable, they are not beyond the scope of present terrestrial activities. For example, the mass of asteroid dust required to sustain the optimum static dust cloud for the period of one year is only an order of magnitude greater than the mass of water held in London's reservoirs [69]. Considering that there are many terrestrial large-scale engineering projects, this suggests that the scope of the challenge is not beyond our imagination. In addition, other solar radiation management methods for geoengineering, as well as some carbon sequestration methods, also require a large-scale engineering effort. For example, the stratospheric aerosol proposal requires the placement of $5 \times 10^9\,\mathrm{kg\,yr^{-1}}$ of sulphur aerosols into the upper atmosphere [83]. This proposal is rated as one of the most near-term options since the injection can be implemented using current technologies, such as sounding rockets or aircraft. Therefore, the key challenge to implement space-based geoengineering is related to the current lack of technology and infrastructure in space.

In this section a broad roadmap for the development of the dust cloud method shall be presented. The focus shall be on the processing and ejection of asteroid material in the vicinity of the L_1 point, with the dust being ejected by a mass driver equipped lander. A representation of this scheme can be seen in Fig. 7.7. This scenario was selected since the technological challenges associated with it are much less than the other dust cloud space-based geoengineering concepts. For example, the gravitational anchoring of a dust cloud at L_1 would involve the capture of an object too great in size to be feasible whilst the Earth ring concept, though requiring less mass when the total lifetime of the dust cloud at L_1 is accounted for, requires a greater change in energy to capture the asteroid material whilst also having a highly uneven insolation reduction profile on Earth. As well as this, the capture of large objects to a medium Earth orbit is likely to pose significant legal and political obstacles, as would the capture of the asteroid Ganymed to the L_1 point.

As for all grand engineering ventures, the technologies involved have evolved over many decades, with increased refinement to enable the construction of the final project. Similarly, for the space-based geoengineering scheme, the technology must be incrementally developed, and successfully demonstrated over many years to enable the final undertaking to occur. Several key milestones will now be described in the following section, which set goals to test the progress and key technologies for the dust cloud methods of space-based geoengineering.

7.5.1 Phase 1 - Asteroid capture demonstration

The key technology that must first be demonstrated is the successful capture of an asteroid. This goal is currently the target of several space venture companies which aim to capture small

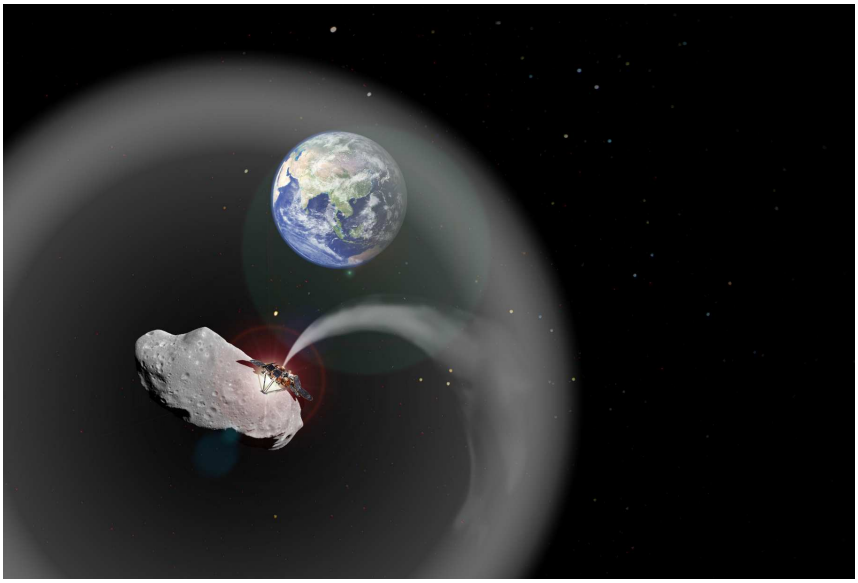

Figure 7.7: Impression of an L_1 positioned dust cloud for space-based geoengineering [Image created by Charlotte Bewick using material from ESA and NASA].

near-Earth objects for resource utilisation. The profitability or commercial sustainability of large-scale space ventures is essential, therefore linking the development of this technology to a strong commercial venture is key. A benefit of this is that no commitment to space-based geoengineering needs to be made now. This is particularly useful considering the political and legal issues that must be agreed upon, as described in Sec. 1.3, which will likely take some time. However, without the involvement of government the technological development will be dependent upon the perceived profitability of the scheme, meaning that the project could be abandoned if returns prove not to be suitable. Therefore it would be prudent to offer an incentive to develop these technologies, perhaps in a similar manner to the X-Prize. The motivation need not be for geoengineering, since resource utilisation of near-Earth objects will have many other benefits. Also, practical experience with manipulating the orbits of asteroids may be useful in diverting a near-Earth object due to impact Earth.

It was suggested in the Keck study, used as the basis of the asteroid capture proposal made by Planetary Resources, that the capture of an object up to 500,000 kg in mass can be achieved by 2025 [22]. This is a challenging target as it is estimated that the upper range of the total flight time, from launch to asteroid capture into a high lunar orbit, is 10 years. This phase of the technology development can be initiated presently, since the key technologies (such as electric propulsion) are widely used, with the exception of a device to grapple the asteroid. Ultimately it is advantageous to slowly implement the new technologies, hence the use of low thrust propulsion, rather than the use of the mass driver to provide the thrust to capture the asteroid for this initial demonstration.

7.5.2 Phase 2 - Mass driver and asteroid mining

Following the capture of an asteroid into the vicinity of L_1, the processing of material and the mass driver system can be demonstrated. These technologies can be under development while the first asteroid is being brought to the Earth-Moon system and then launched to rendezvous with the asteroid after capture. As for the capture of a near Earth asteroid, the demonstration of the material extraction system has a goal in parallel with commercial interests, it is only the mass driver that goes beyond the immediate economic interests of capturing the asteroid. However, if the development of a mass driver is viewed as a method of generating thrust to capture an asteroid then developing mass driver technology may also be of commercial interest. It could be argued that this is counter-productive for the company since the ejection of asteroid material is a reduction in profit, since the material resource is the purpose for the capture of the asteroid. However, it could be viewed as a method of capturing larger objects that could not otherwise have been captured, whilst greatly reducing the mass of the spacecraft to be launched and therefore the cost of the spacecraft. On the other hand, a more likely technology that will be used for the capture of a near-Earth asteroid in this manner may be the solar concentrator concept [50, 107].

Once the lander tasked with testing the extraction mechanism has rendezvoused with the asteroid, the mining system can be demonstrated, followed by the manipulation of the asteroid orbit by the ejection of material using the mass driver. In this phase it is crucial to test the thrust generated by the mass driver system and compared to the expected thrust based on the assumptions of material density and the mass driver power. Several extraction systems can be used, the most common used to date is a drill or scoop, though these have only been used in small-scale scenarios. Several asteroids may be required to test different extraction and orbit manipulation scenarios which will increase the timeframe of testing.

7.5.3 Phase 3 - Capture to L_1

The change in velocity needed to capture a range of small objects into stable orbits around the collinear Lagrange points close to the Earth has been calculated by Sanchez et al. [87]. It can be seen that, with current technologies, an asteroid several metres in diameter can be captured to either the L_1 or L_2 point, with a change in velocity of less than $500\,\mathrm{m\,s^{-1}}$. It was determined that, assuming the same baseline spacecraft proposed in the Keck study, with a dry mass of 5,500kg and 8,100kg of propellant [22], a mass in the region of 44,000kg can be captured into a planar Lyapunov orbit around L_1 [87]. This is assuming the change in velocity required to capture the asteroid 2000 SG344, with the total mass of this asteroid being in the region of 9.6×10^7-

3.1×10^9 kg. The optimum transfer will last 3.35 yr, commencing on 11/03/2025. It is further calculated by Sanchez et al. [87] that assuming low thrust propulsion is used, rather than the impulsive manoeuvres originally calculated, that the mass of this asteroid that can be captured rises to 530,000 kg. Though this is not as large as the total asteroid mass, it demonstrates the capability of current technology to capture near-Earth objects. Currently, the number of known asteroids of a few metres in size is small in comparison to their expected number and therefore it is to be expected that more small asteroids will be discovered. The optimal object on which to test asteroid capture is the body 2006 RH120, where it is estimated that a change in velocity of only $58\,\mathrm{m\,s^{-1}}$ is required [87]. This enables the entire asteroid to be captured, providing its size is not in the uppermost range of the size estimate. The drawback to the capture of this object is that the transfer time is long, in the region of 7-8 years, and that the asteroid will be captured to a halo orbit around the L_2 point, though this is not a significant problem if the aim of the mission is to test the capture technologies. This transfer will begin on 01/02/2021. The capture to the vicinity of the L_1 point can be demonstrated simultaneously to the general capture of asteroids to the Earth-Moon system, since the technologies required will be broadly similar. After the first capture tests have been achieved and the mass driver system has been demonstrated the capture of an asteroid using a mass driver can be demonstrated.

7.5.4 Phase 4 - Cloud generation

Once an object has been captured to the vicinity of the L_1 position, a spacecraft can be launched that will use the asteroid extraction and mass driver mechanisms developed previously to test the generation of the dust cloud. A sample of material will be ejected in the optimum direction and velocity indicated in Chapter 4, providing the size distribution is correctly characterised, and then the dispersion of the dust grains can be observed. This will test the predictions made in this thesis and the fundamental forces acting upon the dust grains. This may be difficult to observe depending on the quantity of dust emitted due to the large distances over which the dust will spread. To observe the dispersion of the dust grains a dedicated spacecraft would likely be required equipped with an IR imaging instrument.

7.5.5 Phase 5 - Insolation reduction

Once the dispersion of the cloud has been observed and verified, a measurable insolation reduction must be implemented to test the mass efficiency of the method. The quantity of mass required, assuming the grain size distribution associated with processed asteroid material (Sec. 5.2.2), to

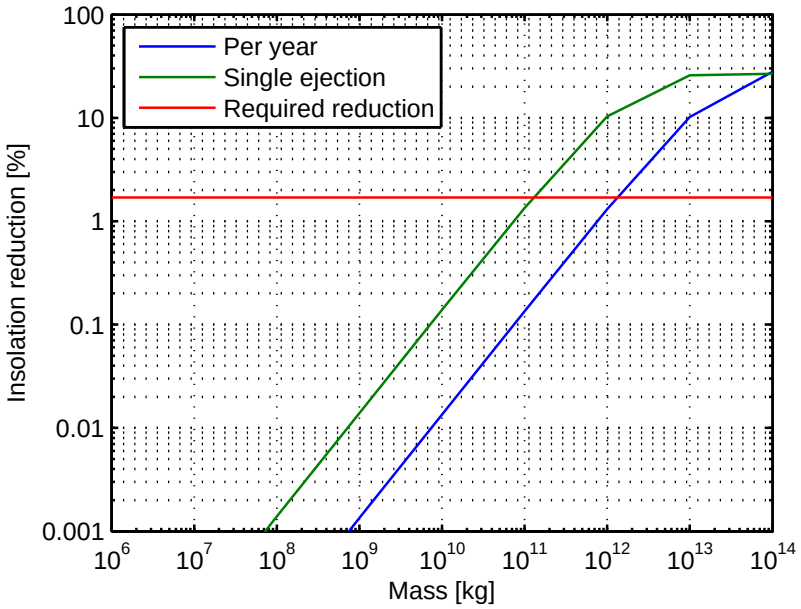

Figure 7.8: Insulation reduction for various mass ejection rates.

achieve a range of insolation reductions can be seen in Fig. 7.8. The insolation reduction, assuming a steady state geoengineering scenario, is shown as well as the maximum insolation reduction expected due to the ejection of the same mass in a single event. Foukal et al. [36] have presented results showing the variation in solar luminosity, with an expected error or $\pm 0.009\,\mathrm{W\,m^{-2}}$, corresponding to an insolation change of 0.0007%. Fig. 7.8 shows that approximately $1 \times 10^9\,\mathrm{kg}$ must be ejected over the course of a year to achieve a steady state reduction of 0.001% over the Earth's disk. This mass would be equivalent to an object with a diameter of 90 m and would represent a significant increase in complexity compared to the capture of the smaller asteroids described in the previous phases. Therefore, more modest tests should first be performed using a smaller asteroid. In this intermediate test the reduction in insolation can be measured between two spacecraft positioned on either side of the dust cloud rather than at the position of the Earth.

7.5.6 Phase 6 - Gradual implementation

Once the initial test has been performed and an observable, albeit small, insolation reduction has been demonstrated, the full implementation of the dust cloud space-based geoengineering scheme can be implemented. As was discussed in Chapter 5, a gradual implementation is necessary, where the insolation reduction is increased in steps over many years. This is to allow observations of the climate system to be made, since the relaxation times of the different processes vary and a comparison between different seasons will be difficult. Therefore, an observation window of one

or two years can be recommended. Under the assumption that 10 steps are taken, where the insolation reduction increases by 0.17%, gives a timeframe for implementation of approximately 20 years. This is a cautious approach and could feasibly be implemented over a shorter timeframe, though at greater risk.

7.5.7 Summary

A technological development roadmap for the dust cloud method had been described in this section and is summarised in Fig. 7.9. The timeframe over which the technology is likely to be developed is long, though naturally this is only an estimate. The long timeframe is due to the large-scale of the undertaking, requiring an ease of access to deep space that is not yet achievable, at least in terms of financial sustainability. This financial sustainability may be a key factor in the speed of the technological development. It has been discussed by Launius [58] that large-scale space ventures, in particular the Apollo program, only occurred due to a unique set of circumstances that enabled the justification of significant investment. It could be imagined that at some point during the 21st century this may also be the case for geoengineering, though for space-based geoengineering to be a feasible option the initial technological development must start soon. Therefore, the possibility of linking the key technological developments of asteroid capture and manipulation to a financially driven commercial endeavour will likely speed up the process. The timeframe shown in Fig. 7.9 shows that the likely implementation of the full dust cloud method will not take place until the last quarter of the century. This assumption is based on the need for a gradual implementation, as detailed previously, but also large advancements in scale between capturing currently feasible near-Earth objects and those large enough to supply the dust cloud. This is not likely to be a rapid process as the difference in mass is many orders of magnitude and there are many smaller, and therefore likely to be more accessible, asteroids which will likely provide a swifter financial return. Therefore, at this stage, an organised research and development programme may be required. The seeds of this level of organisation will need to be planted many years before it is required, to enable the appropriate political and legal infrastructure to be constructed. Taking these factors into account, it is clear that there are many challenges to be overcome before dust cloud methods of space-based geoengineering are regarded as a near-term option for geoengineering.

7.6 Conclusion

This chapter summarises the main engineering aspects associated with generating a dust cloud for the purposes of space-based geoengineeering. It is found that a total of 6×10^{13} kg of asteroid

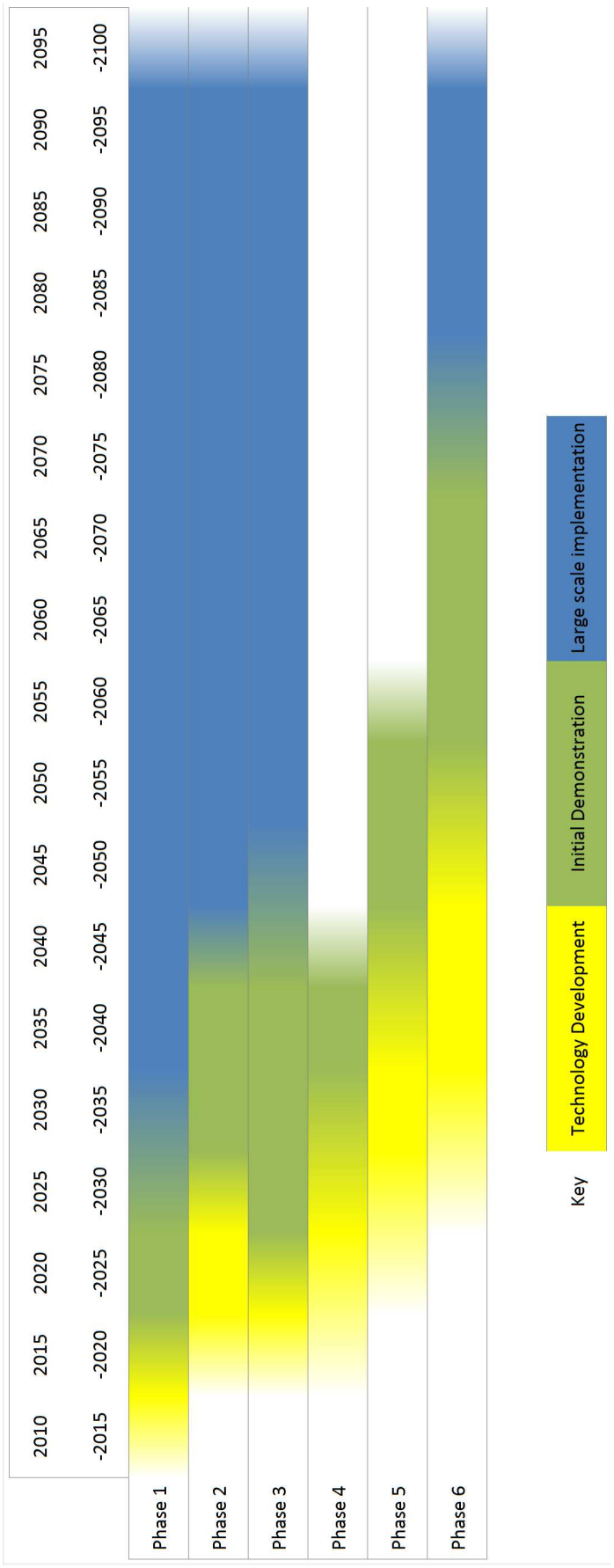

Figure 7.9: Technological development roadmap for the dust cloud method of space-based geoengineering.

material can be captured to the L_1 point below a threshold velocity of $2.7\,\mathrm{km\,s^{-1}}$ [85], the escape velocity of the Moon. An estimate of the quantity of lunar regolith easily accessible on the lunar surface reveals a total of order 10^{17} kg. However, using an extension applied to the solar radiation model described in Chapter 2, for the assumption of a dust size distribution, reveals that the minimum mass required per year is of order 10^{12} kg yr^{-1} and 10^{14} kg yr^{-1} for asteroid regolith and lunar regolith respectively.

In Sec. 7.3 several methods for generating the dust cloud were discussed. These included solar sublimation of material from the surface of an asteroid, the ejection of material using a mass driver and the spin fragmentation of an asteroid. It is concluded that the mass driver is the optimal method for generating a dust cloud due to the greater control that can be placed over the ejected cloud, whilst the solar sublimation method is preferential for asteroid capture given the high ejection velocities that can be achieved. A roadmap for the generation of a dust cloud at the L_1 point has been presented in Sec. 7.5.

Chapter 8

Conclusions

In this chapter a summary of the previous technical chapters shall be made, with a discussion and conclusions of the feasibility of the methods and results of the different geoengineering schemes and a discussion on possible future avenues of research.

8.1 Summary and Conclusions

The key research objective of this thesis is to present macro-scale methods to reduce the pressure on the climate and global resources by the human population of Earth. This is achieved by improving the timeliness and affordability of space-based geoengineering by assessing the feasibility of dust based methods of geoengineering.

The two methods of space-based geoengineering investigated are the use of a large cloud of dust in the vicinity of the Sun-Earth L_1 point and a dust ring around Earth. A summary of these two different methods will be discussed in the sections below with a conclusion on the probable method of implementation. Subsequently, the engineering feasibility of this scenario will be discussed in more detail.

8.1.1 L_1 dust cloud

The L_1 dust cloud has been investigated using three different scenarios.

1. An initially static cloud in the vicinity of the L_1 point

2. A cloud ejected with an initial velocity from a single point in the vicinity of the L_1 point

3. A dust cloud ejected from a large asteroid and anchored by the gravity of the body

All three of these methods include the forces of solar radiation pressure, due to the small size of the dust grains involved, $< 32\mu$m. It is found from observations of the inclusion of this force in the circular restricted three-body problem that the colinear equilibrium position shifts Sun-wards with an increasing force due to solar radiation pressure i.e. smaller particles will have an equilibrium position shifted further Sun-wards than larger particles. Therefore the three dust cloud scenarios must be investigated with respect to both the new equilibrium position and the classical L_1 position for a range of dust grain sizes.

The static L_1 cloud method is viewed as an initial approximation of the L_1 cloud scenario, since to create the cloud an initial velocity must be given to the dust grains. The static cloud is propagated over time, with all time steps being combined to create a steady state cloud. Subsequently the initial density of the static cloud, assumed to be a homogeneous sphere, is optimised to find the mass of dust required for each position, the new equilibrium position or the classical L_1 point, for each dust grain size considered. These results show that smaller dust grains require a lower total mass of dust, due to them having a higher area-to-mass ratio, offsetting a shorter lifetime when released from the classical L_1 point. It is also observed that the mass of dust required when the cloud is released from the new equilibrium position is less than for a cloud released from the classical L_1 point. This is naturally the case since the classical L_1 point is no longer an equilibrium position and will therefore have a reduced stability. The optimum mass results for a cloud released from the new equilibrium and classical L_1 positions are $1.87 \times 10^{10}\,\mathrm{kg\,yr^{-1}}$ and $7.60 \times 10^{10}\,\mathrm{kg\,yr^{-1}}$ respectively. These results are significantly less than other dust based methods of space-based geoengineering and the same order of magnitude as the optimum, solar reflector based, method of space-based geoengineering.

The static cloud does not include the attractive effect of the body from which the cloud will be generated, assumed to be an asteroid. By using the asteroid mass in the four-body problem this was investigated in Chapter 3. It was found that a zero-velocity curve completely encompasses the asteroid from which dust grains ejected from the surface below a threshold velocity cannot escape. The size of this bound region increases with the mass of the asteroid with the observed zero-velocity curve being greatest when the asteroid is placed at the new equilibrium position. When the asteroid is placed at the classical L_1 point the zero velocity curve is seen to shrink rapidly as the particle size decreases, with a sizeable zero velocity curve only being observable for

the largest asteroid masses considered. The maximum reduction in solar insolation possible from the bound dust cloud was first calculated by assuming all light passing through the bound region is blocked. Using this assumption it was observed that for only the largest near-Earth object mass is the bound region large enough to meet the insolation reduction requirement of 1.7%. Considering that the mass used for the largest known near-Earth asteroid, 1036 Ganymed, is 1.7×10^{17} kg the engineering challenges associated with this scheme are too great for it to be considered feasible.

The final dust cloud method in the vicinity of the L_1 point investigates the ejection of material from a single point, to simulate the generation of a dust cloud by ejection from an asteroids surface. A range of values were used for the mean velocity, velocity standard deviation and spread of the particles after ejection. As for the previous two methods the ejection was assumed to occur from either the new equilibrium position or the classical L_1 point. An initial investigation of the mean lifetime of the ejected particles shows that when ejection occurs from the new equilibrium position the optimum lifetime occurs for the lowest velocity considered and lowest spread after ejection. In contrast, when released from the classical L_1 point, the optimum lifetime will occur for a specific velocity that increases as the dust grain size decreases. From this it is concluded that the mass required is likely to be more sensitive to initial ejection conditions when released from the classical L_1 point.

The mass required for the cloud ejected from the surface of an asteroid is observed to decrease significantly as the initial mean ejection velocity decreases. For the dust grains ejected from the classical L_1 point the minimum mass is in the region of the ejection velocity with the optimum lifetime, with the spread after ejection having a significant effect for the highest ejection velocities only. As for the static dust cloud the smaller grain size offers a significantly better mass requirement than larger dust grains. The results observed for the ejection from the new equilibrium position is similar, with the optimum mass being found at a lower velocity, in the region of $1\,\mathrm{m\,s^{-1}}$. In this region the angular spread does not significantly affect the results. The optimum masses for the two scenarios are $5.8 \times 10^{10}\,\mathrm{kg\,yr^{-1}}$ and $1.3 \times 10^{10}\,\mathrm{kg\,yr^{-1}}$ for ejection at the classical L_1 and new equilibrium positions respectively.

In summary, it can be concluded that the use of a dust cloud at L_1 is feasible with masses in the region of $10^{10}\,\mathrm{kg\,yr^{-1}}$ being possible in the optimum conditions. The sensitivity of the mass requirement is greater for the ejected cloud model with high velocities, $>1\,\mathrm{km\,s^{-1}}$, requiring orders of magnitude greater mass. It is also concluded that the mass of the asteroid from which the dust cloud is generated cannot be used to anchor the dust cloud, with only the largest known near-Earth asteroids being able to anchor a dust cloud large enough to affect a significant insolation reduction.

8.1.2 Earth ring

The Earth ring concept, that was previously proposed by Pearson et al. [79], is investigated in this thesis using a more accurate model of the orbital dynamics that includes the effects of solar radiation pressure and the Earth oblateness, J_2, effect. From a study of these dynamics it is found that stable, heliotropic, elliptical orbits exist that enable a long-lived Earth ring to be designed. A trade-off of the time spent in between the Earth and Sun and the minimum grain size possible for a range of orbital parameters enables the optimum ring design to be found. Using this ring, the mass of dust required to achieve the required insolation reduction was calculated. The mass of dust required is 1×10^{12} kg, a value which accounts for the reduced efficiency of the ring due to thermal emission from the dust grains and reflection of sunlight from the ring to Earth.

8.1.3 Dust cloud engineering feasibility

The engineering feasibility of the dust cloud methods, in terms of the availability of asteroid material and the credibility of the cloud generation methods, and the likely geoengineering potential, in the form of a climate model analysis, was discussed in Chapters 6 and 7. The climate modelling used a simple one-dimensional climate model to assess the likely reduction in temperature due to the distribution of the insolation reduction over the Earth's surface. These results suggest that all the dust cloud methods investigated are capable of offsetting the mean global increase in temperature caused by a doubling of the concentration of CO_2 in the atmosphere, also modelled in Chapter 6. A further conclusion is drawn from the study of the climate model that, whilst the mean global temperature can be offset, the temperature reduction is weighted significantly towards the equatorial regions, with the polar regions experiencing a net warming in most cases. This result is seen in most climate modelling studies of geoengineering. It is also seen in these results that the Earth ring has a greater weighting towards the equatorial regions than the dust clouds located in the vicinity of the L_1 point. The negative aspects with regards to the risk to spacecraft and the attenuation of telecommunications signals is commented on in Sec. 5.5. Therefore it can be concluded that the L_1 dust cloud method is preferential from a climate modelling perspective and will more suitably offset the effects of climate change.

The discussion of the engineering feasibility of the dust cloud in Chapter 7 details the material availability, the use of asteroid and lunar dust as a source of material and discusses the possible cloud generation methods. The velocity required to capture each of the known near-Earth objects is used to determine the mass that can be captured below the velocity required to exploit lunar resources. From this it is observed that a total mass of material greater than 10^{13} kg can

be exploited, a value which is significant enough to sustain the optimal L_1 dust clouds discussed previously for 100s of years. However, further observations are made that reduce the mass efficiency of these methods.

The previously used static model at L_1 is extended in Chapter 7 to include a range of unprocessed and processed asteroid regolith size distributions. The range of values for mean and standard deviation of the unprocessed distribution is drawn from estimates of regolith sizes made from remote sensing models found in the literature, with the processed size distribution being drawn from data relating to the current state of terrestrial mineral processing. These results show that the minimum mass required when a size distribution is used is of order $10^{12}\,\mathrm{kg\,yr^{-1}}$, a significant increase in comparison to previous estimates made in this thesis. This new result suggests that exploiting all known near-Earth objects below the velocity required to exploit lunar resources will enable the L_1 cloud to be sustained for several decades. Despite this the use of asteroid material is still preferential to the use of lunar resources. It was found, using the same methods, that the mass of lunar regolith required is of order $10^{14}\,\mathrm{kg\,yr^{-1}}$, due to the larger grain sizes in the lunar regolith size distributions. When the use of a dust grain size distribution is considered the use of the new equilibrium position appears less feasible than for previously discussed scenarios. This is due to there being multiple equilibria for the distribution and therefore the negative aspects of station keeping a large asteroid away from the classical L_1 point appear less worthwhile.

Three cloud generation methods were discussed; sublimation of material from the asteroid surface, in-situ extraction followed by ejection by a mass driver and the fragmentation of a rubble-pile asteroid by increasing its rotation rate. Following a literature review of these three different methods it was concluded that the mass driver mechanism is the most suitable for the ejection of material to form a dust cloud, though the sublimation of material from the surface of an asteroid is more suitable for the capture process. This reasoning is based on the high velocities readily achievable using solar sublimation which will be very suitable for providing thrust to an asteroid, though using these high velocities has previously been shown to be highly inefficient for the purposes of geoengineering. Therefore the mass driver, which enables greater control over the ejection characteristics, is the most suitable method.

8.1.4 Main Conclusions

The main conclusions of this thesis, in summary, are;

- Dust cloud methods of space-based geoengineering are a feasible alternative to solid reflector/refractor methods.

- Smaller grain sizes are more mass efficient for the purposes of space-based geoengineering.
- Dust clouds released/ejected from the equilibrium position of the dust grains require less mass than when released from the classical L_1 point.
- The mass of an asteroid required to gravitationally anchor a dust cloud in the vicinity of the L_1 point is currently, and in the far-term, too great to be feasibly captured.
- The ejection of material from an asteroid surface is sensitive to the initial velocity and angle of ejection, with optimum conditions being found for ejection from the classical L_1 and new equilibrium positions.
- Accounting for a range of ejected grain sizes decreases the mass efficiency of the dust cloud methods, placing significant demands on the grain processing.
- The dust cloud methods of space-based geoengineering are capable of offsetting a predicted increase in mean global temperature of 2°C, though the decrease in local temperature is weighted towards the equatorial regions. This is particularly the case for the Earth ring where the decrease only occurs in low latitude regions such that strong side effects in the local climate are likely.
- The most suitable method for ejecting material from the surface of an asteroid is using a mass driver equipped spacecraft.
- The technical implementation of the full dust cloud geoengineering scheme will take several decades to implement, providing the legal and political mechanisms for implementation are in place.

8.2 Future Research

The investigations conducted in this thesis have enabled a good understanding of the dynamics and feasibility of the space-based geoengineering concepts discussed. This has enabled a number of areas of future research to be identified.

The use of the transition matrix, described in Sec. 2.1.4, to propagate the position of dust grains enables large numbers of particles to be used in comparison to the propagation of the full equations of motion. However, the transitions matrix can only be considered accurate over relatively

short distances and timeframes. Therefore, an investigation of the dust grain positions over much longer timeframes is an interesting future avenue of research. These dynamics should include the perturbations due to the Moon, and other surface forces such as the Poynting-Robertson effect and the solar wind, to determine paths taken by the dust grains after leaving the vicinity of the L_1 point. From this the fraction of particles found to collide with Earth will be a significant result. Also of interest is the average time a dust grain spends within the LEO, MEO and GEO orbit zones and to calculate the flux of particles passing through the L_2 point where some spacecraft are located. Finally, these dust grains may also spend some time directly in-between the Earth and Sun and may therefore block solar radiation, thus decreasing the mass of dust required.

The model using the ejected cloud dynamics determines the final results assuming only a single ejection direction. However, this will lead to an unbalanced acceleration that will require offsetting to maintain the asteroids position. Therefore, the mass of dust required to achieve the required insolation change should be calculated with an additional ejecta cloud in the opposite direction to the optimum. Further advancements to the ejected cloud model will be to investigate the optimum ejection direction when angles out of the rotational plane are considered.

As has been discussed previously, the ejection of a cloud with a given range of dust grain sizes will not have a single equilibrium position. Therefore a future avenue of research will be to find the optimum ejection position, between the classical L_1 point and the furthest known equilibrium position of a given size distribution. As well as the classical L_1 and displaced equilibrium positions a feasible location for a captured asteroid is a planar Lyapunov orbit or other stable orbit around L_1. Therefore the mass of dust required assuming ejection from points on these orbits is another interesting research investigation.

Further research should be performed in the area of material extraction and processing. Ultimately this research should determine whether the mass ejection rates required for the dust cloud methods are feasible and how large the spacecraft systems must be to achieve the required rate. A further goal of research into the material processing is to determine the current, and future, minimum grain size and distribution of sizes of the processed dust grains. Since the mass efficiency is dependent largely upon the size of the dust grains this avenue of research will greatly affect the mass requirement of the dust cloud methods.

The final research direction that has been identified is to use a more complex climate model to determine the effect that the distribution of insolation reduction over the Earth's surface has on the local and global climate. The model used in this thesis can only give a representation on the likely temperature change as a function of latitude band, whilst the climatic effect that the dust cloud methods have on local temperature change, as well as precipitation and other factors, must

be known.

Bibliography

[1] Technical Report on Space Debris. Technical report, UN, A/AC.105/720, 1999.

[2] S. Abe, T. Mukai, N. Hirata, O. S. Barnouin-Jha, A. F. Cheng, H. Demura, R. W. Gaskell, T. Hashimoto, K. Hiraoka, T. Honda, T. Kubota, M. Matsuoka, T. Mizuno, R. Nakamura, D. J. Scheeres, and M. Yoshikawa. Mass and Local Topography Measurements of Itokawa by Hayabusa. *Science*, 312(5778):1344–1347, 2006.

[3] R. G. Allen, R. Trezza, and M. Tasumi. Analytical integrated functions for daily solar radiation on slopes. *Agricultural and Forest Meteorology*, 139(1-2):55 – 73, 2006.

[4] A. Amrouni-Keiling, M. Azriel, A. Calzada, J. Cappaert, T. Pultarova, T. čolakov, L. Surdo, A. Cotuna, Y. Wei, E. Dapp, B. J. Wilcock, A. Daurskikh, N. Wong, D. DeLatte, F. Yang, J. Drew, J. Yu, A. Henry, M. Kane, R. Kovacs, and P. Platzer. EC2LIPSE: Exploring Climate Change Lagrangian 1 Point Solutions for Earth. Master's thesis, International Space University, 2012. MSc Thesis.

[5] R. Angel. Feasibility of cooling the Earth with a cloud of small spacecraft near the inner Lagrange point (L_1). *Proceedings of the National Academy of Sciences*, 103(46):17184–17189, 2006.

[6] S. I. Anisimov, B. S. Luk'yanchuk, and A. Luches. An analytical model for three-dimensional laser plume expansion into vacuum in hydrodynamic regime. *Applied Surface Science*, 96-98: 24–32, 1996.

[7] G. Bala. Problems with geoengineering schemes to combat climate change. *Current Science*, 96:41–48, 2009.

[8] G. Bala, K. Caldeira, M. Wickett, T. J. Phillips, D. B. Lobell, C. Delire, and A. Mirin. Combined climate and carbon-cycle effects of large-scale deforestation. *Proceedings of the National Academy of Sciences*, 104(16):6550–6555, 2007.

[9] G. Bala, P. B. Duffy, and K. E. Taylor. Impact of geoengineering schemes on the global

hydrological cycle. *Proceedings of the National Academy of Sciences*, 105(22):7664–7669, 2008.

[10] O. S. Barnouin-Jha, A. F. Cheng, T. Mukai, S. Abe, N. Hirata, R. Nakamura, R. W. Gaskell, J. Saito, and B. E. Clark. Small-scale topography of 25143 Itokawa from the Hayabusa laser altimeter. *Icarus*, 198(1):108–124, 2008.

[11] M. J. S. Belton, C. R. Chapman, P. C. Thomas, M. E. Davies, R. Greenberg, K. Klaasen, D. Byrnes, L. D'Amario, S. Synnott, T. V. Johnson, A. McEwen, W. J. Merline, D. R. Davis, J. M. Petit, A. Storrs, J. Veverka, and B. Zellner. Bulk density of asteroid 243 Ida from the orbit of its satellite Dactyl. *Nature*, 374(6525):785–788, 1995.

[12] R. Bewick, J. P. Sanchez, and C. R. McInnes. The feasibility of using an L_1 positioned dust cloud as a method of space-based geoengineering. *Advances in Space Research*, 49(7): 1212–1228, 2012.

[13] R. Bewick, J. P. Sanchez, and C. R. McInnes. Gravitationally bound geoengineering dust shade at the inner Lagrange point. *Advances in Space Research*, 50(10):1405–1410, 2012.

[14] R. Bewick, C. Lcking, C. Colombo, J. Sanchez, and C. McInnes. Heliotropic Dust Rings for Earth Climate Engineering. *Advances in Space Research*, 51:1132–1144, 2013.

[15] R. P. Binzel. The torino impact hazard scale. *Planetary and Space Science*, 48(4):297 – 303, 2000.

[16] D. Bodansky. May we engineer the climate? *Climatic Change*, 33(3):309–321, 1996.

[17] C. Bombardelli. Artificial spin-up and fragmentation of sub-kilometre asteroids. *Acta Astronautica*, 65(7-8):1162–1167.

[18] T. C. Bond, S. J. Doherty, D. W. Fahey, P. M. Forster, T. Berntsen, B. J. DeAngelo, M. G. Flanner, S. Ghan, B. Krcher, D. Koch, S. Kinne, Y. Kondo, P. K. Quinn, M. C. Sarofim, M. G. Schultz, M. Schulz, C. Venkataraman, H. Zhang, S. Zhang, N. Bellouin, S. K. Guttikunda, P. K. Hopke, M. Z. Jacobson, J. W. Kaiser, Z. Klimont, U. Lohmann, J. P. Schwarz, D. Shindell, T. Storelvmo, S. G. Warren, and C. S. Zender. Bounding the role of black carbon in the climate system: A scientific assessment. *Journal of Geophysical Research: Atmospheres*, In Press, 2013.

[19] M. Boslough and D. Crawford. Low-altitude airbursts and the impact threat. *International Journal of Impact Engineering*, 35(12):1441 – 1448, 2008.

[20] E. Bowell, B. Hapke, D. Dominique, K. Lumme, J. I. Peltoniemi, and A. W. Harris. *Application of photometric models to asteroids*, pages 524–556. University of Arizona Press, Tucson, 1989.

[21] V. Bronshten. Nature and destruction of the tunguska cosmical body. *Planetary and Space Science*, 48(9):855–870, 2000.

[22] J. Brophy, F. Culick, and L. Friedman. Asteroid Retrieval Feasibility Study. *Keck Institute for Space Studies*, 2012.

[23] M. Bunzl. Researching geoengineering: should not or could not? *Environmental Research Letters*, 4(4):045104, 2009.

[24] K. Caldeira and D. Keith. The need for climate engineering research. *Issues in Science and Technology*, pages 57–62, Fall, 2010.

[25] K. Caldeira and L. Wood. Global and Arctic climate engineering: numerical model studies. *Philosophical Transactions of the Royal Society A: Mathematical, Physical and Engineering Sciences*, 366(1882):4039–4056, 2008.

[26] W. D. Carrier. Particle Size Distribution of Lunar Soil. *Journal of Geotechnical and Geoenvironmental Engineering*, 129(10):956–959, 2003.

[27] W. D. Carrier, III, J. K. Mitchell, and A. Mahmood. The relative density of lunar soil. *Proceedings of the Lunar Science Conference*, 4:2403–2411, 1973.

[28] C. R. Chapman, E. V. Ryan, W. J. Merline, G. Neukum, R. Wagner, P. C. Thomas, J. Veverka, and R. J. Sullivan. Cratering on Ida. *Icarus*, 120(1):77–86, 1996.

[29] S. R. Chesley, P. W. Chodas, A. Milani, and D. K. Yeomans. Quantifying the Risk Posed by Potential Earth Impacts. *Icarus*, 159(2):423–432, 2002.

[30] C. Colombo and C. R. McInnes. Orbital dynamics of smart dust devices with solar radiation pressure and drag. *Journal of Guidance, Control, and Dynamics*, 34(6):1613–1631, 2011.

[31] C. Colombo, C. Lücking, and C. R. McInnes. Orbital Dynamics of High Area-to-Mass Ratio Spacecraft under the Influence of J_2 and Solar Radiation Pressure. In *In: 62nd International Astronautical Congress, Cape Town*, number IAC-11.C1.4.8, 2011.

[32] I. de Pater and J. J. Lissauer. *Planetary Sciences*. Cambridge University Press, 2001.

[33] G. M. Douglas. Can we control El Niño? *Environmental Research Letters*, 4(4):045111, 2009.

[34] J. T. Early. Space-based Solar Shield to Offset Greenhouse Effect. *JBIS*, 42(12):567–569, 1989.

[35] B. Ewing, D. Moore, S. Goldfinger, A. Oursler, A. Reed, and M. Wackernagel. The ecological footprint atlas 2012. *The Global Footprint Network*, 2010.

[36] P. Foukal, C. Froöhlich, H. Spruit, and T. Wigley. Variations in solar luminosity and their effect on the Earths climate. *Nature*, 443:161–166, 2006.

[37] T. A. Fox and L. Chapman. Engineering geo-engineering. *Meteorological Applications*, 18 (1):1–8, 2011.

[38] I. Galindo. Extinction of short wave solar radiation due to El Chichon stratospheric aerosol. *Atmosfera*, 5:259–268, 1992.

[39] B. Govindasamy and K. Caldeira. Geoengineering Earth's radiation balance to mitigate CO_2-induced climate change. *Geophysical Research Letters*, 27(14):2141–2144, 2000.

[40] B. Govindasamy, S. Thompson, P. B. Duffy, K. Caldeira, and C. Delire. Impact of geoengineering schemes on the terrestrial biosphere. *Geophys. Res. Lett.*, 29(22):2061, 2002.

[41] B. Govindasamy, K. Caldeira, and P. B. Duffy. Geoengineering Earth's radiation balance to mitigate climate change from a quadrupling of CO_2. *Global and Planetary Change*, 37(1-2): 157–168, 2003.

[42] D. P. Hamilton and A. V. Krivov. Circumplanetary Dust Dynamics: Effects of Solar Gravity, Radiation Pressure, Planetary Oblateness, and Electromagnetism. *Icarus*, 123(2):503–523, 1996.

[43] A. W. Harris. The Rotation Rates of Very Small Asteroids: Evidence for 'Rubble Pile' Structure. *Lunar and Planetary Science*, 27, 1996.

[44] G. Hong, P. Yang, and F. Weng. Microwave scattering properties of sand particles: Application to the simulation of microwave radiances over sandstorms. *Journal of Quantitative Spectroscopy and Radiation*, 109:684–702, 2008.

[45] International Energy Agency. Key world energy statistics. 2011.

[46] IPCC. Contribution of Working Groups I, II and III to the Fourth Assessment Report of the Intergovernmental Panel on Climate Change. *Core Writing Team, Pachauri, R.K. and Reisinger, A. (Eds.), IPCC, Geneva, Switzerland. pp 104*, 2007.

[47] P. J. Irvine, A. Ridgwell, and D. J. Lunt. Assessing the regional disparities in geoengineering impacts. *Geophys. Res. Lett.*, 37(18):L18702, 2010.

[48] M. Z. Jacobson and J. E. Ten Hoeve. Effects of Urban Surfaces and White Roofs on Global and Regional Climate. *Journal of Climate*, 25:1028–1044, 2012.

[49] A. Jones, J. Haywood, O. Boucher, B. Kravitz, and A. Robock. Geo-engineering by stratospheric SO2 injection: results from the Met Office HasGEM2 climate model and comparison with the Goddard Institute for Space Studies ModelE. *Atmospheric Chemistry and Physics*, 10:5999–6006, 2010.

[50] R. Kahle, E. Khrt, G. Hahn, and J. Knollenberg. Physical limits of solar collectors in deflecting Earth-threatening asteroids. *Aerospace Science and Technology*, 10(3):256–263, 2006.

[51] D. S. Kaufman, D. P. Schneider, N. P. McKay, C. M. Ammann, R. S. Bradley, K. R. Briffa, G. H. Miller, B. L. Otto-Bliesner, J. T. Overpeck, B. M. Vinther, and A. L. k. P. Members. Recent Warming Reverses Long-Term Arctic Cooling. *Science*, 325(5945):1236–1239, 2009.

[52] M.-B. Kellenrode. *Space physics: an introduction to plasmas and particles in the heliosphere and magnetospheres*. Springer, 2004.

[53] H. Kimura and I. Mann. The electric charging of interstellar dust in the solar system and consequences for its dynamics. *The Astrophysical Journal*, 499:454–462, 1998.

[54] D. Koch and J. Hansen. Distant origins of arctic black carbon: A goddard institute for space studies modele experiment. *Journal of Geophysical Research*, 110:D04204, 2005.

[55] W. S. Koon, M. Lo, J. Marsden, and S. Ross. *Dynamical Systems, the Three-Body Problem and Space Mission Design*. Marsden Books, 2006.

[56] A. Krivov and J. Getino. Orbital evolution of high-altitude balloon satellites. *Astronomy and Astrophysics*, 318:308–314, 1997.

[57] A. V. Krivov, L. L. Sokolov, and V. V. Dikarev. Dynamics of Mars-orbiting dust: Effects of light pressure and planetary oblateness. *Celestial Mechanics and Dynamical Astronomy*, 63 (3):313–339, 1995.

[58] R. D. Launius. Why go to the moon? the many faces of lunar policy. *Acta Astronautica*, 70: 165 – 175, 2012.

[59] J. Li, M. F. A'Hearn, and L. A. McFadden. Photometric analysis of Eros from NEAR data. *Icarus*, 172(2):415–431, 2004.

[60] Q. Li, Z. Li, G. Li, J. Meng, and J. Tang. Experimental and numerical seismic investigations of the three gorges dam. *Engineering Structures*, 27(4):501 – 513, 2005.

[61] M. E. Lippmann. In-space fabrication of thin-film structures. *NASA CR-1969*, 1972.

[62] C. Lücking. Space mission applications of high area-to-mass ratio orbital dynamics. *PhD Thesis, University of Strathclyde*, 2013.

[63] M. Lukacs. World's biggest geoengineering experiment 'violates' UN rules. http://www.guardian.co.uk/environment/2012/oct/15/pacific-iron-fertilisation-geoengineering, 2012. Last accessed 01/02/2013.

[64] D. J. Lunt, A. Ridgwell, P. J. Valdes, and A. Seale. "Sunshade World": A fully coupled GCM evaluation of the climatic impacts of geoengineering. *Geophys. Res. Lett.*, 35(12): L12710, 2008.

[65] D. Lupishko and Z. Pozhalova. Near-Earth Objects 400 Years after Galileo: Physical Properties and Internal Structure. *Proceedings of the International Astronomical Union*, 6(Symposium S269):234–239, 2010.

[66] H. D. Matthews and K. Caldeira. Transient climatecarbon simulations of planetary geoengineering. *Proceedings of the National Academy of Sciences*, 104(24):9949–9954, 2007.

[67] M. Mautner. A Space-based Solar Screen against Climatic Warming. *JBIS*, 44(3):135–138, 1991.

[68] K. McGuffie and A. Henderson-Sellers. *A climate modelling primer*. Wiley, 1987.

[69] C. R. McInnes. Space-based geoengineering: challenges and requirements. *Proceedings of the Institution of Mechanical Engineers, Part C: Journal of Mechanical Engineering Science*, 224(3):571–580, 2010.

[70] D. McKay, G. Heiken, A. Basu, G. Blanford, S. Simon, R. Reedy, B. French, and J. Papike. *The Lunar Regolith, In: The Lunar Sourcebook*. Cambridge University Press, 1991.

[71] H. J. e. a. Melosh. *Non-Nuclear Strategies for Deflecting Comets and Asteroids*. University of Arizona Press, 1994.

[72] B. Metz, M. L. O. Davidson, H. C. de Coninck, and L. A. M. (eds.). IPCC, 2005: IPCC Special Report on Carbon Dioxide Capture and Storage. Prepared by and Working Group III of the Intergovernmental Panel on Climate Change.

[73] T. Minato, M. Khler, H. Kimura, I. Mann, and T. Yamamoto. Momentum transfer to interplanetary dust from the solar wind. *Astronomy and Astrophysics*, 424(2):L13–L16, 2004.

[74] J. C. Moore, S. Jevrejeva, and A. Grinsted. Efficacy of geoengineering to limit 21st century sea-level rise. *Proceedings of the National Academy of Sciences*, 107(36):15699–15703, 2010.

[75] J. Morgan, M. Warner, the Chicxulub Working Group, J. Brittan, R. Buffler, A. Camargo, G. Christeson, P. Denton, A. Hildebrand, R. Hobbs, H. Macintyre, G. Mackenzie, P. Maguire, L. Marin, Y. Nakamura, V. Pilkington, Mark andSharpton, D. Snyder, G. Suarez, and A. Trejo. Size and morphology of the Chicxulub impact crater. *Nature*, 390(6659):472–476, 1997.

[76] N. Nakicenovic, J. Alcamo, G. Davis, B. de Vries, J. Fenhann, S. Gaffin, K. Gregory, A. Gribler, T. Y. Jung, T. Kram, E. L. La Rovere, L. Michaelis, S. Mori, T. Morita, W. Pepper, H. Pitcher, L. Price, K. Riahi, A. Roehrl, H.-H. Rogner, A. Sankovski, M. Schlesinger,

P. Shukla, S. Smith, R. Swart, S. van Rooijen, N. Victor, and Z. Dadi. Special report on emissions scenarios. Technical report, IPCC, 2000.

[77] New Scientist. 'Geoengineering' project was about salmon fishery. http://www.newscientist.com/article/mg21628883.600-geoengineering-project-was-about-salmon-fishery.html, 2012. Last accessed 01/02/2013.

[78] J. Olds, A. Charania, M. Graham, and J. Wallace. The League of Extraordinary Machines: A Rapid and Scalable Approach to Planetary Defense Against Asteroid Impactors. Technical report, NASA Institute for Advanced Concepts, 30th April 2004.

[79] J. Pearson, J. Oldson, and E. Levin. Earth rings for planetary environment control. *Acta Astronautica*, 58(1):44–57, 2006.

[80] J. Raven, K. Caldeira, H. Elderfield, O. Hoegh-Guldberg, P. Liss, U. Riebesell, J. Shepherd, C. Turley, A. Watson, R. Heap, R. Banes, and R. Quinn. Ocean acidification due to increasing atmospheric carbon dioxide. June 2005.

[81] M. A. Riner, M. S. Robinson, J. M. Eckart, and S. J. Desch. Global survey of color variations on 433 Eros: Implications for regolith processes and asteroid environments. *Icarus*, 198(1): 67–76, 2008.

[82] M. S. Robinson, P. C. Thomas, J. Veverka, S. Murchie, and B. Carcich. The nature of ponded deposits on Eros. *Nature*, 413(6854):396–400, 2001. 10.1038/35096518.

[83] A. Robock, L. Oman, and G. L. Stenchikov. Regional climate responses to geoengineering with tropical and Arctic SO2 injections. *J. Geophys. Res.*, 113(D16):D16101, 2008.

[84] A. Robock, A. Marquardt, B. Kravitz, and G. Stenchikov. Benefits, risks, and costs of stratospheric geoengineering. *Geophys. Res. Lett.*, 36(19):L19703, 2009.

[85] J. P. Sanchez and C. R. McInnes. Accessibility of the resources of near Earth space using multi-impulse transfers. *AIAA/AAS Astrodynamics Specialist Conference, Toronto, Canada*, 2010.

[86] J. P. Sanchez and C. R. McInnes. Asteroid Resource Map for Near-Earth Space. *Journal of Spacecraft and Rockets*, 48(1):153–165, 2011.

[87] J. P. Sanchez, D. Garcia Yarnoz, E. M. Alessi, and C. R. McInnes. Gravitational capture opportunites for asteroid retrieval missions. In *In: 63rd International Astronautical Congress, 2012-10-01 - 2012-10-05, Naples*, 2012.

[88] H. Schaub and J. L. Junkins. *Analytical Mechanics of Space Systems*. AIAA, 2003.

[89] D. Scheeres, D. Durda, and P. Geissler. *The fate of asteroid ejecta*, pages p.527–544. University of Arizona Press, Tucson, 2002.

[90] D. J. Scheeres, S. J. Ostro, R. S. Hudson, and R. A. Werner. Orbits Close to Asteroid 4769 Castalia. *Icarus*, 121(1):67–87, 1996.

[91] D. J. Scheeres, S. J. Ostro, R. S. Hudson, E. M. DeJong, and S. Suzuki. Dynamics of Orbits Close to Asteroid 4179 Toutatis. *Icarus*, 132(1):53–79, 1998.

[92] H. Schmidt, K. Alterskjr, D. Bou Karam, O. Boucher, A. Jones, J. E. Kristjnsson, U. Niemeier, M. Schulz, A. Aaheim, F. Benduhn, M. Lawrence, and C. Timmreck. Solar irradiance reduction to counteract radiative forcing from a quadrupling of CO_2: climate responses simulated by four earth system models. *Earth Syst. Dynam.*, 3(1):63–78, 2012. ESD.

[93] S. H. Schneider. Geoengineering: Could or should we do it? *Climatic Change*, 33(3):291–302, 1996.

[94] Secretariat of the Convention on Biological Diversity. Assessment and Management of Alien Species that Threaten Ecosystems, Habitats and Species, 2001. BD Technical Paper no. 1.

[95] J. Shepherd, K. Caldeira, P. Cox, and J. Haigh. Geoengineering the climate. *Report of Royal Society working group of Geo-engineering*, 2009.

[96] V. Smetacek, C. Klaas, V. H. Strass, P. Assmy, M. Montresor, B. Cisewski, N. Savoye, A. Webb, F. d/'Ovidio, J. M. Arrieta, U. Bathmann, R. Bellerby, G. M. Berg, P. Croot, S. Gonzalez, J. Henjes, G. J. Herndl, L. J. Hoffmann, H. Leach, M. Losch, M. M. Mills, C. Neill, I. Peeken, R. Rottgers, O. Sachs, E. Sauter, M. M. Schmidt, J. Schwarz, A. Terbruggen, and D. Wolf-Gladrow. Deep carbon export from a Southern Ocean iron-fertilized diatom bloom. *Nature*, 487(7407):313–319, 2012. 10.1038/nature11229.

[97] M. H. Stevens, S. Lossow, J. Fiedler, G. Baumgarten, F.-J. Lbken, K. Hallgren, P. Hartogh, C. E. Randall, J. Lumpe, S. M. Bailey, R. Niciejewski, R. R. Meier, J. M. C. Plane, A. J. Kochenash, D. P. Murtagh, and C. R. Englert. Bright polar mesospheric clouds formed by main engine exhaust from the space shuttle's final launch. *Journal of Geophysical Research: Atmospheres*, 117(D19):n/a–n/a, 2012. ISSN 2156-2202. doi: 10.1029/2012JD017638. URL `http://dx.doi.org/10.1029/2012JD017638`.

[98] C. Struck. The feasibility of shading the greenhouse with dust clouds at the stable lunar Lagrange points. *Journal of the British Interplanetary Society*, 60(3):82–89, 2007.

[99] R. Sullivan, R. Greeley, R. Pappalardo, E. Asphaug, J. M. Moore, D. Morrison, M. J. S. Belton, M. Carr, C. R. Chapman, P. Geissler, R. Greenberg, J. Granahan, J. W. Head Iii, R. Kirk, A. McEwen, P. Lee, P. C. Thomas, and J. Veverka. Geology of 243 Ida. *Icarus*, 120 (1):119–139, 1996.

[100] E. Teller, L. Wodd, and R. Hyde. Global Warming and Ice Ages: Prospects for Physics-

Based Modulation of Global Change. *Lawrence Livermore National Laboratory, UCRL-231636/UCRL JC 128715*, 1997.

[101] K. K. Tung. Simple climate modelling. *Discrete and continuous dynamica systems B*, 7(3): 651–660, 2007.

[102] W. R. Turner, M. Oppenheimer, and D. S. Wilcove. A force to fight global warming. *Nature*, 462(7271):278–279, 2009. 10.1038/462278a.

[103] UNEP Convention on Biological Diversity. Report of the tenth meeting of the conference of the parties to the convention on biological diversity. Technical Report UNEP/CBD/COP/10/27, 2010.

[104] M. C. Urban, B. L. Phillips, D. K. Skelly, and R. Shine. The cane toads (Chaunus [Bufo] marinus)increasing ability to invade Australia is revealed by a dynamically updated range model. *Proceedings of the Royal Society B*, pages 1413–1419, 2007.

[105] M. Vasile. A Behavioral-Based Meta-Heuristic for Robust Global Trajectory Optimization. *IEEE Congress on Evolutionary Computation*, page 20562063, 2007.

[106] M. Vasile and M. Locatelli. A Hybrid Multiagent Approach for Global Trajectory Optimization. *Journal of Global Optimization*, 44(4):461–479, 2009.

[107] M. Vasile and C. Maddock. On the deflection of asteroids with mirrors. *Celestial Mechanics and Dynamical Astronomy*, 107(1):265–284, 2010.

[108] D. G. Victor. On the regulation of geoengineering. *Oxford Review of Economic Policy*, 24 (2):322–336, 2008.

[109] M. Wagner. Interaction of Interplanetary Dust Particles with magnetic clouds and their further orbital evolution. *PhD Thesis: Christian-Albrechts-Universität zu Kiel*, 2007.

[110] M. Wilck and I. Mann. Radiation pressure forces on "typical" interplanetary dust grains. *Planetary and Space Science*, 44(5):493–499, 1996.

[111] R. C. Willson and H. S. Hudson. The Sun's luminosity over a complete solar cycle. *Nature*, 351:42–44, 1991.

[112] O. W. Wingenter, S. M. Elliott, and D. R. Blake. New Directions: Restoring the westerly winds in the Southern Hemisphere: Climates lever. *Atmospheric Environment*, 44(31):3866–3868, 2010.

[113] H. Yano, T. Kubota, H. Miyamoto, T. Okada, D. Scheeres, Y. Takagi, K. Yoshida, M. Abe, S. Abe, O. Barnouin-Jha, A. Fujiwara, S. Hasegawa, T. Hashimoto, M. Ishiguro, M. Kato, J. Kawaguchi, T. Mukai, J. Saito, S. Sasaki, and M. Yoshikawa. Touchdown of the Hayabusa Spacecraft at the Muses Sea on Itokawa. *Science*, 312(5778):1350–1353, 2006.

Appendix A

Earth Ring Appendix

The following is a discussion of the orbital dynamics of the Earth ring concept discussed in Chapter 5. This work was performed by Charlotte Lücking and Camilla Colombo in collaboration with the author.

A.1 Earth Ring Orbital Dynamics

In this section the orbital dynamics of Earth orbiting dust is discussed. The in-plane orbital evolution due to solar radiation pressure and the J_2 effect are investigated analytically. The out-of-plane effects and resulting evolution of the inclination are investigated numerically.

A.1.1 Hamiltonian model of dust orbital dynamics

In order to tackle the problem analytically, a simplified planar model is used. We describe the dynamics of dust in an Earth-centred synodic reference frame. We then consider a dust grain orbiting on a planar orbit (i.e. the orbit has zero inclination) with the simplifying assumption that the equatorial plane is in the ecliptic (i.e. the obliquity angle of the ecliptic with respect to the equator is set to zero). As will be shown later, this simplifying assumption provides an adequate description of the evolution of the dust with the level of accuracy intended for the thesis, while allowing an analytical description of the underlying dynamics of the dust ring.

In the frame as described above, three parameters are needed to define any in-plane orbit.

The eccentricity, e , semi-major axis, a, and the angle between the direction of the solar radiation and the radius of the perigee with respect to the Earth, ϕ. The position of the dust grain is also defined with respect to the direction of the sunlight using the angle θ, where $\theta = \phi + f$ with true anomaly f. Figure A.1 shows the geometry of the reference frame.

Work presented by [42] and [56] on the orbital dynamics of high area-to-mass ratio spacecraft introduces an approximate Hamiltonian for planar orbits under the effects of solar radiation pressure and the Earth's oblateness [56]. This analytical model does not consider eclipses and the tilt of the Earth's rotational axis with respect to the ecliptic plane. As a consequence, the semi-major axis remains constant and the evolution of the orbit can be described only by its eccentricity e, defining the changing shape of the orbit, and solar radiation perigee angle ϕ, defining the orbit orientation. The change of orbital elements due to solar radiation pressure and J_2 with respect to the progression of the angle between the position of the Sun on the ecliptic with respect to the vernal equinox, $\lambda_\odot$, is [56]:

$$\frac{\mathrm{d}e}{\mathrm{d}\lambda_\odot} = -\alpha\sqrt{1-e^2}\sin\phi \tag{A.1}$$

$$\frac{\mathrm{d}\phi}{\mathrm{d}\lambda_\odot} = -\alpha\frac{\sqrt{1-e^2}}{e}\cos\phi + \kappa\frac{1}{\left(1-e^2\right)^2} - 1 \tag{A.2}$$

where α is the radiation pressure parameter and κ the J_2 effect parameter, defined by:

$$\alpha = \frac{3}{2}a_{SRP}\frac{a^2}{\mu}\frac{n}{n_\odot} \tag{A.3}$$

$$\kappa = \frac{3}{2}J_2\frac{R_E^2}{a^2}\frac{n}{n_\odot} \tag{A.4}$$

where $n = \sqrt{\mu/a^3}$ is the orbit angular velocity of the dust grain on its Earth-centred orbit, μ is the gravitational parameter of the Earth, J_2 its second order zonal harmonic coefficient, R_E its radius and $n_\odot$ the orbit rate of the Earth around the Sun. While κ is only a function of the semi-major axis, α is also dependent on a_{SRP}, the acceleration due to solar radiation pressure (SRP). For circular objects with radius r and density δ it can be calculated as follows [57]:

$$a_{SRP} = \frac{F_\odot}{c}\frac{4}{3\delta r} \tag{A.5}$$

where $F_\odot$ is the solar flux and c is the speed of light. The resulting Hamiltonian is [56]:

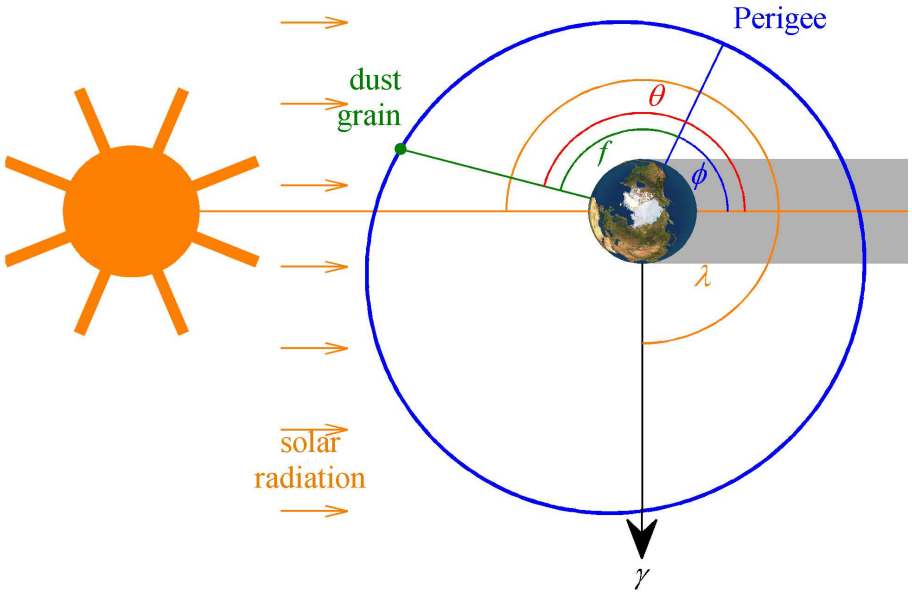

Figure A.1: Geometry of an in-plane orbit in the synodic reference frame.

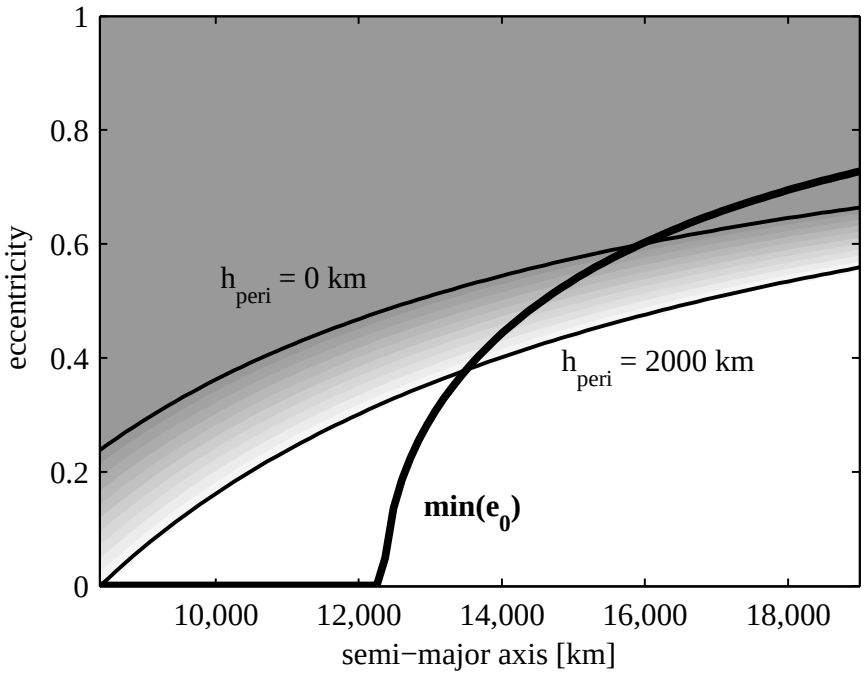

Figure A.2: Minimum eccentricity ($\alpha = 0$) of the heliotropic equilibrium orbit $min(e_0)$ as a function of semi-major axis. The gradient in the background corresponds to perigee altitudes of the corresponding orbit within $h_{peri} = 0\,km$ and $h_{peri} = 2,000\,km$, specifically marked, where the effect of drag is non-negligible.

$$H = -\sqrt{1-e^2} + \alpha e \cos\phi - \frac{\kappa}{3\sqrt{1-e^2}^3} \tag{A.6}$$

For a certain range of semi-major axis and area-to-mass-ratios, the Hamiltonian in Eq. (A.6) allows, among all its stationary points, a stable equilibrium (i.e., $de/d\lambda_\odot = 0$ and $d\phi/d\lambda_\odot = 0$), at $\phi = 0$ with eccentricity e_0 as shown by [31]. This equilibrium point represents frozen orbits with their apogee pointing in the direction of the Sun. These orbits are therefore termed *heliotropic orbits*. If the solar radiation pressure parameter is zero, $\alpha = 0$ (i.e. without the effect of SRP), the equilibrium at e_{0,J_2} corresponds to an orbit with a frozen orientation with respect to the Sun solely due to the J_2 effect. Such an orbit would have its apse-line precessing at the same rate as the Earth's motion around the Sun. While the SRP parameter is zero, the equilibrium exists for any orbit orientation. However, as soon as the SRP parameter is non-zero the equilibrium can only be found for Sun-pointing apogees. For increasing values of the SRP parameter the equilibrium eccentricity e_0 increases, with the J_2-only equilibrium eccentricity e_{0,J_2} (i.e., $\alpha = 0$) being the minimum boundary value at a given semi-major axis [31]. Figure A.2 shows e_{0,J_2} as a function of semi-major axis. In the background a gradient shows the perigee altitude within a range of $h_{peri} = 0\,\text{km}$ and $h_{peri} = 2,000\,\text{km}$ specifically marked. An altitude of 2,000 km is approximately the altitude from which the effect of drag on the orbital evolution is negligible, even for very high area-to-mass ratios [30]. A ring of dust at or beyond this distance from the Earth will remain in place infinitely. It can be seen from the figure that heliotropic orbits do not exist above c. 16,000 km semi-major axis. Above a semi-major axis of c. 13,500 km semi-major axis they become unstable due to drag.

A.1.2 In-plane orbital evolution of dust

A small grain size is desirable as the mass efficiency of geo-engineering is inversely proportional to grain radius. If a grain with a specific area-to-mass ratio is released in any orbit, its orbit will then evolve by librating or rotating around its equilibrium eccentricity [31]. The greater the initial distance from the libration point in the phase space the larger the maximum eccentricity reachable. Therefore, it is more efficient to release the dust grains (with different area-to-mass ratios) at a higher initial eccentricity to prevent them from de-orbiting due to drag. Figure A.3 compares the orbital evolution of grains with different radii when they are released in a circular and elliptical orbit with the same semi-major axis. A grey colour marks the area in which the orbits will experience drag and we consider grains which pass through this area as 'lost". It can be seen that while for an initially circular orbit all grains with a radius smaller than 13 μm will be lost (see Figure A.3a), in the elliptical case grains as small as 6.5 μm survive (see Figure A.3b). It follows that release at

the critical eccentricity yields the best results and that the smallest possible grain radius at any semi-major axis is the one which has its equilibrium point at the critical eccentricity.

A.1.3 Choice of feeder orbit

We can determine the smallest possible grain radius as a function of semi-major axis by finding the particle radius for which the equilibrium eccentricity e_0 is equal to e_{crit}, the critical eccentricity corresponding to the smallest allowable perigee height h_{peri}:

$$e_{crit} = 1 - \frac{R_E + min(h_{peri})}{a} \tag{A.7}$$

To find the minimum particle radius we set $\phi = 0$ in Eq. (A.2), set $d\phi/d\lambda_\odot$ equal to zero, substitute e with e_{crit} in Eq. (A.7), solve for α and combine with Eqs. (A.3) and (A.6) to obtain:

$$r_{min} = \frac{2F_\odot}{cn_\odot\delta}\sqrt{\frac{a}{\mu}}\frac{\sqrt{1-e_{crit}^2}^5}{e_{crit}\left(\kappa(a) - (1-e_{crit}^2)\right)} \tag{A.8}$$

The density δ for the asteroid grains used is $3{,}500\,\mathrm{kg\,m^{-3}}$ as in [110].

Another measure of the efficiency of a ring for geo-engineering is how much of its orbital period a grain spends blocking solar radiation. This is dependent on the orbital geometry and takes into account that a grain travels slower at apogee than at perigee. We term the resulting percentage (of time spent in the useful region) the geometrical efficiency which can be found numerically. Using these indicators of efficiency we can next choose the semi-major axis likely to be most efficient for geo-engineering. Figure A.4 shows the dust grain minimum radius and the geometrical efficiency of a circular orbit and an orbit with $e = e_{crit}$ as a function of semi-major axis. The minimum grain size is important as smaller grains have higher area-to-mass ratios and thus offer better mass efficiency when used to block sunlight. For the geometrical efficiency both the circular and elliptical orbits are considered because we will be releasing grains with a distribution of radii and not all of these have an equilibrium at the critical eccentricity. Thus, some grains will librate in eccentricity between $e \geq 0$ and $e = e_0$. A good compromise between low minimum grain size and high geometrical efficiency is desired. Considering the results in Figure A.4, an advantageous initial orbit for the dust ring, referred thereafter as the feeder orbit, has a Sun-pointing apogee with radius 10,250km ($a = 9318$km) and an eccentricity of $e_f = 0.1$.

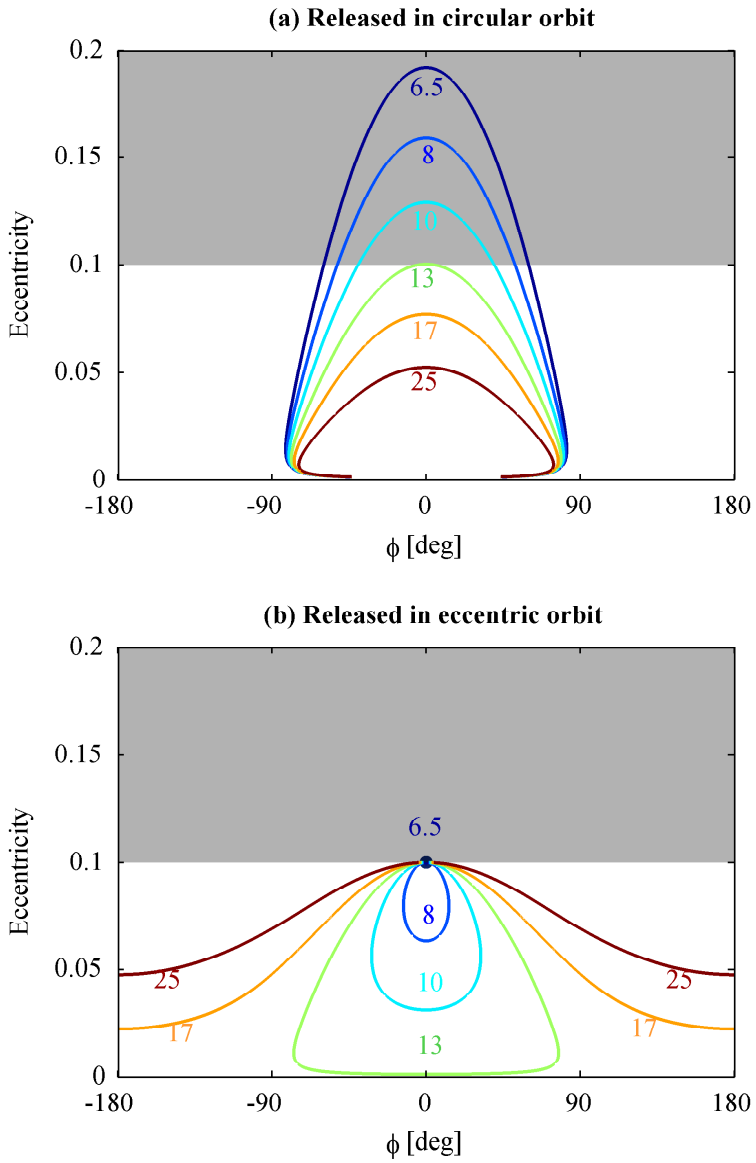

Figure A.3: Orbital evolution in the $e-\phi$ phase space for grains with different radii from $6.5-25\mu m$ microns released at c. 9,300km semi-major axis with $e = 0$ (a) and $e = e_{crit}$ (b). The grey zone marks the area in which the perigee of the orbit is closer than 2,000 km to the surface of the Earth.

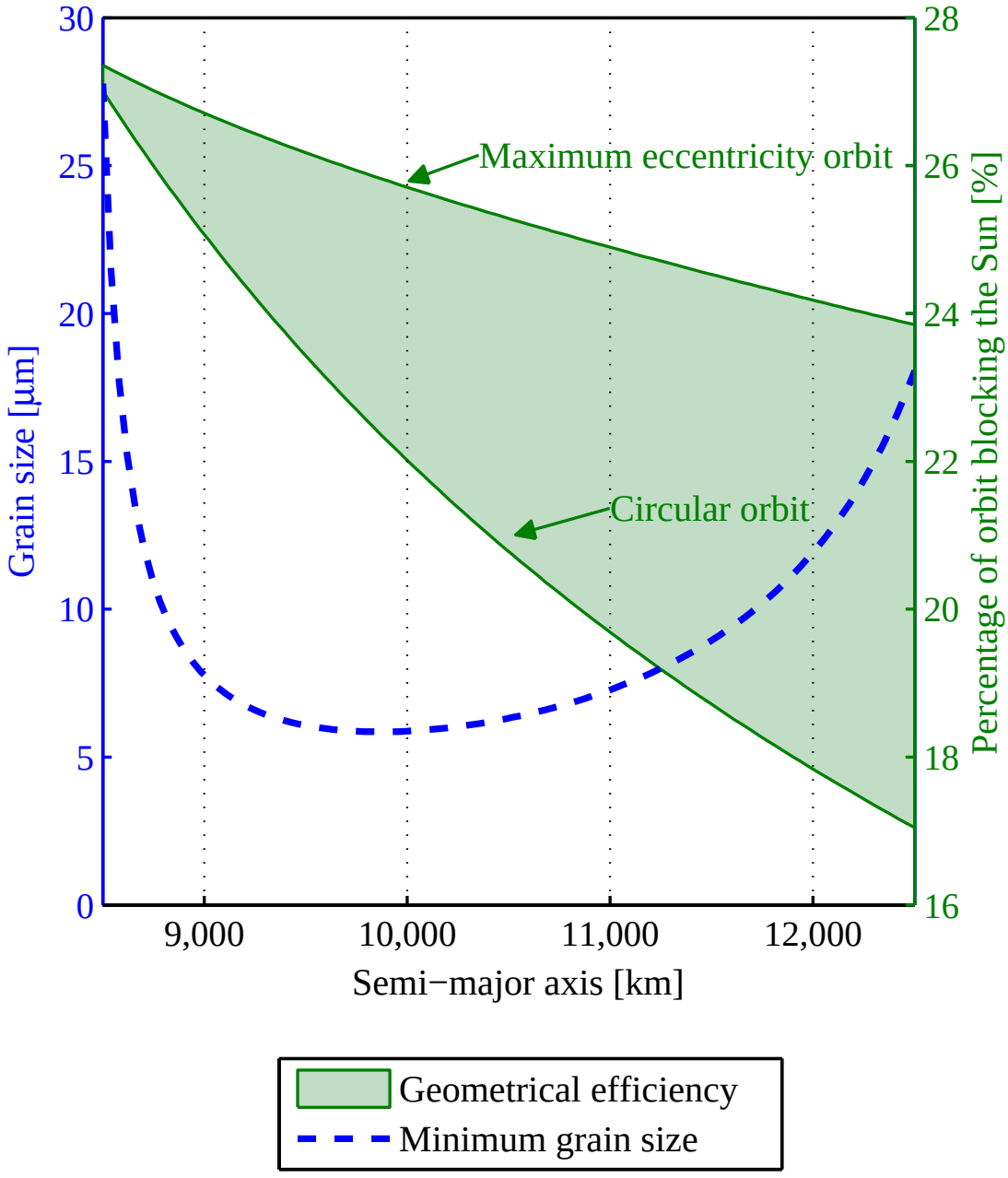

Figure A.4: Geo-engineering efficiency indicators (grain size and orbit geometry) with semi-major axis. The minimum grain size which can be deployed at the given semi-major axis without rapid decay is given on the left axis. The geometrical efficiency is given on the right axis as a range from a circular orbit to an orbit with critical eccentricity and Sun-pointing apogee.

A.1.4 3D orbital evolution of dust

In the following section the simplified assumption used in Section A.1.1 of a zero obliquity angle of the ecliptic with respect to the equator will be removed. The actual evolution of dust particles differs from the one predicted by the Hamiltonian in Eq. (A.6) because of the 23.5° tilt angle of the equator with respect to the ecliptic plane. As a consequence, a dust ring initially positioned on the ecliptic plane will be subject to a nodal drift, due to the effect of J_2 and SRP and out of plane oscillations under solar radiation pressure. As analysed in [31], the simplified planar phase space approximation used in Section A.1.1 maintains its structure for small tilt angle (less than 30° as in the Earth case) and small inclinations. Figure A.5 represents the 3D evolution of the ring over a period of 20 years, propagated through a set of non-singular Lagrangian elements derived by Krivov [57] and reported in [31] to correct a typo in Krivov's paper (in the SRP term). The effect of eclipses is neglected. The harmonic oscillation in the $e-\phi$ phase space is still recognisable, although the single line for a given area-to-mass ratio extends to a band (see Figure A.5a). Note that a three-dimensional definition of the solar radiation perigee angle is adopted here as

$$\phi = \Omega + \omega - (\lambda_{\odot} - \pi) \tag{A.9}$$

where Ω and ω are respectively the argument of the ascending node (from the vernal equinox) and the argument of perigee of the grain's orbit, and $\lambda_{\odot}$ defines the true longitude of the Sun on the ecliptic.

A full characterisation of the Earth ring evolution is given when we consider also the perturbations to the inclination and the ascending node, which describes the vertical structure (see Figure A.5b). The dust grains display complex inclination time history, however the magnitude of the inclination changes are limited to a maximum of 0.2°, this occurring for the smallest grains, as shown in Figure A.6. Depending on the season, the apogee point of the heliotropic orbits will oscillate below and above the ecliptic plane, as can be seen in Figure A.7. This figure represents the seasonal orbital evolution of the ring over 20 years. The colour scale represents the range of dust radii used.

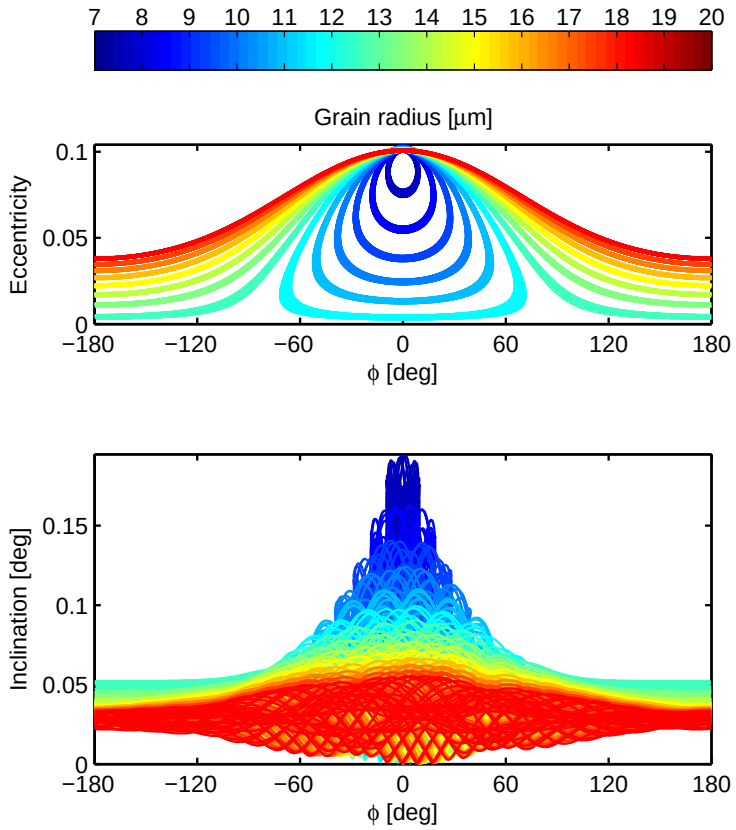

Figure A.5: 3D evolution of the dust ring over a period of 20 years. a) Planar structure in the $e-\phi$ phase space and b) vertical structure in the $i-\phi$ phase space.

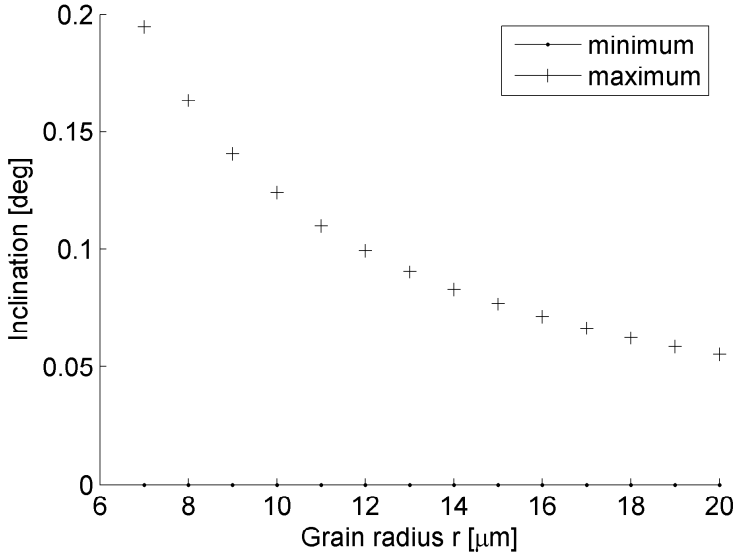

Figure A.6: Maximum (cross) and minimum (dot) inclination change on the equator as function of the grain radius.

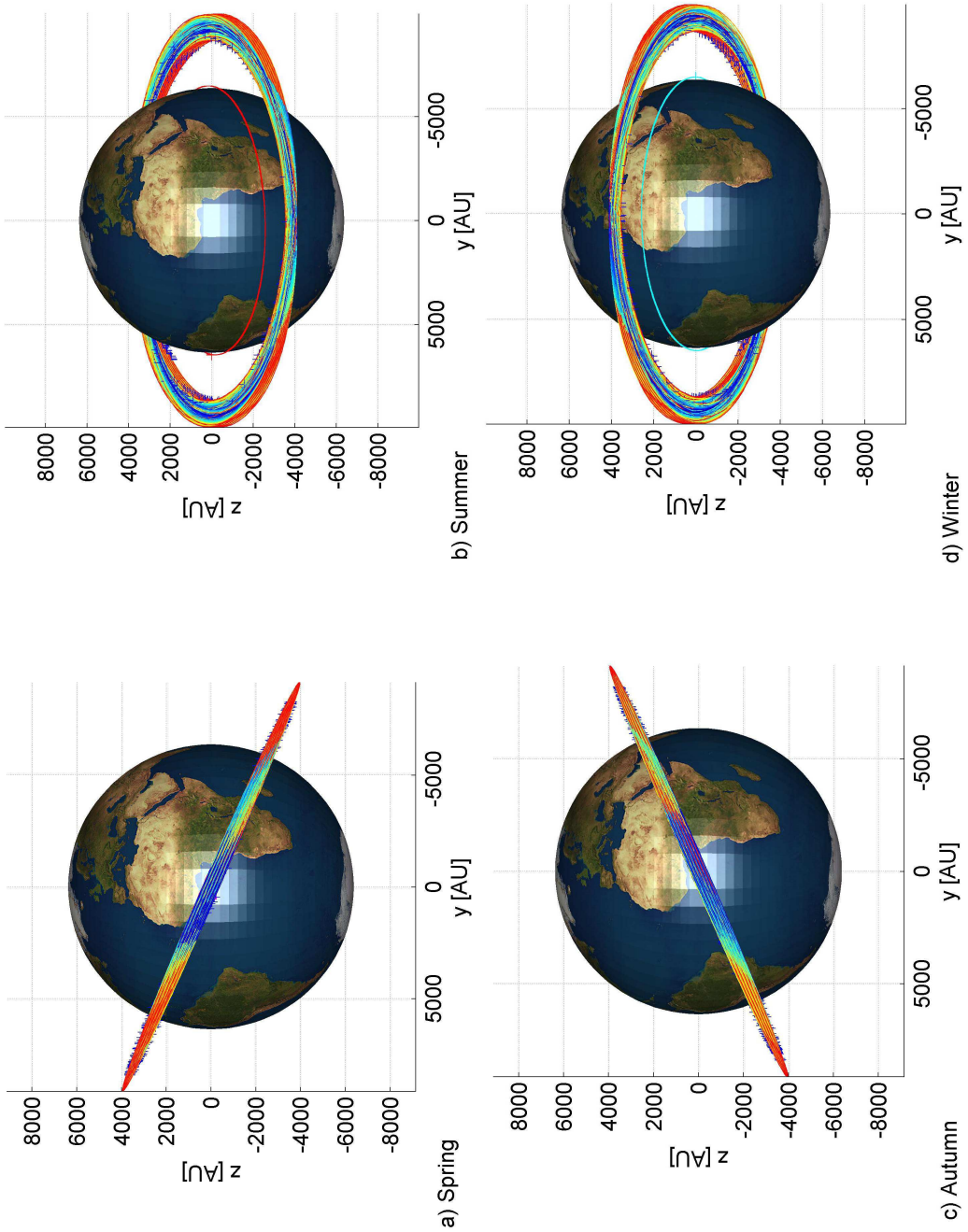

Figure A.7: Ring seasonal evolution over 20 years.

A.2 Ring model

To determine the effect that the ring has on the input of the solar flux the attenuation coefficient, as described in Sec. 5.3, must be determined. To achieve this, a two dimensional model of the ring will be constructed, using the in-plane dynamics discussed before. The attenuation coefficient is then calculated for this in-plane evolution of the dust, which, as seen in Sec. A.1.4, reproduces well the dynamical behaviour of the ring. Then the orbital plane is tilted with respect to the ecliptic plane and the inclination change added. Thus, a third dimension is added by approximating the out-of-plane evolution with a change of plane.

A.2.1 In-plane model

An expression is needed to find the radius of a grain passing through any point (ϕ,e) in the phase space. This can be derived by setting the Hamiltonian Eq. (A.6) with (ϕ,e) equal to the Hamiltonian of the feeder orbit with (0,e_f) and solving for α. Then applying Eqs. (A.3) and (A.5), gives:

$$r(\phi, e) = \frac{\frac{6F_\odot}{cn_\odot\delta}\sqrt{\frac{a}{\mu}}(e_f - e\cos\phi)}{3\left(\sqrt{1-e_f^2} - \sqrt{1-e^2}\right) + \kappa\left(\frac{1}{\sqrt{1-e_f^2}^3} - \frac{1}{\sqrt{1-e^2}^3}\right)} \tag{A.10}$$

The probability of finding any grain in a differential element around a given point in the phase space can then be determined. This is achieved by calculating the required radius of the grain using Eq. (A.10). Then the probability of any grain having the calculated radius can be found with the cumulative probability density function Eqs. (A.11) and (A.12). This gives the fraction of all grains whose evolution passes through the considered differential phase space element:

$$P\left(r \in [r_0 - dr, r_0 + dr]\right) = F_{\mu,\sigma}(r_0 + dr) - F_{\mu,\sigma}(r_0 - dr) \tag{A.11}$$

with

$$F_{\mu,\sigma} = \frac{1}{\sqrt{2\pi}} e^{-\frac{(\ln r - \mu)^2}{2\sigma^2}} \tag{A.12}$$

Next, the specific density at this position is calculated. This is the fraction of grains passing through the differential box in the phase space. Combining the specific density at the location in the phase

space with the probability density and grain size calculated before we will obtain the total fraction of grains in this element of the phase space.

The specific density is found numerically by first calculating the libration period, in the phase space, of a grain of a given size. Then, this is compared with the time derivative of the orbital parameters in the phase space at the given position calculated using Eqs. (A.1) and (A.2). Figure A.8 shows the resulting number density in the phase space for the three distributions of grain radii introduced in Sec. 5.2.2. It is shown relative to the average number density in the phase space. As expected, the highest density can be found in the release position, the feeder orbit, at $(0, e_f)$. The narrowest distribution, D1, shows high density in higher eccentricity orbits with the apogee facing within 45° of the Sun. The wider the grain size distribution the more dispersed the dust cloud is in the phase space. It can be assumed that the narrowest distribution has the highest proportion of grains blocking sunlight. To prove this assumption the dust density around the Earth in polar coordinates is calculated. The results shown in Fig. 5.7 show that the narrowest distribution does have the greatest fraction of the total number of particles between the Earth and Sun.

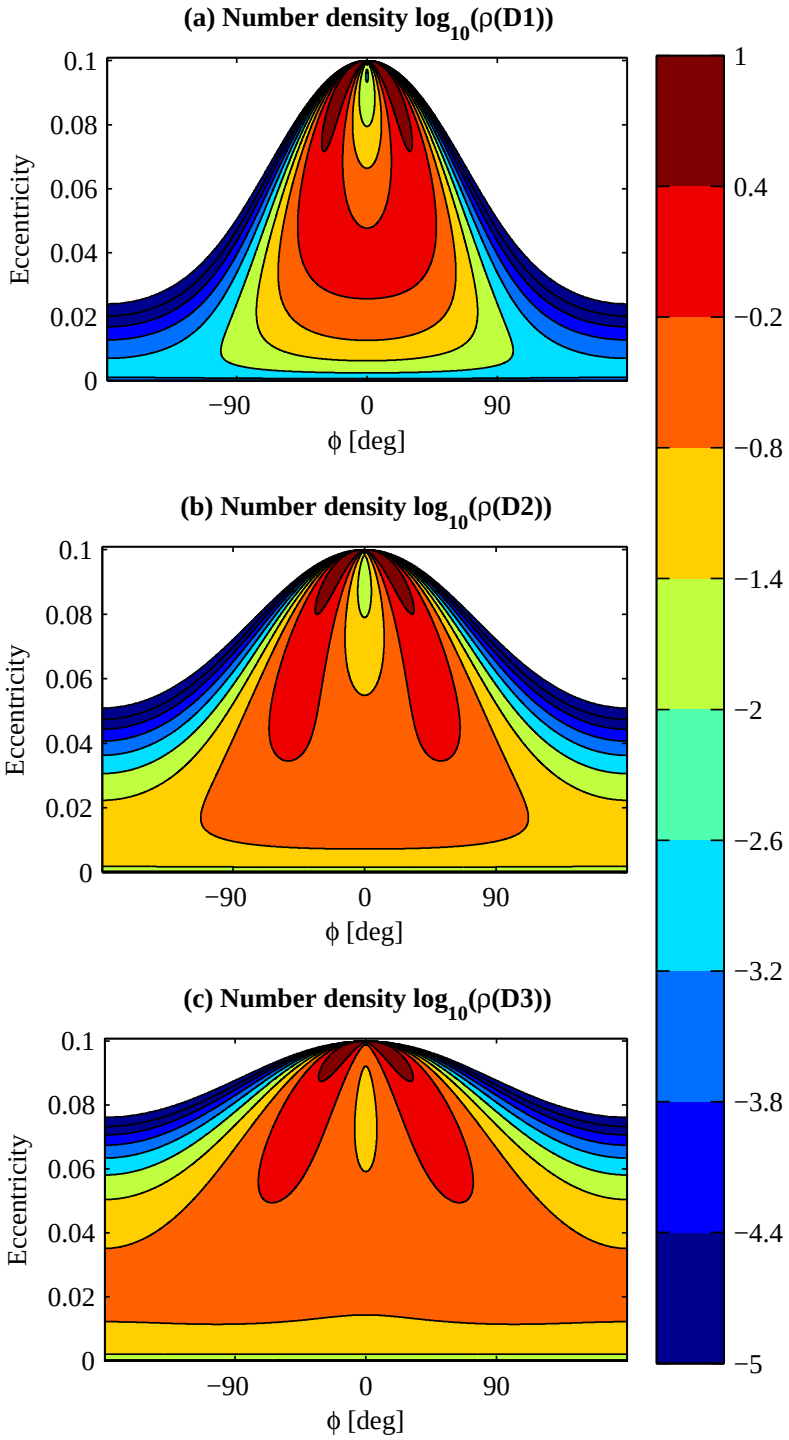

Figure A.8: Number density relative to average number density in the phase space for different grain radius distributions.

Appendix B

Beer-Lambert Law

The general case of the Beer-Lambert law is;

$$I = I_0 e^{-\int \alpha_{gr}(l)\,\mathrm{d}l} \tag{B.1}$$

where I_0 is the incoming flux, l is the path segment and α_{gr} is the attenuation coefficient due to a grain radius of R_{gr} with a number density of ρ_{gr} such that;

$$\alpha_{gr} = \pi R_{gr}^2 \rho_{gr} \tag{B.2}$$

$$= \sigma_{gr} \rho_{gr} \tag{B.3}$$

Here σ_{gr} is the cross-sectional area of a dust grain. For a scenario with a single, homogeneously distributed size of dust grain the Beer-Lambert law simplifies to;

$$I = I_0 e^{-\sigma_{gr} \rho_{gr} l} \tag{B.4}$$

A region with a combination of two grain sizes, each with a homogeneous density, distributed over different volumes can be seen in Fig. B.1. The remaining flux after attenuation in the first section, I_1, which contains two different grain sizes, can be expressed as;

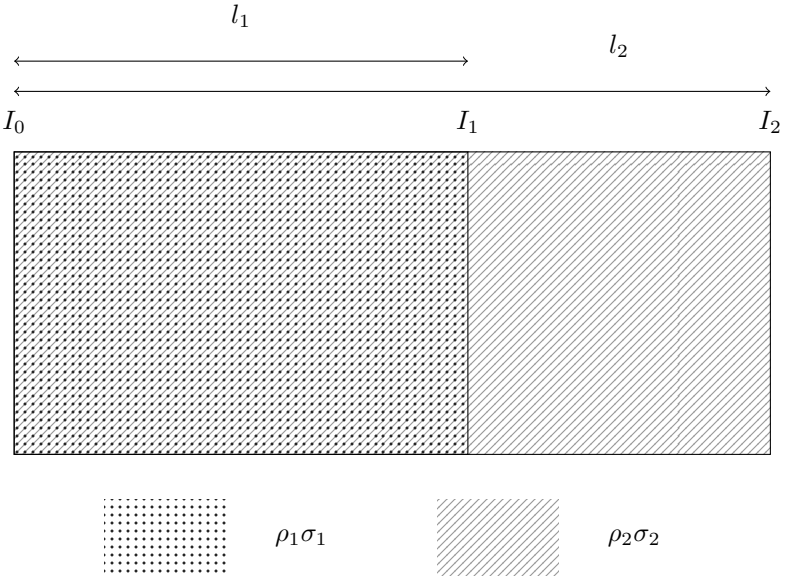

Figure B.1: Variables used in the Beer-Lambert law

$$I_1 = I_0 e^{-(\rho_1\sigma_1+\rho_2\sigma_2)l_1} \tag{B.5}$$

where it can be seen that the attenuation coefficients are simply added together within the exponential over the same path length. Now, from the general form of the Beer-Lambert law, the further attenuation of the incoming flux due to the grains in the second region can be expressed as;

$$I_2 = I_1 e^{-\rho_2\sigma_2(l_2-l_1)} \tag{B.6}$$

thus giving the final, combined, attenuation;

$$I_2 = I_0 e^{-(\rho_1\sigma_1 l_1+\rho_2\sigma_2 l_2)} \tag{B.7}$$

This demonstrates that the attenuation coefficients of multiple grain sizes with varying path lengths integrated along the same line can be easily combined.